



Fermilab

**Search for $\nu_\mu(\bar{\nu}_\mu) \rightarrow \nu_e(\bar{\nu}_e)$ Oscillations in the E815(NuTeV)
Fixed Target Neutrino Experiment at Fermilab**

by

Sergey E Avvakumov

Submitted in Partial Fulfillment

of the

Requirements for the Degree

Doctor of Philosophy

Supervised by

Professor Arie Bodek

Department of Physics and Astronomy

The College

Arts and Sciences

University of Rochester

Rochester, New York

2001

Curriculum Vitae

The author was born in Novosibirsk, Russia on October 8, 1971. He graduated from Moscow Institute of Physics and Technology with a Bachelor of Science degree in 1993. He received a Master of Science degree from Moscow Institute of Physics and Technology in 1995. He came to the University of Rochester in the fall of 1995 to continue his studies in the field of elementary particle physics. He joined the NuTeV neutrino experiment at Fermi National Accelerator Laboratory where he conducted his PhD thesis research under the supervision of Prof. Arie Bodek. In May 1997, he received a Master of Arts degree from the Department of Physics and Astronomy at the University of Rochester.

Abstract

Limits on $\nu_\mu \rightarrow \nu_e$ and $\bar{\nu}_\mu \rightarrow \bar{\nu}_e$ oscillations (separately) are extracted using the NuTeV detector with sign selected ν_μ and $\bar{\nu}_\mu$ beams. A statistical analysis of the longitudinal shower energy deposition in the neutrino target-calorimeter is used to identify the fraction of $\nu_e N$ charged-current interactions in a sample $\nu_\mu N \rightarrow \nu_\mu X$ candidate events. Neutrino energies range from 30 to 350 GeV and ν_μ flight lengths vary from 0.9 to 1.4 km. In $\bar{\nu}_\mu$ mode, the NuTeV data exclude the high Δm^2 $\bar{\nu}_\mu \rightarrow \bar{\nu}_e$ oscillation region favored by the LSND experiment. In addition, if we assume no CP violation in the neutrino sector, the NuTeV results exclude $\nu_\mu(\bar{\nu}_\mu) \rightarrow \nu_e(\bar{\nu}_e)$ oscillations with $\sin^2 2\alpha > 0.9 \times 10^{-3}$ for large $\Delta m^2 \gg 1000 \text{ eV}^2$. For $\sin^2 2\alpha = 1$, $\Delta m^2 > 1.6 \text{ eV}^2$ is excluded.

Contents

1	Introduction	1
1.1	Outline of the Thesis	2
1.2	Neutrino Masses and Oscillations	2
1.2.1	The general case	3
1.2.2	Oscillations for the case of two-neutrino mixing	5
1.3	Neutrino Oscillation Experiments	7
1.3.1	Accelerator Experiments	9
2	Detector	12
2.1	Neutrino Interactions and Their Detectors	12
2.2	Deep inelastic scattering	13
2.3	The NuTeV Detector	16
2.3.1	Calibration Beam	20
2.3.2	The Target Calorimeter	22
2.3.3	Muon Spectrometer	25
2.3.4	Data Acquisition	27
3	Neutrino Flux	30
3.1	Neutrino Beam	30
3.2	Flux Monte Carlo Simulation	32

3.2.1	Flux Tuning	33
3.3	Electron Neutrino Flux Systematic Uncertainties	36
4	Shower Shape Analysis	44
4.1	Possible Final States of Neutrino Interactions in the NuTeV Detector	44
4.1.1	Electromagnetic vs Hadronic Showers	48
4.1.2	The η -parameter	51
4.2	Electron Neutrino Flux Measurement	54
4.3	Adding a Muon to the Short Events	61
4.4	Short Charged-Current Events	63
4.5	Biases and Systematic Effects in the η -analysis: Need for a Monte Carlo Simulation	66
5	Data Selection and Analysis	69
5.1	Shower Selection	69
5.2	Vertex Finding Method	70
5.2.1	Longitudinal Position: “PLACE” Algorithm	70
5.2.2	Transverse Position	73
5.3	Calorimeter Energy	74
5.4	Event Selection	74
5.5	The NuTeV Data Sample	78
6	Monte Carlo Simulation of the η-analysis	81
6.1	NuTeV Monte Carlo simulation packages NUMONTE and McNuTeV	82
6.1.1	NUMONTE	82
6.1.2	McNuTeV	83
6.2	GEANT Simulation of Electromagnetic Showers in the NuTeV Detector	86

6.2.1	Comparison of the GEANT Monte Carlo with Test Beam Data	86
6.3	Simulation of Charged-Current Electron Neutrino Events	88
6.4	Final State Radiation $\mu \rightarrow \mu + \gamma$ in Charged-Current Events	93
6.4.1	The De Rujula Approximation	94
6.4.2	PYTHIA Monte Carlo Generator	95
6.4.3	Correcting the η -distributions of ν_μ Charged-Current Events	96
6.4.4	Systematic Uncertainty from Radiative Photons	98
6.5	Simulation of Neutrino Events in the NuTeV Detector	99
6.5.1	Full Hit-Level Monte Carlo Simulation of Neutrino Interac- tions in the NuTeV detector	101
6.5.2	η -distributions of the Simulated Neutrino Events	103
6.5.3	η -analysis of the Simulated Neutrino Events	105
7	η-analysis Results	114
7.1	Statistical analysis of the η -distributions	114
7.2	Corrections to the measured electron neutrino flux	122
7.3	Systematic Uncertainties	129
8	Results and Conclusions	137
8.1	$\nu_\mu \rightarrow \nu_e$ Oscillations	137
8.2	$\nu_\mu \rightarrow \nu_e$ Oscillation Analysis	140
8.2.1	Extracting the Parameters	141
8.2.2	Results of the analysis in neutrino mode	144
8.2.3	Results of the analysis in anti-neutrino mode	144
8.2.4	Results of the combined analysis of neutrino and anti-neutrino mode	148
8.2.5	Comparison with other oscillation search experiments	153

8.3	Conclusions	156
A	Shower Length Analysis	167
B	Data Fits η_3	188
C	Data Fits η_2	206

List of Figures

1.1	Current status of the excluded region of $\sin^2 2\alpha$ and Δm^2 for $\nu_\mu \rightarrow \nu_e$ oscillations from accelerator experiments. The shaded bands are the LSND 90% (darker) and 99% (lighter) confidence allowed regions. .	11
2.1	Feynman diagram of a charged-current neutrino interaction.	12
2.2	Feynman diagram of the neutral-current interaction.	13
2.3	Schematic diagram of charged-current neutrino-nucleon scattering vi Exchange of W boson.	14
2.4	Schematic picture of the NuTeV detector	17
2.5	An event-display of a ν_μ charged-current interaction in the NuTeV detector.	17
2.6	Event display of a neutral-current event in the NuTeV detector. . .	18
2.7	Accelerator time structure. Note that the interval between the last neutrino ping and the slow spill calibration beam is only 1.4 seconds, allowing a continuous <i>in situ</i> calibration.	20

2.8	A schematic drawing of the NuTeV calibration beam spectrometer system. The elements of the spectrometer are located in the beam line enclosures NEB, NKC and in in the Lab F detector hall. The spectrometer consists of the seven drift chambers - HAPPY, SLEEPY, DOPEY, SNEEZY, GRUMPY, BASHFUL and DOC (yes, the dwarves) and four dipole magnets - NTC1, NTC2, NTC3 and NTCR. Cherenkov detector and the transition radiation detector (TRD) are used for particle identification. The large distances between the chamber stations allow an accurate determination of the test beam momentum.	21
2.9	Geometry of one unit of the calorimeter. One calorimeter-unit layer consists of two counter-unit layers and one drift chamber. This unit is repeated 42 times to make up the entire calorimeter. (One counter-unit layer consists of a scintillation counter and two steel plates - one on each side of the counter).	23
2.10	A schematic drawing of a NuTeV scintillation counter.	24
2.11	Test beam data and fits to the measured hadron energy response and resolution versus reconstructed beam momentum (a) Top - The measured non-linearity of the response and a fit using Groom's parameterization for the fractional electromagnetic component in hadron showers (b) Bottom - The measured hadron energy resolution (extracted from the data assuming a Poisson distribution) compared to a fit of the form $\sigma(E)/E = A \oplus \frac{B}{\sqrt{E}}$. The open square symbols are lower energy runs with slightly different cuts which are not used in the fits.	26
3.1	The Fermilab Tevatron and the NuTeV neutrino beam line.	31

3.2	The Sign Selected Quadrupole Train (SSQT).	32
3.3	Neutrino flux: crosses - data, blue line - untuned Monte Carlo, red - tuned Monte Carlo. Top plot - neutrino mode, bottom plot - anti-neutrino mode.	34
3.4	Beam Monte Carlo simulation of flux spectra for individual neutrino species. Top plot - neutrino mode; Bottom plot - anti-neutrino mode.	36
3.5	Fractional change in the ν_e flux predicted by the beam Monte Carlo simulation from a 1 sigma shift in the K_{e3} branching ratio. Top plot - neutrino mode; Bottom plot - anti-neutrino mode.	38
3.6	Fractional change in the ν_e flux predicted by the beam Monte Carlo simulation from a 1 sigma shift in the absolute hadron energy scale. Top plot - neutrino mode; Bottom plot - anti-neutrino mode.	39
3.7	Fractional change in the ν_e flux predicted by the beam Monte Carlo simulation from a 1 sigma shift in the muon energy scale. Top plot - neutrino mode; Bottom plot - anti-neutrino mode.	40
3.8	Fractional change in the ν_e flux predicted by the beam Monte Carlo simulation from a 1 sigma shift in the electron energy calibration C_e . Top plot - neutrino mode; Bottom plot - anti-neutrino mode.	41
3.9	Fractional change in the ν_e flux predicted by the beam Monte Carlo simulation from a 1 sigma shift in the level of charm hadron pro- duction. Top plot - neutrino mode; Bottom plot - anti-neutrino mode.	42
3.10	Fractional change in the ν_e flux predicted by the beam Monte Carlo simulation from a 1 sigma shift in the level of K_L production. Top plot - neutrino mode; Bottom plot - anti-neutrino mode.	43

4.1	Schematic views of neutrino events in the NuTeV detector: a) ν_μ charged-current, b) ν_μ neutral-current, c) ν_e charged-current, d) ν_e neutral-current	45
4.2	Fraction of electromagnetic energy in a hadronic-shower f_{π^0} initiated by test beam pions as a function of the incident hadron energy for three different hadron shower generators: GHEISHA, GFLUKA, and GCALOR; the Wigmans (dashed curve) and Groom (solid curve) parameterizations are also shown.	46
4.3	The cumulative fractional hadron-shower energy as a function of the total number of consecutive counters from the beginning of the shower. Note that for all hadron energies a total of 20 counters (about 2m of iron) is sufficient for full longitudinal containment of hadron showers.	48
4.4	Comparative lengths of hadronic and electromagnetic showers in the NuTeV calorimeter and the definition of the η_3 parameter.	50
4.5	Distributions of the η_3 parameter for ν_μ and ν_e charged-current events with a calorimeter energy $E_{cal} = 100 - 115 \text{ GeV}$ (ν_μ CC distribution is obtained from the data, ν_e CC is obtained using the procedure described in Section 6.3, that combines the hadronic showers from the data with the electromagnetic showers from Monte Carlo).	52
4.6	Distributions of the η_3 parameter for $\bar{\nu}_\mu$ and $\bar{\nu}_e$ charged-current events with a calorimeter energy $E_{cal} = 100 - 115 \text{ GeV}$ ($\bar{\nu}_\mu$ CC distribution is obtained from the data, $\bar{\nu}_e$ CC is obtained using the procedure described in Section 6.3, that combines the hadronic showers from the data with the electromagnetic showers from Monte Carlo).	53

4.7	Illustration of the statistical analysis of η_3 distributions, neutrino mode. Here, the distribution of short events in the data $\eta_3(Short)$ is fit to a sum of the distributions of long events $\eta_3(Long)$, ν_e charged-current events $\eta_3(\nu_e^{CC})$, ν_μ short charged-current events $\eta_3(Short CC)$ and cosmic events $\eta_3(Cosmic)$. The result of the fit - distribution $\eta_3(Fit)$ is also shown.	56
4.8	Illustration of the statistical analysis of η_3 distributions, anti-neutrino mode. Here, the distribution of short events in the data $\eta_3(Short)$ is fit to a sum of the distributions of long events $\eta_3(Long)$, ν_e charged-current events $\eta_3(\nu_e^{CC})$, ν_μ short charged-current events $\eta_3(Short CC)$ and cosmic events $\eta_3(Cosmic)$. The result of the fit - distribution $\eta_3(Fit)$ is also shown.	57
4.9	a) Muon tracks are added by software to neutrino events in the short sample. b) Muon tracks from the long ν_μ charged-current event sample are used in this procedure.	62
4.10	The η_3 distributions of ν_μ short events before (red) and after (black) a muon track has been added in software.	63
4.11	Schematic view of a short charged-current event	64
4.12	The η_3 distributions of “long” events (red) and of simulated short ν_μ CC events (black) with a second muon track has been added in software.	65
4.13	Feynman diagram of a dilepton event.	66
5.1	Interaction region finding algorithm: a) a long event found, b) a short event found. Energy deposition in each of the 84 scintillation counters is represented by a column of “*”s. The clusters of $S - bit ON$ counters are shown with delimiters $<$ and $>$	71

5.2	$NN - PLACE$ algorithm: dependence of N on calorimeter energy E_{cal}	73
5.3	An event which failed the deep-mu cut 5.11. This event is most likely a neutrino induced deep-mu event.	77
6.1	E_{cal} distributions of “long events” for data (solid circles) and Monte Carlo (solid line). The Monte Carlo prediction for the E_{cal} distributions of ν_e CC events are also shown (dashed line); a) - neutrino mode, b) - anti-neutrino mode.	84
6.2	Electromagnetic showers: fraction of the total shower energy, deposited in counters 84, 83, and 82, circles - test beam data, line - McNuTeV simulation. $P_{TB} = 20 \text{ GeV}$ (a), 30 GeV (b), 50 GeV (c), 75 GeV (d).	87
6.3	Calibration and resolution of the McNuTeV simulation of electromagnetic showers of test beam electrons: a) $\langle E_{cal}/E_e \rangle$ versus electron energy E_e ; b) resolution function σ/E_e versus electron energy E_e . Note that the two terms in the resolution function should be added in quadrature.	89
6.4	Simulation of ν_e CC events with an additional muon: A McNuTeV simulated EM shower is added to a randomly chosen “Long” event with the appropriate hadron energy in the calorimeter.	91
6.5	Examples of η_3 distributions of simulated ν_e events (triangles - neutrino mode, circles - anti-neutrino mode). Here, E_{cal} bins of $50 - 60$, $87 - 95$, $130 - 145$ and $200 - 225 \text{ GeV}$ are shown.	92
6.6	Right - CC event photon emission off the final state muon; left - NC event - no emission possible.	93

6.7	Radiative correction $\Delta(x, y, E_{\nu(\bar{\nu})})$: De Rujula “leading log” approximation - line, PYTHIA simulation - circles, a) neutrino $E_\nu = 50 \text{ GeV}$, b) anti-neutrino $E_{\bar{\nu}} = 50 \text{ GeV}$, c) neutrino $E_\nu = 100 \text{ GeV}$, d) anti-neutrino $E_{\bar{\nu}} = 100 \text{ GeV}$, e) neutrino $E_\nu = 200 \text{ GeV}$, f) anti-neutrino $E_{\bar{\nu}} = 200 \text{ GeV}$; values of PYTHIA parameter C_γ shown.	97
6.8	PYTHIA simulation: spectra of radiative photons a) neutrino mode $E_{had} = 30 - 35 \text{ GeV}$, b) anti-neutrino mode $E_{had} = 30 - 35 \text{ GeV}$, c) neutrino mode $E_{had} = 95 - 105 \text{ GeV}$, d) anti-neutrino mode $E_{had} = 95 - 105 \text{ GeV}$	98
6.9	Correcting η_3 distributions for radiation of final state muons (Long events before correction - circles, after correction - triangles). Shown are E_{cal} bins of $50 - 60, 87 - 95, 130 - 145, 220 - 225 \text{ GeV}$ in neutrino mode.	99
6.10	Correcting η_3 distributions for radiation off final state muons (Long events before correction - circles, after correction - triangles). Shown are E_{cal} bins of $50 - 60, 87 - 95, 130 - 145, 220 - 225 \text{ GeV}$ in anti-neutrino mode.	100
6.11	Calibration and resolution of the Monte Carlo simulation of the hadronic showers.	103
6.12	η_3 distributions of “long” events in neutrino mode (data - circles, Monte Carlo - triangles). Shown are E_{cal} bins of $50 - 60, 87 - 95, 130 - 145, 220 - 225 \text{ GeV}$	104
6.13	η_3 distributions of “long” events in anti-neutrino mode (data - circles, Monte Carlo - triangles). Shown are E_{cal} bins of $50 - 60, 87 - 95, 130 - 145, 220 - 225 \text{ GeV}$	105

6.14	Top plot - mean values of η_3 of “long” events neutrino mode (data - circles, Monte Carlo - triangles). Bottom plot - ratio $\langle \eta_3 \rangle_{Data} / \langle \eta_3 \rangle_{MC}$.	106
6.15	Top plot - mean values of η_3 of “long” events in anti-neutrino mode (data - circles, Monte Carlo - triangles). Bottom plot - ratio $\langle \eta_3 \rangle_{Data} / \langle \eta_3 \rangle_{MC}$.	107
6.16	Correction to the measured electron neutrino flux due to imperfect modeling of ν_e CC events, based on Monte Carlo simulation of the shower shape analysis.	108
6.17	Correction to the measured electron neutrino flux due to imperfect modeling of the short CC events, based on Monte Carlo simulation of the shower shape analysis.	110
6.18	Correction to the measured electron neutrino flux due to the shift in the mean momentum of the muon tracks (which were added to the short events) based on a full Monte Carlo simulation of the shower shape analysis.	111
6.19	Correction to the measured electron neutrino flux from the effect of adding muon tracks at $NN - PLACE$, based on a full Monte Carlo simulation of the shower shape analysis.	112

- 7.1 Fit of the η_3 distributions for $E_{cal} = 115 - 130 \text{ GeV}$ in neutrino mode. Even *PLACE* events - top left plot, odd *PLACE* events - top right plot. The distribution of short events (solid circles), is fit to a sum of the distributions of the long events (solid squares), ν_e CC events (upside-down triangles), short CC events (open circles), and cosmic events (open squares), the best fit distribution is also shown (triangles). The fractional difference between the “best fit” and data distributions - even *PLACE* events - bottom left, odd *PLACE* events - bottom right. 117
- 7.2 Fit of the η_3 distributions for $E_{cal} = 115 - 130 \text{ GeV}$ in anti-neutrino mode. Even *PLACE* events - top left plot, odd *PLACE* events - top right plot. The distribution of short events (solid circles), is fit as a sum of the distributions of the long events (solid squares), ν_e CC events (upside-down triangles), short CC events (open circles), and cosmic events (open squares), the best fit distribution is also shown (triangles). The fractional difference between the “best fit” and data distributions - even *PLACE* events - bottom left, odd *PLACE* events - bottom right. 118
- 7.3 Fit of η_2 distributions for $E_{cal} = 115 - 130 \text{ GeV}$ in neutrino mode. Even *PLACE* events - top left plot, odd *PLACE* events - top right plot. The distribution of short events (solid circles), is fit as a sum of the distributions of the long events (solid squares), ν_e CC events (upside-down triangles), short CC events (open circles), and cosmic events (open squares), the best fit distribution is also shown (triangles). The fractional difference between the “best fit” and data distributions - even *PLACE* events - bottom left, odd *PLACE* events - bottom right. 120

- 7.4 Fit of η_2 distributions for $E_{cal} = 115 - 130 \text{ GeV}$ in anti-neutrino mode. Even *PLACE* events - top left plot, odd *PLACE* events - top right plot. The distribution of short events (solid circles), is fit as a sum of the distributions of the long events (solid squares), ν_e CC events (upside-down triangles), short CC events (open circles), and cosmic events (open squares), the best fit distribution is also shown (triangles). The fractional difference between the “best fit” and data distributions - even *PLACE* events - bottom left, odd *PLACE* events - bottom right. 121
- 7.5 Result of the η_3 analysis, neutrino mode. Top plot - ν_e flux: beam Monte Carlo prediction (no oscillations) - line, η_3 measurement - circles. Bottom plot - ratio $(\# \nu_e(measured) - \# \nu_e(MC)) / \# \nu_e(MC)$. 125
- 7.6 Result of η_3 analysis, anti-neutrino mode. Top plot - ν_e flux: beam Monte Carlo prediction (no oscillations) - line, η_3 measurement - circles. Bottom plot - ratio $(\# \nu_e(measured) - \# \nu_e(MC)) / \# \nu_e(MC)$. 126
- 7.7 Result of η_2 analysis, neutrino mode. Top plot - ν_e flux: beam Monte Carlo prediction (no oscillations) - line, η_2 measurement - circles. Bottom plot - ratio $(\# \nu_e(measured) - \# \nu_e(MC)) / \# \nu_e(MC)$. 127
- 7.8 Result of η_2 analysis, anti-neutrino mode. Top plot - ν_e flux: beam Monte Carlo prediction (no oscillations) - line, η_2 measurement - circles. Bottom plot - ratio $(\# \nu_e(measured) - \# \nu_e(MC)) / \# \nu_e(MC)$. 128
- 7.9 Systematic uncertainty from the electron energy scale: change in the measured number of ν_e ’s from a one sigma shift in C_e 135
- 7.10 Systematic uncertainty from emission of radiative photons. 136

8.1	Electron neutrino flux in the NuTeV detector: Beam MC prediction for no oscillations is compared to the additional electron neutrino flux that would originate from $\nu_\mu \rightarrow \nu_e$ oscillations for $\Delta m^2 = 50, 100, 1000 \text{ eV}^2$ and $\sin^2 2\theta = 0.005$, for neutrino mode - top, anti-neutrino mode - bottom.	138
8.2	Oscillation parameter fits in neutrino mode: Top plot - best fit $\sin^2 2\theta$; Bottom plot - χ^2 at the minimum.	146
8.3	Sensitivity and upper limits at 90% confidence level for $\nu_\mu \rightarrow \nu_e$ oscillations. The excluded region of $\sin^2(2\theta)$ and Δm^2 is the area to the right of the solid curve.	148
8.4	Oscillation parameter fits in neutrino mode: Values of the systematic coefficients C_1 through C_8 after χ^2 minimization.	149
8.5	Oscillation parameter fits in neutrino mode: Values of the systematic coefficients C_9 through C_{16} after χ^2 minimization.	150
8.6	Oscillation parameter fits in anti-neutrino mode: Top plot - best fit $\sin^2 2\theta$; Bottom plot - χ^2 at the minimum.	151
8.7	Sensitivity and upper limits at 90% confidence level for $\bar{\nu}_\mu \rightarrow \bar{\nu}_e$ oscillations. The excluded region of $\sin^2(2\theta)$ and Δm^2 is the area to the right of the solid curve.	153
8.8	Oscillation parameter fits in anti-neutrino mode: Values of the systematic coefficients C_1 through C_8 after χ^2 minimization.	154
8.9	Oscillation parameter fits in anti-neutrino mode: Values of the systematic coefficients C_9 through C_{16} after χ^2 minimization.	155
8.10	Oscillation parameter fits in neutrino and anti-neutrino modes combined: Top plot - best fit $\sin^2 2\theta$; Bottom plot - χ^2 at the minimum.	156

8.11	Sensitivity and upper limits at 90% confidence level for the combined data for $(\nu_\mu, \bar{\nu}_\mu) \rightarrow (\nu_e, \bar{\nu}_e)$ oscillations. The excluded region of $\sin^2(2\theta)$ and Δm^2 is the area to the right of the solid curve.	157
8.12	Oscillation parameter fits in neutrino and anti-neutrino modes combined: Values of the systematic coefficients C_1 through C_8 after χ^2 minimization.	158
8.13	Oscillation parameter fits in neutrino and anti-neutrino modes combined: Values of the systematic coefficients C_9 through C_{16} after χ^2 minimization.	159
8.14	Sensitivity and upper limits at 90% confidence level for $\nu_\mu \rightarrow \nu_e$ oscillations compared to data from other experiments. The excluded region of $\sin^2(2\theta)$ and Δm^2 is the area to the right of the solid curve.	160
8.15	Sensitivity and upper limits at 90% confidence level for $\bar{\nu}_\mu \rightarrow \bar{\nu}_e$ oscillations compared to data from other experiments. The excluded region of $\sin^2(2\theta)$ and Δm^2 is the area to the right of the solid curve.	161
8.16	Sensitivity and upper limits at 90% confidence level for the combined data for $(\nu_\mu, \bar{\nu}_\mu) \rightarrow (\nu_e, \bar{\nu}_e)$ oscillations compared to data from other experiments. The excluded region of $\sin^2(2\theta)$ and Δm^2 is the area to the right of the solid curve.	162
A.1	Results of the analysis using the shower length distributions in neutrino mode. Top plot: ν_e flux. The beam Monte Carlo prediction (no oscillations) are shown as the solid line; the measurements using the shower length distributions are the circles. Bottom plot: The ratio $(\#\nu_e(measured) - \#\nu_e(MC))/\#\nu_e(MC)$	168

A.2	Result of the analysis of shower length distributions in anti-neutrino mode. Top plot: ν_e flux. The beam Monte Carlo prediction (no oscillations) are shown as the solid line; the measurements using the shower length distributions are the circles. Bottom plot: The ratio $(\#\nu_e(measured) - \#\nu_e(MC))/\#\nu_e(MC)$	169
-----	--	-----

List of Tables

1.1	Values of the parameter $(\Delta m^2)_0$ qualitatively characterizing the sensitivity of a given experiment searching for neutrino oscillations. E and L are the neutrino energy and the source-detector distance typical of the experiment.	8
2.1	Amount of material in one structural unit of the NuTeV target-calorimeter in cm, in units of radiation length X_0 , and in nuclear interaction length λ_I	25
2.2	NuTeV trigger list with descriptions	29
3.1	Fractional neutrino fluxes from various sources.	35
4.1	Calorimeter energy (E_{cal}) bins.	58
5.1	NuTeV data sample, neutrino mode. The numbers of events that passed all analysis cuts are shown for each bin of the calorimeter energy E_{vis} . The number of short ν_μ charged-current events, predicted by Monte Carlo is shown in the last column.	79

5.2	NuTeV data sample, anti-neutrino mode. The numbers of events that passed all analysis cuts are shown for each bin of the calorimeter energy E_{vis} . The number of short ν_μ charged-current events, predicted by Monte Carlo is shown in the last column.	80
6.1	Values of the PYTHIA parameter C_γ , tuned to reproduce the De Rijula calculation of the radiative corrections for $E_{\nu,p} = 50, 100, 200 \text{ GeV}$	95
7.1	The η_3 fit results in neutrino mode. Shown are the central values and standard deviations of the parameters α and β , the correlation $c_{\alpha\beta}$, and the χ^2/DOF	119
7.2	The η_3 fit results in anti-neutrino mode. Shown are the central values and standard deviations of the parameters α and β , the correlation $c_{\alpha\beta}$, and the χ^2/DOF	122
7.3	The η_2 fit results in neutrino mode. Shown are the central values and standard deviations of the parameters α and β , the correlation $c_{\alpha\beta}$, and the χ^2/DOF	123
7.4	The η_2 fit results in anti-neutrino mode. Shown are the central values and standard deviations of the parameters α and β , the correlation $c_{\alpha\beta}$, and the χ^2/DOF	124
7.5	Neutrino mode. Numbers of electron neutrino events: Predicted by the beam Monte Carlo simulation; Extracted from the η_3 fits with corresponding statistical error; Extracted from the η_2 fits with corresponding statistical error; Difference between η_3 and η_2 measurements.	129

7.6	Anti-neutrino mode. Numbers of electron neutrino events: Predicted by the beam Monte Carlo simulation; Extracted from the η_3 fits with corresponding statistical error; Extracted from the η_2 fits with corresponding statistical error; Difference between η_3 and η_2 measurements.	130
7.7	ν_e CC modeling correction.	131
7.8	Short CC modeling correction.	131
7.9	Muon momentum correction.	132
7.10	$NN - PLACE$ correction.	132
7.11	Electron neutrino flux in neutrino mode: Predicted by the beam Monte Carlo simulation; Extracted from the η_3 fits (after pull corrections) with corresponding statistical error; Extracted from the η_2 fits (after pull corrections) with corresponding statistical error; Difference between the η_3 and η_2 measurements.	133
7.12	Electron neutrino flux in anti-neutrino mode: Predicted by the beam Monte Carlo simulation; Extracted from the η_3 fits (after pull corrections) with corresponding statistical error; Extracted from the η_2 fits (after pull corrections) with corresponding statistical error; Difference between the η_3 and η_2 measurements.	134
8.1	Oscillation parameter fits in neutrino mode: Δm^2 , central value of $\sin^2 2\theta$, 1σ error, sensitivity, 90% CL upper limit.	145
8.2	Oscillation parameter fits in anti-neutrino mode: Δm^2 , central value of $\sin^2 2\theta$, 1σ error, sensitivity, 90% CL upper limit.	147
8.3	Oscillation parameter fits from a combined analysis of data in neutrino and anti-neutrino modes: Δm^2 , central value of $\sin^2 2\theta$, 1σ error, sensitivity, 90% CL upper limit.	152

Chapter 1

Introduction

Neutrinos are the least understood particles among the well-established fundamental fermions. Although neutrinos have been successfully used as powerful probes of elementary interactions, very little is known about the general properties of neutrinos themselves. For example, the masses and magnetic moments of the various types of neutrinos are not known. We also do not know if neutrinos are Dirac particles (i.e. if the anti-neutrino is the anti-particle of the neutrino), or if neutrinos and anti-neutrinos are two helicity states of the same particle. The question of whether neutrinos have mass has important implications for fundamental problems in both particle physics and cosmology. The possibility of neutrino mass appears in a variety of topics such as lepton family number conservation, the mass of the universe, and the experimentally observed neutrino deficit from solar and atmospheric sources. Neutrino oscillations are one likely consequence of a non-zero neutrino mass. If there are neutrino oscillations, the neutrino mass eigenstates are not the same as the pure weak-interaction eigenstates.

The strong evidence in favor of the oscillations of atmospheric neutrinos reported by the Super-Kamiokande experiment [11] was a major experimental break-

through. These results transformed the field of neutrino oscillations from a theoretical hypothesis into a universally accepted phenomenon.

1.1 Outline of the Thesis

In this thesis we describe a search for $\nu_\mu \rightarrow \nu_e$ oscillations performed with the NuTeV detector. The data sample was collected during the 1996-1997 fixed target run at Fermilab. As a result of this search we present new limits on $\nu_\mu \rightarrow \nu_e$, $\bar{\nu}_\mu \rightarrow \bar{\nu}_e$ oscillations, obtained from an analysis of neutrino and anti-neutrino data separately. In addition we combine both sets of data and present limits on $\nu_\mu(\bar{\nu}_\mu) \rightarrow \nu_e(\bar{\nu}_e)$ oscillations.

The chapters of the thesis are organized as follows: Chapter 1 gives an introduction to the neutrino oscillations formalism. Chapter 2 describes the NuTeV detector. Chapter 3 describes the determination of the predicted neutrino flux, its Monte Carlo simulation and systematic uncertainties. Chapter 4 describes the analysis method used in the direct measurement of the ν_e flux from the event sample. Chapter 5 describes the data selection process and Chapter 6 describes the analysis Monte Carlo. The ν_e flux measurement results are presented in Chapter 7. The results of the oscillation analysis is presented in Chapter 8.

1.2 Neutrino Masses and Oscillations

The possibility of neutrino oscillations was first considered by B.Pontecorvo [1] in 1957-58, when he proposed that the neutrinos produced in weak interaction processes may not be the mass eigenstates of the overall Hamiltonian, but are a superposition of other neutrino states with definite mass. This is analogous to the case of the $|K^0\rangle$, $|\bar{K}^0\rangle$ particles which are superpositions of $|K_1\rangle$, $|K_2\rangle$ - i.e.

meson states with definite mass and width. At the time of Pontecorvo's paper only one type of neutrino was known to exist. Theoretical work in later years ([2],[3]) extended this hypothesis to the case of possible mixing between three or more neutrino flavors. The first phenomenological theories of massive neutrinos were based on the Majorana neutrino model as discussed in [4]. Massive neutrino with Dirac masses are discussed in [5] and the general case of the Dirac-Majorana scheme is discussed in [6]. The fact that a number of experiments ([7]-[18]) have presented data supporting the possibility of neutrino oscillations (and consequently the possibility of massive neutrinos) sparked great interest in this topic. The current state of the field of neutrino oscillations and mixing is summarized in several recent review articles [20], [21].

1.2.1 The general case

Let's introduce the general formalism that represents the mixing of neutrino flavors, which is analogous to the CKM formalism describing quark mixing. The left handed components of the neutrino fields $\nu_{\alpha L} (\alpha = e, \mu, \tau)$ are unitary linear combinations of the left handed components of n (Dirac or Majorana) neutrino fields ν_k ($k = 1, \dots, n$) with masses m_k :

$$\nu_{\alpha L} = \sum_{k=1}^n U_{\alpha k} \nu_{kL} . \quad (1.1)$$

The number of massive neutrinos (n) depends on the model and in the general case can be more than three (e.g. it can include some number of unobservable sterile neutrinos). If all the mass differences are small, then a neutrino flavor state ν_{α} produced in a weak interaction process (as the $\pi^+ \rightarrow \mu^+ \nu_{\mu}$ decay) with momentum $p_k \gg m_k$ is described by a coherent superposition of neutrino mass eigenstates:

$$|\nu_\alpha\rangle = \sum_{k=1}^n U_{\alpha k}^* |\nu_k\rangle . \quad (1.2)$$

Here $|\nu_\alpha\rangle$ are flavor eigenstates and $|\nu_k\rangle$ are mass eigenstates with masses m_k . In the ultra-relativistic limit, the neutrino energy is

$$E_k = \sqrt{p^2 + m_k^2} \simeq p + \frac{m_k^2}{2p} . \quad (1.3)$$

If we assume that equation (1.2) describes the state of the neutrino at time $t = 0$, then according to the Schrödinger equation the mass eigenstates $|\nu_k\rangle$ evolve with time with the phase factors $\exp(-iE_k t)$. Therefore at time t we have

$$|\nu_\alpha\rangle_t = \sum_{k=1}^n U_{\alpha k}^* e^{-iE_k t} |\nu_k\rangle . \quad (1.4)$$

Using the unitarity of the mixing matrix U we can invert equation (1.1) and obtain

$$|\nu_k\rangle = \sum_{\beta=e,\mu,\tau} U_{\beta k} |\nu_\beta\rangle . \quad (1.5)$$

Substituting this into equation (1.4) we get

$$|\nu_\alpha\rangle_t = \sum_{\beta=e,\mu,\tau} |\nu_\beta\rangle \sum_{k=1}^n U_{\beta k} e^{-iE_k t} U_{\alpha k}^* = \sum_{\beta=e,\mu,\tau} |\nu_\beta\rangle A_{\nu_\alpha \rightarrow \nu_\beta}(t) . \quad (1.6)$$

Here we introduce the amplitude $A_{\nu_\alpha \rightarrow \nu_\beta}(t)$ for $\nu_\alpha \rightarrow \nu_\beta$ transition, which is given by

$$A_{\nu_\alpha \rightarrow \nu_\beta}(t) = \sum_{k=1}^n U_{\beta k} e^{-iE_k t} U_{\alpha k}^* . \quad (1.7)$$

This yields the following expression for the $\nu_\alpha \rightarrow \nu_\beta$ transition probability

$$P_{\nu_\alpha \rightarrow \nu_\beta}(t)$$

$$P_{\nu_\alpha \rightarrow \nu_\beta}(t) = \left| A_{\nu_\alpha \rightarrow \nu_\beta}(t) \right|^2 = \left| \sum_{k=1}^n U_{\beta k} e^{-iE_k t} U_{\alpha k}^* \right|^2. \quad (1.8)$$

Using the unitarity relation

$$\sum_{k=1}^n U_{\beta k} U_{\alpha k}^* = \delta_{\alpha\beta}, \quad (1.9)$$

and the ultra-relativistic approximation (equation (1.3)), and $t \simeq L$ (where L is the distance from the interaction point), we can rewrite equation (1.8) as

$$P_{\nu_\alpha \rightarrow \nu_\beta} = \left| \delta_{\alpha\beta} + \sum_{k=2}^n U_{\beta k} U_{\alpha k}^* \left[\exp\left(-i \frac{\Delta m_{k1}^2 L}{2E}\right) - 1 \right] \right|^2, \quad (1.10)$$

where $\Delta m_{kj}^2 \equiv m_k^2 - m_j^2$. As expected in case if there is no mixing ($U = I$) the transition probability $P_{\nu_\alpha \rightarrow \nu_\beta}(t) = \delta_{\alpha\beta}$ so no neutrino flavor oscillations are possible.

It also can be seen from equation 1.10 that the transition probability becomes very small if

$$\Delta m_{ik}^2 \ll E/L \quad (1.11)$$

for all possible values of i, k . So an oscillation search experiment with the characteristic neutrino energy - E and the neutrino travel path from the point of creation to the detector - L is insensitive to the neutrino oscillations if the condition 1.11 is true.

1.2.2 Oscillations for the case of two-neutrino mixing

In this simplified case the unitary mixing matrix can be written as

$$U = \begin{pmatrix} \cos \theta & \sin \theta \\ -\sin \theta & \cos \theta \end{pmatrix}, \quad (1.12)$$

where θ is the mixing angle. For the transition probability (equation (1.10)) we obtain

$$P_{\nu_\alpha \rightarrow \nu_\beta} = \left| \delta_{\alpha\beta} + U_{\beta 2} U_{\alpha 2}^* \left[\exp(-i \frac{\Delta m^2 L}{2E}) - 1 \right] \right|^2, \quad (1.13)$$

where $\Delta m^2 = m_2^2 - m_1^2$ and α, β are e, μ or μ, τ or e, τ . Substituting equation (1.12) into equation (1.13) the transition probability becomes

$$P_{\nu_\alpha \rightarrow \nu_\beta} = \frac{1}{2} \sin^2 2\theta (1 - \cos \frac{\Delta m^2 L}{2E}). \quad (1.14)$$

Here, equation (1.14) is in the units of $\hbar = c = 1$. It can also be written in the following form

$$P_{\nu_\alpha \rightarrow \nu_\beta} = \sin^2 2\theta \sin^2 \left(\frac{1.27 \Delta m^2 (eV^2) L (km)}{E (GeV)} \right). \quad (1.15)$$

Considering the limits of very small and very large L it can be seen that the transition probability (equation (1.15)) is very small for $L \rightarrow 0$, and has a rapid oscillatory behavior for $L \rightarrow \infty$. The most effective measurement is obtained if a detector which is sensitive to these transitions is placed at a distance

$$L_{best} \sim L_{osc} = \frac{4\pi E}{\Delta m^2} \simeq 2.48 \frac{E (GeV)}{\Delta m^2 (eV^2)} km, \quad (1.16)$$

where L_{osc} is the oscillation length parameter. Reversing the argument we can determine that the existing NuTeV detector has the best sensitivity for neutrino

oscillations with

$$\Delta m^2(\text{NuTeV best sensitivity}) \simeq \frac{\pi}{2} \frac{\langle E \rangle}{1.27 \langle L \rangle} \sim 100 \text{ eV}^2 ,$$

where we substituted the average neutrino energy and flight length at NuTeV

$$\langle E \rangle \sim 100 \text{ GeV}, \quad \langle L \rangle \sim 1 \text{ km} .$$

1.3 Neutrino Oscillation Experiments

Neutrino oscillation experiments fall into one of the two categories depending on the type of search performed. In “appearance” searches, an experiment looks for the anomalous excess of ν_β type neutrinos in a beam of predominantly ν_α type neutrinos. Finding such neutrinos would constitute evidence of $\nu_\alpha \leftrightarrow \nu_\beta$ oscillations. On the other hand, an “disappearance” measurement is made by examining the change in flux of a given neutrino type, ν_α with distance. If the measured flux of neutrinos should turn out to be less than the flux expected in the absence of oscillations, it would constitute evidence of the $\nu_\alpha \leftrightarrow \nu_x$ oscillations.

Since neutrino oscillations have not been observed, in most of the literature the experimental data is analyzed under the simplest assumption, that of oscillation between two states. Results of such experiments are usually presented as a region in the two-dimensional parameter space $(\Delta m^2, \sin^2 2\theta)$ allowed or excluded at 90% level of confidence.

To date, four major methods to search for neutrino oscillations have been employed:

- **Accelerators:** A neutrino beam is generated in decays of pions and kaons produced when a proton beam from an accelerator strikes a production tar-

get. The neutrino flux for such experiments is in general very well understood. Typical experiments involve searching for either appearance or disappearance of a particular flavor neutrino from the beam.

- **Reactors:** $\bar{\nu}_e$ are created by the β^- decays of fission products in the core of a nuclear reactor. These type of experiments search for a $\bar{\nu}_e$ deficit some distance away from the source.
- **Atmospheric neutrinos:** Cosmic rays, mostly protons or α particles, interact in the atmosphere producing pions and kaons, some of which decay before reaching the earth. These experiments measure the $(\nu_\mu + \bar{\nu}_\mu)/(\nu_e + \bar{\nu}_e)$ flux ratio and compare it to the expected ratio.
- **Solar neutrinos:** ν_e are produced by nuclear reactions inside the sun. The measured flux is compared against standard solar model (SSM) calculations.

Typical values of the parameter $(\Delta m^2)_0$ that can be probed in these types of experiments are given in Table 1.1.

Neutrino source	E (MeV)	L (m)	$(\Delta m^2)_0$ (eV ²)
Reactor	1	10^2	10^{-2}
Meson factory	10	10^2	10^{-1}
High-energy accelerator	10^4	10^3	10
Atmospheric neutrinos	10^3	10^7	10^{-4}
Sun	1	10^{11}	10^{-11}

Table 1.1: Values of the parameter $(\Delta m^2)_0$ qualitatively characterizing the sensitivity of a given experiment searching for neutrino oscillations. E and L are the neutrino energy and the source-detector distance typical of the experiment.

A large number of experiments have been performed to search for neutrino oscillations using both terrestrial and extra-terrestrial sources of neutrinos. Below

is a list with a brief description of the accelerator experiments that performed search for $\nu_\mu \rightarrow \nu_e$ or $\bar{\nu}_\mu \rightarrow \bar{\nu}_e$ oscillations.

1.3.1 Accelerator Experiments

- **BNL-E734** The Brookhaven E734 experiment ran during three different periods in 1981, 1983, and 1986. The main purpose of the experiment was to study neutral and charged-current elastic neutrino interactions using a total absorption calorimeter-target with a total mass of 170 tons. At the 90% confidence level, $\sin^2 2\theta < 3.4 \times 10^{-3}$ was excluded for large Δm^2 values. At full mixing, *i.e.* $\sin^2 2\theta = 1$, $\Delta m^2 > .4 \text{ eV}^2$ was excluded [15].
- **BNL-E776** The Brookhaven E776 experiment, performed in 1985, searched for ν_e appearance in a narrow band ν_μ beam with a mean energy $\langle E_\nu \rangle = 1.4 \text{ GeV}$. A second run was taken in 1986 for a search for $\nu_e(\bar{\nu}_e)$ above expected background in a $\nu_\mu(\bar{\nu}_\mu)$ wide band beam. The detector was a 230 metric ton finely segmented electromagnetic calorimeter target. At the 90% confidence level, $\sin^2 2\theta < 3.0 \times 10^{-3}$ was excluded for large Δm^2 values. At full mixing, *i.e.* $\sin^2 2\theta = 1$, $\Delta m^2 > .075 \text{ eV}^2$ was excluded [16].
- **KARMEN** The KARMEN (KArlsruhe RuTherford interMediate Energy Neutrino) collaboration searches for the appearance of $\bar{\nu}_e$ detected via the charged-current reaction on the protons (hydrogen) of the scintillator in the detector. The signature of such an interaction is the emission of a positron and up to three γ rays within $100 \mu\text{s}$ after the positron corresponding to the binding energy of the neutron. The data sample consists of 147 events. At the 90% confidence level $\sin^2 2\theta < 5.9 \times 10^{-3}$ was excluded for large Δm^2 values. At full mixing, *i.e.* $\sin^2 2\theta = 1$, $\Delta m^2 > .1 \text{ eV}^2$ was excluded [17].

KARMEN hopes to improve their Δm^2 sensitivity by reducing backgrounds.

- **LSND** The LSND collaboration, using a liquid scintillator neutrino target has reported a signal consistent with $\bar{\nu}_\mu \rightarrow \bar{\nu}_e$ oscillations at $\sin^2 2\theta \approx 10^{-2}$ at large Δm^2 with values down to 1 eV^2 [18]. Most of the allowed region has been ruled out by the above mentioned experiments and so a possible signal is only consistent if $\sin^2 2\theta \lesssim 3 \times 10^{-3}$ or Δm^2 is below 1 eV^2 .
- **CCFR** The CCFR collaboration has previously reported a limit on $\nu_\mu \rightarrow \nu_e$ oscillations using the the same technique as the one described in this thesis. The lowest 90% confidence upper limit in $\sin^2 2\theta$ of 1.1×10^{-3} is obtained at $\Delta m^2 \approx 350 \text{ eV}^2$ [19].

These limits, together with the 90% and 99% confidence allowed regions from LSND are shown in Figure 1.1.

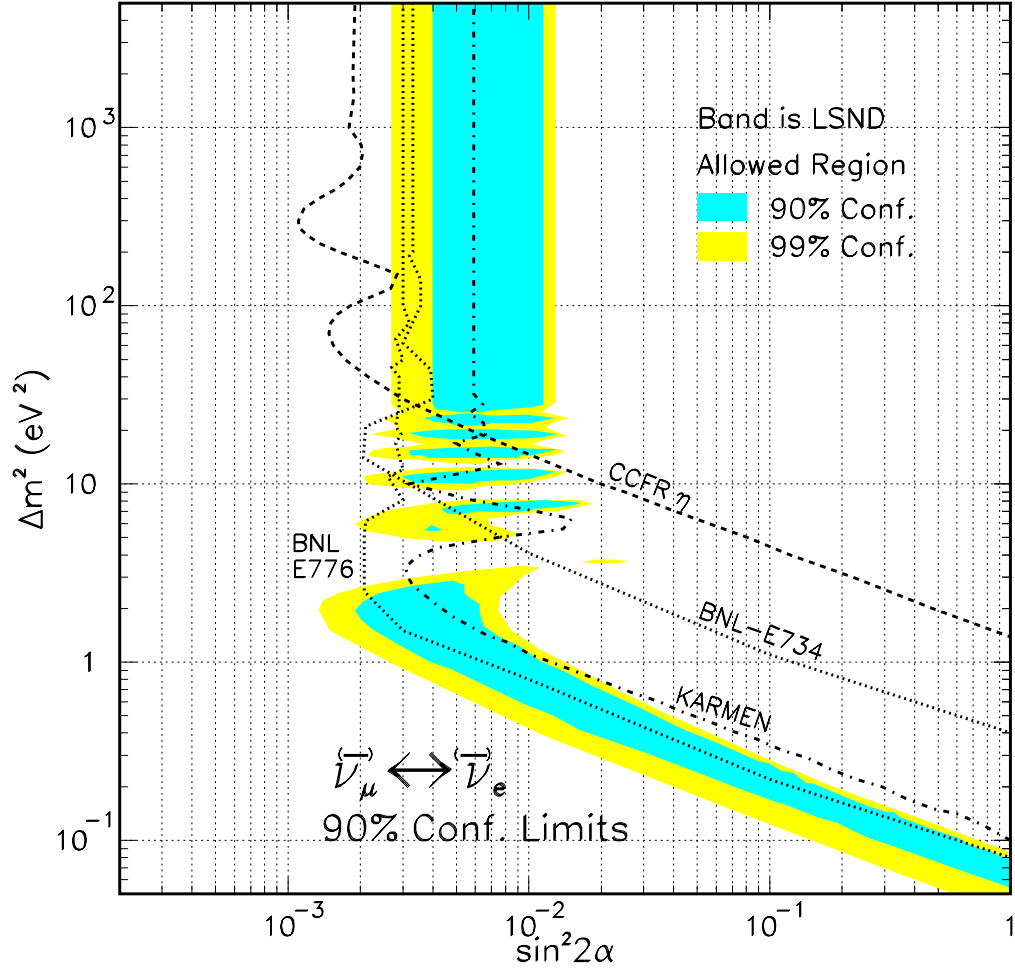


Figure 1.1: Current status of the excluded region of $\sin^2 2\alpha$ and Δm^2 for $\nu_\mu \rightarrow \nu_e$ oscillations from accelerator experiments. The shaded bands are the LSND 90% (darker) and 99% (lighter) confidence allowed regions.

Chapter 2

Detector

The detection of neutrino events in the NuTeV experiment is described in this chapter. We begin with section 2.1, which is a brief introduction to neutrino interactions and the various possible final states. The NuTeV detector design, calibration procedure and data acquisition system are presented in section 2.3.

2.1 Neutrino Interactions and Their Detectors

As described in Chapter 1, neutrinos are neutral particles with extremely small mass. Neutrinos are very difficult to detect since they do not interact via the strong

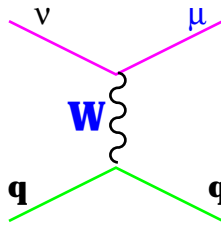


Figure 2.1: Feynman diagram of a charged-current neutrino interaction.

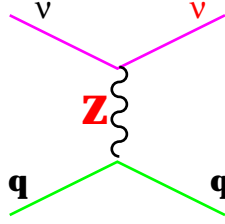


Figure 2.2: Feynman diagram of the neutral-current interaction.

or electromagnetic force. Neutrinos are capable of traveling very large distances through matter without interacting. The vast majority of the neutrinos produced in accelerator experiments pass through the particle detectors without leaving any trace. The only way to observe a neutrino is to observe the products of a neutrino interaction. Note that for a 100 GeV neutrino traversing the entire Earth the probability of interaction is only $\sim 5 \times 10^{-3}$. Therefore, a massive detector is needed in order to accumulate a reasonable number of neutrino events. Consequently neutrino detectors are among the most massive instruments in particle physics.

2.2 Deep inelastic scattering

In the most general case, neutrino-nucleon inelastic scattering proceeds via the exchange of a either charged or neutral vector boson (W or Z) as shown in Figures 2.1 and 2.2:

$$\nu N \rightarrow l X \tag{2.1}$$

$$\nu N \rightarrow \nu X \tag{2.2}$$

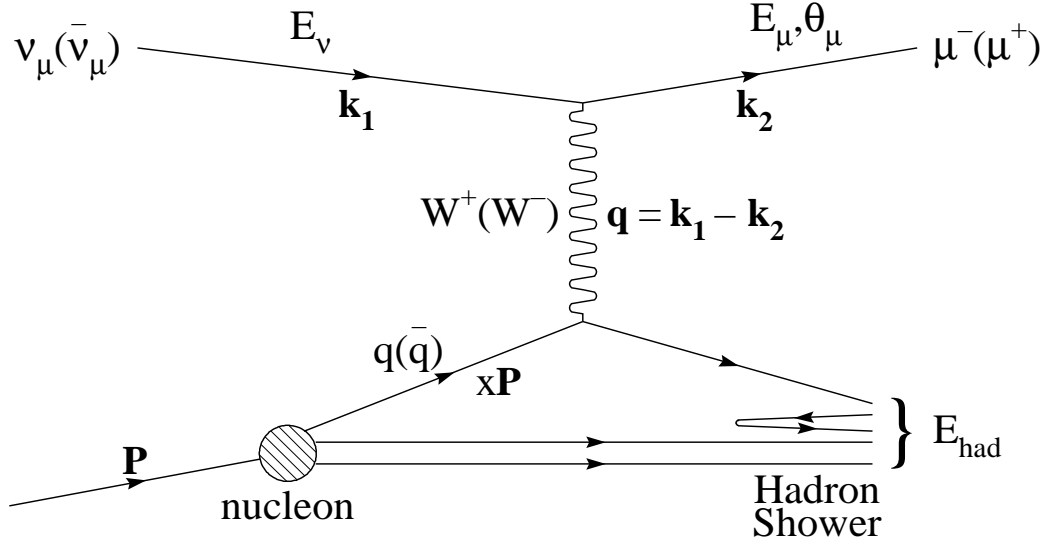


Figure 2.3: Schematic diagram of charged-current neutrino-nucleon scattering via Exchange of W boson.

where N represents the nucleon and X represents the hadronic final state particles. Since lepton number is conserved, there must be a final state lepton *. After the scattering, the excited nucleon fragments into a hadronic final state X .

The kinematic variables used to describe scattering process are illustrated in Figure 2.3. The associated four vectors for the incoming and outgoing leptons are k and k' , respectively. Here P is the four momentum for the target (or incoming) nucleon.

$$Q^2 = -q^2 = -(k - k')^2 > 0 \quad (2.3)$$

- the square of the four momentum transfer (Q^2 , the mass squared of the virtual boson) determines the “hardness” of the interaction;

$$W^2 = (P + q)^2 \quad (2.4)$$

*In the case of charged-current $\nu_\mu - N$ scattering, l' is muon.

- the square of the center-of-mass energy of the intermediate boson-nucleon system;

$$\nu = \frac{P \cdot q}{M} \quad (2.5)$$

- in the rest frame of the target, ν is equal to the energy of the intermediate boson E_{had} ;

$$y = \frac{P \cdot q}{P \cdot k} \quad (2.6)$$

- the variable y is the inelasticity of the interaction, which is equal to the fractional energy transferred between the lepton and the hadron systems, the y distribution also reflects the spin structure of the interaction;

$$x = \frac{Q^2}{2P \cdot q} \quad (2.7)$$

- the variable x is interpreted in the quark-parton model as the fractional momentum of the incoming nucleon carried by the struck quark.

Only three of the above quantities are independent variables in two-body deep inelastic scattering.

In neutrino (ν_μ) nucleon scattering experiments, the three independently measured variables in a charged-current event are the outgoing muon momentum (p_μ), the outgoing muon angle (θ_μ), and the observed energy of the final state hadrons (E_{had}). From these measured parameters the neutrino energy follows as $E_\nu = E_{had} + E_\mu$.

The derivation of the formulae for inclusive charged-current neutrino scattering is very similar to the case of $e - \mu$ scattering. Both do not require any knowledge of the dynamics inside the nucleon. The unknown couplings of the lepton-current to the nucleon are absorbed in the definition of the structure function F_i . In the case of elastic (muon,electron) or quasi-elastic (neutrino) scattering, these can

be interpreted as the Fourier transforms of the spatial charge distribution in the nucleon.

The general form of the differential cross section for neutrino-nucleon scattering, mediated by the W boson (in the case of charged-current scattering) is given in terms of three structure functions:

$$\frac{d^2\sigma}{dxdy} = \frac{G^2 ME}{\pi} \left[(1 - y - \frac{Mxy}{2E})F_2 + \frac{y^2}{2}2xF_1 \pm (1 \pm \frac{y}{2})xF_3 \right] \quad (2.8)$$

where the $+$ ($-$) terms correspond to neutrino (anti-neutrino) scattering. Here G_F is the Fermi weak coupling constant. The structure function, F_i are process dependent, and are functions of the kinematics variable, x and Q^2 .

The difference in sign between neutrino and anti-neutrino scattering leads to the difference in the y -distributions of the cross-sections $d\sigma^{\nu N}/dy$, $d\sigma^{\bar{\nu} N}/dy$. In the case of scattering from quarks in the nucleon (i.e. neglecting the scattering from the anti-quarks in the sea) the differential cross sections take the form:

$$\frac{d\sigma^{\nu N}}{dy} \sim 1 \quad (2.9)$$

$$\frac{d\sigma^{\bar{\nu} N}}{dy} \sim (1 - y)^2 \quad (2.10)$$

2.3 The NuTeV Detector

NuTeV is a neutrino-nucleon deep inelastic scattering experiment located at Fermilab. Its main goals are to improve on measurements made by its predecessor - the CCFR experiment. This is made possible by the increased intensity of the Fermilab Tevatron proton beam, a new sign selected neutrino beam, an upgraded neutrino target-calorimeter, and a continuous hadron/electron/muon calibration

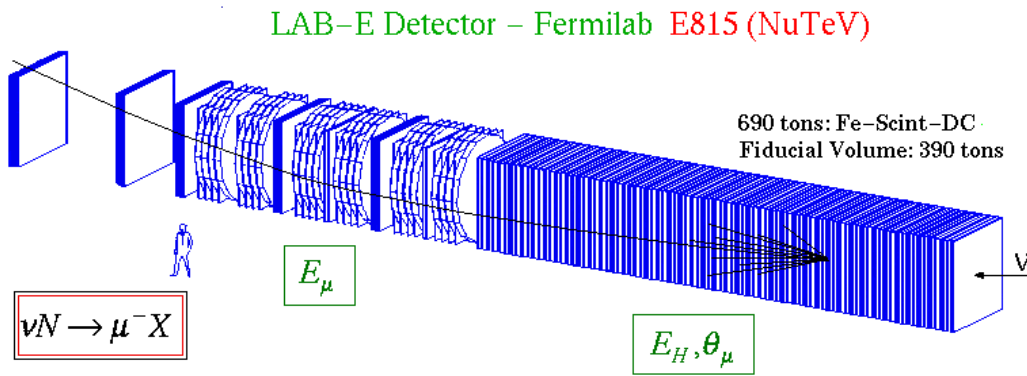


Figure 2.4: Schematic picture of the NuTeV detector

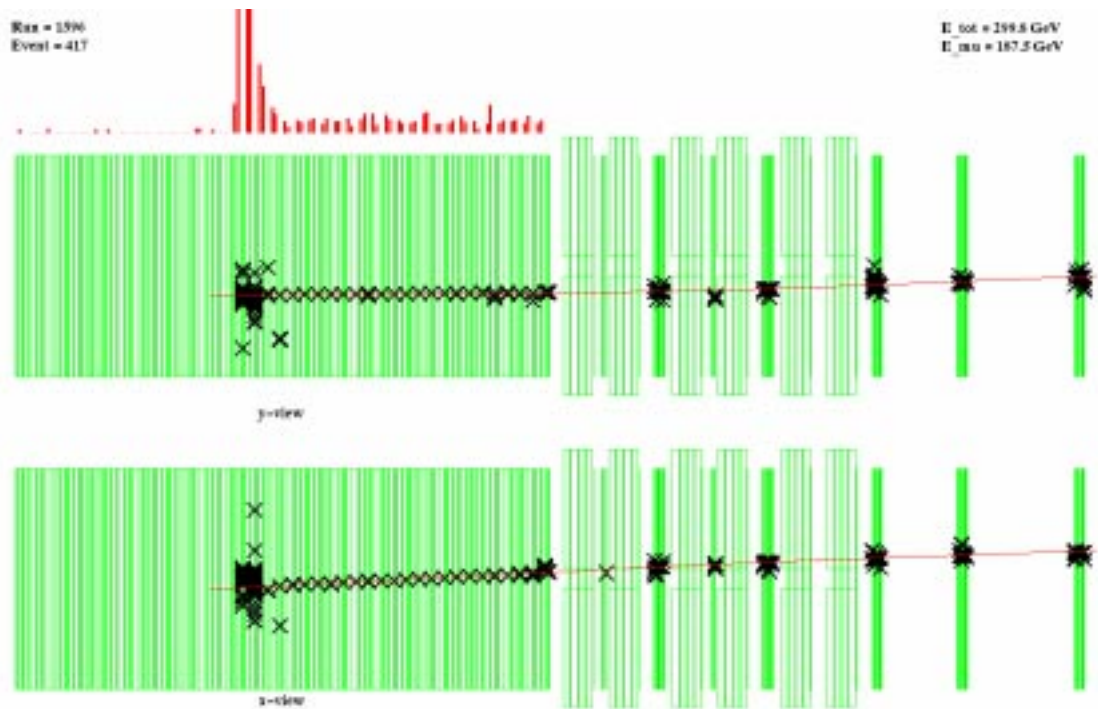


Figure 2.5: An event-display of a ν_μ charged-current interaction in the NuTeV detector.

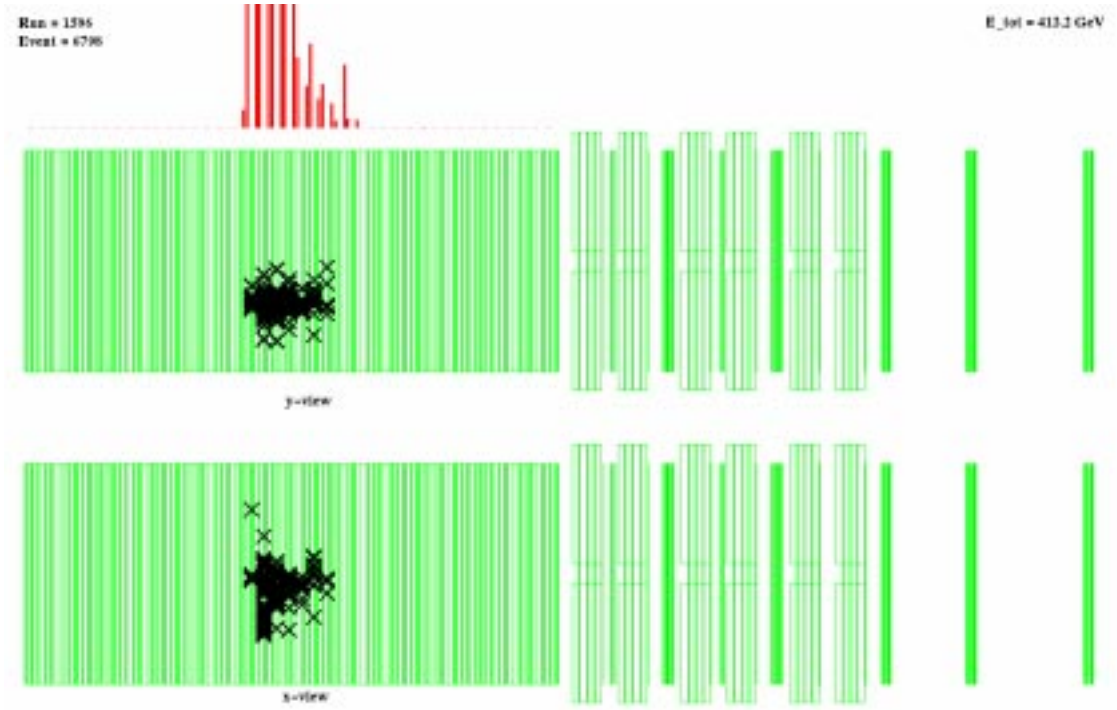


Figure 2.6: Event display of a neutral-current event in the NuTeV detector.

beam. Deep-inelastic neutrino scattering processes probe both the electro-weak and strong forces in unique ways that are both competitive and complementary to other measurements at hadron and electron colliders (the topic of precision measurements with neutrino beams is discussed in [22]).

The NuTeV data taking period took place during the Fermilab 1996-1997 fixed target run. The experiment recorded over three million neutrino and anti-neutrino interactions. The main physics goals of the NuTeV experiment include:

1. A precise measurement of the electro-weak mixing angle
2. A measurement of nucleon structure functions and the strong coupling constant (from QCD scaling violations)

3. A better measurement of the strange quark sea
4. A search for neutral heavy leptons and other new processes

A schematic diagram of the Tevatron and the neutrino beam line is presented in Figure 3.1. High-purity neutrino and anti-neutrino beams are provided by a new Sign Selected Quadrupole Train (SSQT). Neutrinos originate from the decays of pions and kaons produced in the interactions of 800 GeV protons in a BeO target. The initial proton beam is not aimed at the detector, thus minimizing the electron-neutrino background from prompt sources and from decays of neutral kaons. Dipole magnets immediately downstream of the proton target bend pions and kaons of specified charge in the direction of the NuTeV detector, while wrong-sign and neutral mesons are stopped in beam dumps. The resulting beam is almost purely neutrino or anti-neutrino depending on the selected sign of the parent mesons. The measured $\bar{\nu}_\mu$ contamination in the ν_μ beam is less than 1/1000, and the ν_μ contamination in the $\bar{\nu}_\mu$ beam is less than 1/500. In addition, the beam is almost purely muon-neutrino with a small (and well understood) contamination of electron neutrinos (1.3% in neutrino mode and 1.1% in anti-neutrino mode).

For neutrino detection, the experiment uses an upgraded version of the CCFR detector, shown in Figure 2.4, with new scintillator oil, new green-extended photo multiplier tubes and refurbished drift chambers. The detector is located approximately 1.5 km downstream of the proton target. It consists of an 18 m long, 690 ton steel-scintillator sampling target calorimeter followed by an instrumented iron-toroid spectrometer. In the detector, neutrino interactions produce a hadronic shower from the outgoing struck quark and, in charged-current events, an associated outgoing muon (event display of a charged-current interaction in the NuTeV detector is shown in Figure 2.5, and an event display of a neutral-current interaction is shown in Figure 2.6). The scintillation counters provide triggering information

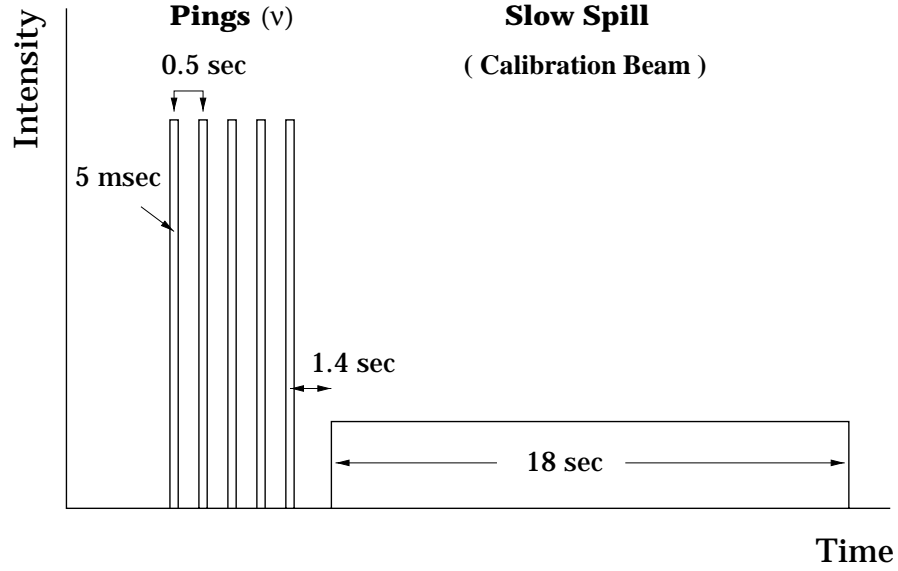


Figure 2.7: Accelerator time structure. Note that the interval between the last neutrino ping and the slow spill calibration beam is only 1.4 seconds, allowing a continuous *in situ* calibration.

as well as determination of the longitudinal event vertex, event length and the total visible energy deposition. The mean position of the hits in the drift chambers is used to establish the transverse event vertex. The toroidal spectrometer, which determines the muon sign and momentum, is not directly used in this analysis.

The detector was calibrated continuously through exposure to test beam hadrons, electrons and muons (of various energies) delivered in a separate beam line during each accelerator cycle.

2.3.1 Calibration Beam

The NuTeV experiment was designed to be calibrated continuously during neutrino data taking. This was done once every minute by taking test beam data within the same accelerator cycle, but separated from neutrino data by 1.4 seconds, (see

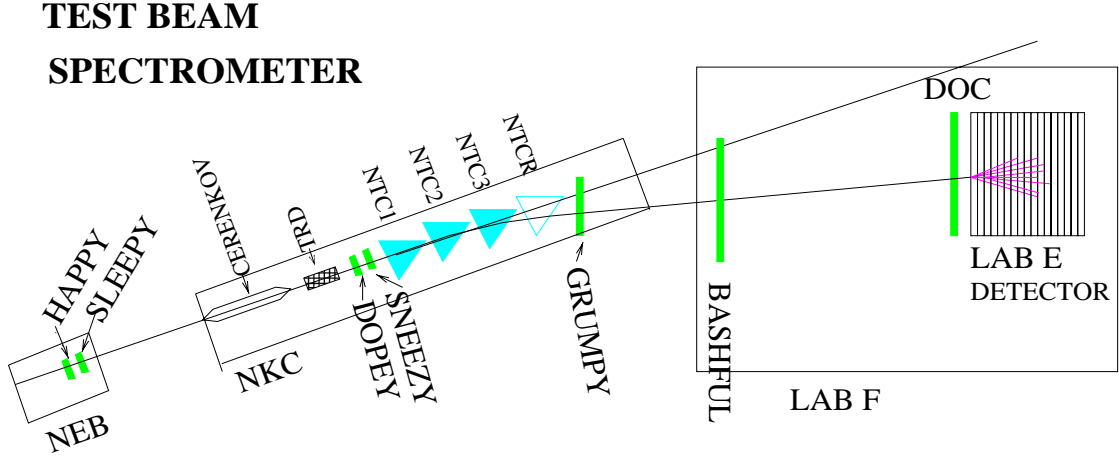


Figure 2.8: A schematic drawing of the NuTeV calibration beam spectrometer system. The elements of the spectrometer are located in the beam line enclosers NEB, NKC and in the Lab F detector hall. The spectrometer consists of the seven drift chambers - HAPPY, SLEEPY, DOPEY, SNEEZY, GRUMPY, BASHFUL and DOC (yes, the dwarves) and four dipole magnets - NTC1, NTC2, NTC3 and NTCR. Cherenkov detector and the transition radiation detector (TRD) are used for particle identification. The large distances between the chamber stations allow an accurate determination of the test beam momentum.

Figure 2.7). The calibration beam was used to set the absolute energy scale for the experiment, and to measure the response of the calorimeter to hadrons, electrons, and muons. The test beam data were also used as input for detailed simulations of neutrino interactions in the target-calorimeter.

The calibration period within each 1 minute accelerator cycle lasted 18 seconds. The typical incident angle of the test beam with respect to the center of the NuTeV calorimeter was 43 mrad in the horizontal direction and 0 mrad in the vertical direction, with small dispersion. The calibration beam line transported particles of energies from 4.8 GeV to 190 GeV . Depending on the settings of the beam line parameters, high purity beams of electrons, hadrons, or muons could be produced for energies above 30 GeV .

The beam line is instrumented effectively as a low mass spectrometer with a long lever arm as shown in Figure 2.8. The distance between the most upstream chambers in the spectrometer and the momentum-analyzing magnets (equilateral triangles) is 83.3 m , and the distance between the most downstream chamber and the magnets is 69.2 m . For such separation, a modest alignment uncertainty of 1 mm translates into only a 0.1% uncertainty in the absolute value of beam momentum. The event-by-event resolution of the spectrometer, dominated by multiple scattering, is typically less than 0.3% at most test beam energies. The beam line instrumentation was augmented for several runs with a removable Cherenkov detector and a transition radiation detector array (TRD) that were used to measure particle composition of the beam.

Over the course of the experiment, standard runs were taken at least once a week with 50 and 100 GeV hadrons, and once a month for hadron energies between 4.8 GeV and 190 GeV . Overall, NuTeV accumulated a total of 17 million calibration events.

The full procedure of calibration of the NuTeV calorimeter is described in detail in [34].

2.3.2 The Target Calorimeter

The NuTeV calorimeter consists of 168 plates of steel of dimensions $3\text{ m}(H) \times 3\text{ m}(W) \times 5.1\text{ cm}(L)$, interspersed with 84 scintillation counters of dimension $3\text{ m}(H) \times 3\text{ m}(W) \times 2.5\text{ cm}(L)$ and 42 drift chambers. One counter-unit layer consists of a scintillation counter and two steel plates (one on each side of the counter). One calorimeter-unit layer consists of two counter-unit layers and one drift chamber. The geometry of one calorimeter-unit is shown in Figure 2.9. This calorimeter-unit is repeated 42 times to make up the entire calorimeter. Table 2.1

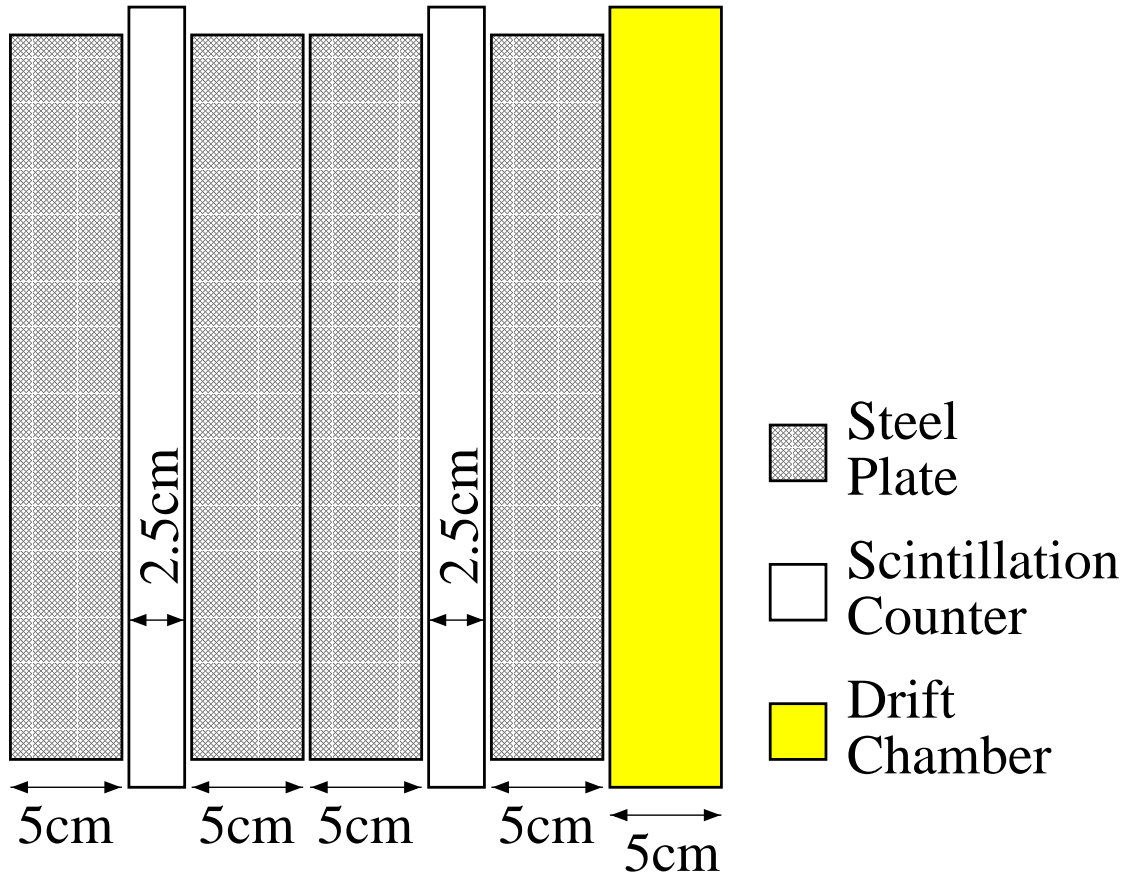


Figure 2.9: Geometry of one unit of the calorimeter. One calorimeter-unit layer consists of two counter-unit layers and one drift chamber. This unit is repeated 42 times to make up the entire calorimeter. (One counter-unit layer consists of a scintillation counter and two steel plates - one on each side of the counter).

summarizes the materials and their longitudinal sizes in units of cm, radiation length, and interaction length, for one unit of the calorimeter's longitudinal layer. A schematic drawing of a NuTeV scintillation counter is shown in Figure 2.10.

The NuTeV calorimeter response to hadrons and electrons was measured using the momentum analyzed calibration beam. The energy dependence of the calorimeter response to hadrons is shown in Figure 2.11. Note that the non-linearity of

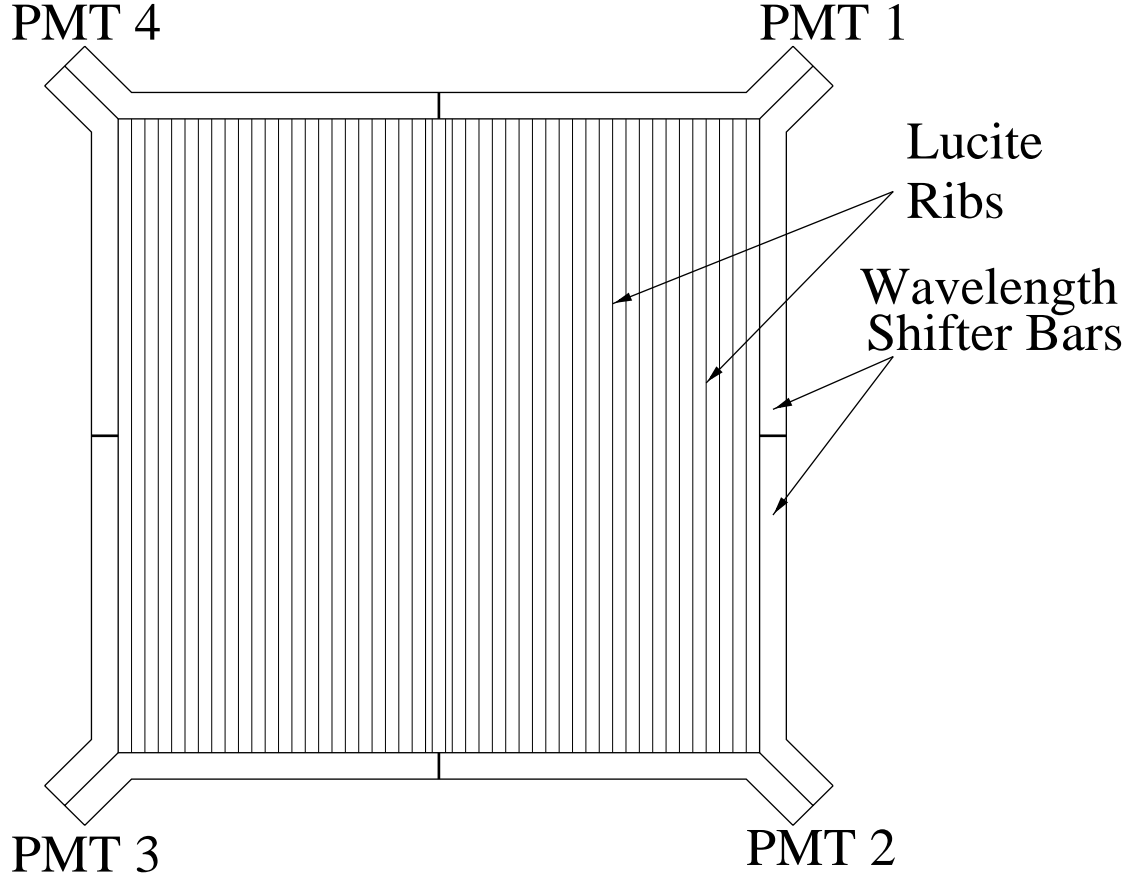


Figure 2.10: A schematic drawing of a NuTeV scintillation counter.

the calorimeter between 10 *GeV* and 190 *GeV* is only 3%. This comes from the fact that electrons and hadrons have a very similar response. Therefore, although the fractional electromagnetic component of the shower changes as a function of energy, it does not result in a large change in the reconstructed energy. The resolution function is fitted to the standard form $\sigma(E)/E = A \oplus \frac{B}{\sqrt{E}} \oplus \frac{C}{E}$, where A is a constant term coming from calibration uncertainties, B is the stochastic term from the sampling of the shower, and C is from noise due to pedestal fluctuations. Here, all the terms in the resolution function are added in quadrature. Since the

Component	(<i>cm</i>)	X_0	λ_I
4 Steel Plates	20.7	11.75	1.24
2 Scint. Counters	3.7	0.51	0.16
1 Drift Chamber	3.7	0.17	0.03
Dead Space (air)	6.0	$2 \cdot 10^{-4}$	$8 \cdot 10^{-5}$
Total	43.4	12.43	1.43

Table 2.1: Amount of material in one structural unit of the NuTeV target-calorimeter in cm, in units of radiation length X_0 , and in nuclear interaction length λ_I

data show no evidence for a noise term, the parameter C has been removed from the fit. The measured resolution function

$$\frac{\sigma(E)}{E} = 0.022 \pm 0.001 \oplus \frac{0.86 \pm 0.01}{\sqrt{E}} \quad (2.11)$$

is shown in Figure 2.11.

The electron energy calibration constant C_e which is defined to be the ratio of the calorimeter responses to electrons and to hadrons at 75 *GeV* is measured using momentum analyzed test beam electrons:

$$C_e = 1.08 \pm 0.02 \quad (2.12)$$

2.3.3 Muon Spectrometer

The muon spectrometer consists of the three large solid steel toroidal magnets located immediately downstream of the target-calorimeter. Trigger scintillation counters and 3×3 *m* drift chambers are located in the spaces between each of the three toroid magnets. The magnetic field is generated by four copper coils which carry a DC current of 1250 *A*. The magnetic field in the iron ranges from

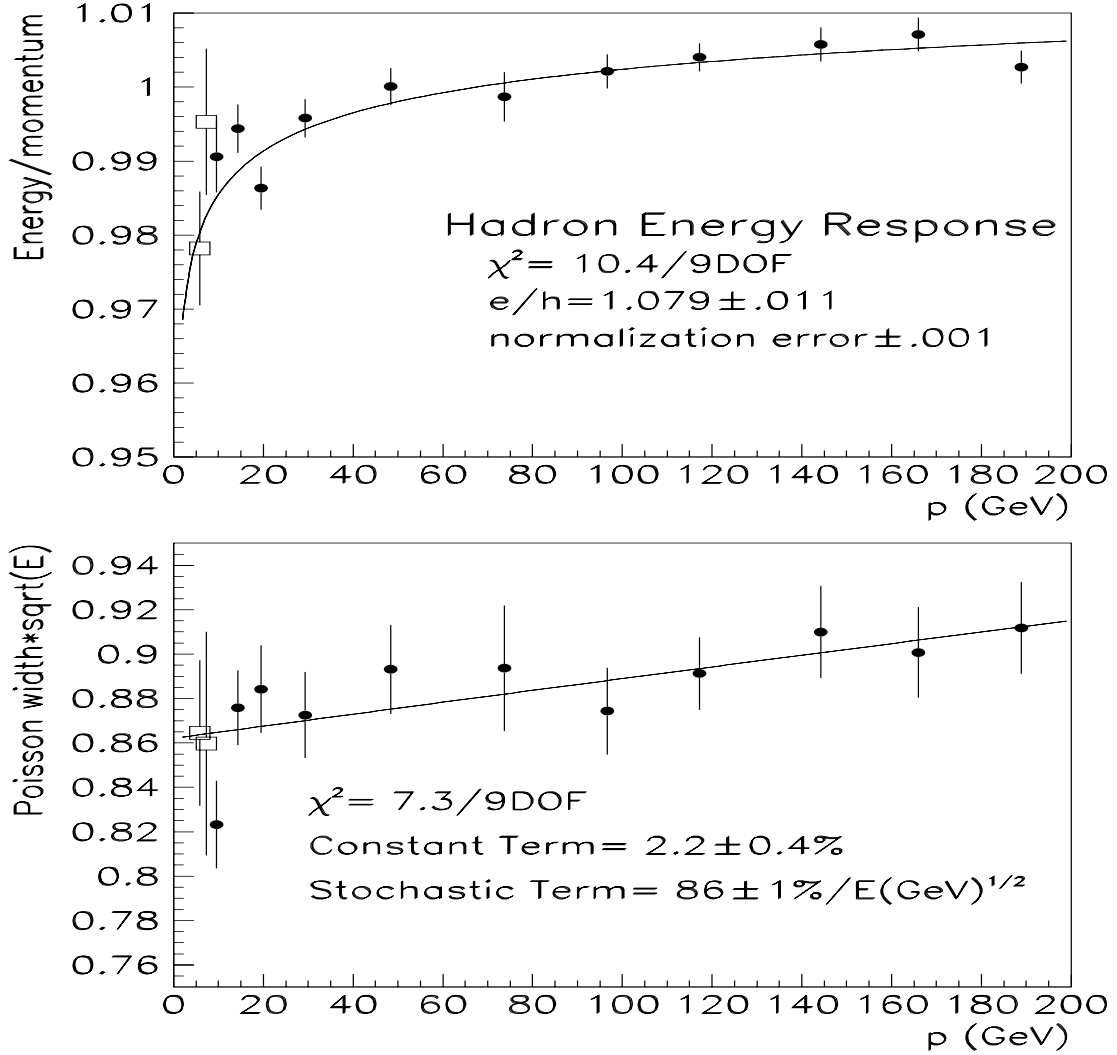


Figure 2.11: Test beam data and fits to the measured hadron energy response and resolution versus reconstructed beam momentum (a) Top - The measured non-linearity of the response and a fit using Groom's parameterization for the fractional electromagnetic component in hadron showers (b) Bottom - The measured hadron energy resolution (extracted from the data assuming a Poisson distribution) compared to a fit of the form $\sigma(E)/E = A \oplus \frac{B}{\sqrt{E}}$. The open square symbols are lower energy runs with slightly different cuts which are not used in the fits.

1.9 T near the center of the toroid to 1.5 T near the edge. A muon, traveling the entire length of the spectrometer receives an additional 2.4 GeV/c in transverse momentum.

The muon track through the spectrometer is reconstructed using the drift chamber hits. The muon momentum is extracted using an iterative fitting procedure that includes the magnetic bend, the ionization energy loss, and the multiple Coulomb scattering experienced by the muon in the toroid steel.

The calibration and resolution of the muon spectrometer was determined using calibration beam momentum analyzed muons. The absolute muon energy scale is determined to an uncertainty of 0.25% in neutrino mode and 0.4% in anti-neutrino mode [†]

2.3.4 Data Acquisition

The NuTeV detector and its electronics are designed to detect various charged particles by converting the results of their interactions with the elements of the detector (drift chambers, scintillation counters) into electrical signals. The Data Acquisition System (or simply DAQ) is used to determine when an event which consists of final state particles passing through the detector is “interesting”. Once the detector is triggered by an interesting event, the DAQ system converts all the signals from the detector into recordable data and writes the event on tape for later analysis. The decision if the event is of physics interest has to be made in a very short time - approximately 200 nanoseconds. Therefore, the criteria of selecting/rejecting an event are based on a small subset of the signals from

[†]Polarity of the toroid magnet is reversed for anti-neutrino mode running so the determination of the absolute energy scale is performed for neutrino and anti-neutrino mode running separately. The larger sample of calibration beam muons was accumulated during neutrino mode running, thus the resulting uncertainty in the absolute muon energy scale is smaller.

the detector that can be read out very fast. The two main types of readout information are pulse heights from the photo tubes of the scintillation counters and timing pulses from the drift chambers. Since the response from the drift chambers is usually much slower than 200 ns , only signals from photo tubes are used for event selection. Once the selection criteria have been satisfied, the data acquisition system is triggered to record the full detector response and save it as an “event”. A total of seven different sets of selection criteria (called “event triggers”) are used in the NuTeV experiment. A summary of the triggers for various physics processes is given in Table 2.2.

<i>Trigger</i>	<i>Name</i>	<i>Requirements</i>
1	Charged-Current Trigger	<ul style="list-style-type: none"> • counters ON- upstream of toroid 1 • counters ON- in toroid gaps • no upstream veto
2	Neutral-Current Trigger	<ul style="list-style-type: none"> • $E_{had} > 5$ GeV in 8 consecutive counters • $E_{had} > 0.15$ GeV in 2 out of 4 consecutive counters • no upstream veto
3	Range-Out/Exit Trigger	<ul style="list-style-type: none"> • 1/4 MIP in more than 16 counters • 4 GeV energy in any 8 adjacent counters • no upstream veto
4	Charged-Current Trigger II	<ul style="list-style-type: none"> • shower energy • hits in first cart upstream of toroid • muon track through one toroid quadrant
5	Test Beam Trigger	<ul style="list-style-type: none"> • slow spill
6	Straight through μ Trigger	<ul style="list-style-type: none"> • hits in each cart and one toroid quadrant
8	Cosmic Ray Trigger	<ul style="list-style-type: none"> • 40 counter muon requirement
10,11,12	Pedestal Triggers	<ul style="list-style-type: none"> • No other triggers

Table 2.2: NuTeV trigger list with descriptions

Chapter 3

Neutrino Flux

3.1 Neutrino Beam

The NuTeV neutrino beam originates from decays of secondary particles produced in the interactions of 800 *GeV* protons in a *BeO* target. A schematic diagram of the Tevatron and the neutrino beam line is shown in Figure 3.1. The Sign Selected Quadrupole Train (SSQT), shown in Figure 3.2, is located immediately downstream of the proton target. Dipole magnets (shown as triangles) bend secondary particles of a selected charge in the direction of the decay pipe, while particles of the opposite sign are directed towards a beam dump. Approximately 5% of the secondary particles of the selected sign decay in the 320 *m* pipe, which is the source of the neutrinos. As shown in the figure, neutral and wrong sign secondaries are stopped in the second beam dump.

The dominant processes that produce muon-neutrinos (or anti-neutrinos) in the positive (or negative) focusing mode of the SSQT beam line are $\pi \rightarrow \nu_\mu \mu$, $K \rightarrow \nu_\mu \mu$, $K \rightarrow \pi^0 \nu_\mu \mu$.

In order to reduce the fraction and uncertainty in the electron neutrino flux

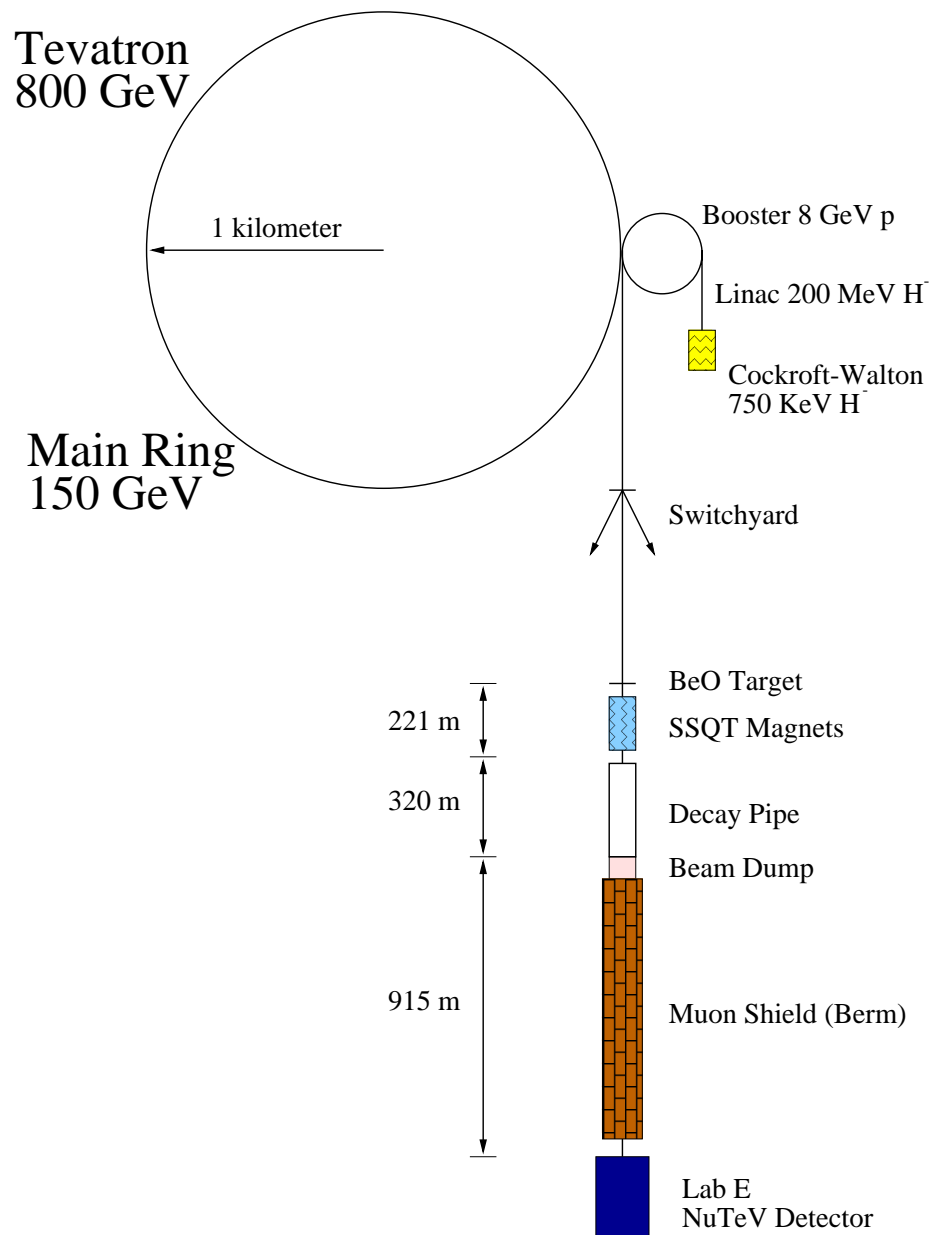


Figure 3.1: The Fermilab Tevatron and the NuTeV neutrino beam line.

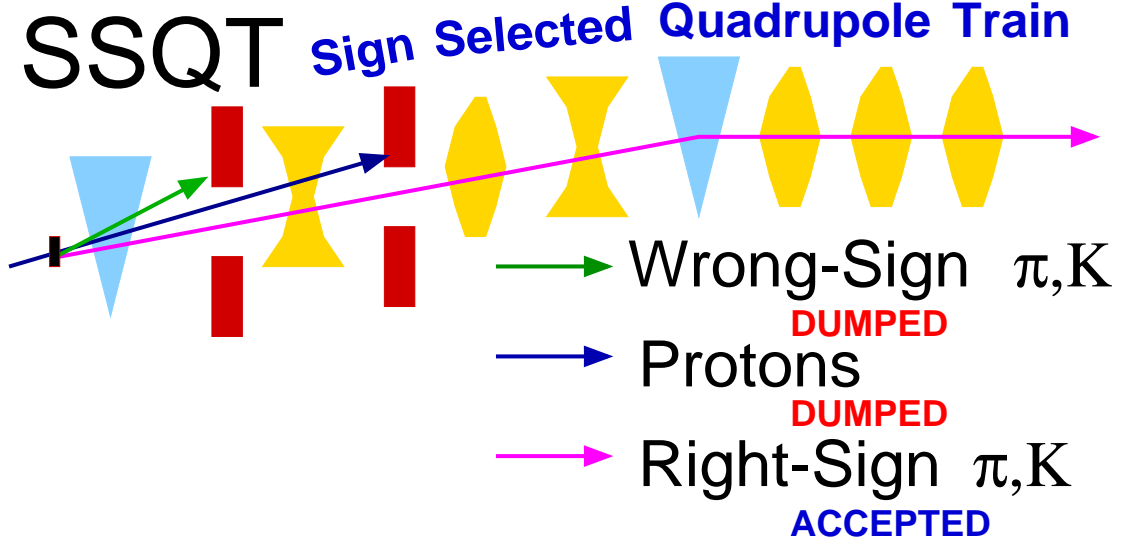


Figure 3.2: The Sign Selected Quadrupole Train (SSQT).

the primary proton beam is not aimed in the direction of the NuTeV detector. Therefore the electron-neutrino flux originating from the decays of neutral kaons and from prompt decays (e.g. charm particles) is very small. The dominant source of electron-neutrinos (anti-neutrinos) in the beam are charged K_{e3}^+ (K_{e3}^-) decays $K^+ \rightarrow \pi^0 \nu_e e^+$ ($K^- \rightarrow \pi^0 \bar{\nu}_e e^-$).

3.2 Flux Monte Carlo Simulation

The neutrino flux Monte Carlo is based on the DECAY TURTLE program ([23]). We use the charged-pion and kaon production data from Atherton *et al* ([24]) as parameterized for thick targets by Malensek ([25]).

The flux extraction procedure for muon-neutrinos and anti-neutrinos uses the observed sample of muon-neutrino interactions in the NuTeV detector. A broad sample of charged-current events, roughly equivalent to the structure function neu-

trino event sample is used * Because this sample is very large, it has the advantage of providing copious statistics for checks as a function of time, but has the disadvantage of coupling the neutrino flux determination to the neutrino charged-current cross-section model.

3.2.1 Flux Tuning

The beam Monte Carlo ν_μ and $\bar{\nu}_\mu$ fluxes from the above three neutrino sources are determined by adjusting parameters in the Monte Carlo to fit the observed spectra of neutrino energy and transverse vertex position of charged-current muon-neutrino events in the detector. The parameters are adjusted by applying scaling factors to:

1. The Monte Carlo beam center vertex position offsets in the X and Y views
2. The K^+/π^+ and K^-/π^- production cross section ratios at the proton target
3. The energy scale factors $f_{E_\nu}^X$ for the mean energies of the secondary particles in the beam (where X is π^+ , K^+ , π^- , π^+)

The result of the fits to the E_ν spectra is shown in Figure 3.3. The peak in the energy spectrum at low energy is from neutrinos that originate from charge-pion decays, and the peak at high energy is from neutrinos that originate from charged-kaon decays. The extracted scaling factors are very close to 1.0, thus indicating that the Monte Carlo predictions, before adjusting the parameters to fit the observed spectra, are close to being correct.

*The sample of ν_μ charged-current interactions that pass a set of strict reconstruction cuts that ensure full reconstruction of the event kinematics (E_{had} , E_μ , θ_μ), is used for the structure function analysis and is often referred to as the “structure function sample”.

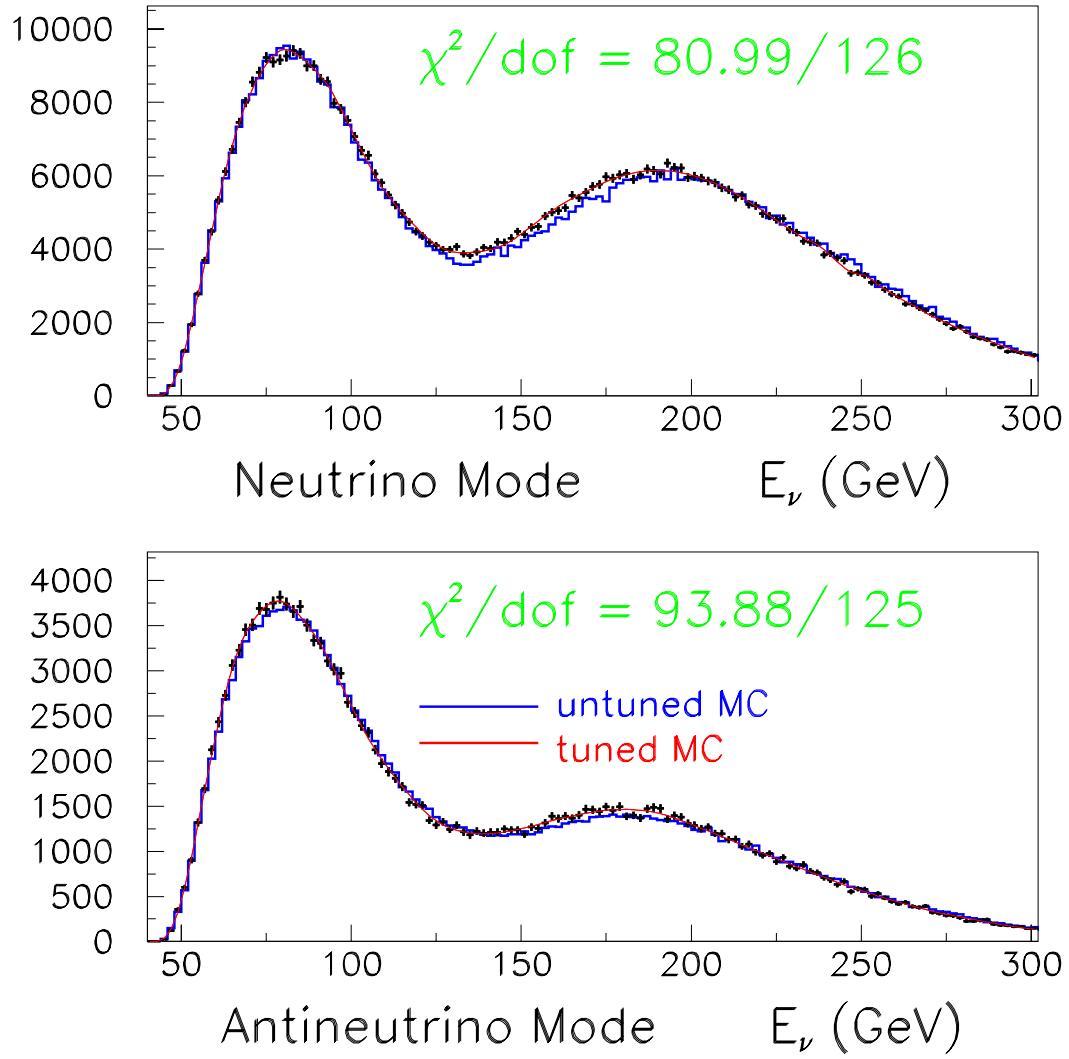


Figure 3.3: Neutrino flux: crosses - data, blue line - untuned Monte Carlo, red - tuned Monte Carlo. Top plot - neutrino mode, bottom plot - anti-neutrino mode.

Source	ν Mode	$\bar{\nu}$ Mode
$\pi^\pm, K^\pm \rightarrow \mu^\pm(\bar{\nu}_\mu)$	0.982	0.973
K_{e3}^\pm, π_{e2}^\pm	0.0157 ± 0.0003	0.0115 ± 0.0002
K_{Le3}, K_{Se3}	0.00065 ± 0.00007	0.00290 ± 0.0003
Charm Meson $\rightarrow \nu_e$	0.00042 ± 0.00006	0.00155 ± 0.0002
$\mu \rightarrow \nu_e$	0.00007 ± 0.00001	0.00010 ± 0.00001
$\Lambda_c, \Lambda, \Sigma$	0.00003 ± 0.00003	0.00023 ± 0.0002

Table 3.1: Fractional neutrino fluxes from various sources.

The electron-neutrino flux is estimated using a detailed beam Monte Carlo. Most of the observed ν_e 's originate from $K^\pm \rightarrow \pi^0 e^\pm(\bar{\nu}_e)$ decay. The beam simulation can be tuned to describe ν_e and $\bar{\nu}_e$ production from charged-kaon decays with high accuracy because the K^\pm decay contribution is well constrained by the measurements of the observed ν_μ and $\bar{\nu}_\mu$ fluxes (as shown in Figure 3.3). Because of the precise alignment of the beam line elements and the low acceptance for neutral particle propagation in the SSQT beam line, the largest uncertainty in the predicted electron-neutrino flux originates from the 1.4% uncertainty in the $K^\pm \rightarrow \pi^0 e^\pm(\bar{\nu}_e)$ branching ratio. The uncertainty in the predicted electron-neutrino flux in the NuTeV experiment is a factor of three smaller than the corresponding flux uncertainty in the previous CCFR experiment. (In the CCFR experiment there was a significant contribution to the electron-neutrino flux from neutral-kaon decays, since the proton beam was aimed directly in the direction of the CCFR neutrino detector).

The Monte Carlo calculations of the expected neutrino flux spectra for SSQT running in neutrino and anti-neutrino modes is shown in Figure 3.4. Table 3.1 lists the fractional neutrino fluxes from each source along with the estimated uncertainties.

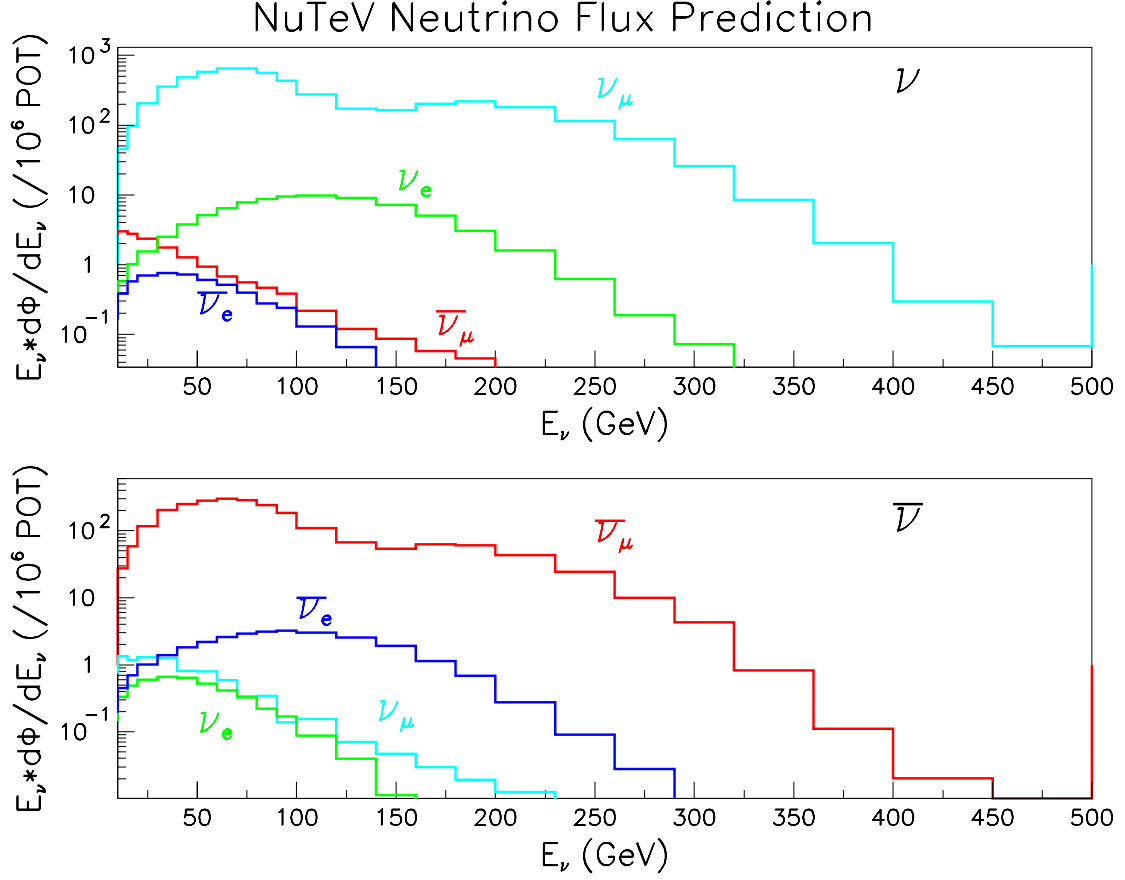


Figure 3.4: Beam Monte Carlo simulation of flux spectra for individual neutrino species. Top plot - neutrino mode; Bottom plot - anti-neutrino mode.

3.3 Electron Neutrino Flux Systematic Uncertainties

The systematic uncertainties of the electron neutrino flux at the NuTeV detector were estimated using the beam Monte Carlo simulation. For each of the experimental uncertainties we calculated the change in the predicted ν_e flux due to a one sigma shift of the corresponding systematic parameter. The following are the main

sources of systematic uncertainty in the Monte Carlo predictions of the expected number of electron-neutrino events in the NuTeV detector:

1. The measured K_{e3} branching ratio is only known with an uncertainty of 1.4%. The fractional change in the ν_e flux from a 1 sigma shift in $BR(K_{e3})$ is shown in Figure 3.5.
2. The hadron energy scale. The absolute hadron energy scale has been measured with the hadron calibration test beam with a error of 0.43%. The fractional change in the ν_e flux from a 1 sigma shift in the hadron energy scale is shown in Figure 3.6.
3. The muon energy scale. Muon energy scale has been measured with an uncertainty of 0.25% in neutrino mode and 0.4% in anti-neutrino mode. The fractional change in the ν_e flux from a 1 sigma shift in the muon energy scale is shown in Figure 3.7.
4. The ratio of the electron/pion response of the NuTeV calorimeter (defined at 75 GeV to be C_e). The calibration constant C_e has been measured using an electron calibration test beam with a 2% uncertainty. The fractional change in the ν_e flux from a 1 sigma shift in C_e is shown in Figure 3.8.
5. Production of charm hadrons. The systematic uncertainty in the cross section for the production of charm hadrons in the NuTeV proton target is estimated to be 15%. The fractional change in the ν_e flux from a 1 sigma shift in the level of charm hadron production is shown in Figure 3.9.
6. Production of K_L 's. The systematic uncertainty of the level of the production of neutral Kaons at the NuTeV proton target is estimated to be 10%. The

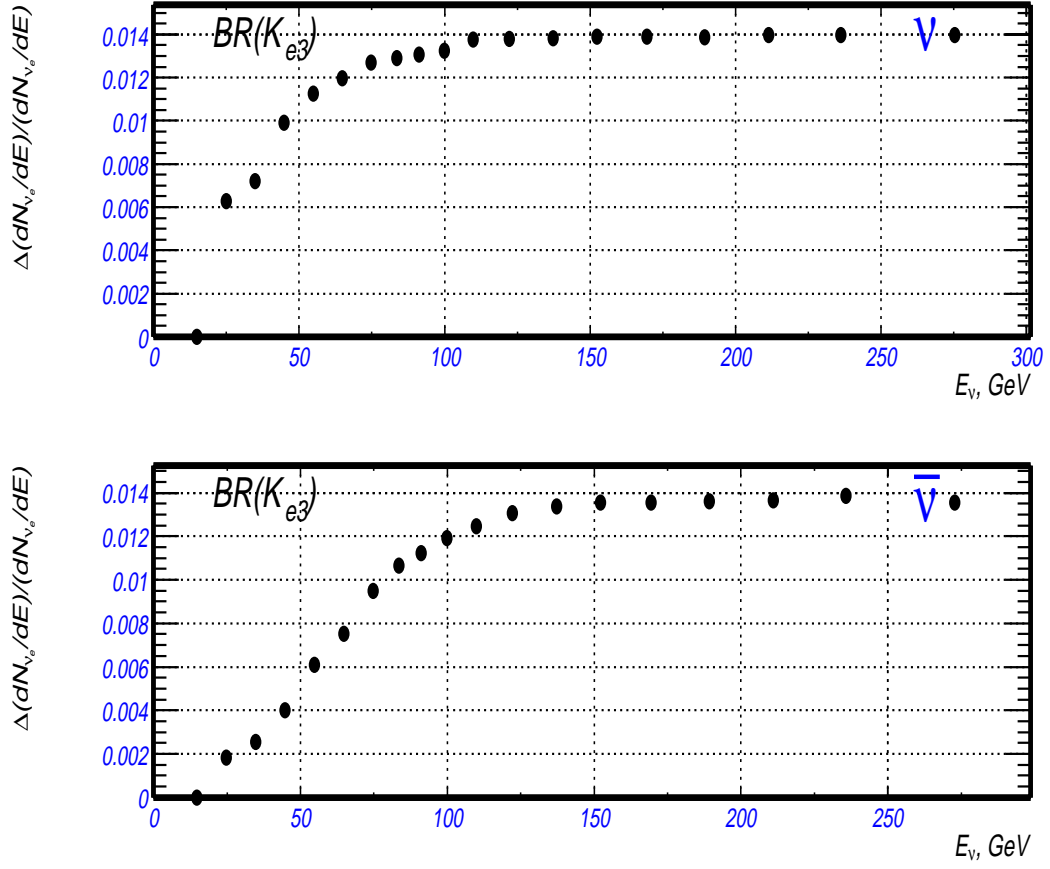


Figure 3.5: Fractional change in the ν_e flux predicted by the beam Monte Carlo simulation from a 1 sigma shift in the K_{e3} branching ratio. Top plot - neutrino mode; Bottom plot - anti-neutrino mode.

fractional change in the ν_e flux from a 1 sigma shift in level of K_L production is shown in Figure 3.10.

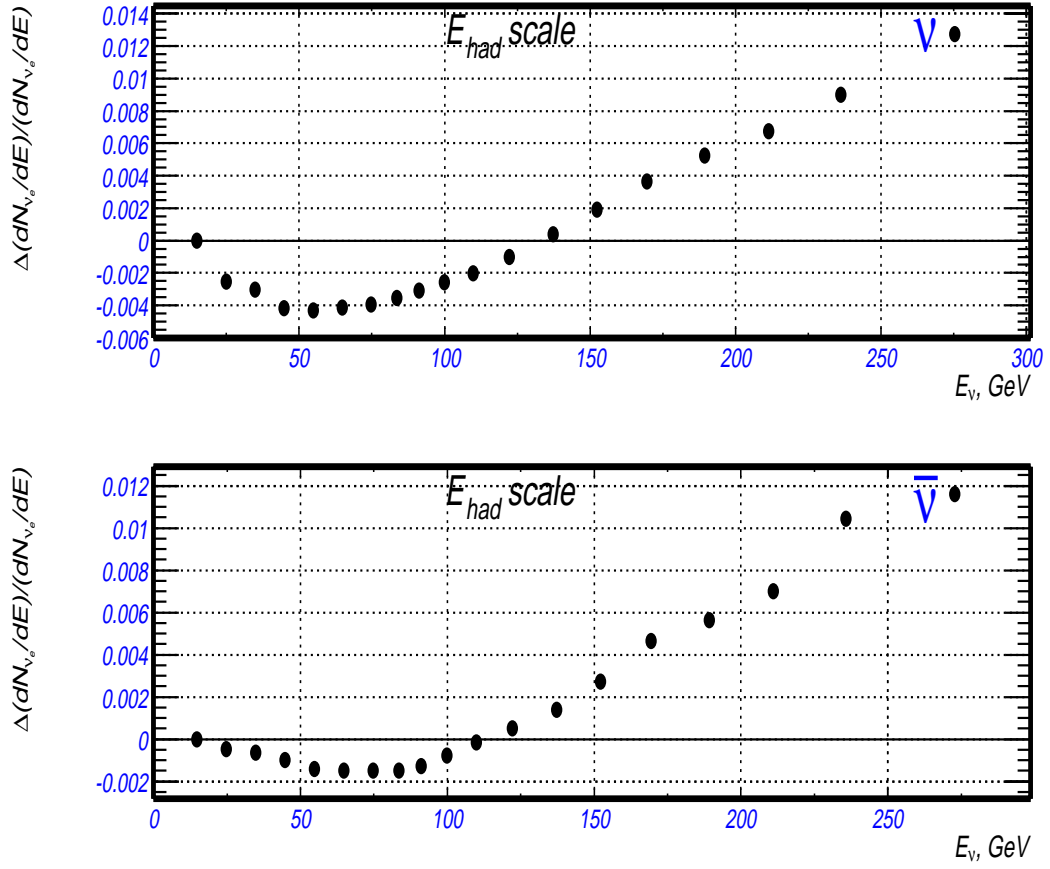


Figure 3.6: Fractional change in the ν_e flux predicted by the beam Monte Carlo simulation from a 1 sigma shift in the absolute hadron energy scale. Top plot - neutrino mode; Bottom plot - anti-neutrino mode.

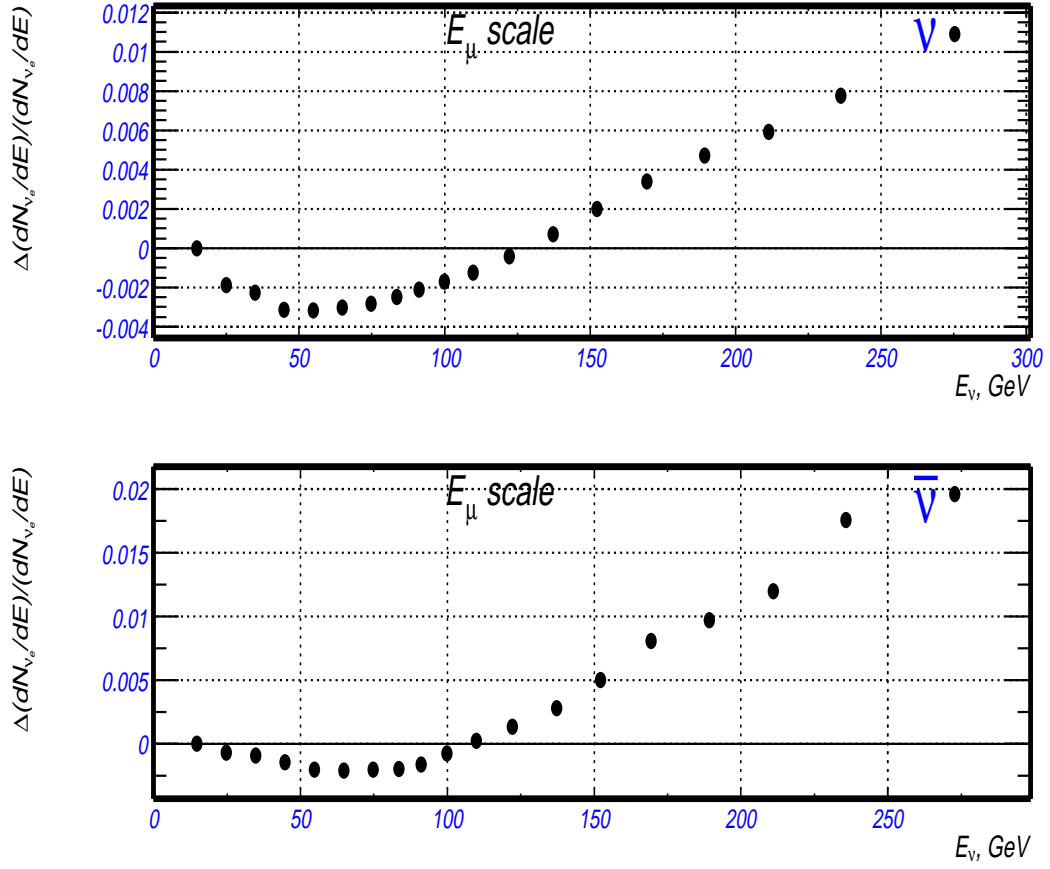


Figure 3.7: Fractional change in the ν_e flux predicted by the beam Monte Carlo simulation from a 1 sigma shift in the muon energy scale. Top plot - neutrino mode; Bottom plot - anti-neutrino mode.

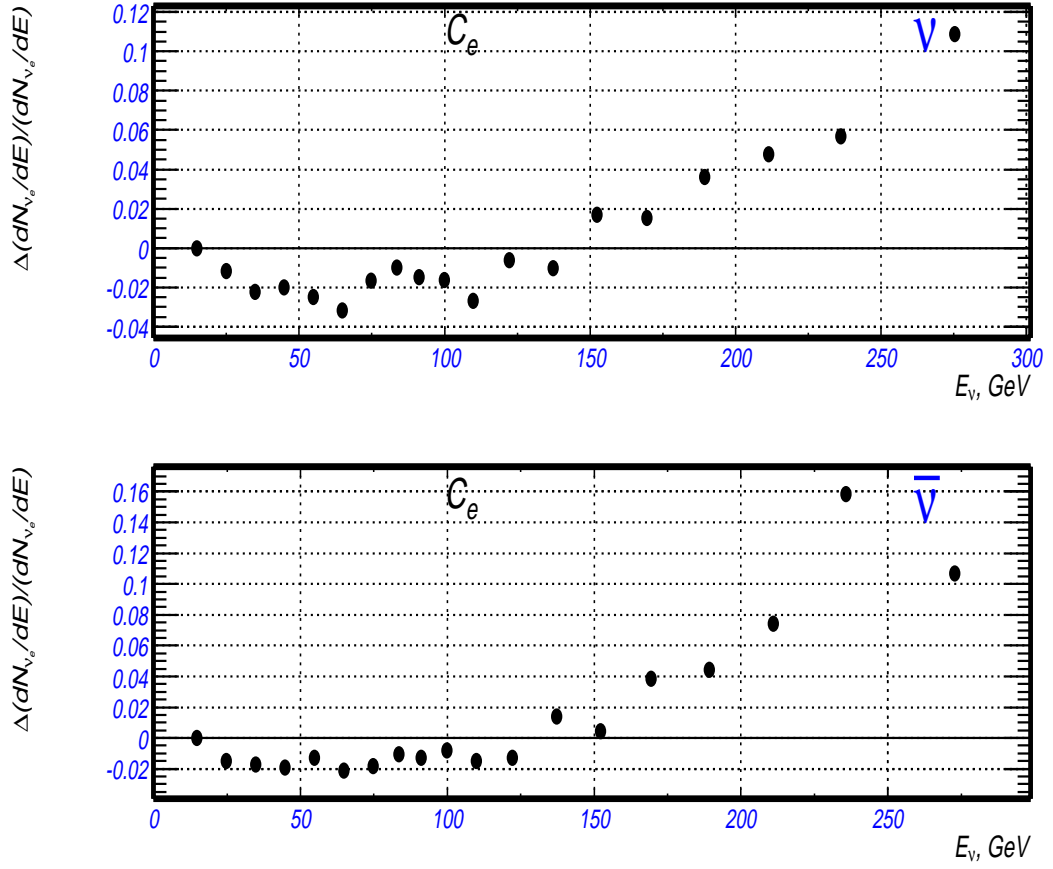


Figure 3.8: Fractional change in the ν_e flux predicted by the beam Monte Carlo simulation from a 1 sigma shift in the electron energy calibration C_e . Top plot - neutrino mode; Bottom plot - anti-neutrino mode.

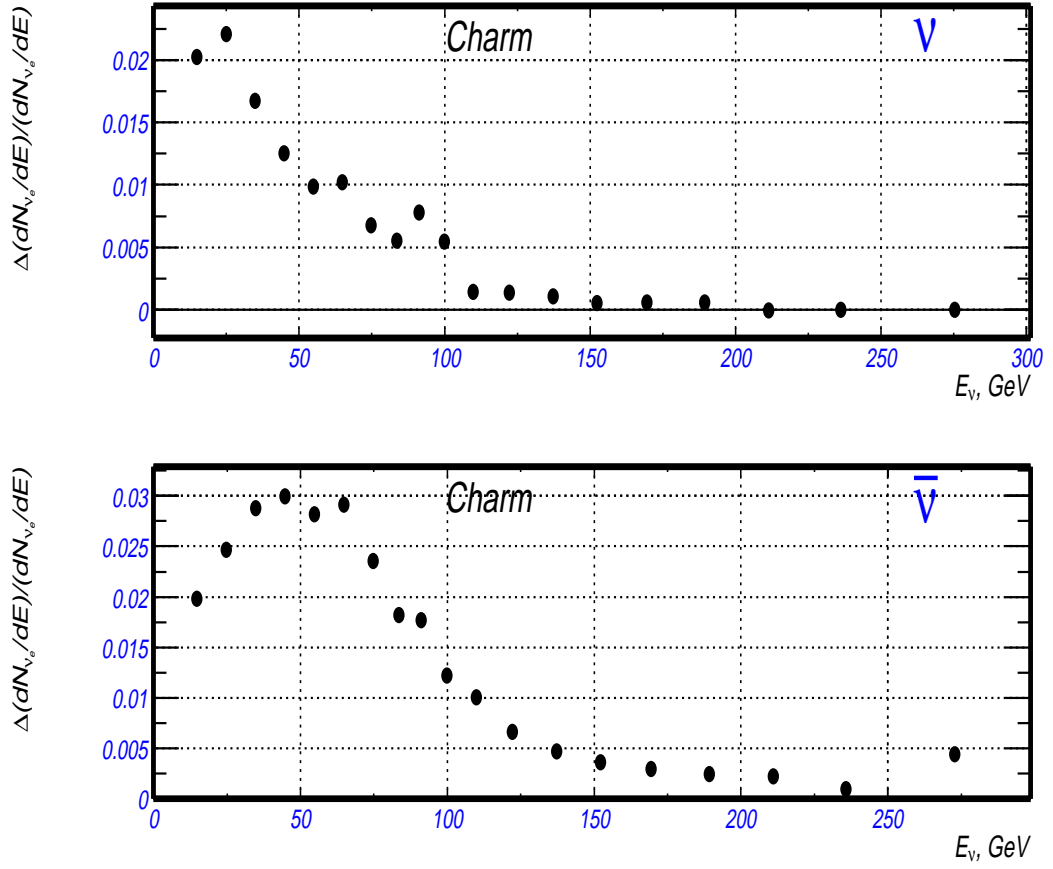


Figure 3.9: Fractional change in the ν_e flux predicted by the beam Monte Carlo simulation from a 1 sigma shift in the level of charm hadron production. Top plot - neutrino mode; Bottom plot - anti-neutrino mode.

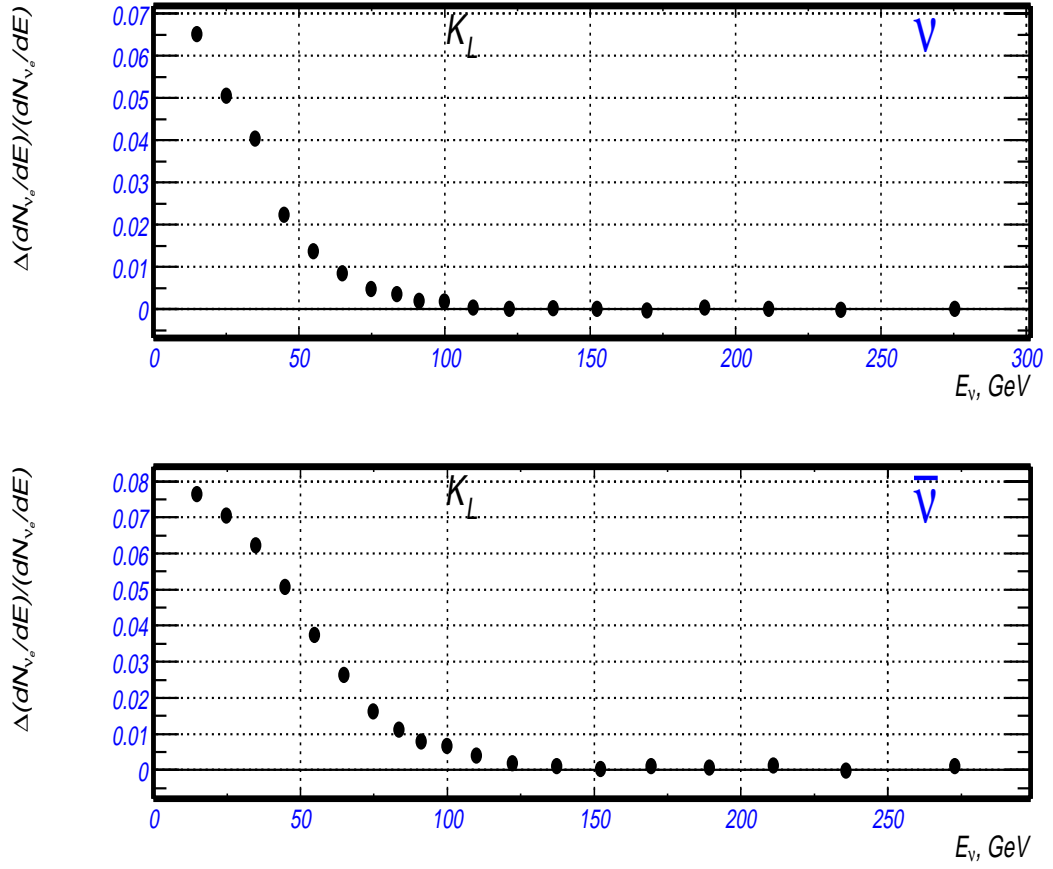


Figure 3.10: Fractional change in the ν_e flux predicted by the beam Monte Carlo simulation from a 1 sigma shift in the level of K_L production. Top plot - neutrino mode; Bottom plot - anti-neutrino mode.

Chapter 4

Shower Shape Analysis

The goal of the analysis is to search for $\nu_\mu \rightarrow \nu_e$ oscillations by measuring the electron neutrino flux in the NuTeV detector, and comparing the observed rate to the absolute prediction of the flux from a Monte Carlo. As discussed in Chapter 3, the neutrinos in the NuTeV beam are predominantly muon-neutrinos, with a very small fraction of electron-neutrinos. Since the fraction of electron-neutrinos in the beam is very well known, any excess in the observed number of electron-neutrinos can be considered as evidence for $\nu_\mu \rightarrow \nu_e$ oscillations. As mentioned in Section 1.3, oscillation searches of this type are referred to as “appearance experiments”.

4.1 Possible Final States of Neutrino Interactions in the NuTeV Detector

This section presents the experimental method used to measure the electron-neutrino flux in the NuTeV detector. We begin by listing all the possible final states of ν_e -induced events in the NuTeV detector (the NuTeV detector is described in Section 2.1).

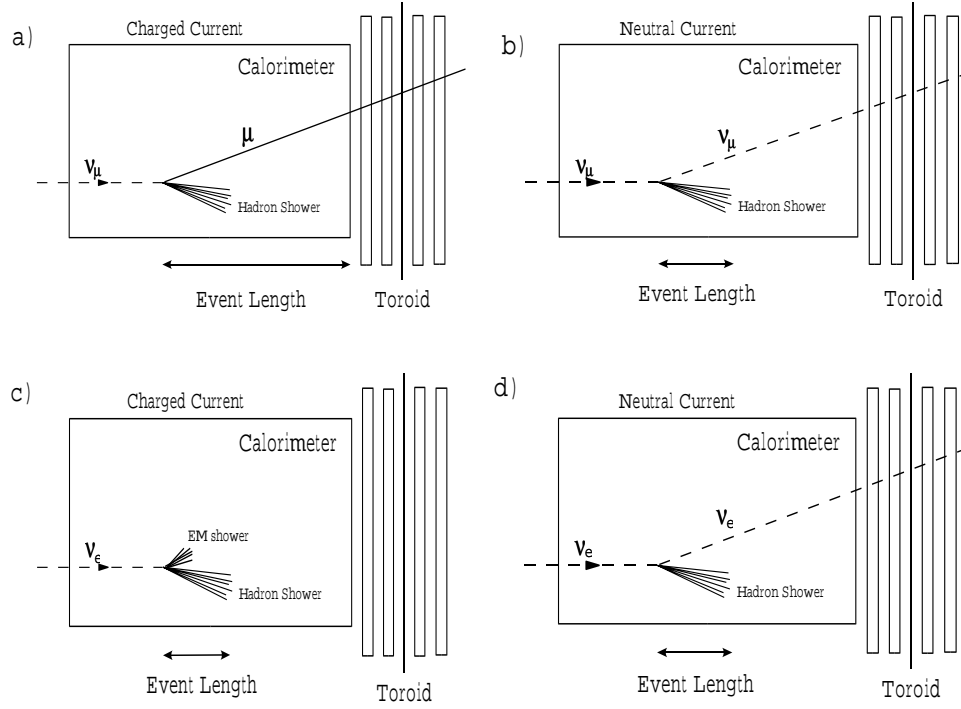


Figure 4.1: Schematic views of neutrino events in the NuTeV detector: a) ν_μ charged-current, b) ν_μ neutral-current, c) ν_e charged-current, d) ν_e neutral-current

Charged-current (CC) neutrino interactions are shown in Figures 2.1 and 2.5 first. Since muon-neutrino CC events have a muon in the final state they are easy to identify. Typically, the final-state muon either penetrates the entire target-calorimeter, or penetrates a substantial fraction of the detector before exiting through one of its sides (with the exception of very low energy muons that range out in the calorimeter). Events with final-state muons are usually “long” in a sense that a significant number (> 20) of consecutive scintillation counters show an energy deposition which is above the threshold of 0.25 MIPs (where a MIP is the mean energy deposition of a minimum ionizing particle). In charged-current

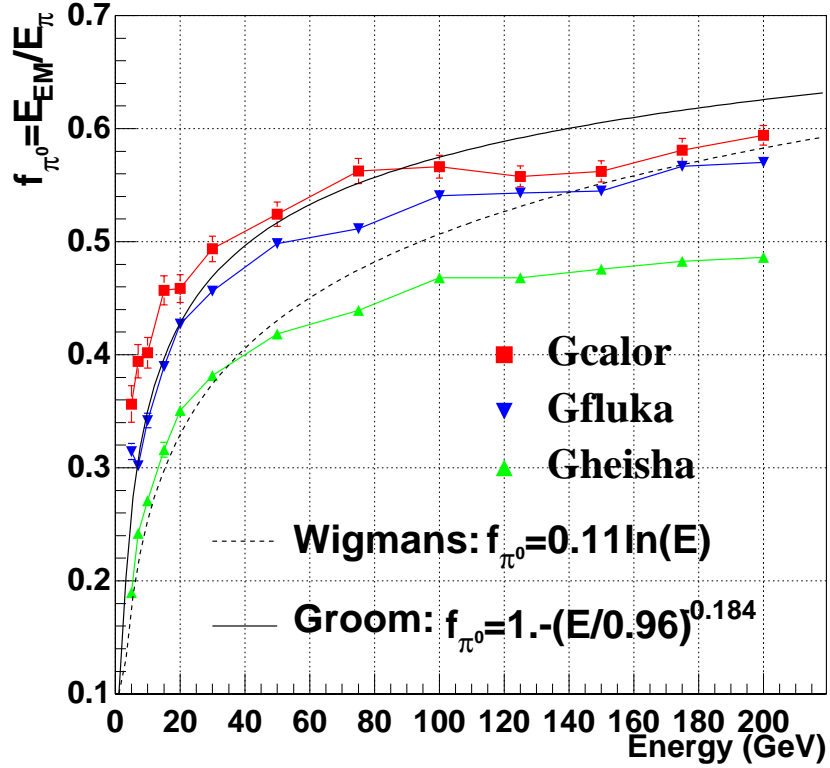


Figure 4.2: Fraction of electromagnetic energy in a hadronic-shower f_{π^0} initiated by test beam pions as a function of the incident hadron energy for three different hadron shower generators: GHEISHA, GFLUKA, and GCALOR; the Wigmans (dashed curve) and Groom (solid curve) parameterizations are also shown.

events, the muon tracks are also reconstructed by the drift chamber hits in the target and in the toroid spectrometer.

In a neutrino interaction, the struck quark fragments into final-state hadrons which initiate a hadronic-shower. This shower is observed in the NuTeV detector in both the drift chambers (as a cluster of drift chamber hits immediately downstream of the interaction vertex) and in the counters (as ionization energy deposited in the scintillation counters). The characteristic length of a hadronic

cascade is the nuclear interaction length λ_I . Since the amount of material between any two consecutive scintillation counters of the NuTeV calorimeter (about 10cm of steel) corresponds to approximately 0.6 of a hadronic interaction length λ_I (see Table 2.1), the typical length of a hadronic-shower is $\sim 10 - 15$ counters. A schematic view of the final state of a ν_μ charged-current interaction, as observed in the NuTeV detector is shown in Figure 4.1a.

Electron-neutrino charged-current interactions produce final state electrons (instead of muons). This results in a dramatic difference in the observed final state in the NuTeV detector. The electron initiates an electromagnetic cascade with a characteristic radiation length X_0 . As shown in Table 2.1, the amount of material between two consecutive scintillation counters corresponds to approximately $6X_0$. This means that the typical length of an electromagnetic cascade in the calorimeter is ~ 3 counters. As shown in the schematic view in Figure 4.1c, ν_e charged-current events are “short” - i.e. the number of consecutive scintillation counters that have an energy deposition above 0.25 MIPS is determined by the length of the hadronic cascade, which is typically less than 20 counters.

The observed final states for ν_e and ν_μ neutral-current events (Figures 2.2 and 2.6) are identical. Here, the outgoing neutrino escapes detection, and only the hadronic shower from the final-state struck quark is observed. Therefore, neutral-current events cannot be used to study electron-neutrino interactions. All neutrino detectors are “neutrino-flavor blind” for neutral-current events. Schematic views of ν_μ and ν_e neutral-current events are shown in Figures 4.1b and 4.1d. These events are also “short” because their length is determined by the length of the hadron shower.

(We assume $\nu_\mu - \nu_e$ universality throughout this analysis [26]).

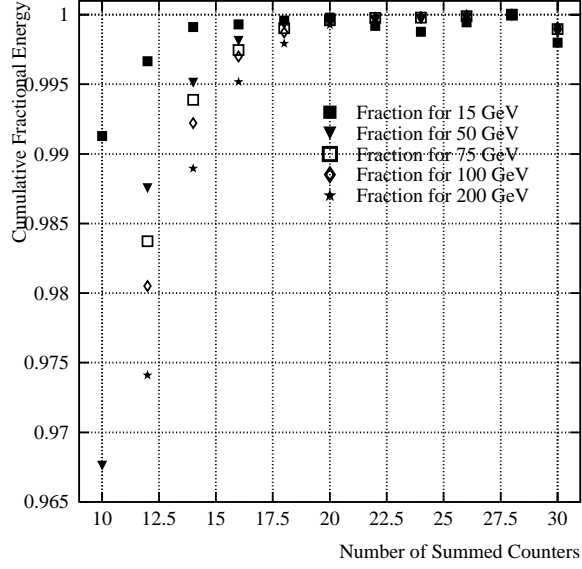


Figure 4.3: The cumulative fractional hadron-shower energy as a function of the total number of consecutive counters from the beginning of the shower. Note that for all hadron energies a total of 20 counters (about 2m of iron) is sufficient for full longitudinal containment of hadron showers.

4.1.1 Electromagnetic vs Hadronic Showers

The method used in this analysis to measure the electron-neutrino flux in the NuTeV detector is based on the difference in event length between hadronic and electromagnetic showers in the calorimeter. The technique involves the use the calorimeter information almost exclusively. To illustrate the technique we consider difference and similarity in the basic properties of electromagnetic and hadronic cascades

The electromagnetic cascade is initiated by an electron through bremsstrahlung and pair production processes. Electrons interact with electromagnetic field of

nuclei and radiate secondary photons. After traversing one radiation length X_0 of material, a fraction $(1 - 1/e)$ of energy is radiated on average. Subsequently, the photons convert to electron-positron pairs and the process continues. The produced electron-positron pairs radiate additional photons that convert into e^+e^- pairs. Therefore, the number of particles in the cascade increases exponentially with the cascade length l :

$$N_{particles} \approx 2^{l/X_0}$$

Note that the energy loss due to ionization as a function of length is proportional to the number of particles in the cascade. When the energies of the particles in the cascade fall below a critical energy E_c , the energy loss due to ionization becomes more important than energy loss due to radiative processes and the development of the cascade comes to an end. After this point all particles deposit their energy in the calorimeter through ionization. Since the scintillation counters sample the energy loss in the calorimeter, the counters provide a measure of the total energy in the cascade.

Because of multiple Coulomb scattering, the electromagnetic shower also spreads in the lateral direction with a characteristic size of one Moliere radius as given by

$$R_m = 21(X_0/E_c),$$

where E_c is in MeV. For the NuTeV detector $E_c \approx E_c(Fe) = 24 MeV$. Therefore, $R_m \sim X_0$ and the lateral spread of an electromagnetic shower is very small.

The physics of hadron showers is different from that of electron initiated showers. The initial hadron undergoes an inelastic nuclear collision which results in the production of secondary hadrons. Aside from neutral pions, these secondary hadrons interact via subsequent inelastic nuclear collisions and produce more sec-

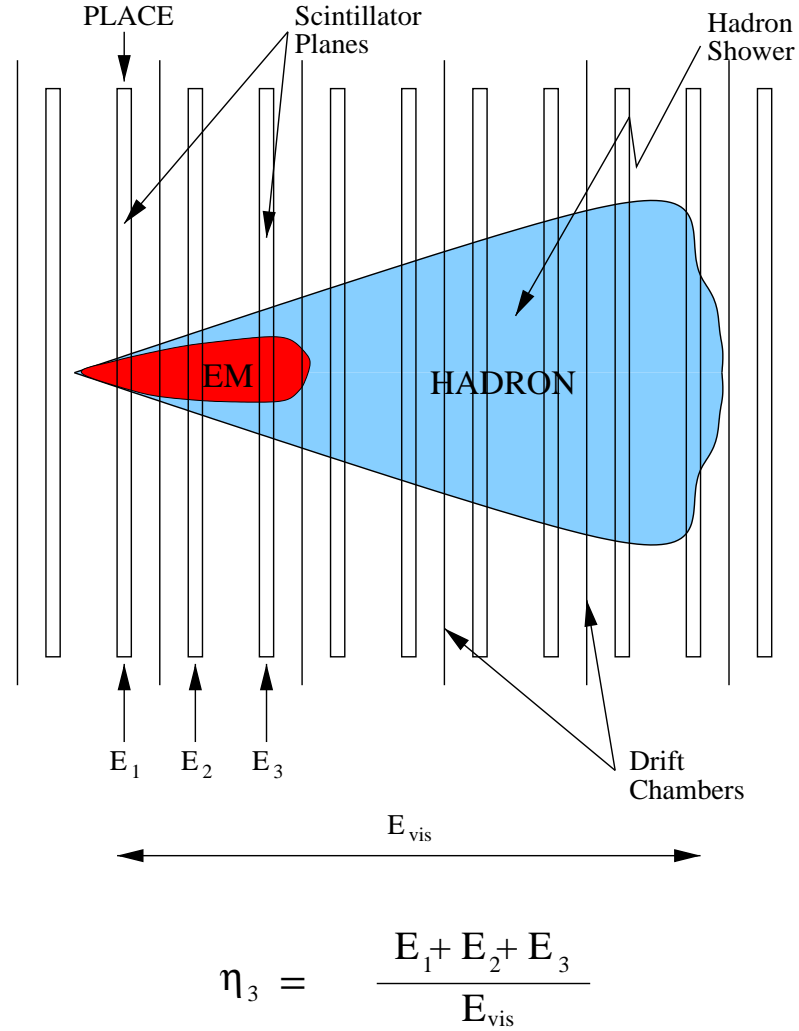


Figure 4.4: Comparative lengths of hadronic and electromagnetic showers in the NuTeV calorimeter and the definition of the η_3 parameter.

ondary hadrons, etc. A hadron shower can be described in an analogous way with an electromagnetic (EM) shower by the replacement of the radiation length X_0 with the nuclear absorption length λ_I as the characteristic length scale. The ratio X_0/λ_I sets the relative longitudinal size of hadron and EM showers. Contrary to the case of an EM shower, a non-negligible fraction of the energy of the in-

cident hadron does not result in any observable signal in the calorimeter. This unobserved energy is the energy lost to nuclear processes such nuclear excitation, nuclear breakup and evaporation neutrons. It is also important to note that a significant fraction of the hadron shower energy is also deposited in the form of an EM cascade which is initiated by neutral pions in the hadron shower. For a test beam pion, the fraction of energy in the hadron cascade that manifests itself in the form of final state neutral pions (f_{π^0}) is not precisely known since it requires a detailed knowledge of all the processes that take place in a hadron shower. However, this fraction can be calculated or modeled using various Monte Carlo generators as shown in Figure 4.2.

For the NuTeV calorimeter the ratio of the typical length scales of EM and hadron showers is given by

$$X_0/\lambda_I \approx 0.11$$

This implies that while EM showers are fully contained in 3–4 consecutive counters for all incident energies, the containment of hadron showers require approximately 20 counters (as shown in Figure 4.3). A comparison of the relative size of EM and hadron showers is shown in Figure 4.4. The large difference in the containment lengths implies that the longitudinal profile of energy deposition in the calorimeter is dramatically different for EM and hadron induced showers. In the next section we introduce the parameter η which is used to quantitatively describe the longitudinal profile of the energy deposition for various types of showers.

4.1.2 The η -parameter

First introduced in the CCFR experiment, the η_3 -parameter:

$$\eta_3 = \frac{E_1 + E_2 + E_3}{E_{cal}} \quad (4.1)$$

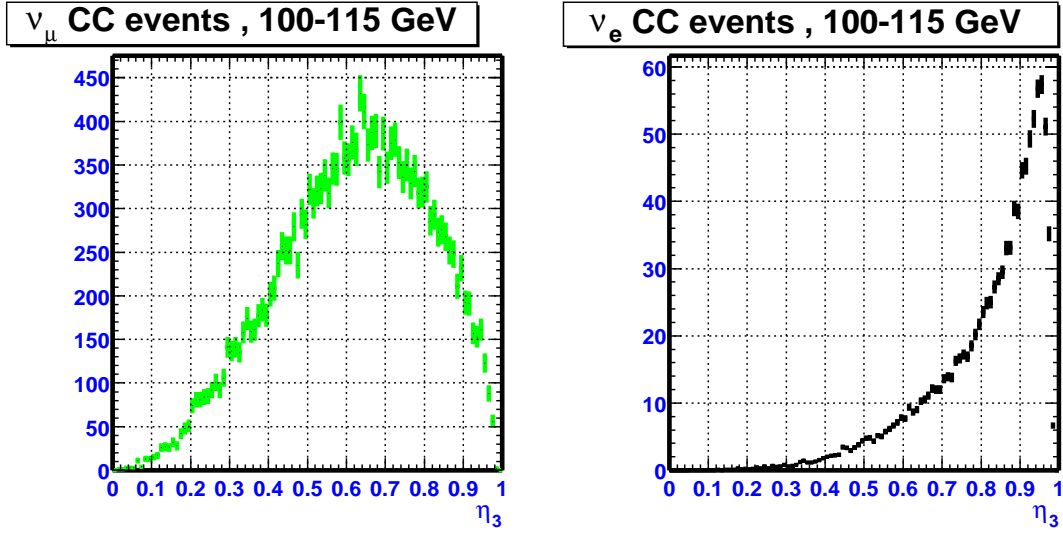


Figure 4.5: Distributions of the η_3 parameter for ν_μ and ν_e charged-current events with a calorimeter energy $E_{cal} = 100 - 115 \text{ GeV}$ (ν_μ CC distribution is obtained from the data, ν_e CC is obtained using the procedure described in Section 6.3, that combines the hadronic showers from the data with the electromagnetic showers from Monte Carlo).

where E_1 , E_2 and E_3 are the energy deposition in three most upstream counters of the event (see also Figure 4.4). This parameter can be used as a measure of the longitudinal shower profile in the NuTeV calorimeter [27]. Here η_3 is the ratio of the energy deposited in the first three scintillation counters downstream of the interaction point to the total energy measured in the calorimeter (E_{cal}). The η_3 distributions of ν_μ and ν_e induced charged-current (CC) events (shown in Figures 4.5 and 4.6) are dramatically different. For ν_μ events (Figure 4.1a), both a final state muon and a hadronic-shower are observed in the detector. The corresponding η_3 distribution for the ν_μ CC events is wide because the fraction of the shower energy deposited in the first three counters fluctuates significantly. These fluctuations correspond to the fluctuations in the fraction of neutral pions

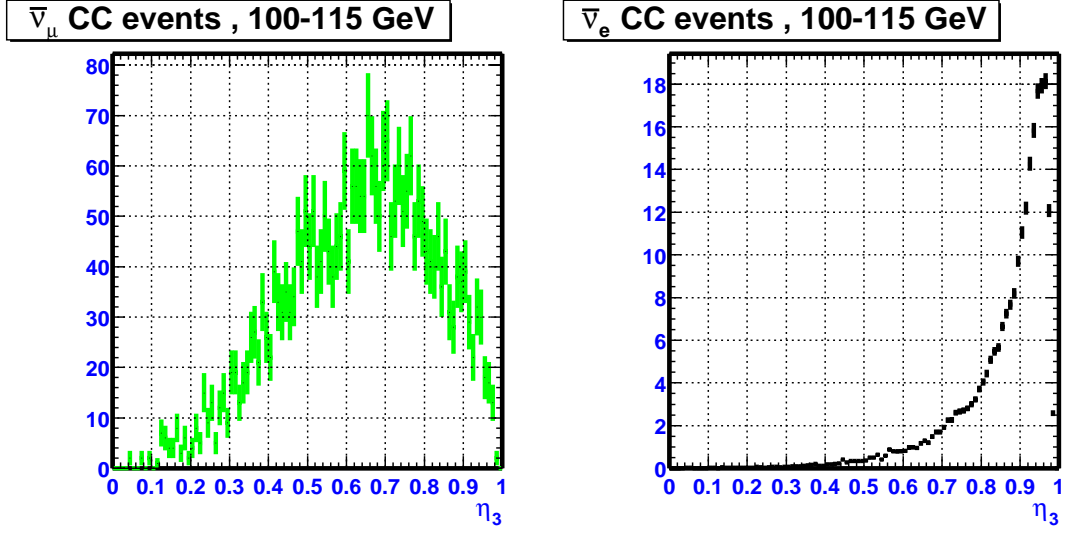


Figure 4.6: Distributions of the η_3 parameter for $\bar{\nu}_\mu$ and $\bar{\nu}_e$ charged-current events with a calorimeter energy $E_{cal} = 100 - 115 \text{ GeV}$ ($\bar{\nu}_\mu$ CC distribution is obtained from the data, $\bar{\nu}_e$ CC is obtained using the procedure described in Section 6.3, that combines the hadronic showers from the data with the electromagnetic showers from Monte Carlo).

produced in the initial neutrino interaction.

The η_3 distribution for ν_μ events peaks at approximately $\eta_3 = 0.7$. For ν_e CC events (see Figure 4.1c) the contributions of the electromagnetic and hadronic shower components cannot be separately observed. What is observed in the calorimeter is the sum of hadronic and electromagnetic shower components. The η_3 distribution for ν_e CC events is sharply peaked at $\sim 0.9 - 0.95$ because the first three counters contain 100% of the energy of the electromagnetic shower from the final state electron and roughly 70% (on average) of the energy of the hadron shower. The difference in the η_3 distributions between ν_e and $\bar{\nu}_e$ events originates from the difference in the y -dependence of the cross-sections for ν and $\bar{\nu}$ events given in Equations 2.9-2.10. Since the y distribution is mainly flat for neutrinos,

the neutrino energy (on average) is evenly divided between electromagnetic and hadronic showers. In contrast, since the y distribution decreases as $(1 - y)^2$ for anti-neutrinos, a larger part of the incident anti-neutrino energy is carried by the final state positron. Consequently, the η_3 -distribution for $\bar{\nu}_e$ events is peaked at ~ 0.95 (which is closer to 1.0 than for ν_e events).

For ν_μ and ν_e neutral-current events, only the hadronic shower is observed in the detector. Therefore, the η_3 for distribution for those NC events is very similar to that of ν_μ charged-current events. Note however that there is a final state muon which is present in ν_μ CC events (but not in NC events). Since this final state muon deposits only a little energy in the first three counters (than the hadron shower), its effect on the η_3 distribution is handled as a small correction as described in Section 4.3.

4.2 Electron Neutrino Flux Measurement

The identification of ν_e induced events in the NuTeV detector begins with the selection of the short events from the total NuTeV data sample. The short event sample used in this analysis is almost identical to the sample used in the NuTeV neutral-current analysis [28] (a precise determination of the electroweak parameters). As mentioned earlier, for each event, the length (L) is defined as the number of scintillation counters between the interaction vertex and the last counter consistent with at least single muon energy deposition. Events with a short length are primarily NC induced. The short event sample used consists of events with $L \leq 28$ counters in neutrino running mode, and $L \leq 27$ in anti-neutrino running mode. A pure sample of $\nu_\mu N \rightarrow \mu^- X$ ν_μ charged-current events is obtained from a “long” sample with $L > 28$ counters in neutrino running mode, and $L > 27$ counters in anti-neutrino running mode.

The short event sample includes ν_e CC and NC events and ν_μ NC events. Since the fraction of ν_e 's in the NuTeV beam is small $\sim 1\%$, the signal/background ratio for such a sample of short events is also small, thus making this search difficult. Initially, it was proposed [27] to use η_3 parameter to improve the signal/background ratio by introducing a cut of $\eta_3 > 0.9$. It is clear from Figures 4.5 and 4.6 that most ν_e CC events pass this cut, and most NC events fail this cut. Although this simple cut analysis is possible in principle, it suffers from one major problem. Namely, one needs to estimate the fraction of NC events that pass the η_3 cut and remain in the sample. The uncertainty in this background estimate results in a background subtraction error. Therefore, this type of a simple cut analysis can only be done when background \ll signal. This situation is only true for events with $E_{cal} > 250 \text{ GeV}$. For this high energy sample, virtually all the NC events are removed by the η_3 cut. In general, this method does not allow for a measurement of the energy spectrum of ν_e events at lower energies. Therefore, a more sophisticated analysis is needed.

Since the neutrino energy spectrum of any oscillation signal is sensitive to the neutrino squared mass difference Δm^2 , it is necessary to measure the energy spectrum of electron neutrinos in order to search for a possible $\nu_\mu \rightarrow \nu_e$ oscillation signal. In this analysis we used an improved version of the CCFR statistical analysis of the η_3 distributions. This statistical technique can be used to measure the energy spectrum of electron neutrinos [37] at all energies. The NuTeV analysis “builds on” the CCFR procedure and introduces additional improvements. In the following we describe the outline of the analysis procedure.

Together with the classification of the data events by length into the “short” and “long” samples, all events are binned into 17 energy bins according to the energy measured in the calorimeter (E_{cal}), as given in Table 4.1. Then the η_3 distributions of the “short” and “long” events are filled separately for each of the energy bins.

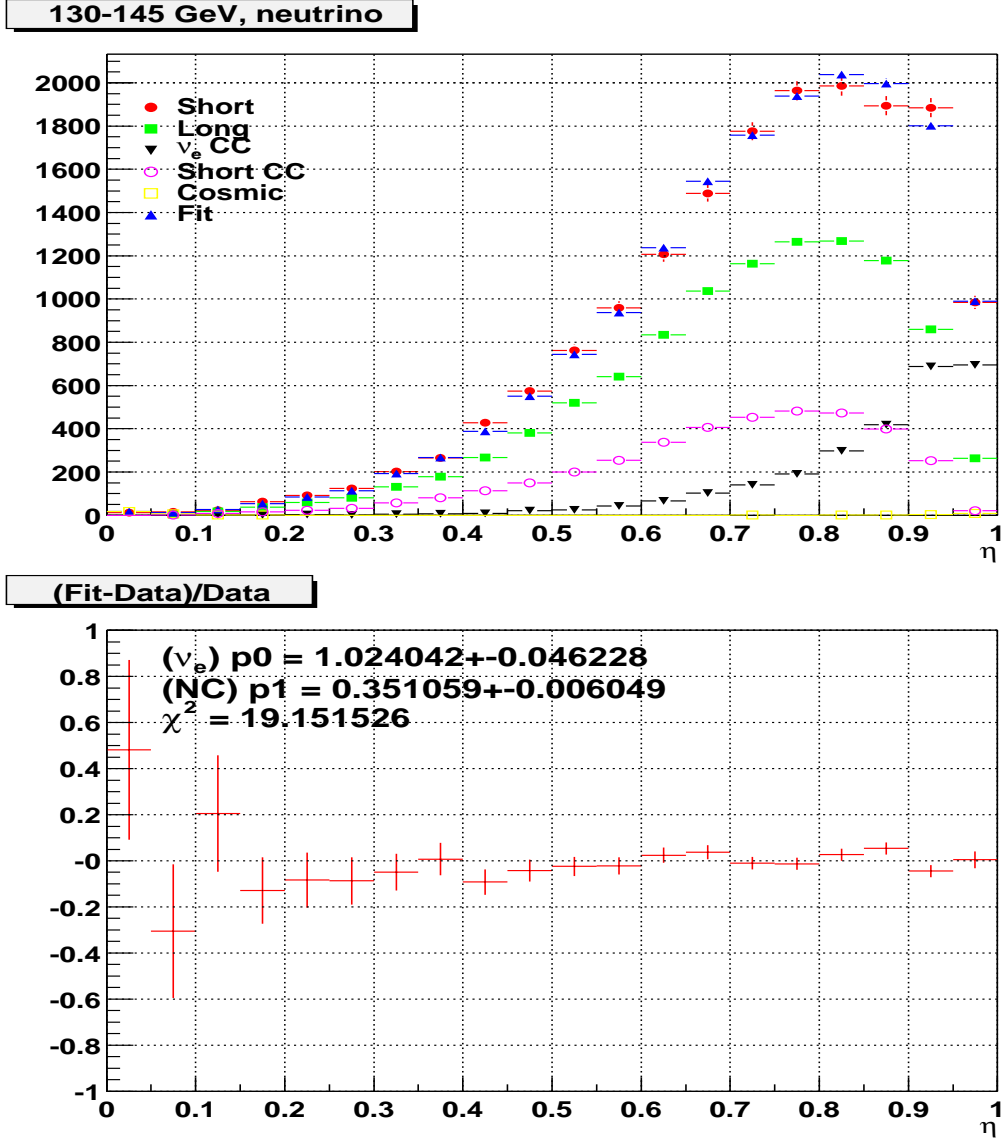


Figure 4.7: Illustration of the statistical analysis of η_3 distributions, neutrino mode. Here, the distribution of short events in the data $\eta_3(Short)$ is fit to a sum of the distributions of long events $\eta_3(Long)$, ν_e charged-current events $\eta_3(\nu_e^{CC})$, ν_μ short charged-current events $\eta_3(Short\ CC)$ and cosmic events $\eta_3(Cosmic)$. The result of the fit - distribution $\eta_3(Fit)$ is also shown.

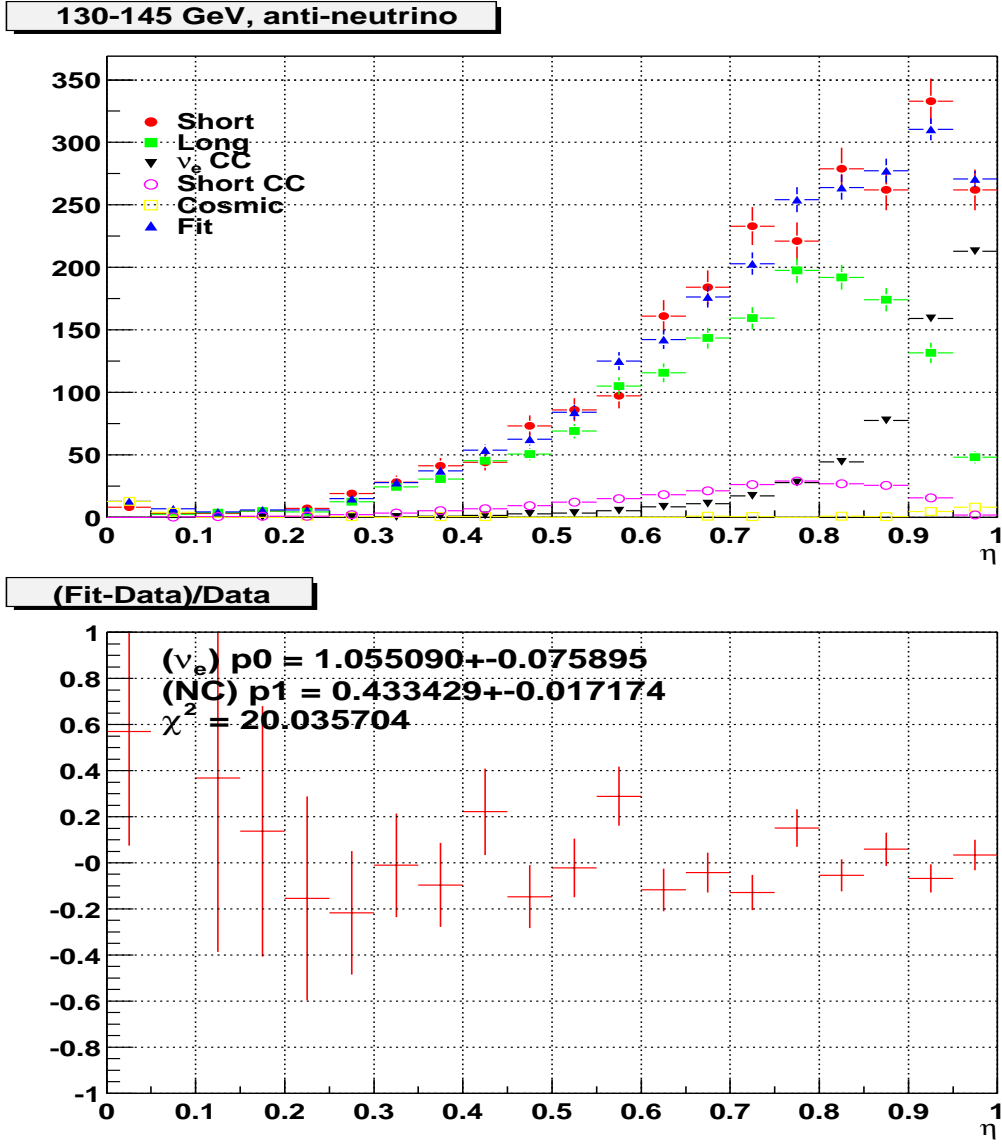


Figure 4.8: Illustration of the statistical analysis of η_3 distributions, anti-neutrino mode. Here, the distribution of short events in the data $\eta_3(Short)$ is fit to a sum of the distributions of long events $\eta_3(Long)$, ν_e charged-current events $\eta_3(\nu_e^{CC})$, ν_μ short charged-current events $\eta_3(Short\ CC)$ and cosmic events $\eta_3(Cosmic)$. The result of the fit - distribution $\eta_3(Fit)$ is also shown.

E_{vis} , GeV	Bin	E_{vis} , GeV	Bin
30 – 40	1	115 – 130	10
40 – 50	2	130 – 145	11
50 – 60	3	145 – 160	12
60 – 70	4	160 – 180	13
70 – 80	5	180 – 200	14
80 – 87.5	6	200 – 225	15
87.5 – 95	7	225 – 250	16
95 – 105	8	250 – 350	17
105 – 115	9		

Table 4.1: Calorimeter energy (E_{cal}) bins.

As previously mentioned, the “short sample” includes all the ν_μ and ν_e neutral-current events, as well as all the ν_e charged-current events. Therefore the η_3 distribution of the short event sample can be written as a sum of two contributions

$$\eta_3[Short] = \alpha \eta_3[\nu_\mu, \nu_e NC] + \beta \eta_3[\nu_e CC] \quad (4.2)$$

where $\eta_3[\nu_\mu, \nu_e NC]$ is the η_3 distribution of the neutral-current events and $\eta_3[\nu_e CC]$ is the η_3 distribution of ν_e charged-current events. The main assumption made in the above equation is that the η_3 distributions of ν_μ neutral and charged-current events differ only by the presence of the muon in the final state in charged-current events. Therefore, one can define the distribution $\eta_3[\nu_\mu, \nu_e NC + \mu]$ as the distribution that results when a muon is added each NC event. Similarly, one can add a final state muon to short events to form the distribution $\eta_3[Short + \mu]$. Under the assumption that the composition of the hadron showers for CC and NC events are the same, the $\eta_3[\nu_\mu, \nu_e NC + \mu]$ distribution can be replaced with $\eta_3[\nu_\mu CC] = [Long]$. However, if we are interested in the η_3 distributions of the ν_e induced charged-current interactions, there is no direct way of extracting these distributions from the data (because as mentioned earlier, we can not separate

these from the neutral-current events on an individual event by event basis). To obtain the η_3 distributions for ν_e charged-current events we rely on a method that combines data with Monte Carlo simulation. At present, there are no reliable hadronic shower Monte Carlo generators. The GEANT based hadronic shower Monte Carlo generators GHEISHA ([29]), GFLUKA ([30]) and GCALOR ([31]) generators have been compared to the test beam data by the NuTeV collaboration and found to provide only qualitative agreement with the data ([34]). In contrast, the GEANT ([35]) based simulation of electromagnetic showers in the NuTeV detector has been tested and is in an excellent agreement with electron test beam data. Therefore, we only use the Monte Carlo to provide the longitudinal energy deposition profiles for electron (positron) induced electromagnetic showers. The profiles for the hadronic part of the shower is extracted from the “long” events. The predicted total shower profile for electron neutrino charge-current events is obtained by taking the electromagnetic shower profile and adding it to a hadronic-shower profile from a long event with a hadron energy that corresponds to the hadron energy of the simulated ν_e event. This procedure is described in detail in Section 6.3. Note that the events simulated using this technique differ from the real ν_e CC events by the presence of the muon track coming from the long event.

Summarizing the previous paragraph, we can rewrite 4.2 as:

$$\eta_3[Short + \mu] = \alpha\eta_3[Long] + \beta\eta_3[\nu_e CC + \mu] \quad (4.3)$$

Now to extract the number of ν_e CC events in the “short sample”, we fit the $\eta_3[Short + \mu]$ distribution by varying parameters α and β in 4.3, minimizing the χ^2 function given by

$$\chi^2 = \sum_{i=1}^{nbins} (\eta_3[Short + \mu]_i - \alpha\eta_3[Long]_i - \beta\eta_3[\nu_e CC + \mu]_i) / (\sigma_{Stat}^2)_i \quad (4.4)$$

Here the quantity $\eta_3[\]_i$ is the number of entries in the i -th bin of the corresponding histogram. The statistical error $(\sigma_{Stat}^2)_i$ is given by

$$(\sigma_{Stat}^2)_i = \eta_3[Short + \mu]_i + \alpha_0^2 \eta_3[Long]_i + \beta_0^2 \eta_3[\nu_e CC + \mu]_i \quad (4.5)$$

The minimization of the χ^2 function is an iterative procedure - during each step of the iteration, the values of the parameters α_0 and β_0 calculated in the previous iteration are used to calculate the statistical error 4.5. The minimization usually requires only 3 – 4 iterations until the values of parameters α and β converge.

Note that there are two additional backgrounds in the short sample - one is the background from cosmic ray events, and the other is the background from ν_μ short charged-current events in which the final state muons ranged out or exited the side of the target. We refer to such events as “Short CC” events, they are described in more detail in Section 4.4. Adding both contributions in (4.3), we can rewrite it as:

$$\begin{aligned} \eta_3[Short + \mu] &= \alpha\eta_3[Long] + \beta\eta_3[\nu_e CC + \mu] \\ &+ C_1\eta_3[Short CC + \mu] + C_2\eta_3[Cosmic + \mu] \end{aligned} \quad (4.6)$$

In this equation C_1 and C_2 are constant parameters. The cosmic ray background is well known from the ratio of the total integrated detector live-time for all neutrino-running and cosmic-ray-running data taking periods (gates), it provides us with the value of C_2 . The short CC background is predicted by a Monte Carlo simulation

of the NuTeV detector. The χ^2 function then becomes:

$$\chi^2 = \sum_{i=1}^{nbins} (\eta_3[Short + \mu]_i - \alpha\eta_3[Long]_i - \beta\eta_3[\nu_e CC + \mu]_i - C_1\eta_3[Short CC + \mu]_i - C_2\eta_3[Cosmic + \mu]_i) / (\sigma_{Stat}^2)_i \quad (4.7)$$

And the statistical error $(\sigma_{Stat}^2)_i$:

$$(\sigma_{Stat}^2)_i = \eta_3[Short + \mu]_i + \alpha_0^2\eta_3[Long]_i + \beta_0^2\eta_3[\nu_e CC + \mu]_i + \quad (4.8)$$

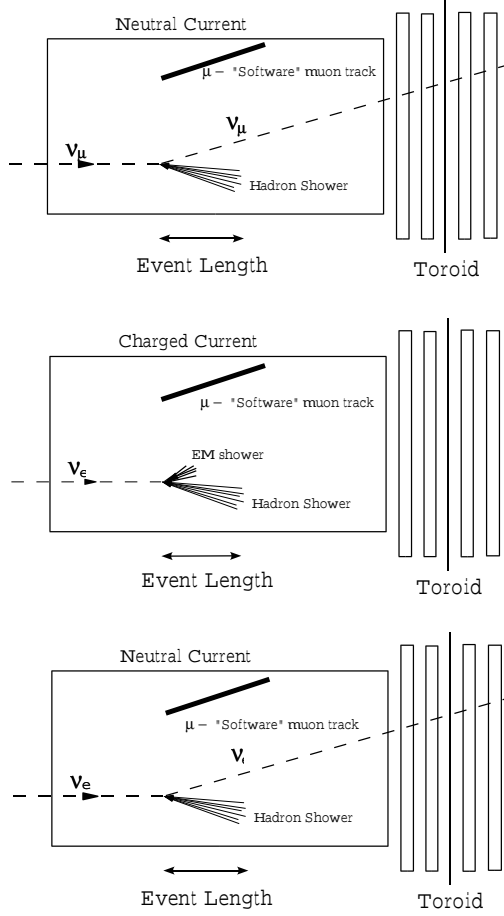
$$C_1^2\eta_3[Short CC + \mu]_i - C_2^2\eta_3[Cosmic + \mu]_i$$

To illustrate this procedure the plots with the fit results for the bin $E_{cal} = 130 - 145 \text{ GeV}$ are shown in Figures 4.7 - neutrino mode and 4.8 - anti-neutrino mode.

4.3 Adding a Muon to the Short Events

The final state muon, which is present in ν_μ CC events, slightly changes the longitudinal profile of the energy deposition in the counters in the region of the hadron shower (compared to hadron showers in ν_μ NC events). To compensate for this difference, all events in the short sample are modified by adding (in software) pulse heights corresponding to a muon track (to the the pulse height in each calorimeter counter in the region of the hadron showers) . The muon tracks are obtained from the data by using the pulse heights of muons in the “long” event sample (for each of the E_{cal} bins separately). To ensure that the muon tracks are uncontaminated by the tails from the hadron showers we use pulse heights that begin 10 counters downstream of the end of the hadron shower. This procedure is shown schematically in Figure 4.9. The comparison of the η_3 distributions of the ν_μ NC events

a) "Short" events – muon track added by software.



b) Muon tracks from "long" events stored.

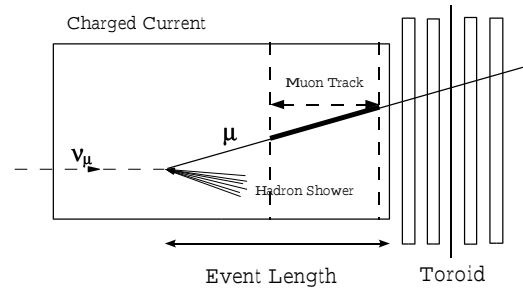


Figure 4.9: a) Muon tracks are added by software to neutrino events in the short sample. b) Muon tracks from the long ν_μ charged-current event sample are used in this procedure.

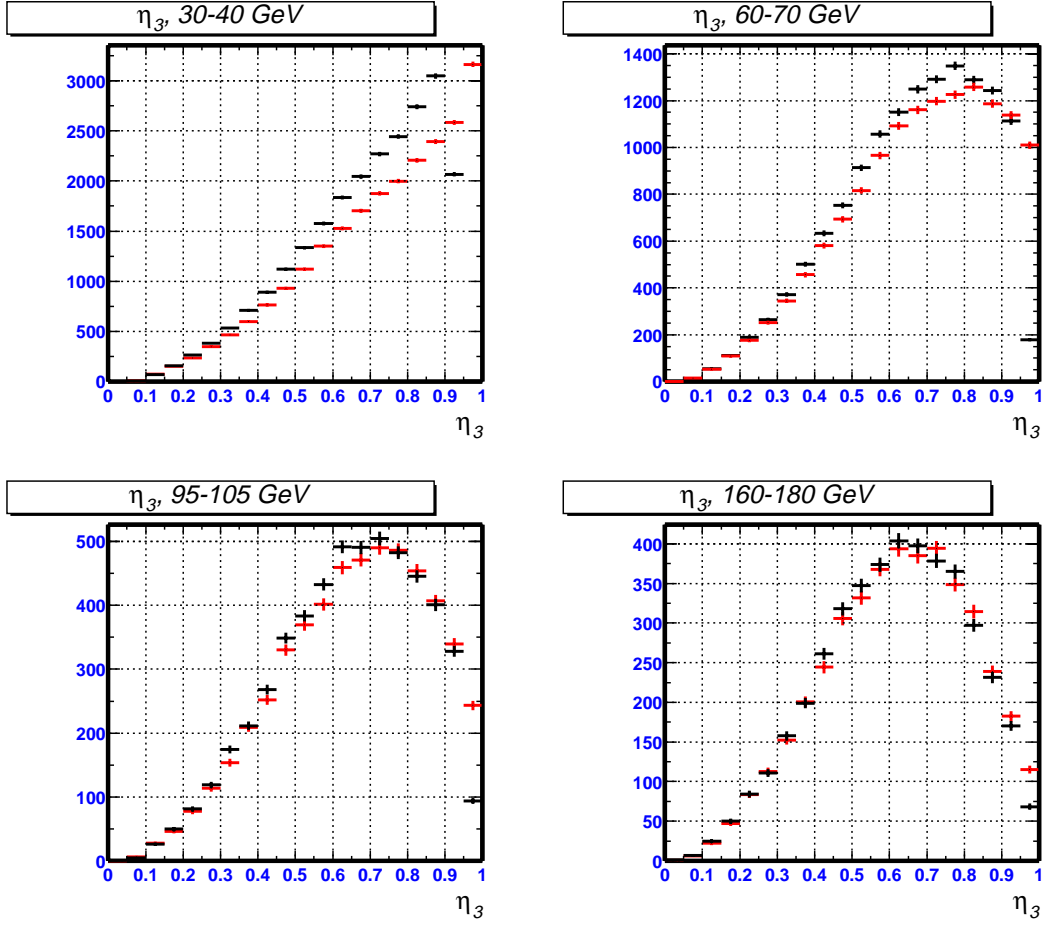


Figure 4.10: The η_3 distributions of ν_μ short events before (red) and after (black) a muon track has been added in software.

before and after the muon track is added by software is shown in Figure 4.10.

4.4 Short Charged-Current Events

The short event sample also contains a fraction of CC events which happen to have a low energy muon (which doesn't exit the shower or leaves the side of the

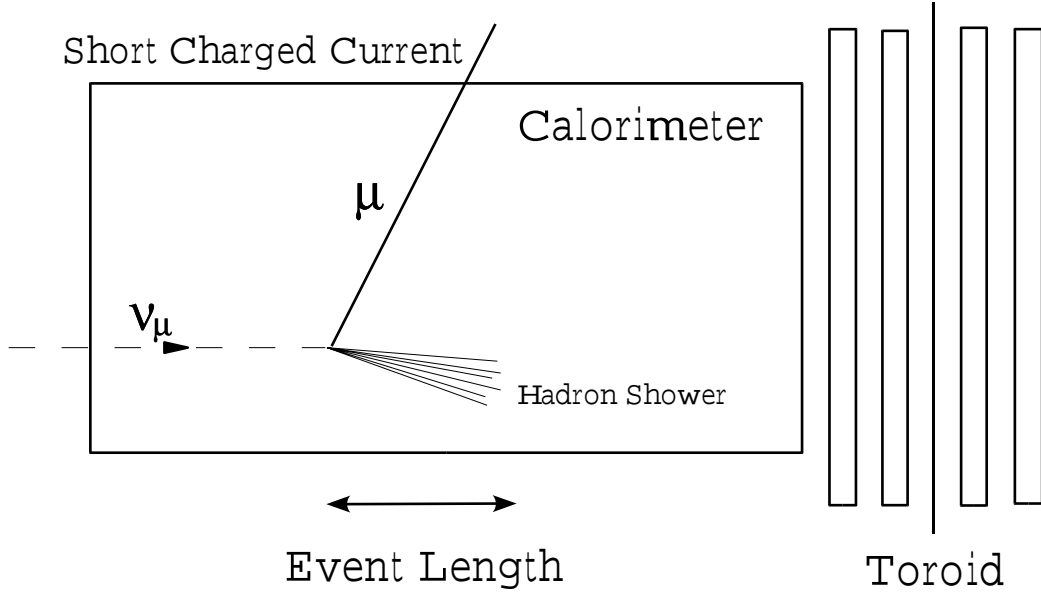


Figure 4.11: Schematic view of a short charged-current event

calorimeter). The schematic plot of a short CC event where muon exits the side of the calorimeter is shown in Figure 4.11. Therefore, this fraction of CC events in the short sample now have two muon tracks. One of the muon tracks corresponds to the initial short muon track from final state muon on the CC neutrino interaction, and a second longer muon track corresponding to the extra muon track what has been added in software. Since this category of events is not present in the long sample, a correction for this is applied. The number of ν_μ CC events with a low energy muon in the short sample is estimated from the Monte Carlo (as given in Tables 5.1 and 5.2). A simulated sample of such events is obtained by choosing “long” events with the right energy distribution from the data to which a second muon track is added in software. The pulse heights deposited by the second muon in each counter are corrected by a factor of $1/\cos\theta$, where θ is the angle of the

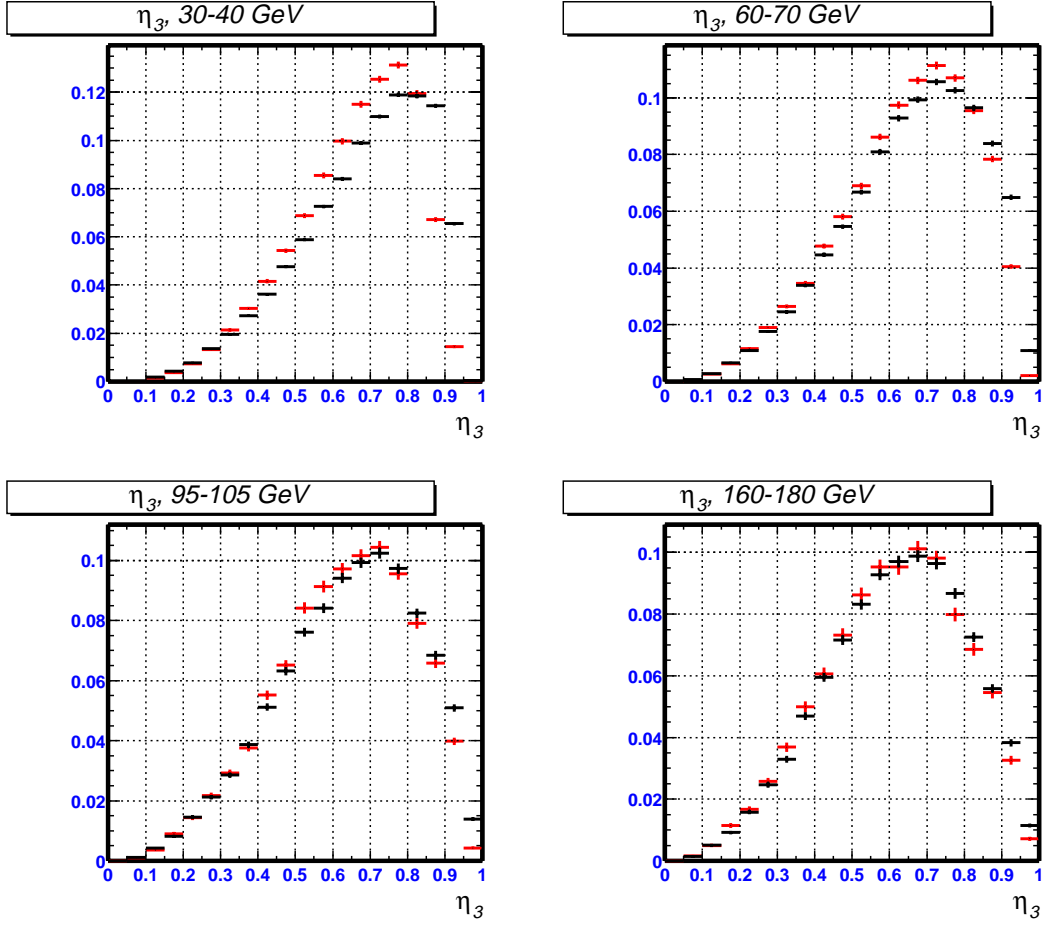


Figure 4.12: The η_3 distributions of “long” events (red) and of simulated short ν_μ CC events (black) with a second muon track has been added in software.

muon track with respect to the direction of the incident neutrino. The length of the second short muon track and its angular distribution are obtained from a Monte Carlo of short ν_μ CC events. The comparison of the η_3 distributions of the short ν_μ CC events (with two muons) and “long” CC events (with one muon) is shown in Figure 4.12.

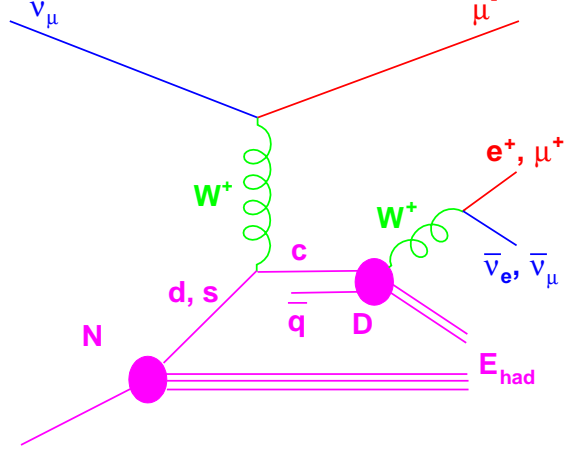


Figure 4.13: Feynman diagram of a dilepton event.

4.5 Biases and Systematic Effects in the η -analysis: Need for a Monte Carlo Simulation

In this section we discuss additional effects that complicate the analysis and need to be taken into account.

First, the assumption that final state hadron showers for neutral and charged-current events are the same is not totally correct. In charged-current events, bremsstrahlung photons are emitted by the final state muon in the scattering process. These photons, which contribute to the experimentally observed final state shower in the calorimeter, are not accounted for in the above procedure.

Then, we compensate the presence of muons in CC events by adding muon tracks to all short events in software. But since the interaction vertex is not

known exactly, the muon is added starting the vertex position, smeared by the experimental resolution.

Another effect is that because of the procedure of selection of the muon tracks to be added to the short events these tracks have slightly different energy and angular distributions than muons in CC events.

Second, our method of modeling ν_e CC events provides only an approximation of the η_3 distributions of the real ν_e CC events. It must be verified that the use of such an approximation results in an unbiased measurement of electron neutrino flux, or a correction should be applied to the measured flux.

Third, the method, described in Section 4.4, that is used to obtain η_3 distributions of short CC events also is an approximation. There are several features of the real short CC events, that this procedure does not reproduce. For example, muon tracks that exit through the side of the detector deposit energy in the outermost region of several scintillation counters, where the response functions change rapidly. Our simulation procedure does not account for that, because all the stored muon tracks do not exit the detector. The resulting effect is that the energy deposited by a muon in a real short CC event is slightly higher than the energy, deposited by a software added muon, in a simulated short CC events.

And finally, some of the CC interactions produce a heavy charm-quark in the final state (the Feynman diagram of this CC process is shown in Figure 4.13). The c -quark fragments into a charm-meson with a very short lifetime. Subsequently, the charm-meson can undergo a semileptonic decay in which a second lepton (μ or e) is produced in the final state. Events with two muons are removed from all our samples. However, since almost all of the $\mu + e$ events are identified as “long” because of the presence of the first muon, we must correct for the presence of $\mu + e$ events in the “long” sample.

To account for all of these effects a detailed Monte-Carlo simulation of the

shower shape analysis has been developed. This simulation is described in detail in Chapter 6.

Chapter 5

Data Selection and Analysis

This chapter describes the procedures used for data selection and analysis. Section 5.1 describes the initial shower selection algorithm; Section 5.2 the neutrino interaction vertex determination; Section 5.3 the definition of calorimeter energy E_{cal} used in this analysis; Section 5.4 the analysis cuts; Section 5.5 summarizes the statistics of the collected data sample.

5.1 Shower Selection

The following algorithm is used to find an interaction region in the NuTeV calorimeter.

1. Find all the scintillation counters with energy deposition greater than 0.25 minimum ionizing:

$$E(CounterI) > 0.25 \text{ MIP} \quad (5.1)$$

These counters are referred to as “*S – bit ON*” counters*

*“*S – bit*” (single minimum ionizing bit) is really a hardware signal - the output of *HIGH* ADC from each counter is amplified by a factor of 100 and is sent through a discriminator. The

2. Find clusters with consecutive “*S – bit ON*” counters.
3. Merge clusters separated by one or two “*S – bit OFF*” counters. The scintillation counters are not 100% efficient in detecting muons. If a muon passes through one of the “ribs” in a counter it often deposits less than 0.25 MIP which results in a “*S – bit OFF*”. The merging is done to prevent an incorrect determination of the event length in cases of counter inefficiency.
4. Select a cluster with the highest energy. This cluster is chosen as a neutrino interaction region.

This procedure is illustrated in Figure 5.1. The most upstream counter of the selected interaction region is referred to as *START* and the most downstream as *EXIT*.

5.2 Vertex Finding Method

The transverse and longitudinal positions of the neutrino interaction vertex are determined separately. The longitudinal position is found using the calorimeter counter information. The transverse position algorithm uses the drift chamber hits.

5.2.1 Longitudinal Position: “PLACE” Algorithm

The majority of neutrino interactions occur in the steel plates, placed between the scintillation counters. Since neutrino cross-sections are extremely small, only a negligible fraction of the neutrinos in the beam interact in the NuTeV detector.

discriminator level for each counter is set such that the resulting *S – bit* is on if the energy deposition in the counter is greater than 0.25 MIP .

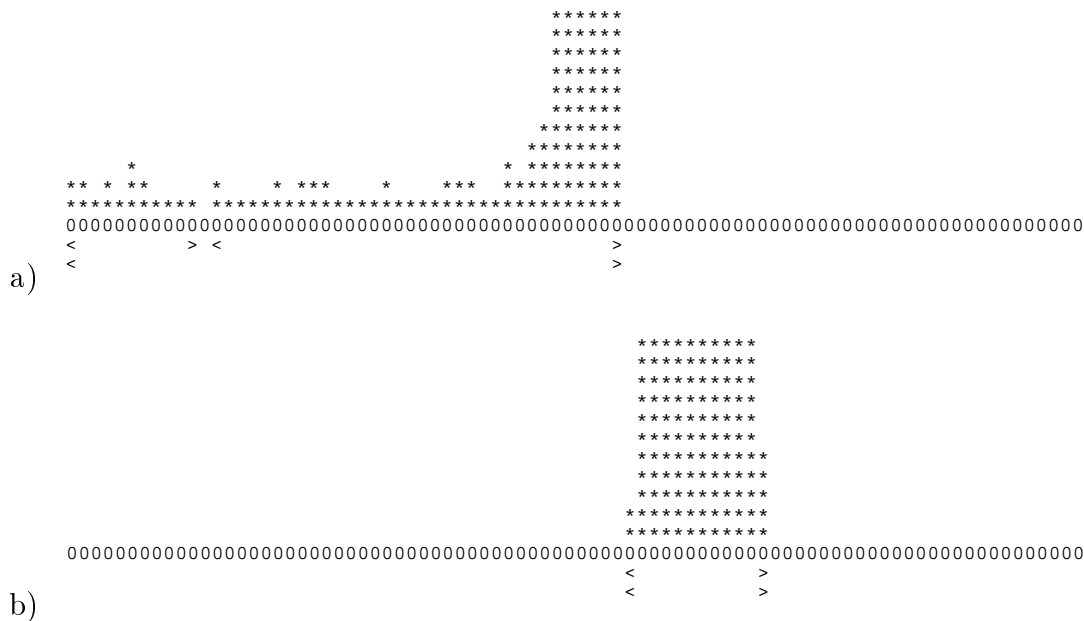


Figure 5.1: Interaction region finding algorithm: a) a long event found, b) a short event found. Energy deposition in each of the 84 scintillation counters is represented by a column of “*”s. The clusters of $S-bitON$ counters are shown with delimiters $<$ and $>$.

Therefore, the intensity of the neutrino beam does not change along the z -axis. Since the source of neutrinos (the decay pipe) is located ~ 1 km upstream of the detector, the beam divergence over the detector length is negligible. This means that neutrino interactions are uniformly distributed along the z -axis. This analysis does not attempt to determine the exact location of the longitudinal vertex inside the steel plate. Instead we find the closest scintillation counter downstream of the interaction point. This counter is referred to as the interaction “*PLACE*”. Counter *PLACE* is the first counter in the shower region of the calorimeter where the energy deposition is large. The scale of “large” and “small” energy depositions is set by the energy loss of a minimum ionizing particle (1 *MIP*). The simplest

choice of *PLACE* is defined as the upstream counter of two consecutive counters with energy depositions greater than $N - MIPs$. The initial choice of $N = 4$ has been somewhat arbitrary. A Monte Carlo study showed however, that a 4, 4 algorithm introduces an energy dependent bias into the determination of *PLACE*. For some fraction of the neutrino events, the 4, 4 algorithm for *PLACE* systematically shifts *PLACE* upstream of the true z vertex. This is caused by the “albedo” effect - some of the low energy hadrons produced at the initial interaction point have momentum directed upstream and produce a signal in the scintillation counter upstream of the true *PLACE*. The size of the “albedo” depends on the energy of the hadronic system, and is higher at higher energy. Therefore, the mean shift between 4, 4 - *PLACE* and true *PLACE* is also energy dependent. It is possible to remove this bias by making the choice of N dependent on the energy of the hadron shower. It was found (as described in [37]) that the bias is minimized with the choice of N parameterized by:

$$N = -1.0679 + 0.9660 \times \sqrt{E_{cat}} \quad (5.2)$$

This function is shown in Figure 5.2. As mentioned in Section 4.5, it’s also necessary to find the first counter in hadron showers for neutral- and charged-current events without introducing any bias between the two classes of events. This is essential in our analysis which makes use of the longitudinal shower profiles. There are two effects that must be considered:

- A N, N cut on neutral-current events is equivalent to a $(N - 1), (N - 1)$ cut on charged-current events (because charged-current events have a muon that deposits roughly 1 *MIP* in each counter)
- $E_{cat} = E_{cat}(Shower) + E_{cat}(Muon)$ for charged-current events, so the value

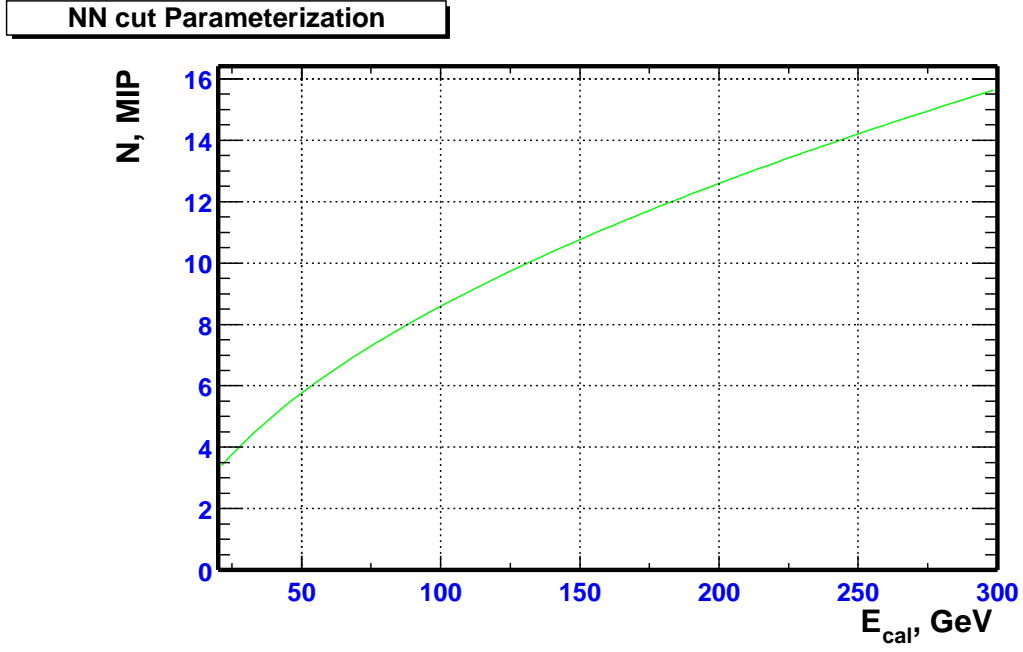


Figure 5.2: $NN - PLACE$ algorithm: dependence of N on calorimeter energy E_{cal} .

of N , as calculated with Equation 5.2 is higher than that for neutral-current events

These two effects have opposite sign and partially cancel each other. A correction described in Section 6.5.3 is applied to the analysis to eliminate any residual bias between neutral-current and charged-current events.

5.2.2 Transverse Position

The transverse position of the neutrino interaction is determined to be the energy weighted mean of the x and y positions of the drift chamber hits in the two drift chambers immediately downstream of $PLACE$. More details on the algorithm are

be found in reference [38].

5.3 Calorimeter Energy

The measurement of the energy deposited in the calorimeter is necessary to reconstruct the kinematics of a neutrino event (needed in all NuTeV physics analyses).

There are several different definitions of E_{cal} used in NuTeV. In this analysis we use the *EHAD20* definition, that is the sum of the energies deposited in 20 consecutive scintillation counters starting one counter upstream of *PLACE*:

$$EHAD20 = \sum_{I=PLACE+1}^{PLACE-19} E(Counter\ I) \quad (5.3)$$

Note that the CCFR/NuTeV convention is such that counter 84 is the most upstream counter and counter 1 is the most downstream counter. A total of 20 scintillation counters (about 2m of steel) correspond to approximately 15 nuclear absorption lengths (λ_I). This definition is used in the calorimeter energy calibration in the hadron test beam [34]. It guarantees the full containment of the hadron shower (Figure 4.3) up to the maximum beam energy.

5.4 Event Selection

All data events are required to pass a set of “analysis cuts”. This section describes all the cuts used in the shower shape analysis.

Beam Cut

Events are recorded only during spills when the beam monitors measure more than 0.5×10^{11} protons per spill incident on the NuTeV production target. This

ensure the presence of a neutrino beam and minimizes the cosmic ray subtraction.

Event Gate

Only events in the neutrino gates (gates 1 – 5) and cosmic ray gates (gate 7) are selected. This removes events taken during the time of the test beam. Events taken during the cosmic gate are kept separately, but analyzed in the same as neutrino events. Later the cosmic ray gate sample is used for background subtractions.

Event Timing Cut

The timing of the event is measured using the time-to-digital converters. Signals from the active scintillation counters are fed into TDC's which have a time resolution of 4 ns . The timing cut

$$|T_{trigger} - T_{active\ counters}| < 100\text{ ns} \quad (5.4)$$

is used to remove the “out of time” events that are not associated with the neutrino event trigger.

Straight Through Muon Cut

Two most upstream counters (counters 83 and 84) are used as a veto to remove muons and other charged particles entering through the front face of the detector by requiring:

$$START \leq 82 \quad (5.5)$$

Fiducial Cuts

Events are required to pass a set of fiducial cuts that allow accurate and unbiased measurements of the event length and visible energy. The transverse position of

the interaction vertex is required to be within a $45in \times 45in$ box:

$$|VERT_X| < 45in \quad (5.6)$$

$$|VERT_Y| < 45in \quad (5.7)$$

This transverse fiducial cut guarantees full containment of the hadronic shower in the transverse direction. Since this cut removes events near the edge of the detector, it also reduces the contamination of short ν_μ CC events (where muons exit out the side) in the short sample.

In the longitudinal direction, the first counter in the shower region - *PLACE* - is required to be at least 5 counters away from the most upstream calorimeter plate of the detector. Similarly it is required to be at least *LENGTH_CUT* + 3 counters away from the downstream end of the detector. This latter requirement is needed in order for an event to be classified in the long or short category:

$$PLACE \leq 78 \quad (5.8)$$

$$PLACE > 31 \text{ } (\nu - mode) \quad (5.9)$$

$$PLACE > 30 \text{ } (\bar{\nu} - mode) \quad (5.10)$$

Deep- μ Cut

Muons passing through the detector deposit, on average, one MIP per scintillation counter due to ionization losses. It is also possible for muons to lose energy catastrophically as a result of interactions in the detector. These showers are electromagnetic in nature. For a low y neutrino charged-current event with a muon track (ν_μ CC), the place finding algorithm will fail to find the start of the neutrino interaction at the event vertex (since there is very little hadron energy there) but

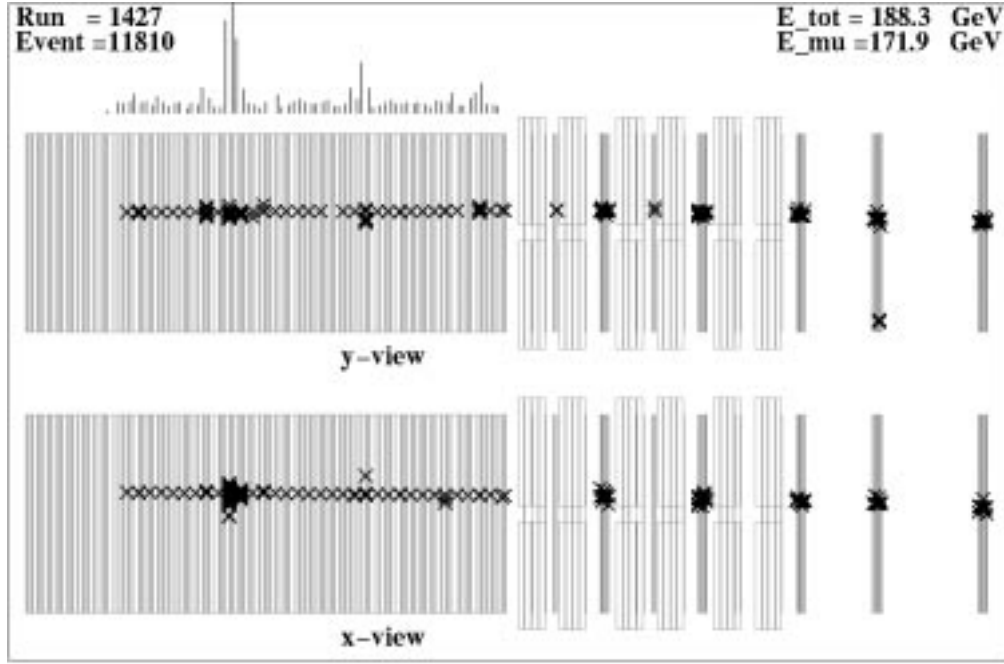


Figure 5.3: An event which failed the deep-mu cut 5.11. This event is most likely a neutrino induced deep-mu event.

will instead identify the location of a catastrophic energy loss of the muon (which we call deep μ) as the interaction vertex. Figure 5.3 shows an example of such an event.

Since deep- μ events have a muon track, these events are assigned to the long sample. In our analysis the long sample is used to obtain a sample of hadron showers are assumed to be purely hadronic. The presence of electromagnetic showers in the long sample from deep- μ events mimics the signature of ν_e CC interactions (which are present in the short sample). Therefore, it is important to remove these events from the long sample of hadron showers.

In order to find a cut that removes deep- μ events without introducing a strong bias in the neutrino event sample, we studied the distribution of the number of

counters between the beginning of the neutrino interaction region as the determined by the first presence of a minimum ionizing signal, *START*, and the beginning of the hadron shower region as defined by *PLACE*. Based on these studies, we require:

$$START - PLACE < 5, \quad (5.11)$$

which eliminate most of the deep- μ events.

Visible Energy

A minimum calorimeter energy cut is required:

$$E_{cal} > 30 \text{ GeV} \quad (5.12)$$

- This cut ensures high efficiency of the neutral-current hadron energy trigger
- It rejects low energy events, which span only a few counters. With our sampling, it is difficult to perform an accurate measurement of the longitudinal energy deposition profile at low energy.
- This cut reduces the cosmic-ray and deep- μ contamination.

5.5 The NuTeV Data Sample

As described in Section 4.1.2 all data events are classified according to the event length. We define “short” and “long” data samples. The length of the event is defined by the number of consecutive active counters in the calorimeter:

$$LENGTH = PLACE - EXIT + 1 \quad (5.13)$$

E_{vis} , GeV	<i>Short</i>	<i>Cosmic</i>	<i>Long</i>	<i>Short CC</i>
30 – 40	69629	4352	148144	16615.3
40 – 50	62308	1698	123788	17515.2
50 – 60	54182	1055	100835	16896.9
60 – 70	45877	536	80963	15468.6
70 – 80	38031	396	62899	13364.1
80 – 87.5	23122	167	37917	8121.48
87.5 – 95	19517	145	31369	6552.53
95 – 105	21015	160	35176	6605.14
105 – 115	16756	115	29050	4637.54
115 – 130	20592	135	37550	4783.84
130 – 145	16698	93	31944	3756.17
145 – 160	14963	62	27455	3436.15
160 – 180	17009	67	29414	4464.07
180 – 200	13355	84	21475	4086.46
200 – 225	11403	37	17263	3859.07
225 – 250	6606	18	9214	2405.78
250 – 350	6049	38	7200	2617.33
<i>Total</i>	536319	28197	1002415	148523

Table 5.1: NuTeV data sample, neutrino mode. The numbers of events that passed all analysis cuts are shown for each bin of the calorimeter energy E_{vis} . The number of short ν_μ charged-current events, predicted by Monte Carlo is shown in the last column.

The short sample is selected by the following cut:

$$LENGTH \leq 28 \text{ } (\nu - mode) \quad (5.14)$$

$$LENGTH \leq 27 \text{ } (\bar{\nu} - mode) \quad (5.15)$$

All the events that do not pass the short sample cut (equation 5.14) are placed into the long sample category.

The summary tables below (Tables 5.1 and 5.2) list the number of events, selected for this analysis, in bins of calorimeter energy E_{cal} . The predicted number of ν_μ CC events that pass the “short” cut 5.14 is also shown. The total accumulated

E_{vis}, GeV	<i>Short</i>	<i>Cosmic</i>	<i>Long</i>	<i>Short CC</i>
30 – 40	21742	5141	44219	2175.66
40 – 50	15351	1969	31010	1924.44
50 – 60	11526	861	22618	1629.13
60 – 70	8668	572	16259	1448.03
70 – 80	6428	322	11732	1159.2
80 – 87.5	3870	211	6639	710.453
87.5 – 95	3103	130	5212	559.203
95 – 105	3270	168	5446	535.131
105 – 115	2594	130	4285	349.622
115 – 130	2978	83	4912	331.5
130 – 145	2349	83	3929	219.14
145 – 160	1870	71	2889	181.046
160 – 180	1883	56	2842	216.197
180 – 200	1337	26	1856	193.941
200 – 225	992	18	1244	176.186
225 – 250	557	16	613	101.678
250 – 350	379	27	410	96.6062
<i>Total</i>	123536	31156	228715	14257.8

Table 5.2: NuTeV data sample, anti-neutrino mode. The numbers of events that passed all analysis cuts are shown for each bin of the calorimeter energy E_{vis} . The number of short ν_μ charged-current events, predicted by Monte Carlo is shown in the last column.

statistics includes ~ 1.5 million events in neutrino mode and $\sim 350,000$ events in anti-neutrino mode.

Chapter 6

Monte Carlo Simulation of the η -analysis

This chapter describes the software packages used in the Monte Carlo simulation of the neutrino flux, the cross-section model, the NuTeV detector, and the shower shape analysis. Section 6.1 introduces the NuTeV specific software simulation packages NUMONTE and McNuTeV. Section 6.3 describes the simulation of ν_e CC events, which involves combining hadron showers from “long” data events with Monte Carlo electromagnetic showers simulated with GEANT. Section 6.4 describes the Monte Carlo simulation of the emission of radiative photons in ν_μ CC events. Finally, Section 6.5 describes the full Monte Carlo simulation of the shower shape analysis.

6.1 NuTeV Monte Carlo simulation packages NUMONTE and McNuTeV

There are two Monte Carlo simulation packages (written by the members of the CCFR/NuTeV collaboration) used in the simulation of the neutrino cross-section and detector response. The NUMONTE “fast Monte Carlo” is used for the simulation of the physics model of neutrino interactions. NUMONTE also simulates the overall response of the neutrino detector using parameterizations of the hadron and muon energy resolutions. In contrast, the McNuTeV Monte Carlo incorporates a full hit-level simulation of the response of the neutrino detector.

6.1.1 NUMONTE

NUMONTE starts with a physics model simulation of neutrino interactions in the NuTeV detector. It includes: (a) the event generation which yields a sample of events according to a physics model, and (b) the detector simulation which mimics the reconstruction of the generated events by simulating experimental effects such as acceptance and resolution smearing. NUMONTE uses neutrino flux files, produced by the neutrino beam line simulation program, as input (the beam line simulation program is described in Section 3.2). The flux files contain information about the neutrino flux at the NuTeV detector $\Phi(E_\nu^i, V_x^j, V_y^k)$ in bins of neutrino energy E_ν and transverse position V_x, V_y . The neutrino cross-section model, implemented in NUMONTE is based on the standard deep inelastic scattering formalism described in Section 2.2. A modified Bouras-Gaemers parameterization ([40]) of the parton distribution functions is used (as described in detail in reference [39]). After the generation of a given neutrino event kinematics according to the chosen cross-section model, NUMONTE simulates the observed quantities such as

the calorimeter energy (E_{cal}), muon energy as measured by the toroid spectrometer (E_μ), and the interaction vertex location ($VERT_X$, $VERT_Y$, $PLACE$), by smearing the generated quantities according to measured resolution functions of the NuTeV detector.

NUMONTE is primarily used in the simulation of the detector acceptance and smearing effects for various NuTeV physics analyses. Since NUMONTE does not include a full hit level simulation of the detector, the generation of extremely large statistical samples of Monte Carlo events is possible.

In this analysis, NUMONTE is used to simulate the E_{cal} distribution of ν_e CC events and the E_{cal} distribution of the “long” events (which are used for overall normalization). Both distributions are shown in Figure 6.1. The E_{cal} distributions of “long” events in data are in excellent agreement with the NUMONTE predictions.

NUMONTE is also used to write out the values of the kinematic variables E_ν , x , y , V_x , V_y , V_z etc of all the generated neutrino events into “pipe” files. These files are used as an input by McNuTeV - the hit level Monte Carlo simulation of the NuTeV detector. This capability allows both Monte Carlo generators to use the same identical cross-section model and Monte Carlo event samples.

6.1.2 McNuTeV

McNuTeV is a GEANT-based software package that provides a full hit-level Monte Carlo simulation of the NuTeV detector. GEANT ([35]) is a software package for the simulation of the passage of particles through matter. GEANT has been extensively used in simulations of particle physics detectors in high energy physics experiments.

All the active and passive elements of the NuTeV detector are rigorously defined

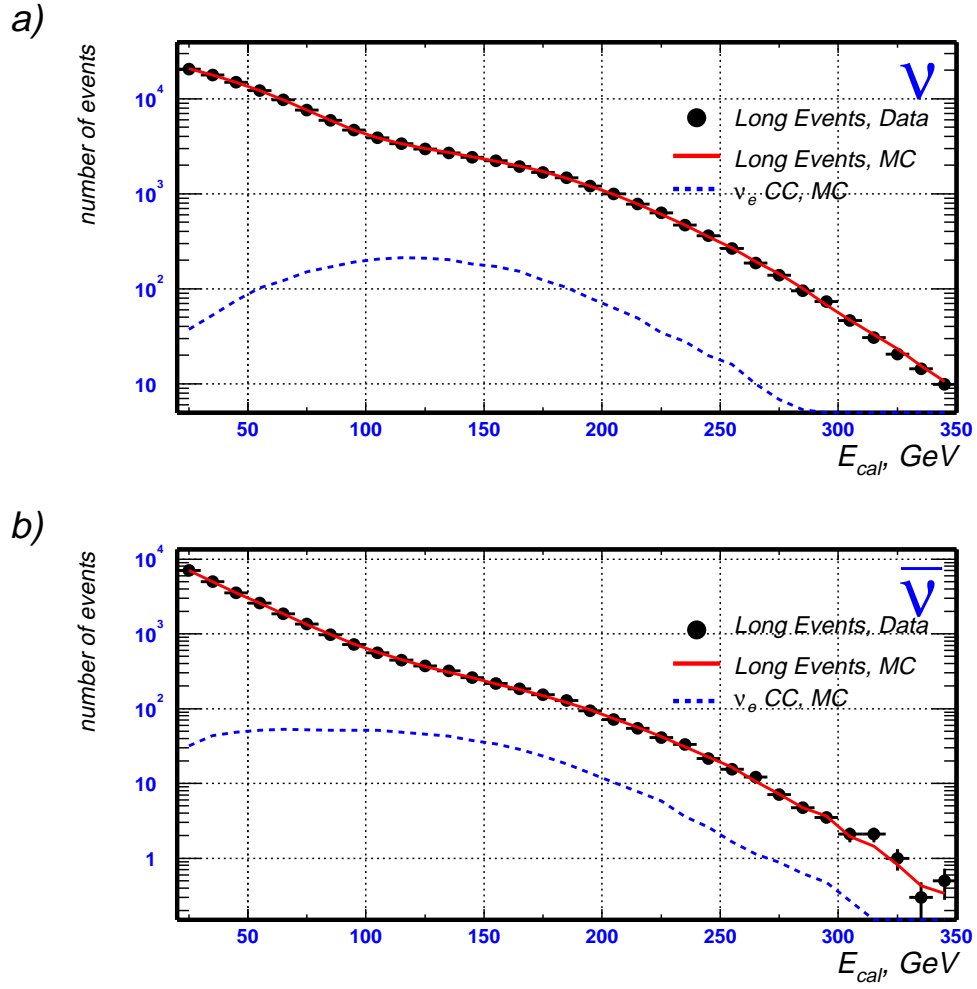


Figure 6.1: E_{cal} distributions of “long events” for data (solid circles) and Monte Carlo (solid line). The Monte Carlo prediction for the E_{cal} distributions of ν_e CC events are also shown (dashed line); a) - neutrino mode, b) - anti-neutrino mode.

in the geometry files in GEANT. The response of the active parts of the detector (the scintillation counters and drift chambers) also includes a simulation of the electronics readout system. McNuTeV produces the data files in the same format as the data acquisition system of the NuTeV detector.

The energy deposited in scintillation counters yields scintillation light which is detected by photo multiplier tubes (PMT's). The electron avalanche in the 10-stage PMT's is smeared statistically at each stage. The number of photoelectrons used in the smearing is tuned to match the widths of muon dE/dx deposition in the data. Pedestals, gains, and the digitization of all electronics channels are also simulated.

McNuTeV is also used as a stand alone package to simulate test beam data. Here, the parameters of the test beam (e.g. particle id, particle momentum, location of the beam center, and the mean spread of the beam from centerline) are read from the test beam configuration files.

The neutrino cross-section interaction model is not implemented in McNuTeV. Therefore, the simulation of neutrino data is done by using the “pipe” files which include the neutrino event kinematics, as generated by NUMONTE.

The deep inelastic scattering formalism describes an inclusive $\nu + n \rightarrow \mu + X$, $\nu + X$ process. However, the neutrino cross-section model does not provide the full particle composition of the hadronic final state X . Most measurements of inclusive neutrino-nucleon scattering provide only inclusive cross-sections. Therefore, a complete simulation of the hadronic final state in neutrino interactions is difficult. The original McNuTeV program used a simple “ 3π ” model for the particle composition of the hadronic final state. i.e. all the hadronic energy $E_{had} = E_\nu y$ was randomly divided among the three final state pions - π^+ , π^- and π^0 . In this analysis, the Monte Carlo has been greatly improved by including a simulation of the fragmentation and hadronization of the final state quarks using the LEPTO

([32]) Monte Carlo (as described in Section 6.5).

6.2 GEANT Simulation of Electromagnetic Showers in the NuTeV Detector

The simulation of electromagnetic showers in the NuTeV detector is an absolutely essential part of this analysis. The ν_e CC events can not be identified on an individual event by event basis. Therefore, the η_3 distributions can not be identified on an individual event by event basis. Therefore, the η_3 distributions of ν_e CC events can not be obtained from data. As mentioned in Section 4.1.2, the final state of a ν_e CC interaction in the calorimeter is a combination of the hadronic and electromagnetic showers. In this analysis we determine the η_3 distributions of ν_e CC events by combining the hadronic showers from events in the “long” sample with Monte Carlo simulated electromagnetic showers. Section 6.2.1 describes the procedure used in verifying that the McNuTeV simulation of electromagnetic showers is in good agreement with the test beam data.

6.2.1 Comparison of the GEANT Monte Carlo with Test Beam Data

The Monte Carlo simulation of the electromagnetic showers in ν_e CC interactions is tested by using the same simulation to compare to electron test beam data. The momentum span covered by the electron test beam ranged from 5 to 170 GeV. At “ultra-low” test beam momenta (between 5 to 15 *GeV*), the electron beam also includes a contamination of charged pions. Therefore, only test beam data above 20 *GeV* is used in these tests.

McNuvTeV was run in a “stand alone” mode to simulate the detector response to

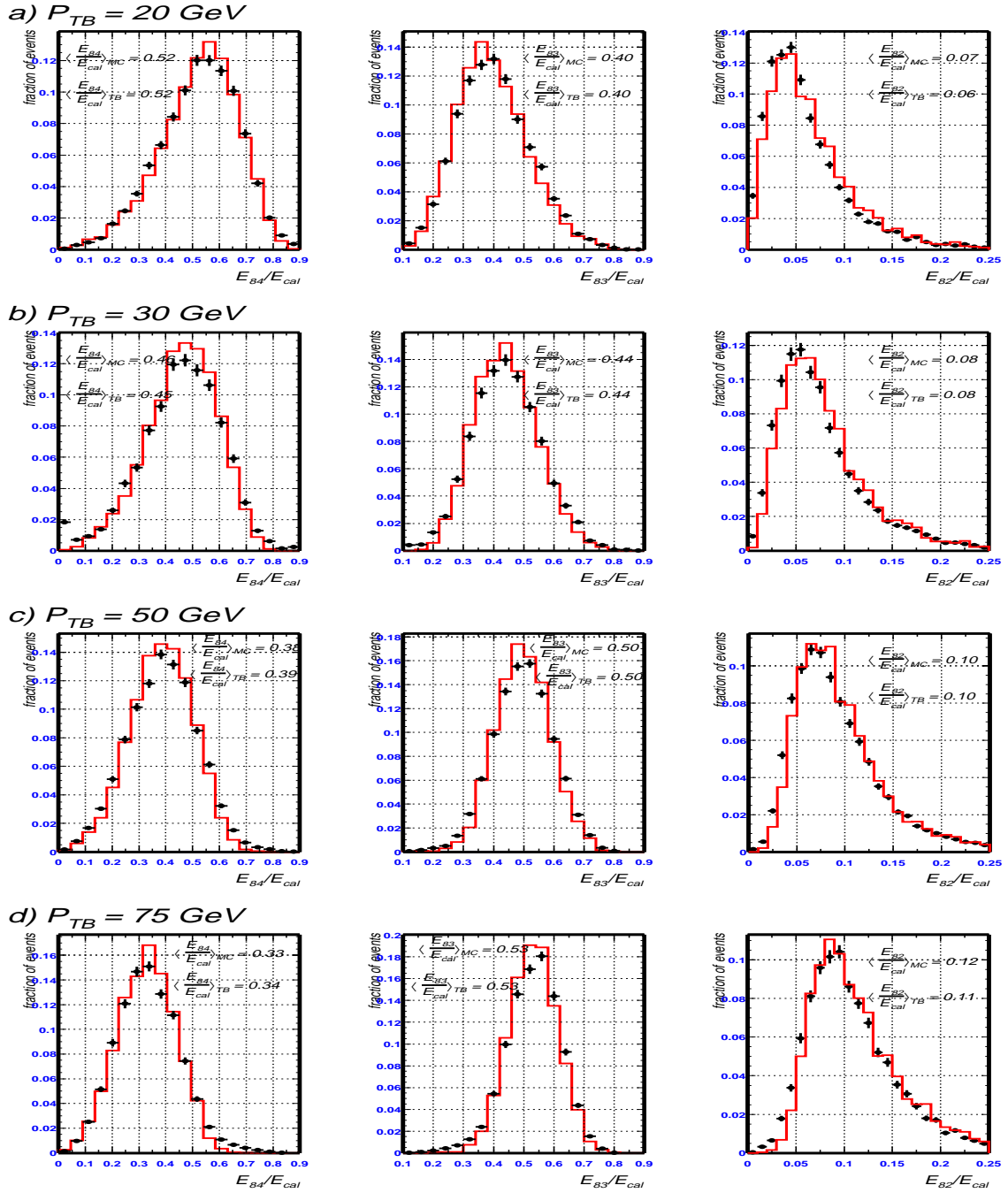


Figure 6.2: Electromagnetic showers: fraction of the total shower energy, deposited in counters 84, 83, and 82, circles - test beam data, line - McNuTeV simulation. $P_{TB} = 20 \text{ GeV}$ (a), 30 GeV (b), 50 GeV (c), 75 GeV (d).

test beam electrons. The electrons in the test beam interacted at the approximate center of the most upstream counter (counter 84) of the calorimeter.

The Monte Carlo simulation of the detector is compared with the detector response to test beam electrons. The longitudinal energy deposition profiles of electron showers is characterized by the fraction of the total calorimeter energy deposited in counters 84, 83 and 82. These counters contain approximately 99% of the total energy of electromagnetic showers. Figure 6.2 shows that there is excellent agreement between the McNuTeV simulation of the distributions of the fractional energy depositions in the counters (84, 83 and 82) and the test beam electron data.

The absolute calibration of the McNuTeV simulation of EM showers is determined by simulating electron showers with a uniform longitudinal starting position in the calorimeter (as shown in Figure 6.3)

$$C_e^{MC} = 1.096 \pm 0.0003 \quad (6.1)$$

The Monte Carlo resolution function is in agreement with test beam data and is well described by the function:

$$\frac{\sigma}{E_e} = \frac{0.61}{\sqrt{E}} \oplus \frac{0.040}{E} \quad (6.2)$$

6.3 Simulation of Charged-Current Electron Neutrino Events

As described in section 4.3, in the analysis the energy deposition of a muon track is added in software to all “short” events which satisfy the analysis cuts. Consequently, all ν_e CC events in the sample have the longitudinal energy deposition of

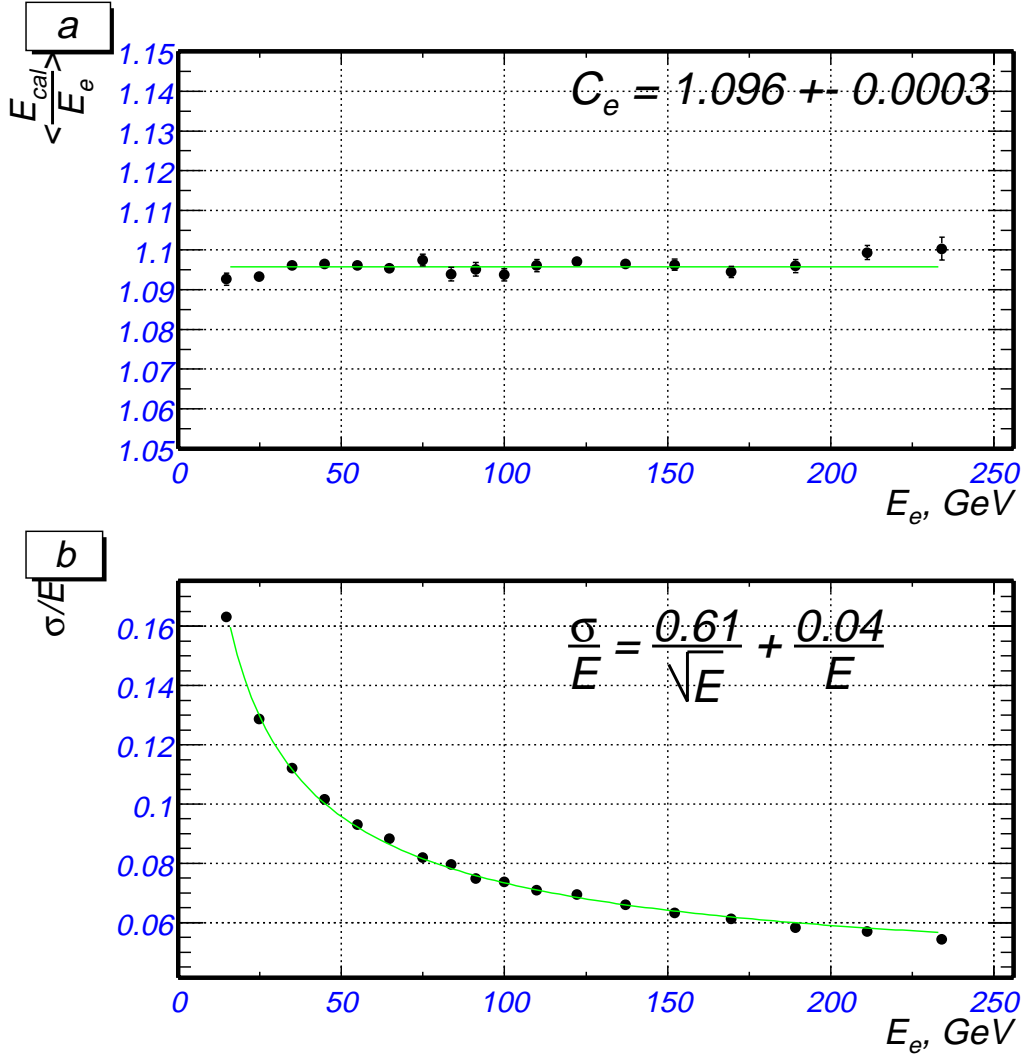


Figure 6.3: Calibration and resolution of the McNuTeV simulation of electromagnetic showers of test beam electrons: a) $\langle E_{cal}/E_e \rangle$ versus electron energy E_e ; b) resolution function σ/E_e versus electron energy E_e . Note that the two terms in the resolution function should be added in quadrature.

this additional muon track added to the energy deposition of the EM and hadron showers. To simulate the longitudinal energy deposition profile of such a sample of ν_e CC events the following procedure is used:

1. A sample of electron-neutrino CC interactions is generated with the NUMONTE fast Monte Carlo. For each event, the kinematic variables E_{had}^{MC} , E_e^{MC} and θ_e^{MC} are stored in a “pipe” file.
2. The calorimeter response to the generated ν_e CC event is simulated as a sum of the response to the electromagnetic shower, originating from the electron and the response to the hadronic shower. The response to the electron is simulated by McNuTeV hit level Monte Carlo. To simulate the response to the hadronic system, we obtain the “visible” energy of the shower E_{had} by smearing the generated energy E_{had}^{MC} , according to the calorimeter resolution function 2.11. Then we randomly select a data “long” event with the calorimeter energy E_{cal} within 1% of E_{had} .
3. The energy depositions of the electromagnetic shower and of the selected “long” event are added counter by counter to form a simulated electron-neutrino charged-current event.

This procedure is illustrated in Figure 6.4. As a result of this procedure we obtain a sample of events which contain a hadron shower, an electromagnetic electron shower and a muon track. The events in this simulated sample have the same E_{cal} distributions and the same fraction of calorimeter energy deposited via EM shower as real ν_e CC events. Therefore, the longitudinal energy profile of these simulated events is an excellent approximation of the profile of real ν_e CC events.

Examples of the resulting η_3 -distributions of simulated ν_e CC events are shown in Figure 6.5.

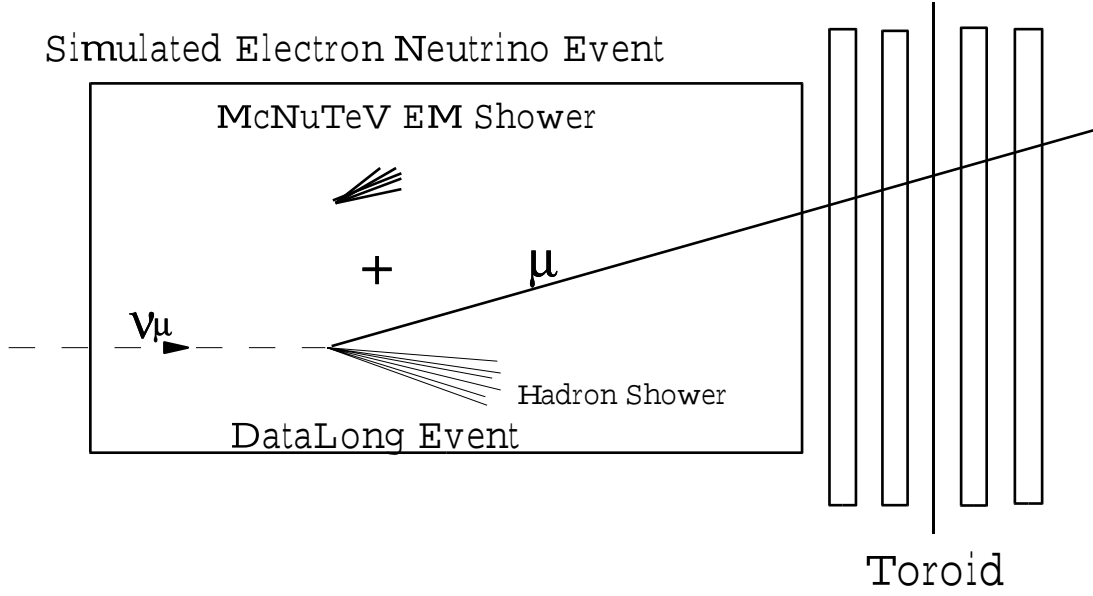


Figure 6.4: Simulation of ν_e CC events with an additional muon: A McNuTeV simulated EM shower is added to a randomly chosen “Long” event with the appropriate hadron energy in the calorimeter.

The absolute calibration of the NuTeV detector response to electromagnetic showers (C_e) is extracted from the electron test beam data ([34]):

$$C_e = 1.08 \pm 0.02 \quad (6.3)$$

There are several factors which limit the accuracy in the extraction of C_e from test beam data. First a correction must be applied for the difference in the interaction point between test beam electrons and electrons from neutrino interactions. Test beam electrons begin to shower immediately as they enter the detector, while EM showers initiated by ν_e CC interactions are uniformly distributed within the detector. Secondly, a correction must be applied to account for the fraction of the

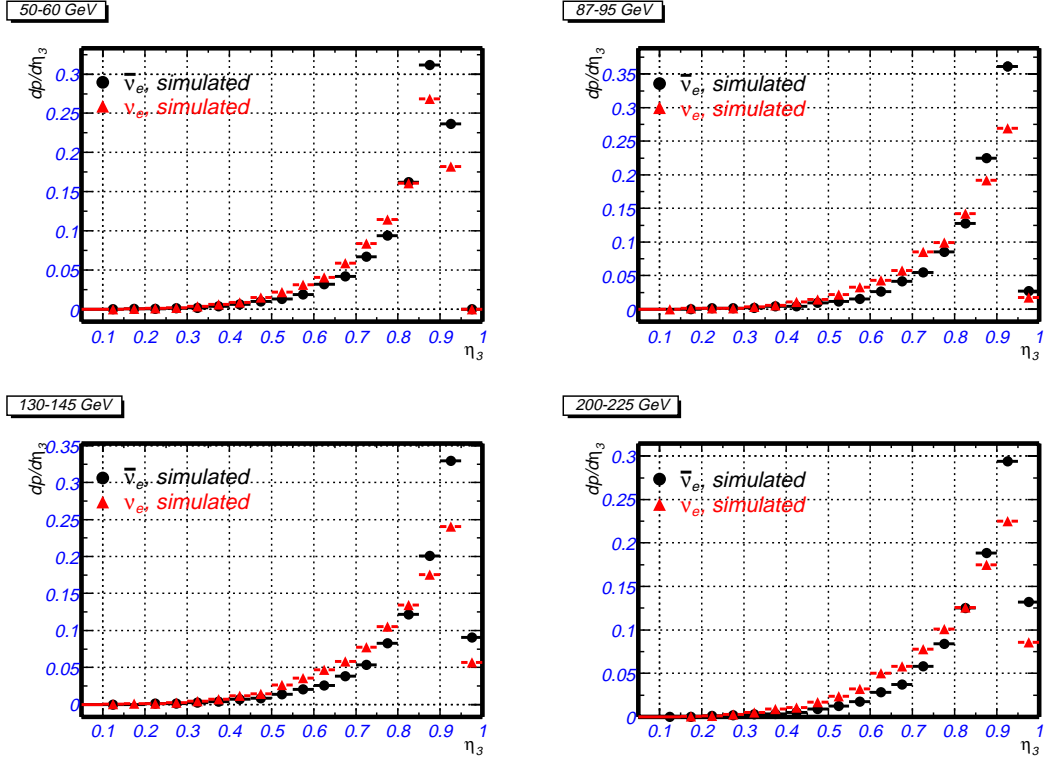


Figure 6.5: Examples of η_3 distributions of simulated ν_e events (triangles - neutrino mode, circles - anti-neutrino mode). Here, E_{cal} bins of 50 – 60, 87 – 95, 130 – 145 and 200 – 225 GeV are shown.

test beam electrons which begin to shower in upstream material (e.g. counters, chambers and vacuum pipe windows upstream of the neutrino calorimeter). A third uncertainty originates from the fact that the energy of test beam electrons is measured by only the most upstream three counters (counters 84, 83 and 82). Therefore, the uncertainty in the calibration of these three counters, relative to the average gain of the remaining 80 counters in the calorimeter, adds to the overall error in the electron energy calibration.

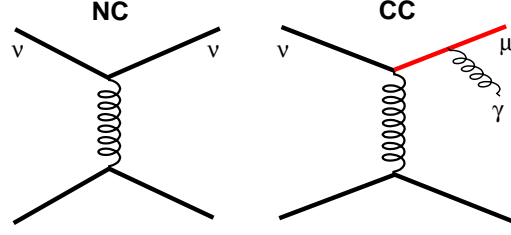


Figure 6.6: Right - CC event photon emission off the final state muon; left - NC event - no emission possible.

This 2% error in the measurement of C_e is the most significant systematic uncertainty in the analysis. To estimate the effect of this uncertainty on the electron neutrino flux measurement, an analysis done with an assumed EM calibration constant of 1.1 is compared to the analysis done with the central value of $C_e = 1.08$.

6.4 Final State Radiation $\mu \rightarrow \mu + \gamma$ in Charged-Current Events

The procedure used to measure the electron neutrino flux in this analysis is based on the assumption that the final states of muon neutrino CC interactions differ from the final states of NC interactions only by the presence of the additional muon. The underlying assumption is that the particle composition of the hadronic showers is the same in CC and NC events. As mentioned in section 4.5 this assumption doesn't account for the effect of the radiation of photons by the final state muon in CC events. This process is shown in Figure 6.6. There is no corresponding process in NC events, because the outgoing final state neutrino is neutral. The presence of radiated photons in CC events changes the electromagnetic component

of showers in the calorimeter and introduces a bias in the measurement. The correction procedure which is used is to subtract a simulated distribution of CC events with radiated photons from the data sample of CC events. This section describes the procedure used to estimate the effect of radiated photons and the correction method.

The effect of these radiated photons is also known as a “radiative correction” to neutrino DIS processes. The effect of these radiated photons on the measured CC neutrino differential cross-sections is to shift events from low to higher values of y . There are several prescriptions used to account for radiative corrections [43], [41], [42] in DIS processes. In the NuTeV structure function analysis, the prescription of Bardin [41] is used it accounts for all EW radiative corrections to the tree level neutrino scattering. This correction is calculated by the re-weighting of Monte Carlo simulated events [38]. However, in this analysis we are only interested in radiative corrections that originate from photon emission by final state muons. The theoretical calculation of the radiative corrections in neutrino scattering by De Rujula [43] only includes the effect of radiation by the final state muon (and does not include any of the other EW radiative corrections).

6.4.1 The De Rujula Approximation

The theoretical calculation of the radiative corrections in neutrino scattering by De Rujula [43] is based in the “leading log” approximation. The “lepton leg” radiative correction is defined as

$$\Delta(x, y, E_\nu) = \frac{\frac{d\sigma_0(E_\nu)}{dxdy} - \frac{d\sigma_B(E_\nu)}{dxdy}}{\frac{d\sigma_B(E_\nu)}{dxdy}} \quad (6.4)$$

E_{beam}	ν	$\bar{\nu}$
50 <i>GeV</i>	1.51	1.92
100 <i>GeV</i>	1.47	2.02
200 <i>GeV</i>	1.44	1.99

Table 6.1: Values of the PYTHIA parameter C_γ , tuned to reproduce the De Rujula calculation of the radiative corrections for $E_{\nu,\bar{\nu}} = 50, 100, 200 \text{ GeV}$.

where $\frac{d\sigma_B(E_\nu)}{dx dy}$ is the “bare” cross-section and $\frac{d\sigma_0(E_\nu)}{dx dy}$ is the cross-section in the “leading log” approximation. The quantity $\Delta(x, y, E_\nu)$, calculated for neutrino energies of 50, 100 and 200 *GeV*, is shown in Figure 6.7. This approximation has been used extensively in the analyses of previous neutrino experiments. It yields an excellent estimate (to 10%) of the radiative correction everywhere except in the region of very high y .

In this analysis we use the De Rujula approximation to check and “tune” the PYTHIA Monte Carlo simulation of radiated final state photons in neutrino interactions.

6.4.2 PYTHIA Monte Carlo Generator

We use the PYTHIA [36] Monte Carlo simulation program to generate a sample of neutrino DIS CC events including final state photon emission. Examples of the generated energy spectra of the final state photons in bins of hadronic energy E_{had} are shown in Figure 6.8. Using this PYTHIA Monte Carlo event sample, we construct the radiative correction ratio $\Delta(x, y, E_\nu)$ as in 6.4 and compare it with the De Rujula calculation. The PYTHIA program has an “adjustable” parameter C_γ for scaling (up or down) the probability for the radiation of final state photons with respect to default value of 1.0. We generate two Monte Carlo samples - one with the default value of C_γ and one with $C_\gamma = 2.0$. Then using a simple fitting procedure we determine the value of C_γ that best reproduces the value of the radiative correction

$\Delta(x, y, E_\nu)$ as calculated by De Rujula. This procedure is repeated for samples of neutrino and anti-neutrino events with energies of $E_{\nu(\bar{\nu})} = 50, 100, 200 \text{ GeV}$. The best fit values of C_γ^ν and $C_\gamma^{\bar{\nu}}$ for different neutrino and anti-neutrino energies are presented in Table 6.1. A comparison of the De Rujula radiative corrections $\Delta(x, y, E_\nu)$ and the corrections calculated using the PYTHIA samples with the best fit values of C_γ^ν and $C_\gamma^{\bar{\nu}}$ are shown in Figure 6.7.

Based on these comparisons with De Rujula calculation, we chose PYTHIA parameters values of $C_\gamma^\nu = 1.5$ and $C_\gamma^{\bar{\nu}} = 2.0$. Finally, to obtain the the energy spectra of the final state radiated photons, we generate a sample of neutrino and anti-neutrino CC events with an input neutrino flux which corresponds to the flux measured by the NuTeV experiment. We then bin the photon spectra in bins of hadronic energy E_{had} . A few of the resulting photon spectra are shown in Figure 6.8.

6.4.3 Correcting the η -distributions of ν_μ Charged-Current Events

The η distributions of “Long” events are corrected to remove the contribution from the radiative photons. We simulate a sample of events with radiated photons by adding EM showers to the “Long” events. The photon EM energies are chosen randomly according to the photon emission spectra from Figure 6.8. We normalize this sample by the total probability of photon emission (with the cutoff energy of $E_\gamma = 0.01 \text{ GeV}$) and subtract its η distribution from that of the “Long” sample. The η distributions for “Long” events before and after this correction are shown in Figures 6.9 and 6.10.

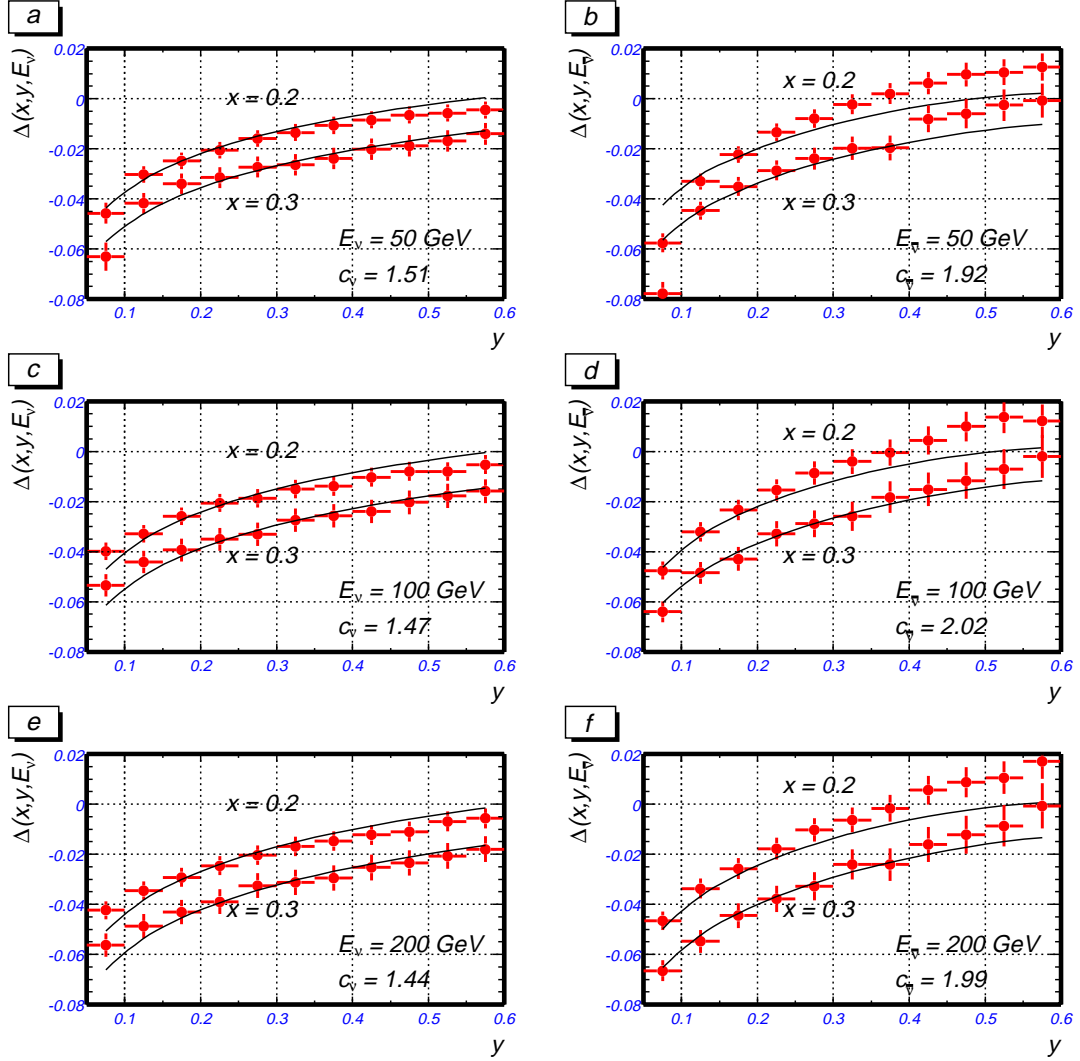


Figure 6.7: Radiative correction $\Delta(x, y, E_{\nu(p)})$: De Rujula “leading log” approximation - line, PYTHIA simulation - circles, a) neutrino $E_\nu = 50 \text{ GeV}$, b) anti-neutrino $E_{\bar{\nu}} = 50 \text{ GeV}$, c) neutrino $E_\nu = 100 \text{ GeV}$, d) anti-neutrino $E_{\bar{\nu}} = 100 \text{ GeV}$, e) neutrino $E_\nu = 200 \text{ GeV}$, f) anti-neutrino $E_{\bar{\nu}} = 200 \text{ GeV}$; values of PYTHIA parameter C_γ shown.

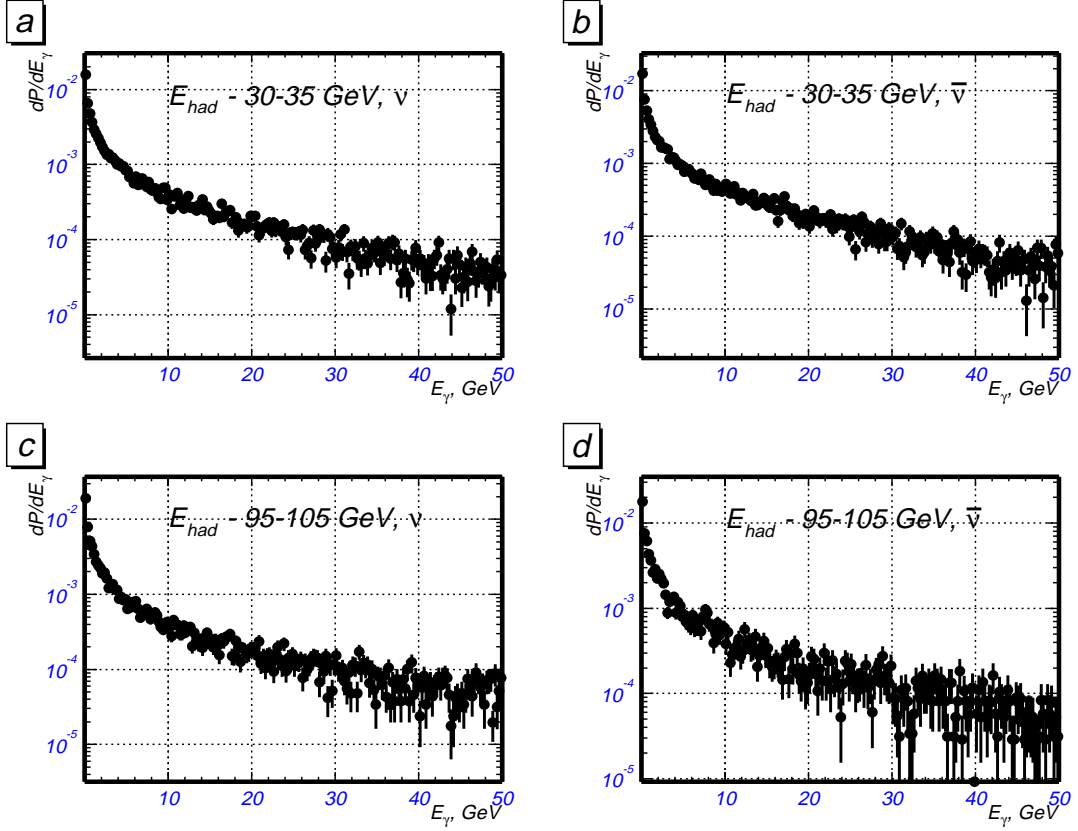


Figure 6.8: PYTHIA simulation: spectra of radiative photons a) neutrino mode $E_{had} = 30 - 35 \text{ GeV}$, b) anti-neutrino mode $E_{had} = 30 - 35 \text{ GeV}$, c) neutrino mode $E_{had} = 95 - 105 \text{ GeV}$, d) anti-neutrino mode $E_{had} = 95 - 105 \text{ GeV}$.

6.4.4 Systematic Uncertainty from Radiative Photons

The estimated uncertainty in the radiative corrections calculated using the De Rujula procedure is 10%. We account for the effect of this uncertainty by varying the radiation parameter C_γ in the PYTHIA program by 10% and repeating the procedure described above to obtain a second sample of corrected “Long” events. This second sample is used to estimate the effect of the uncertainty in the radiative correction on the extracted electron neutrino flux.

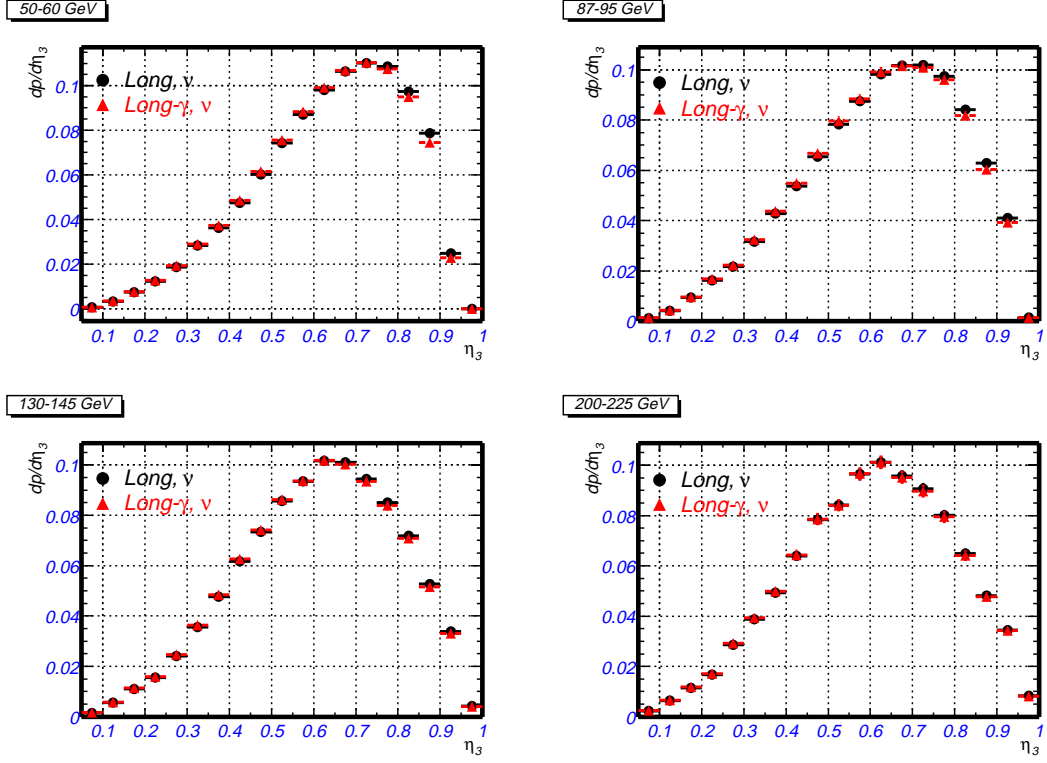


Figure 6.9: Correcting η_3 distributions for radiation of final state muons (Long events before correction - circles, after correction - triangles). Shown are E_{cal} bins of 50 – 60, 87 – 95, 130 – 145, 220 – 225 GeV in neutrino mode.

6.5 Simulation of Neutrino Events in the NuTeV Detector

As mentioned in Section 4.2 this analysis has developed from the original method used in the CCFR experiment. The biggest drawback of the CCFR analysis was the absence of a detailed hit-level Monte Carlo simulation. Such a simulation is extremely CPU intensive, and at the time of CCFR analysis it was practically impossible.

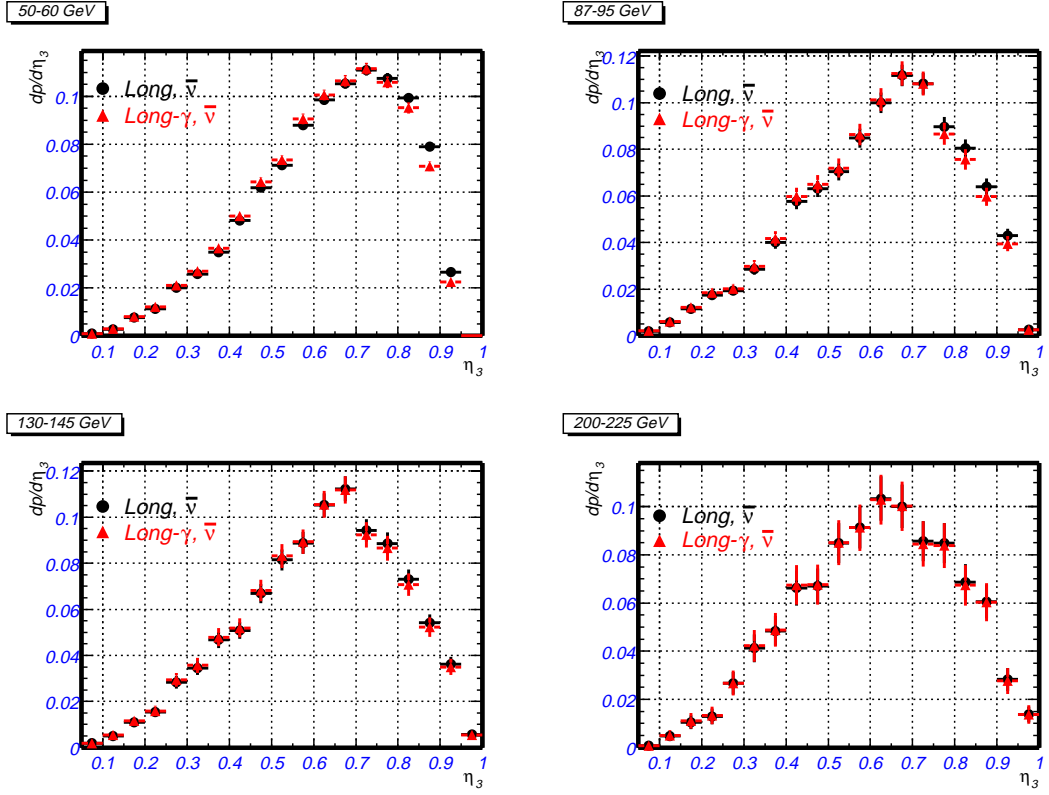


Figure 6.10: Correcting η_3 distributions for radiation off final state muons (Long events before correction - circles, after correction - triangles). Shown are E_{cal} bins of 50 – 60, 87 – 95, 130 – 145, 220 – 225 GeV in anti-neutrino mode.

Recent advances in the field of computer technology have made possible the implementation of a hit level Monte Carlo (although it is still a very time-consuming task). The CPU time needed for a full hit-level simulation of one neutrino event in the NuTeV detector with Pentium 500 MHz computer is approximately 1 s . Therefore, the total amount of computer time needed for a simulation of a sample of ~ 10 million neutrino events is approximately $3\ CPU \times years$.

6.5.1 Full Hit-Level Monte Carlo Simulation of Neutrino Interactions in the NuTeV detector

First, neutrino interactions in the NuTeV detector are simulated by the NUMONTE fast Monte Carlo based on neutrino input flux files and a neutrino cross-section model. The event kinematics information is written out into a “pipe” file. Subsequently, the event kinematic information is read by the McNuTeV program. McNuTeV uses the LEPTO Monte Carlo simulation program to generate the particle composition of the hadronic final state. Then all the particles produced at the interaction vertex are tracked through the NuTeV detector by GEANT, and all the detector responses including drift chamber hits and calorimeter pulse heights are simulated.

The first step of this Monte Carlo simulation which involves the NUMONTE simulation is discussed in Section 6.1.1. The the next two steps of the hit-level simulation are described below.

LEPTO: Fragmentation and Hadronization

LEPTO is a program for Monte Carlo simulation of lepton-nucleon DIS events. It is based on a leading-order electroweak cross-sections for the underlying parton level scattering processes. The fragmentation of produced partons into observable hadrons is performed with the Lund string hadronization model. There is generally good agreement between LEPTO simulation and data on hadronic final states from muon and neutrino experiments such as EMC, WA21 and WA25. Therefore, the models and procedures used by the LEPTO program have been validated by experimental data.

For this analysis we did not use LEPTO’s implementation of the neutrino cross-section model, since the event kinematics are provided by NUMONTE. Only

the fragmentation of the initial partons into the observed hadronic final state is performed by LEPTO. All the particles generated by LEPTO are used as input into the GEANT program and tracked through the detector.

GEANT/GHEISHA: Hadronic Showers

As seen in Figure 6.2, the Monte Carlo simulation of the EM showers in GEANT is in excellent agreement with test beam data. The main reason behind this good agreement is the fact the physics processes that govern EM shower development are well understood and accurately implemented by the GEANT Monte Carlo program. The situation is very different for hadronic showers. Here, much of the phenomena especially in the “nuclear sector” are not understood as well. These are also much more complicated to implement because of the great variety of processes that may occur. Therefore, the software packages commonly used to simulate hadronic calorimeters such as GHEISHA, FLUKA and CALOR can not be totally relied on for precise predictions of the response and resolution of hadron calorimeters.

Therefore, in this analysis we only use the hit-level Monte Carlo to determine the changes in the results from varying parameters or procedures (i.e. comparing two Monte Carlo predictions under different assumptions). None of the results that are used in the analysis require any direct comparison of Monte Carlo to data.

For this analysis we use the GHEISHA program to simulate hadronic showers in the NuTeV detector. Figure 6.11 shows the calibration and resolution function of the detector, predicted by the Monte Carlo simulation. A comparison with the test beam measurements described in Section 2.3.2 shows that the detector response and non-linearity are simulated fairly well, but the detector resolution, simulated by GHEISHA program is approximately 15% worse than the measured

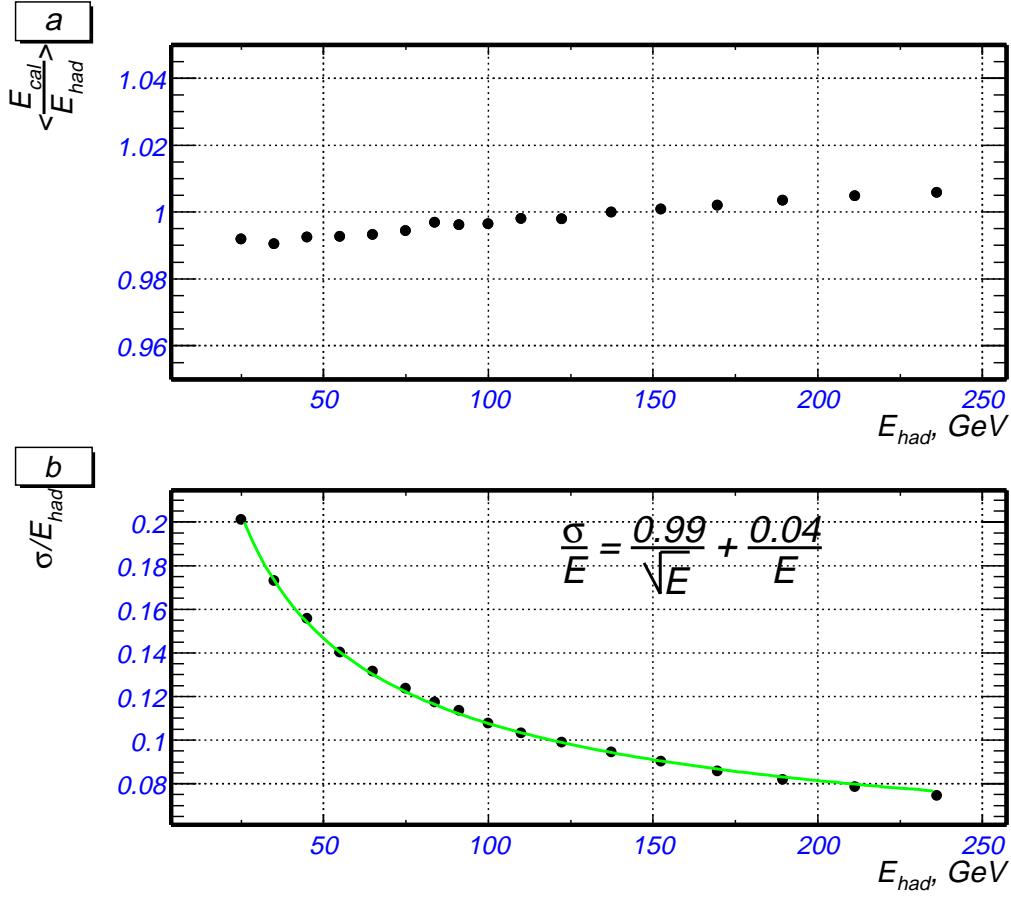


Figure 6.11: Calibration and resolution of the Monte Carlo simulation of the hadronic showers.

resolution.

6.5.2 η -distributions of the Simulated Neutrino Events

We are most interested in how well the full Monte Carlo simulation represents the longitudinal energy distribution of hadronic showers. We can only compare directly the data and Monte Carlo η_3 distributions of “long” events. This sample consists almost entirely of the CC ν_μ events. These comparisons for E_{cal} bins of

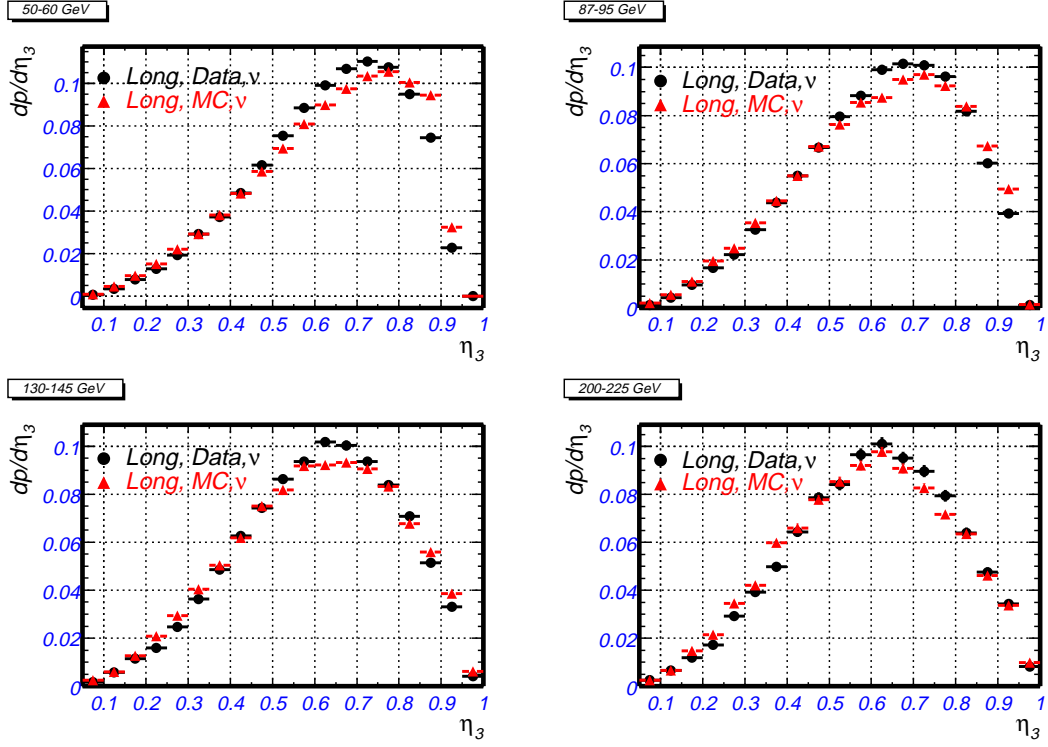


Figure 6.12: η_3 distributions of “long” events in neutrino mode (data - circles, Monte Carlo - triangles). Shown are E_{cal} bins of 50 – 60, 87 – 95, 130 – 145, 220 – 225 GeV .

50 – 60, 87 – 95, 130 – 145, 220 – 225 GeV are shown in Figures 6.12 (for neutrino mode) and 6.13 (for anti-neutrino mode). In addition, comparisons of the mean values of the η_3 distributions “long” events in data and Monte Carlo are shown in Figures 6.14 and 6.15, for neutrino and anti-neutrino modes, respectively.

Although the simulation of hadronic showers is not precise, it works very well. The shower shape analysis Monte Carlo procedure is not very sensitive to the details of the hadronic shower simulation, as long as all the showers are simulated consistently using the same program. In addition, as mentioned earlier, in this analysis we only use the hit-level Monte Carlo to determine the changes in the

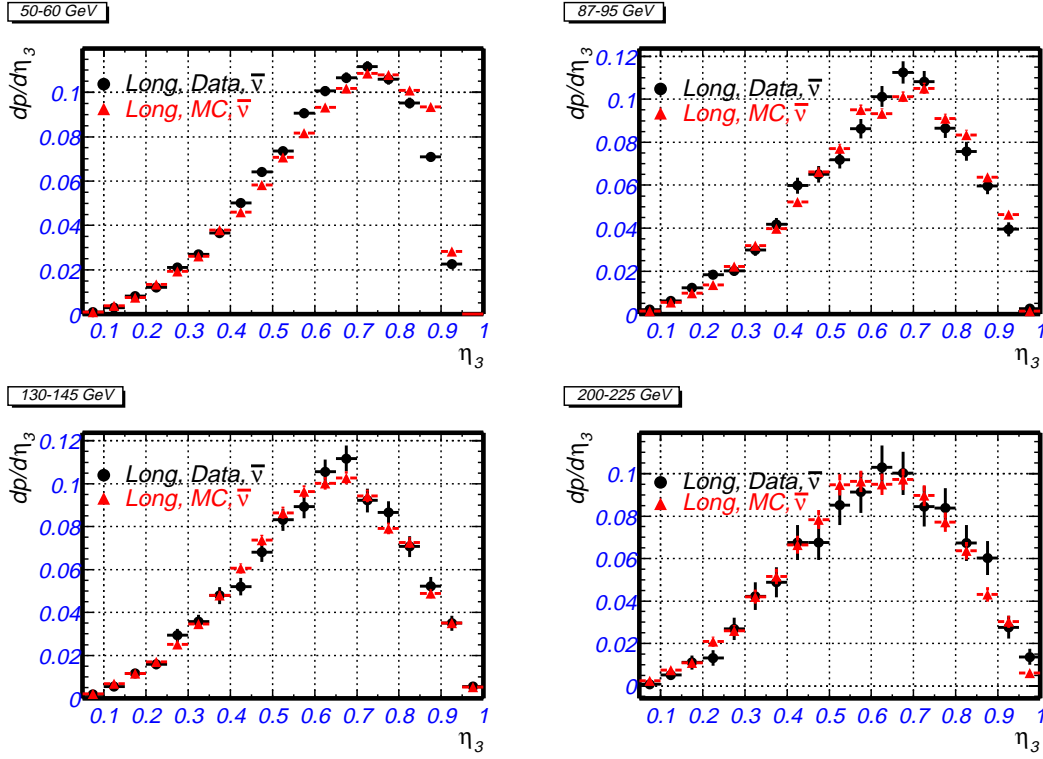


Figure 6.13: η_3 distributions of “long” events in anti-neutrino mode (data - circles, Monte Carlo - triangles). Shown are E_{cal} bins of 50 – 60, 87 – 95, 130 – 145, 220 – 225 GeV .

results from varying parameters or procedures (i.e. comparing two Monte Carlo predictions under different assumptions). None of the results that are used in the analysis require any direct comparison of Monte Carlo to data.

6.5.3 η -analysis of the Simulated Neutrino Events

The simulated neutrino events are processed in the the same way as the data events. We add the predicted fraction of Monte Carlo electron neutrinos to the mostly muon neutrino Monte Carlo sample. The prediction for the expected fraction of

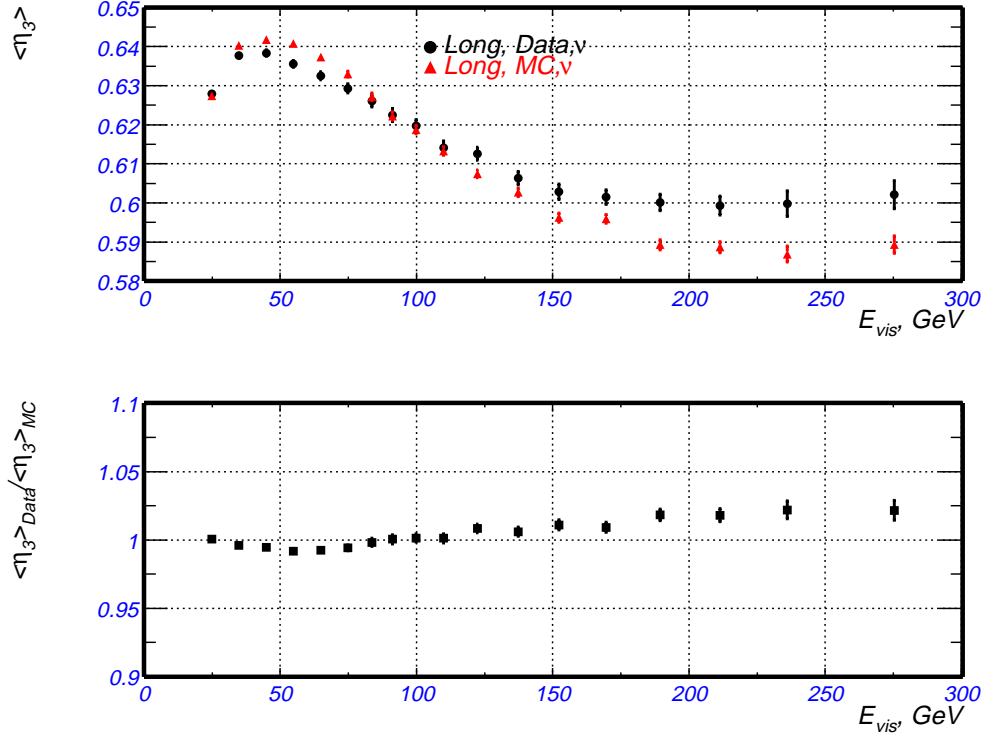


Figure 6.14: Top plot - mean values of η_3 of “long” events neutrino mode (data - circles, Monte Carlo - triangles). Bottom plot - ratio $\langle \eta_3 \rangle_{Data} / \langle \eta_3 \rangle_{MC}$.

electron neutrino events is obtained from the beam Monte Carlo. We then form the η_3 parameter distributions for the Monte Carlo samples and perform the statistical analysis described in Section 4.2 to extract the number of electron neutrino events in the Monte Carlo sample. We determine the correction factors for each of the systematic effects described in this section as the difference between the number of electron neutrino extracted from the Monte Carlo sample using the default version of the shower shape analysis and the modified version, that “removes” each corresponding systematic effect. These corrections are then normalized to reflect the difference in the statistics between the data and Monte Carlo, and applied to

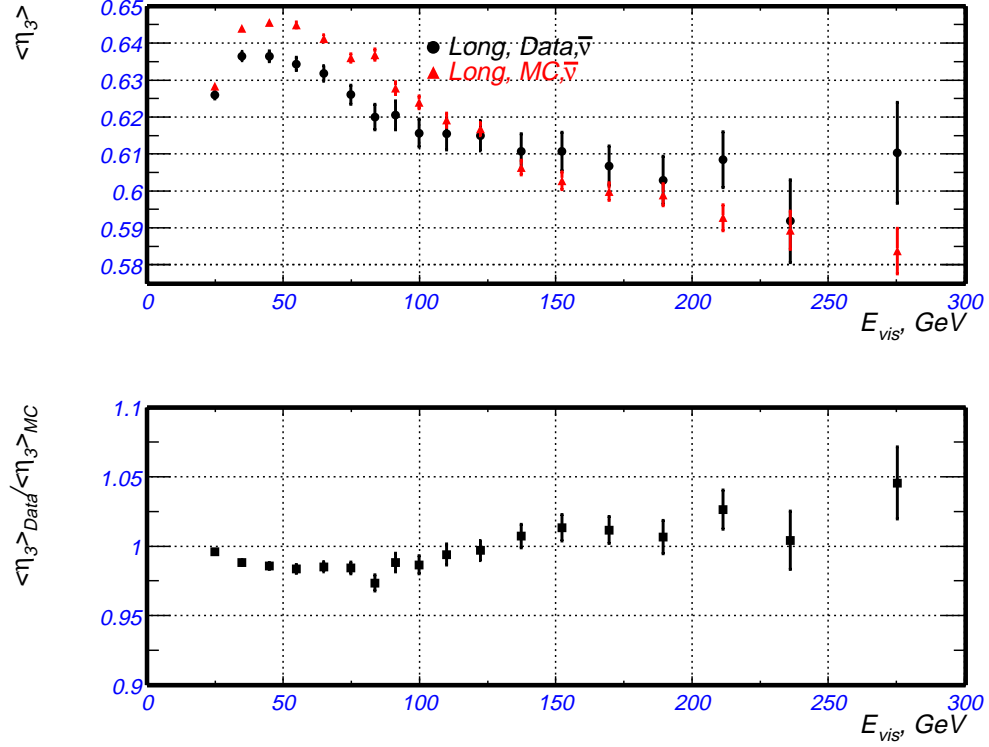


Figure 6.15: Top plot - mean values of η_3 of “long” events in anti-neutrino mode (data - circles, Monte Carlo - triangles). Bottom plot - ratio $\langle \eta_3 \rangle_{Data} / \langle \eta_3 \rangle_{MC}$.

our measurement of electron neutrino flux in the data as described in Section 7.2.

ν_e CC imperfect modeling correction

We use the procedure of adding the GEANT simulated electromagnetic showers to the simulated long events, as described in Section 6.3, to simulate/model the η_3 distributions of ν_e CC events. As mentioned earlier, our procedure of simulating/modeling ν_e CC events provides an excellent approximation of the E_{cal} , E_{had} , E_{EM} distributions as the real ν_e events. However, the simulation is

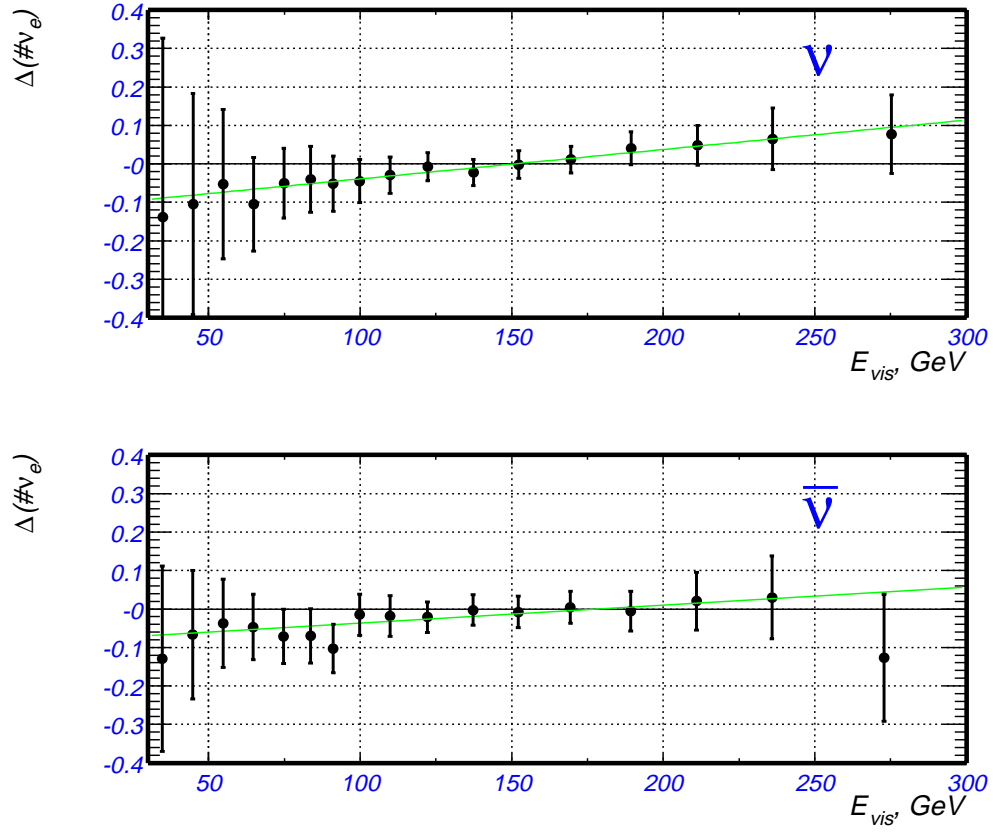


Figure 6.16: Correction to the measured electron neutrino flux due to imperfect modeling of ν_e CC events, based on Monte Carlo simulation of the shower shape analysis.

not perfect because of the following possible effects:

- The resolution smearing in a steeply falling spectrum may be somewhat different for the hadron showers in electron neutrino events versus the showers obtained from the long sample in the the same visible energy bin in the calorimeter

- The GEANT simulated electromagnetic shower is added to a hadronic shower not at the true interaction *PLACE*, but at the beginning of the hadronic shower as determined by the *NN – PLACE* algorithm

To correct for these possible differences between the real and simulated/modeled ν_e CC events we use the Monte Carlo sample to perform the shower shape analysis using the “real” (as they are fully simulated by NUMONTE/LEPTO/GEANT) ν_e CC events. This modified ν_e flux measurement is then compared to the one obtained using the default procedure of simulating/modeling electron neutrino events (i.e. by adding GEANT electromagnetic showers to hadron showers from long events). The fractional difference is shown in Figure 6.16. This correction to ν_e flux measurement is proportional to the measured flux itself and is applied as a multiplicative factor.

Short CC simulation/modeling correction

Similar to the simulation of ν_e CC events we use the procedure, described in Section 4.4 to simulate the η_3 distributions of the short CC events. A second muon track is added to a Monte Carlo long event, to simulate a short CC event where the muon ranged out or exited through the side of the detector. The real muons that exit the detector deposits energy very close to the edges of several scintillation counters, where the counter response function increases very rapidly. This effect is not simulated by our procedure and as a result the measured energy deposition of the muons from real short CC events is higher than in the simulated events. To correct for this effect we use the Monte Carlo simulation to perform the shower shape analysis using the “real” (i.e. fully-simulated) short CC events. The difference in the extracted ν_e flux between using the fully-simulated short CC events and default procedure for modeling short CC events is shown in Figure 6.17.

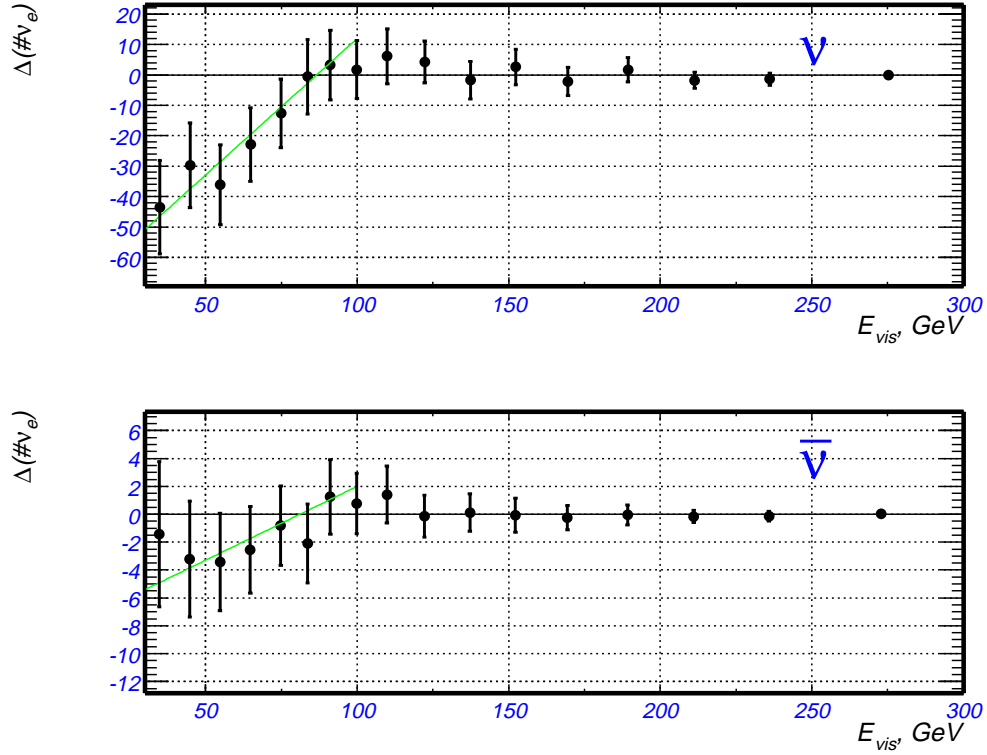


Figure 6.17: Correction to the measured electron neutrino flux due to imperfect modeling of the short CC events, based on Monte Carlo simulation of the shower shape analysis.

Muon energy deposition correction

We add muon tracks to all short events as described in Section 4.3 to compensate the presence of a muon in ν_μ CC events. However, the muon tracks are selected from the long data events downstream of the shower region. Because of the ionization energy loss, the mean momentum of such selected muon tracks is approximately 2 *GeV* lower than the energy of the muons in the region of the hadron shower. Therefore, the mean calorimeter energy deposited by these muons

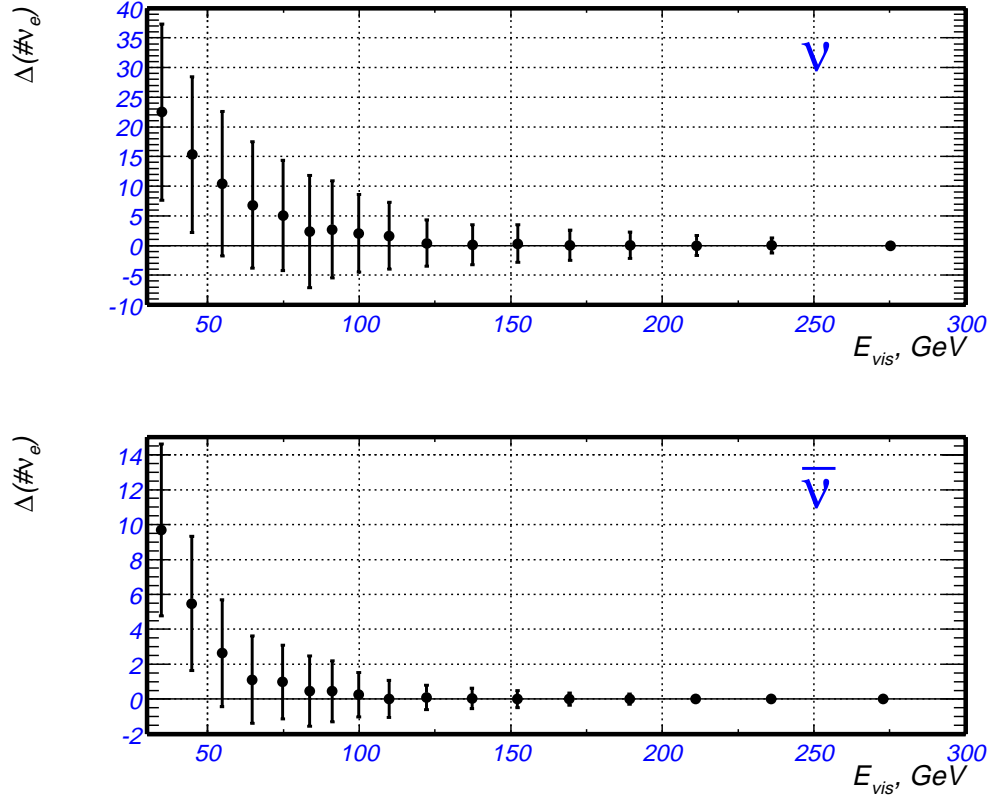


Figure 6.18: Correction to the measured electron neutrino flux due to the shift in the mean momentum of the muon tracks (which were added to the short events) based on a full Monte Carlo simulation of the shower shape analysis.

(which are added to the short events) is slightly lower than the energy deposited by muons in the region of the hadron shower in the long sample. The shower shape analysis, performed on the Monte Carlo sample was modified to remove this bias by correcting the mean energy deposition of the muons added to the short events in software such that it is equal to the mean energy deposition of the muon tracks in ν_μ CC events. The difference between the flux extracted using the modified (i.e. fully correct) and the default procedure is shown in Figure 6.18.

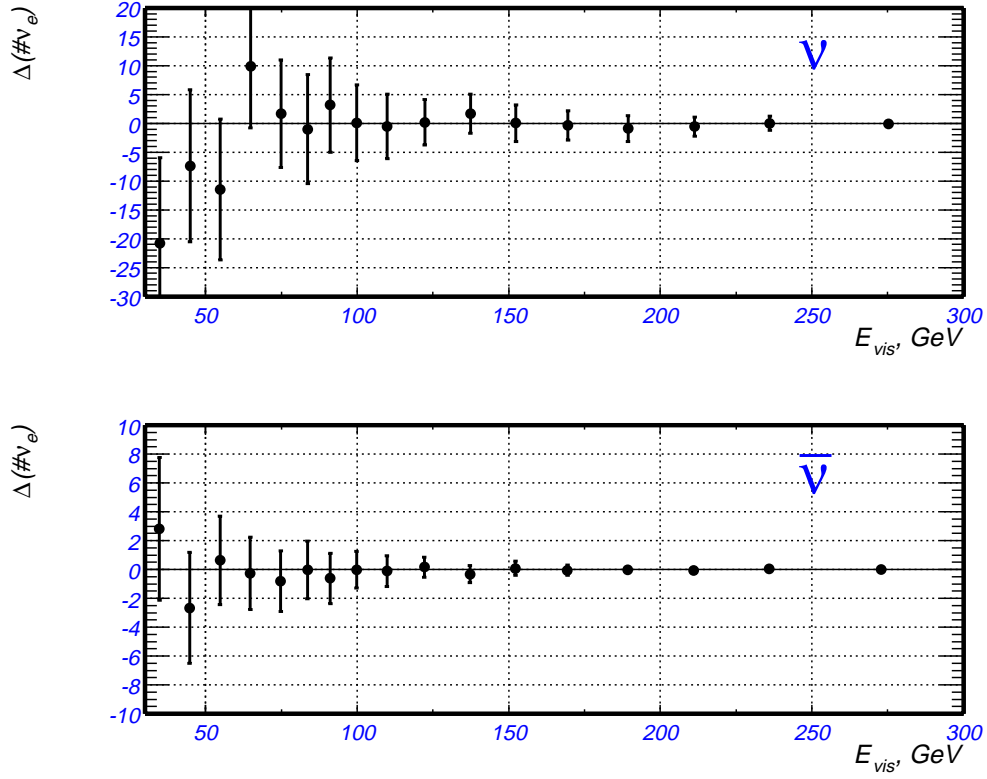


Figure 6.19: Correction to the measured electron neutrino flux from the effect of adding muon tracks at $NN - PLACE$, based on a full Monte Carlo simulation of the shower shape analysis.

$NN - PLACE$ correction

The muon tracks are added to the short events starting at the beginning of the shower region as determined by the $NN - PLACE$ algorithm. In contrast, the muon tracks in real ν_μ CC events start at the true neutrino interaction vertex. The $NN - PLACE$ algorithm provides a very good determination of the z interaction point of neutrino events, but it is not entirely perfect. To correct for a bias from this effect, the shower shape analysis as performed on the Monte Carlo sample

was modified to add muon tracks exactly at the true location of the interaction vertex. The difference between the flux extracted with the modified and the default procedure is shown in Figure 6.19.

Chapter 7

η -analysis Results

This chapter presents the results of the measurement of the ν_e flux in the NuTeV detector using the shower shape analysis. Section 7.1 describes the fitting procedure of the η -distributions and the results of the fits. The corrections made to the measured ν_e flux (as based on Monte Carlo studies) are described in Section 7.2. The systematic uncertainties on the measurement of the ν_e flux are described in Section 7.3.

7.1 Statistical analysis of the η -distributions

The outline of the method used to measure the electron neutrino flux, based on the longitudinal profile of the energy deposition in the calorimeter, is described in Section 4.2. This method assumes that the detector is uniform in the longitudinal direction such that the longitudinal energy profile observed in the calorimeter does not depend on the location of *PLACE* (the counter location where the shower begins). This “symmetry” is slightly violated by the fact that there are 84 scintillation counters but only 42 drift chambers in the NuTeV detector. The drift

chambers are located upstream of every odd numbered counter. Therefore, the amount of upstream material is a little different for odd and even numbered scintillation counters. To account for this difference we fill the η_3 distributions for events starting in the even- and odd-numbered counters separately. The fits of the distributions of η_3 parameter are performed by minimizing the χ^2 function -

$$\chi^2 = \chi_{Even}^2 + \chi_{Odd}^2 \quad (7.1)$$

The χ^2 function χ_{Even}^2 is calculated as in (4.7)-

$$\begin{aligned} \chi_{Even}^2 = \sum_{i=1}^{nbins} ([Short + \mu]_i^{Even} - \alpha[Long]_i^{Even} - \beta[\nu_e CC + \mu]_i^{Even} \\ - C_1[Short CC + \mu]_i^{Even} - C_2[Cosmic + \mu]_i^{Even}) / (\sigma_{Stat}^2)_i^{Even} \end{aligned} \quad (7.2)$$

where the statistical error $(\sigma_{Stat}^2)_i^{Even}$ is:

$$\begin{aligned} (\sigma_{Stat}^2)_i^{Even} = [Short + \mu]_i^{Even} + \alpha_0^2 [Long]_i^{Even} + \beta_0^2 [\nu_e CC + \mu]_i^{Even} + \\ C_1^2 [Short CC + \mu]_i^{Even} - C_2^2 [Cosmic + \mu]_i^{Even} \end{aligned} \quad (7.3)$$

The notation used $[Short + \mu]_i^{Even}$ is number of events in the i -th bin of the η_3 distribution of short events with even-numbered *PLACE*. The function χ_{Odd}^2 is completely analogous to that for even counters. This procedure fits the distributions of *PLACE - even* and *PLACE - odd* events simultaneously.

There are two free parameters α and β which correspond to the fractions of ν_μ NC events and ν_e CC events among all short events. The normalization of the η_3 distributions of ν_e CC events is such that the total number of events in each energy bin is set equal to the number predicted by the beam Monte Carlo simula-

tion. This means that the value of parameter β is the ratio of measured/predicted electron neutrino flux.

The statistical error depends on the values of the fit parameters α and β . Therefore, an iterative procedure is used where values of the parameters, calculated in the previous step of the iteration - α_0 and β_0 , are used to calculate the statistical error. The iterations continue until the values of α and β converge. This procedure usually requires 3 or 4 iterations. The actual minimization procedure is performed by MINUIT ([33]).

The fitting procedure is performed for each of 17 bins of the calorimeter energy E_{cal} listed in Table 4.1. Neutrino mode fits for $E_{cal} = 115 - 130 \text{ GeV}$ are shown in Figure 7.1, anti-neutrino mode fits are shown in Figure 7.2. Fit results for all energy bins are summarized in Tables 7.1 (neutrino mode) and 7.2 (anti-neutrino mode). Listed in the tables are the central value α and the standard deviation $\delta\alpha$ of the first parameter, the central value β and the standard deviation $\delta\beta$ of the second parameter, the correlation factor between the two parameters $c_{\alpha\beta}$, and the minimum of the χ^2 function, divided by the number of degrees of freedom $DOF = 38$. Plots of the η_3 fits for all energy bins can be found in Appendix B.

In order to estimate the systematic uncertainty on the shower shape analysis we also performed fits of the η_2 parameter distributions. Analogous to the η_3 parameter definition (see Figure 4.4) the η_2 parameter is defined as the fraction of the total calorimeter energy deposited in the first two counters of the shower

$$\eta_2 = \frac{E_1 + E_2}{E_{cal}} \quad (7.4)$$

These two measurements are not independent since the η_2 and η_3 parameters are very strongly correlated. The difference in the electron neutrino flux as measured using the η_2 and η_3 distributions is added to the total systematic uncertainty on

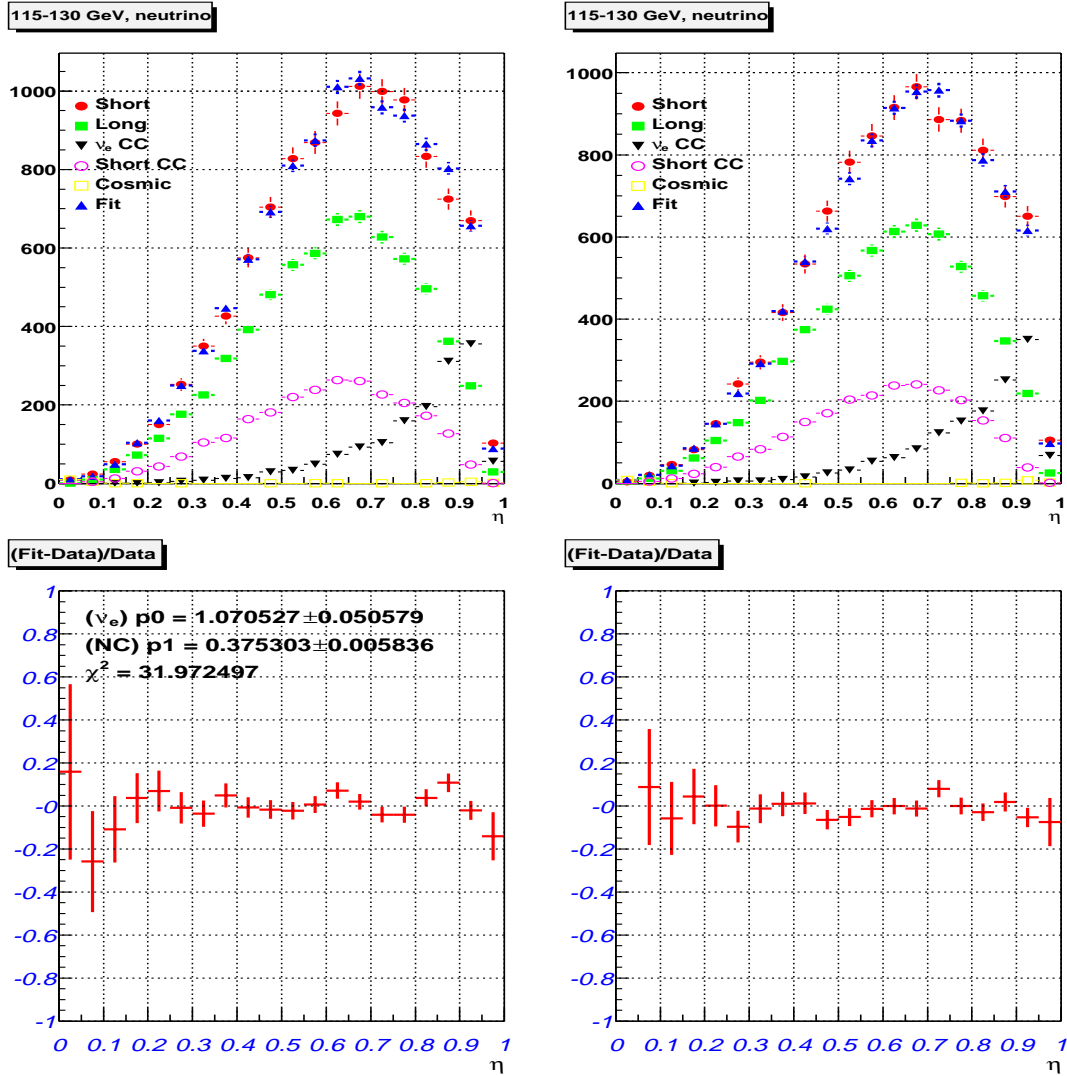


Figure 7.1: Fit of the η_3 distributions for $E_{cal} = 115 - 130 \text{ GeV}$ in neutrino mode. Even *PLACE* events - top left plot, odd *PLACE* events - top right plot. The distribution of short events (solid circles), is fit to a sum of the distributions of the long events (solid squares), ν_e CC events (upside-down triangles), short CC events (open circles), and cosmic events (open squares), the best fit distribution is also shown (triangles). The fractional difference between the "best fit" and data distributions - even *PLACE* events - bottom left, odd *PLACE* events - bottom right.

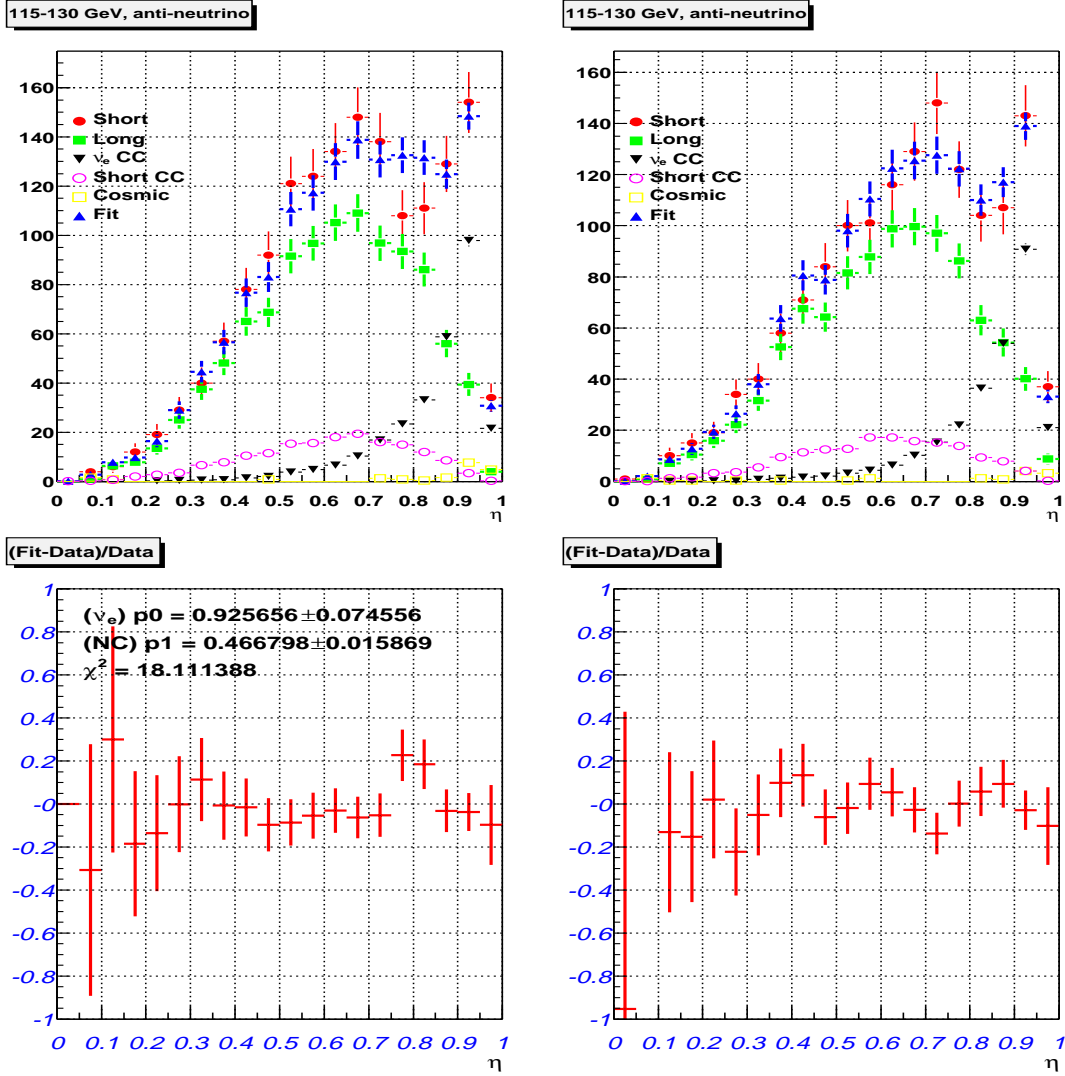


Figure 7.2: Fit of the η_3 distributions for $E_{cal} = 115 - 130$ GeV in anti-neutrino mode. Even *PLACE* events - top left plot, odd *PLACE* events - top right plot. The distribution of short events (solid circles), is fit as a sum of the distributions of the long events (solid squares), ν_e CC events (upside-down triangles), short CC events (open circles), and cosmic events (open squares), the best fit distribution is also shown (triangles). The fractional difference between the “best fit” and data distributions - even *PLACE* events - bottom left, odd *PLACE* events - bottom right.

E_{cal}, GeV	α	$\delta\alpha$	β	$\delta\beta$	$c_{\alpha\beta}$	χ^2/DOF
30 – 40	0.376	0.00285	-0.0694	0.488	-0.621	1.01
40 – 50	0.386	0.00314	0.28	0.301	-0.588	1.26
50 – 60	0.392	0.00359	0.698	0.22	-0.586	0.843
60 – 70	0.393	0.00409	0.983	0.162	-0.581	1.43
70 – 80	0.403	0.00475	1.08	0.128	-0.571	0.77
80 – 87.5	0.396	0.00613	1.12	0.118	-0.574	1.35
87.5 – 95	0.401	0.00682	1.23	0.103	-0.566	1.1
95 – 105	0.399	0.00631	0.923	0.0737	-0.565	0.985
105 – 115	0.377	0.00671	1.16	0.0661	-0.559	1.03
115 – 130	0.375	0.00584	1.07	0.0506	-0.569	0.841
130 – 145	0.348	0.006	1.04	0.0463	-0.551	1.45
145 – 160	0.358	0.00663	1.11	0.0505	-0.554	1.55
160 – 180	0.369	0.00655	1.07	0.0479	-0.539	0.869
180 – 200	0.381	0.00813	1.09	0.0638	-0.559	1.42
200 – 225	0.394	0.00924	1.18	0.0787	-0.538	1.31
225 – 250	0.433	0.0134	0.961	0.114	-0.537	1.71
250 – 350	0.443	0.0168	1.12	0.156	-0.577	1.66

Table 7.1: The η_3 fit results in neutrino mode. Shown are the central values and standard deviations of the parameters α and β , the correlation $c_{\alpha\beta}$, and the χ^2/DOF .

the measured ν_e flux.

The fitting of η_2 distributions is illustrated in Figures 7.3(neutrino mode) and 7.4(anti-neutrino mode). The fit results for all energy bins are listed in Tables 7.3 and 7.4. Plots of the η_2 fits for all energy bins can be found in Appendix C.

As seen from the tables, the errors on the β parameter are $\sim 20\%$ higher for the η_2 parameter fits, despite the fact that both distributions have equal statistics. This indicates that the η_3 parameter is more “sensitive” to the difference between the electromagnetic and hadronic showers in the NuTeV detector.

Finally, Tables 7.5 and 7.6 summarize the results of all the ν_e flux measurements using both the η_2 and η_3 distributions. For each energy bin the table shows the numbers of ν_e CC events predicted by the beam Monte Carlo and the measured

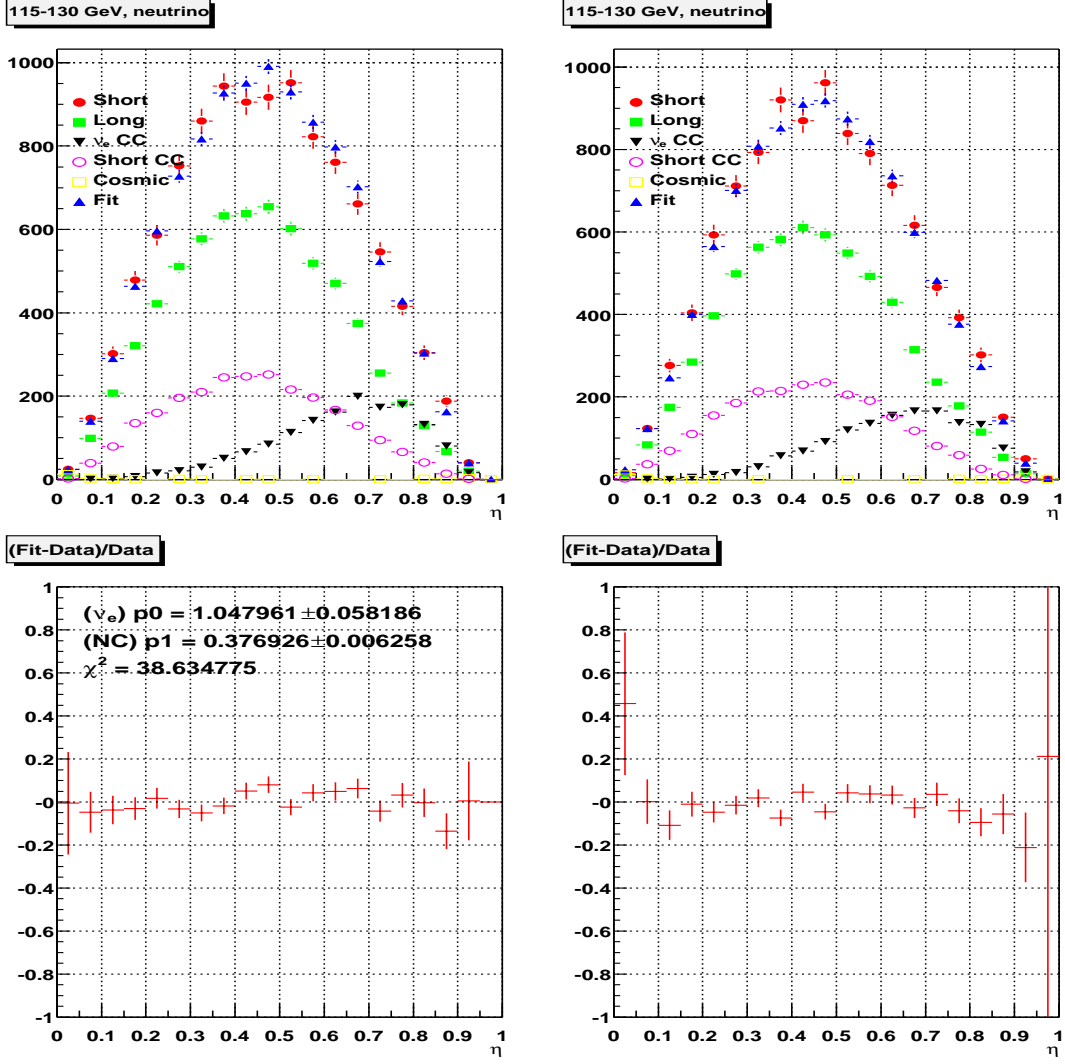


Figure 7.3: Fit of η_2 distributions for $E_{cal} = 115 - 130 \text{ GeV}$ in neutrino mode. Even *PLACE* events - top left plot, odd *PLACE* events - top right plot. The distribution of short events (solid circles), is fit as a sum of the distributions of the long events (solid squares), ν_e CC events (upside-down triangles), short CC events (open circles), and cosmic events (open squares), the best fit distribution is also shown (triangles). The fractional difference between the "best fit" and data distributions - even *PLACE* events - bottom left, odd *PLACE* events - bottom right.

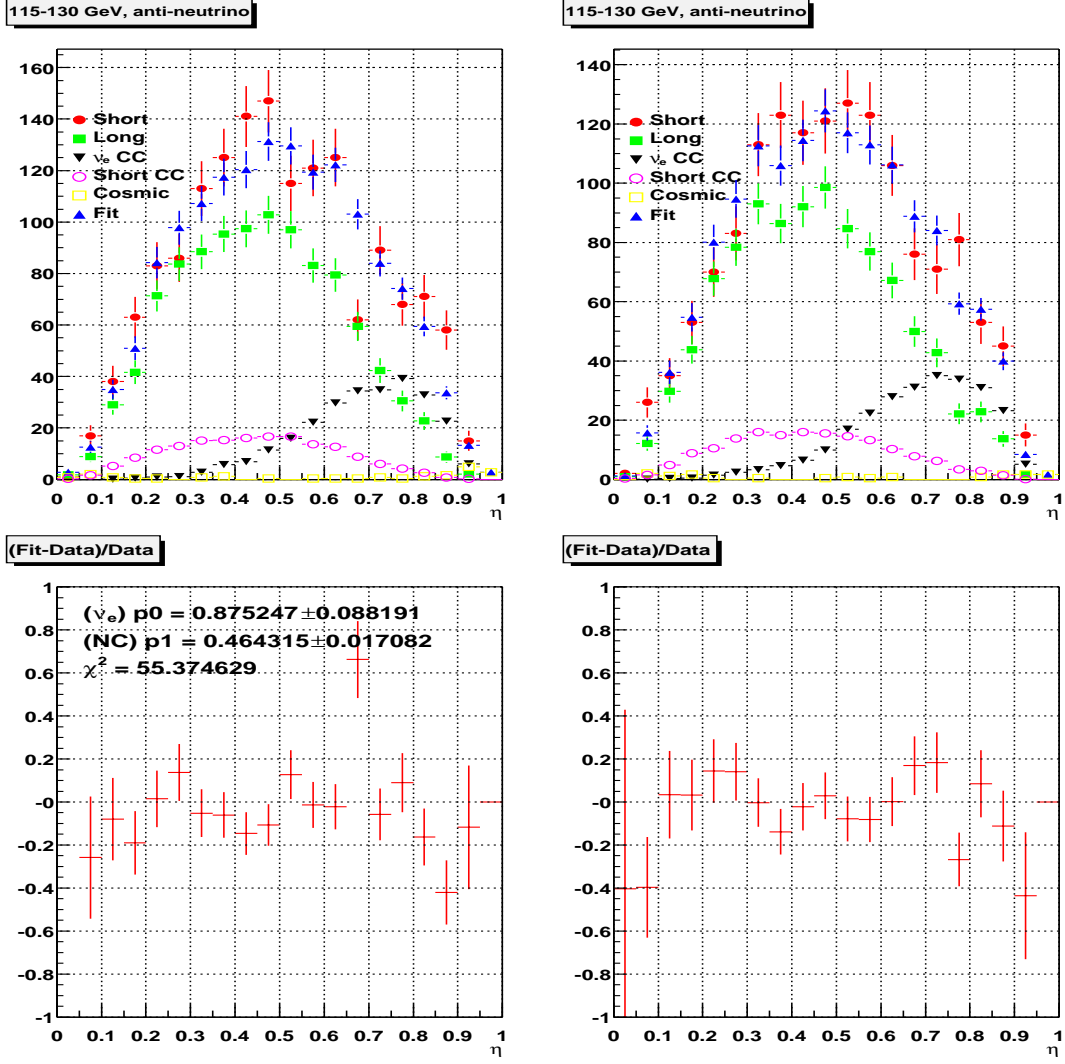


Figure 7.4: Fit of η_2 distributions for $E_{cal} = 115 - 130$ GeV in anti-neutrino mode. Even *PLACE* events - top left plot, odd *PLACE* events - top right plot. The distribution of short events (solid circles), is fit as a sum of the distributions of the long events (solid squares), ν_e CC events (upside-down triangles), short CC events (open circles), and cosmic events (open squares), the best fit distribution is also shown (triangles). The fractional difference between the “best fit” and data distributions - even *PLACE* events - bottom left, odd *PLACE* events - bottom right.

E_{cal}, GeV	α	$\delta\alpha$	β	$\delta\beta$	$c_{\alpha\beta}$	χ^2/DOF
30 – 40	0.435	0.00507	0.701	0.406	−0.608	0.605
40 – 50	0.435	0.00609	1.39	0.271	−0.515	1.08
50 – 60	0.449	0.00714	0.973	0.201	−0.487	0.722
60 – 70	0.446	0.00828	1.25	0.171	−0.46	1.07
70 – 80	0.453	0.01	0.911	0.136	−0.45	0.517
80 – 87.5	0.457	0.0134	1.02	0.138	−0.428	0.907
87.5 – 95	0.464	0.0153	0.893	0.125	−0.446	1.02
95 – 105	0.453	0.015	0.976	0.103	−0.444	0.685
105 – 115	0.456	0.0168	0.91	0.09	−0.436	1.33
115 – 130	0.467	0.0159	0.926	0.0746	−0.439	0.477
130 – 145	0.43	0.0169	1.06	0.0747	−0.424	0.742
145 – 160	0.47	0.0211	0.926	0.0868	−0.46	0.492
160 – 180	0.0451	0.00175	0.93	0.0694	−0.404	0.835
180 – 200	0.0391	0.00198	1.3	0.101	−0.389	0.811
200 – 225	0.0374	0.00221	1.1	0.117	−0.408	0.712
225 – 250	0.0354	0.00321	1.38	0.212	−0.473	1
250 – 350	0.0309	0.0034	0.684	0.234	−0.465	1.07

Table 7.2: The η_3 fit results in anti-neutrino mode. Shown are the central values and standard deviations of the parameters α and β , the correlation $c_{\alpha\beta}$, and the χ^2/DOF .

numbers extracted using η_3 and η_2 parameters. Also shown are the statistical errors in each of the two measurements and the difference between the two measurements.

7.2 Corrections to the measured electron neutrino flux

The results of η_3 and η_2 parameter fits are corrected for the systematic biases described in Section 6.5.3. Based on the Monte Carlo studies, we apply the following four corrections to our measurement:

- Short CC modeling correction. Table 7.8 contains the corrections $\Delta^{Short\ CC} = (\#\nu_e)_{measured}^{MC} - (\#\nu_e)_{true}^{MC}$. The measured numbers of ν_e events in each bin

E_{cal}, GeV	α	$\delta\alpha$	β	$\delta\beta$	$c_{\alpha\beta}$	χ^2/DOF
30 – 40	0.377	0.00303	-0.478	0.576	-0.673	1.21
40 – 50	0.387	0.00333	0.096	0.364	-0.646	1.18
50 – 60	0.391	0.00382	0.762	0.269	-0.65	1.37
60 – 70	0.394	0.00438	0.889	0.201	-0.652	1.42
70 – 80	0.407	0.00511	0.898	0.157	-0.646	0.961
80 – 87.5	0.398	0.00656	1.06	0.14	-0.64	0.89
87.5 – 95	0.403	0.00733	1.16	0.123	-0.641	1.3
95 – 105	0.396	0.00679	0.965	0.089	-0.643	1.02
105 – 115	0.373	0.00718	1.2	0.0774	-0.633	1.99
115 – 130	0.377	0.00626	1.05	0.0582	-0.64	1.02
130 – 145	0.348	0.00644	1.04	0.0529	-0.624	2.04
145 – 160	0.358	0.00718	1.1	0.0586	-0.634	1.6
160 – 180	0.373	0.00713	1.02	0.0562	-0.629	1.68
180 – 200	0.386	0.00884	1.03	0.0749	-0.642	1.61
200 – 225	0.392	0.0101	1.2	0.0956	-0.635	1.29
225 – 250	0.434	0.0148	0.983	0.144	-0.643	1.03
250 – 350	0.452	0.0189	0.967	0.199	-0.685	1.63

Table 7.3: The η_2 fit results in neutrino mode. Shown are the central values and standard deviations of the parameters α and β , the correlation $c_{\alpha\beta}$, and the χ^2/DOF .

of calorimeter energy E_{cal} , listed in Tables 7.5 and 7.6 are corrected, by subtracting the values $\Delta^{Short\ CC}$ from Table 7.8.

- Muon energy deposition correction. The measured numbers of ν_e events are corrected by subtracting the values of $\Delta^{dE_\mu/dx}$ listed in Table 7.9.
- $NN - PLACE$ correction. The measured numbers of ν_e events are corrected by subtracting the values of $\Delta^{NN-PLACE}$ listed in Table 7.10.
- ν_e CC modeling correction. As mentioned in Section 6.5.3 this correction is proportional to the measured electron neutrino flux and thus is applied as a multiplicative factor. Table 7.7 contains the correction factors $\delta^{\nu_e} = [(\#\nu_e)_{measured}^{MC} - (\#\nu_e)_{true}^{MC}]/(\#\nu_e)_{true}^{MC}$, after all other corrections have been

E_{cal}, GeV	α	$\delta\alpha$	β	$\delta\beta$	$c_{\alpha\beta}$	χ^2/DOF
30 – 40	0.431	0.00515	1.05	0.465	-0.613	1.07
40 – 50	0.433	0.0065	1.48	0.327	-0.597	0.826
50 – 60	0.448	0.0076	0.998	0.246	-0.574	0.89
60 – 70	0.444	0.00906	1.27	0.214	-0.567	0.925
70 – 80	0.448	0.0106	1.02	0.166	-0.542	0.607
80 – 87.5	0.456	0.0144	1.04	0.171	-0.537	0.754
87.5 – 95	0.46	0.0164	0.9	0.147	-0.54	1.04
95 – 105	0.437	0.0156	1.09	0.117	-0.526	1.21
105 – 115	0.46	0.018	0.9	0.106	-0.535	1.09
115 – 130	0.464	0.0171	0.875	0.0882	-0.548	1.46
130 – 145	0.422	0.0181	1.1	0.0873	-0.533	0.782
145 – 160	0.466	0.0221	0.927	0.0897	-0.523	0.639
160 – 180	0.0451	0.0019	0.879	0.0808	-0.532	1.46
180 – 200	0.0383	0.00213	1.38	0.117	-0.504	0.677
200 – 225	0.0369	0.00241	1.18	0.147	-0.536	0.612
225 – 250	0.0367	0.00333	1.23	0.236	-0.556	1.01
250 – 350	0.0362	0.00397	0.588	0.335	-0.617	0.441

Table 7.4: The η_2 fit results in anti-neutrino mode. Shown are the central values and standard deviations of the parameters α and β , the correlation $c_{\alpha\beta}$, and the χ^2/DOF .

applied the numbers of electron neutrino events in each bin of E_{cal} are multiplied by $1 - \delta^{\nu_e}$.

The corrected results of the shower shape analysis are presented in Tables 7.11 and 7.12 (the layout of these tables is the same as Tables 7.5 and 7.6).

The results are also shown in Figures 7.5 - η_3 -analysis, neutrino mode, 7.6 - η_3 -analysis, anti-neutrino mode, 7.7 - η_2 -analysis, neutrino mode and 7.8 - η_2 -analysis, anti-neutrino mode.

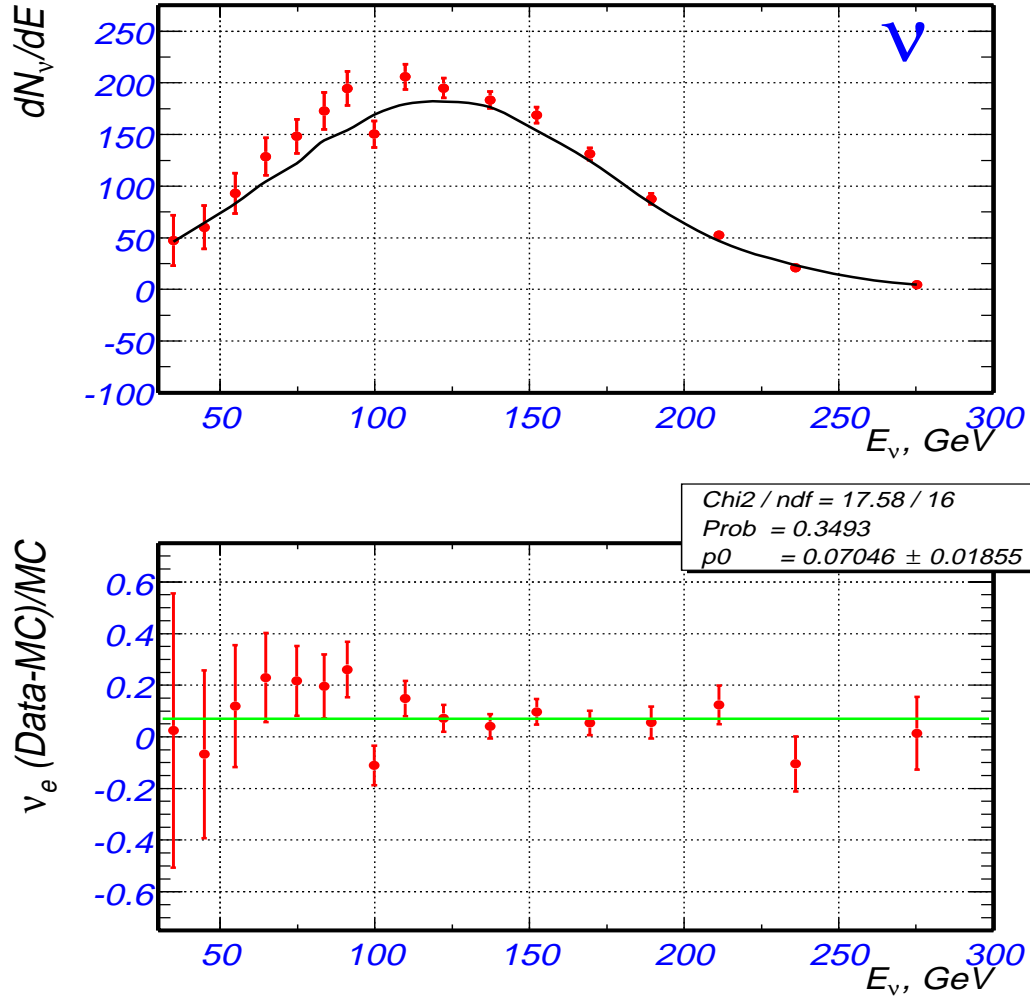


Figure 7.5: Result of the η_3 analysis, neutrino mode. Top plot - ν_e flux: beam Monte Carlo prediction (no oscillations) - line, η_3 measurement - circles. Bottom plot - ratio $(\#\nu_e(\text{measured}) - \#\nu_e(\text{MC}))/\#\nu_e(\text{MC})$.

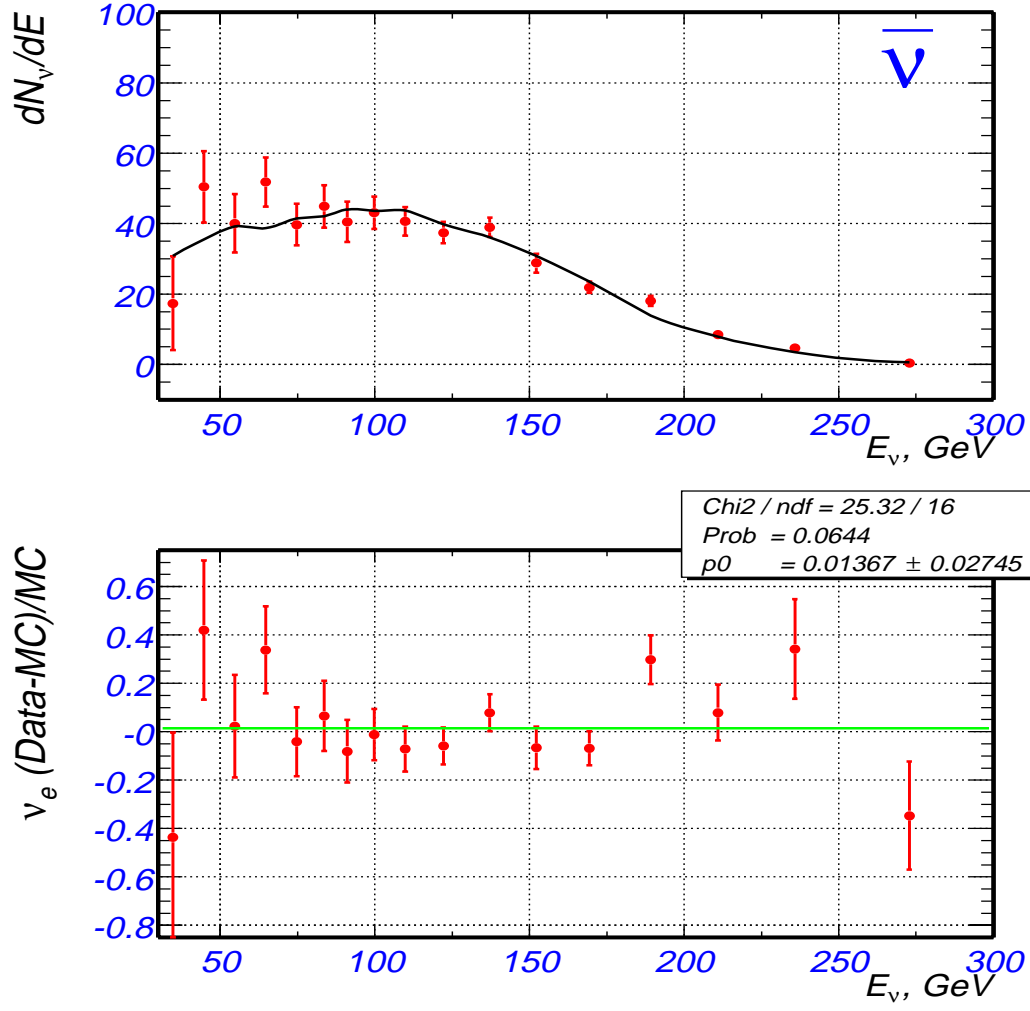


Figure 7.6: Result of η_3 analysis, anti-neutrino mode. Top plot - ν_e flux: beam Monte Carlo prediction (no oscillations) - line, η_3 measurement - circles. Bottom plot - ratio $(\#\nu_e(\text{measured}) - \#\nu_e(\text{MC}))/\#\nu_e(\text{MC})$.

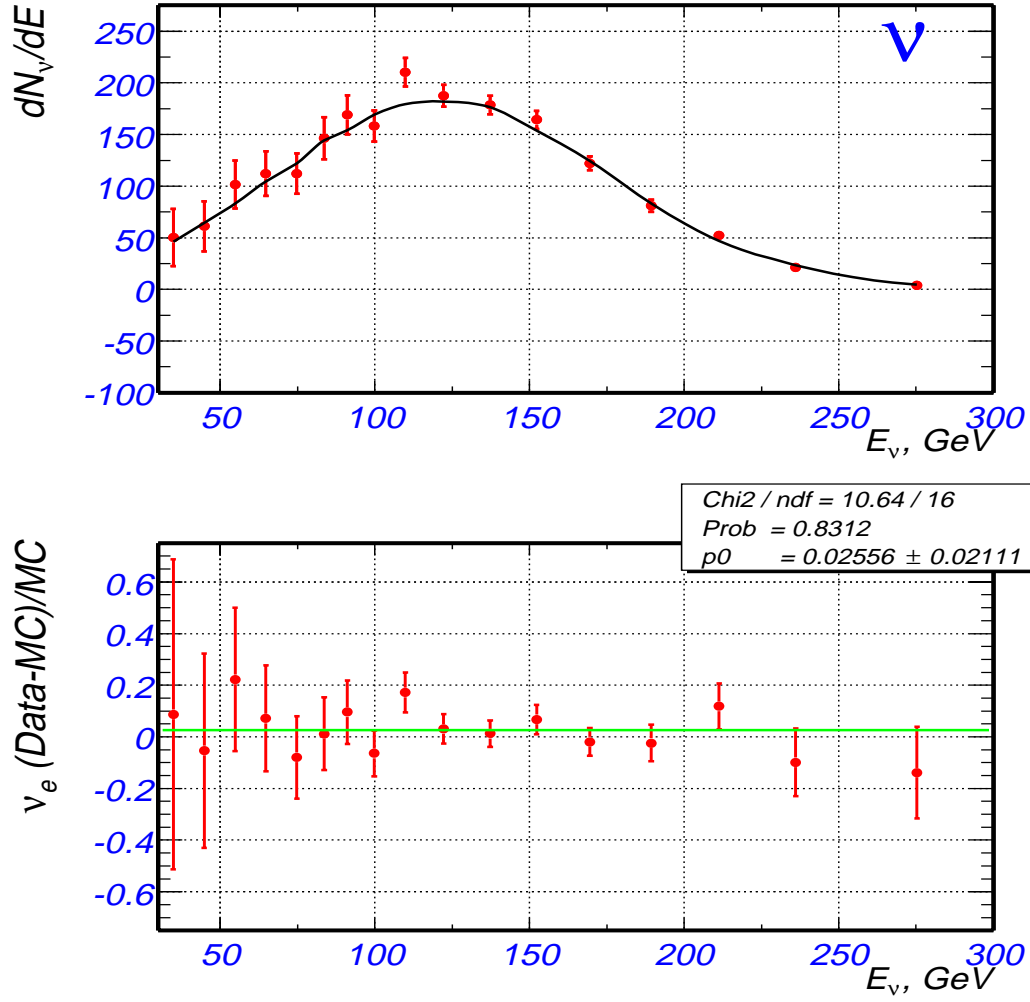


Figure 7.7: Result of η_2 analysis, neutrino mode. Top plot - ν_e flux: beam Monte Carlo prediction (no oscillations) - line, η_2 measurement - circles. Bottom plot - ratio $(\#\nu_e(\text{measured}) - \#\nu_e(\text{MC}))/\#\nu_e(\text{MC})$.

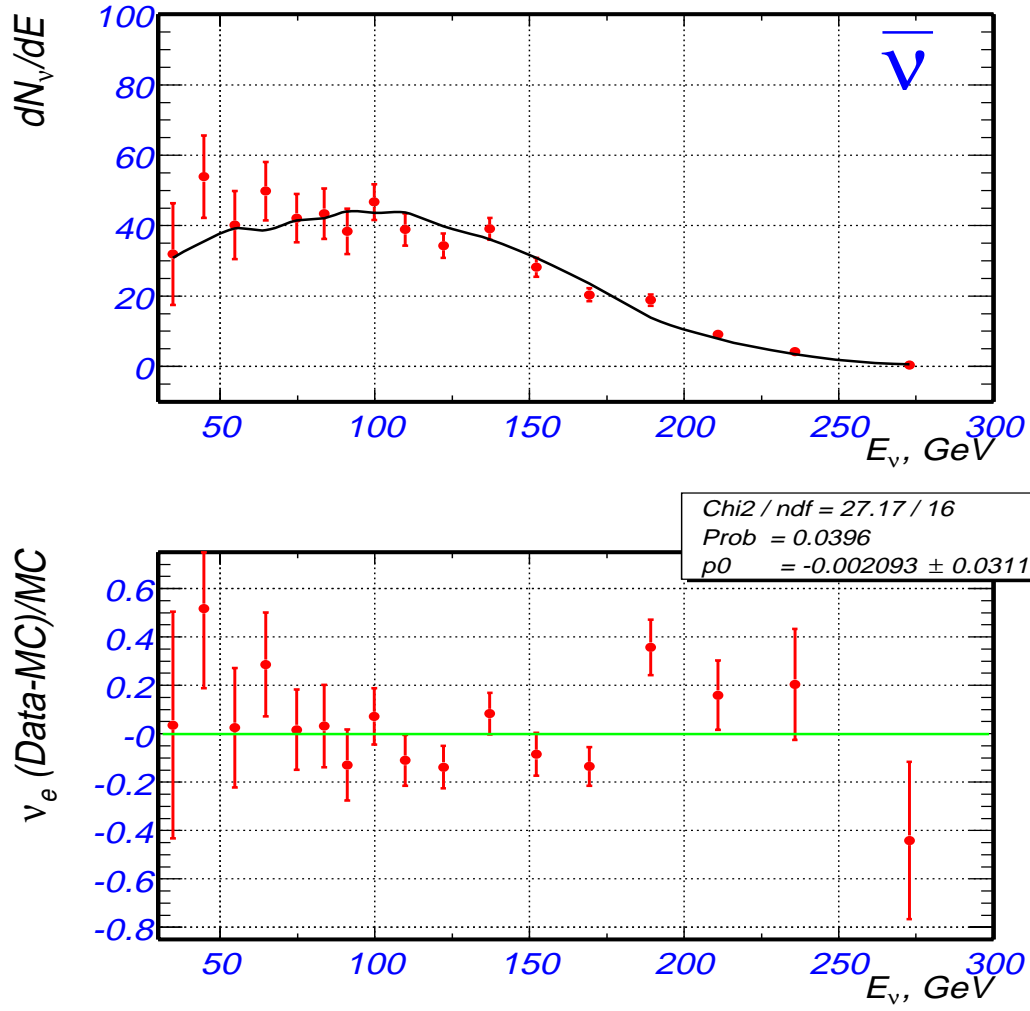


Figure 7.8: Result of η_2 analysis, anti-neutrino mode. Top plot - ν_e flux: beam Monte Carlo prediction (no oscillations) - line, η_2 measurement - circles. Bottom plot - ratio $(\#\nu_e(\text{measured}) - \#\nu_e(\text{MC}))/\#\nu_e(\text{MC})$.

E_{cal}, GeV	$\# \nu_e, MC$	$\# \nu_e, \eta_3$	$\delta(\# \nu_e), \eta_3$	$\# \nu_e, \eta_2$	$\delta(\# \nu_e), \eta_2$	$\# \nu_e, \eta_3 - \eta_2$
30 – 40	461.91	–32.06	225.26	–220.85	266.27	188.79
40 – 50	644.75	180.48	193.94	61.884	234.42	118.59
50 – 60	831.17	579.77	182.87	633.6	223.98	–53.837
60 – 70	1045.7	1028.2	169.25	929.52	210.42	98.723
70 – 80	1218.7	1319.3	155.86	1094.1	190.84	225.22
80 – 87.5	1083.8	1210.3	127.5	1151.8	151.41	58.531
87.5 – 95	1157.5	1428	118.74	1346.4	142.07	81.604
95 – 105	1690.5	1559.7	124.59	1632	150.49	–72.35
105 – 115	1794.1	2072.8	118.65	2146.5	138.78	–73.718
115 – 130	2729.7	2922.2	138.06	2860.6	158.83	61.598
130 – 145	2645.5	2757.7	122.48	2742	140.07	15.77
145 – 160	2308.2	2556.3	116.47	2545.5	135.17	10.72
160 – 180	2489.7	2668.6	119.25	2542.5	139.95	126.11
180 – 200	1662.7	1813.9	106.06	1715.3	124.53	98.589
200 – 225	1170.9	1381.9	92.116	1405	111.95	–23.043
225 – 250	588.83	565.92	67.088	578.85	84.624	–12.932
250 – 350	441.99	496.64	68.91	427.36	87.954	69.284

Table 7.5: Neutrino mode. Numbers of electron neutrino events: Predicted by the beam Monte Carlo simulation; Extracted from the η_3 fits with corresponding statistical error; Extracted from the η_2 fits with corresponding statistical error; Difference between η_3 and η_2 measurements.

7.3 Systematic Uncertainties

There are several systematic uncertainties that affect the measurement of the electron neutrino flux using the shower shape analysis.

Electron Energy Scale

The uncertainty in the response of the NuTeV detector to EM showers leads to an uncertainty in the simulation of ν_e CC events as described in Section 6.3. We estimate the resulting uncertainty in the measured electron-neutrino flux by performing the analysis with the default sample of ν_e CC events, simulated using the central value of $C_e = 1.08$, and the systematic error sample, simulated with

E_{cal}, GeV	$\# \nu_e, MC$	$\# \nu_e, \eta_3$	$\delta(\# \nu_e), \eta_3$	$\# \nu_e, \eta_2$	$\delta(\# \nu_e), \eta_2$	$\# \nu_e, \eta_3 - \eta_2$
30 – 40	308.1	215.9	124.9	323.8	143.4	–107.9
40 – 50	355.2	495.3	96.11	524.9	116.3	–29.67
50 – 60	391.6	381	78.63	390.7	96.48	–9.674
60 – 70	387.3	485.9	66.18	490.9	82.87	–5.01
70 – 80	414.3	377.3	56.2	424.5	68.89	–47.18
80 – 87.5	316	321.8	43.71	328.7	53.89	–6.922
87.5 – 95	330.3	294.9	41.19	297.4	48.61	–2.452
95 – 105	436	425.4	44.75	475.9	50.87	–50.53
105 – 115	437.3	398	39.37	393.5	46.37	4.495
115 – 130	597.1	552.7	44.52	522.6	52.66	30.1
130 – 145	541.3	574.8	40.45	593.3	47.26	–18.48
145 – 160	462	427.7	40.12	428.3	41.42	–0.5684
160 – 180	470.7	437.6	32.69	413.6	38.03	24.02
180 – 200	278.1	362.9	28.1	384.2	32.67	–21.3
200 – 225	196.7	215.8	23.07	232.8	28.83	–16.96
225 – 250	87.19	120.1	18.48	107.7	20.55	12.46
250 – 350	56.37	38.54	13.21	33.17	18.9	5.363

Table 7.6: Anti-neutrino mode. Numbers of electron neutrino events: Predicted by the beam Monte Carlo simulation; Extracted from the η_3 fits with corresponding statistical error; Extracted from the η_2 fits with corresponding statistical error; Difference between η_3 and η_2 measurements.

$C_e = 1.1$ (i.e. shifted by 1 sigma). We take the difference in the number of electron-neutrino events, measured using these two samples as the systematic error in the shower shape analysis which originates from the uncertainty in the electron energy calibration. This difference is shown in Figure 7.9.

$\mu \rightarrow \mu + \gamma$ **Radiation**

As described in Section 6.4.4 we account for the uncertainty in the modeling of the emission of radiative photons by varying the values of the parameters C_γ by 10%. The difference in the results of the analysis from this variation is taken as the systematic error, as shown in Figure 7.10.

E_{cal}, GeV	$\Delta(\#\nu_e)/\#\nu_e, \eta_3$	$\Delta(\#\nu_e)/\#\nu_e, \eta_2$	$\Delta(\#\bar{\nu}_e)/\#\bar{\nu}_e, \eta_3$	$\Delta(\#\bar{\nu}_e)/\#\bar{\nu}_e, \eta_2$
30 – 40	–0.0889	–0.0413	–0.0666	–0.00723
40 – 50	–0.0813	–0.0351	–0.062	–0.0056
50 – 60	–0.0736	–0.0289	–0.0573	–0.00398
60 – 70	–0.066	–0.0227	–0.0527	–0.00235
70 – 80	–0.0584	–0.0165	–0.048	–0.000728
80 – 87.5	–0.0516	–0.011	–0.0439	0.000713
87.5 – 95	–0.0458	–0.00634	–0.0404	0.00193
95 – 105	–0.0392	–0.000931	–0.0364	0.00334
105 – 115	–0.0315	0.0053	–0.0317	0.00497
115 – 130	–0.022	0.013	–0.026	0.00698
130 – 145	–0.0105	0.0223	–0.019	0.00942
145 – 160	0.000931	0.0316	–0.0121	0.0119
160 – 180	0.0141	0.0423	–0.00407	0.0146
180 – 200	0.0292	0.0546	0.00513	0.0179
200 – 225	0.0461	0.0683	0.0152	0.0214
225 – 250	0.065	0.0837	0.0268	0.0254
250 – 350	0.095	0.108	0.044	0.0314

Table 7.7: ν_e CC modeling correction.

E_{cal}, GeV	$\Delta(\#\nu_e), \eta_3$	$\Delta(\#\nu_e), \eta_2$	$\Delta(\#\bar{\nu}_e), \eta_3$	$\Delta(\#\bar{\nu}_e), \eta_2$
30 – 40	–461.2	–488.2	–32.7	–29.37
40 – 50	–375.5	–370	–26.81	–22.33
50 – 60	–289.8	–251.9	–20.93	–15.31
60 – 70	–204.2	–133.8	–15.05	–8.295
70 – 80	–118.4	–15.44	–9.169	–1.265
80 – 87.5	–31.87	66.92	–2.965	3.724
87.5 – 95	16.48	75.55	0.3519	7.549
95 – 105	100.6	56.36	8.08	6.521
105 – 115	67.33	28.86	4.896	3.951
115 – 130	61.55	18.97	3.963	3.198
130 – 145	33.71	6.954	1.868	1.508
145 – 160	18.51	2.56	0.8833	0.7129
160 – 180	12.39	1.083	0.4986	0.4024
180 – 200	5.613	0.2893	0.1851	0.1494
200 – 225	2.909	0.08336	0.07787	0.06284
225 – 250	1.081	0.016	0.02247	0.01813
250 – 350	0.9003	0.004684	0.01416	0.01143

Table 7.8: Short CC modeling correction.

E_{cal}, GeV	$\Delta(\#\nu_e), \eta_3$	$\Delta(\#\nu_e), \eta_2$	$\Delta(\#\bar{\nu}_e), \eta_3$	$\Delta(\#\bar{\nu}_e), \eta_2$
30 – 40	224.9	136.1	96.83	59.59
40 – 50	153.2	82.04	54.8	28.14
50 – 60	104.2	61.25	26.3	16.05
60 – 70	68.29	37.03	11.17	8.144
70 – 80	50.74	34.12	9.775	8.279
80 – 87.5	17.74	11.61	3.433	1.303
87.5 – 95	20.41	17.1	3.425	3.064
95 – 105	20.45	6.511	2.559	2.212
105 – 115	16.46	13.54	0.1832	−0.2111
115 – 130	6.02	0.8939	1.61	1.657
130 – 145	1.949	1.308	0.4867	0.6802
145 – 160	4.674	3.295	−0.003074	0.02517
160 – 180	0.4849	−1.668	0.04171	0.1231
180 – 200	0.7882	1.082	0.01815	0.06465
200 – 225	0.04021	0.3264	0.005729	0.0379
225 – 250	0.1976	0.2563	−0.007707	0
250 – 350	−0.01024	0.1311	0	0

Table 7.9: Muon momentum correction.

E_{cal}, GeV	$\Delta(\#\nu_e), \eta_3$	$\Delta(\#\nu_e), \eta_2$	$\Delta(\#\bar{\nu}_e), \eta_3$	$\Delta(\#\bar{\nu}_e), \eta_2$
30 – 40	−162.5	−253	0.9048	−6.659
40 – 50	−116.4	−181.1	0.6479	−4.768
50 – 60	−70.2	−109.3	0.3915	−2.881
60 – 70	−24.09	−37.51	0.1354	−0.9963
70 – 80	0	0	0	0
80 – 87.5	0	0	0	0
87.5 – 95	0	0	0	0
95 – 105	0	0	0	0
105 – 115	0	0	0	0
115 – 130	0	0	0	0
130 – 145	0	0	0	0
145 – 160	0	0	0	0
160 – 180	0	0	0	0
180 – 200	0	0	0	0
200 – 225	0	0	0	0
225 – 250	0	0	0	0
250 – 350	0	0	0	0

Table 7.10: $NN - PLACE$ correction.

E_{cal}, GeV	$\# \nu_e, MC$	$\# \nu_e, \eta_3$	$\delta(\# \nu_e), \eta_3$	$\# \nu_e, \eta_2$	$\delta(\# \nu_e), \eta_2$	$\# \nu_e, \eta_3 - \eta_2$
30 – 40	461.91	473.15	245.29	502.02	277.27	–28.867
40 – 50	644.75	601.45	209.69	610.51	242.65	–9.0518
50 – 60	831.17	930.1	196.33	1015.9	230.45	–85.809
60 – 70	1045.7	1285.6	180.42	1120.5	215.19	165.12
70 – 80	1218.7	1482.4	164.95	1121.6	193.99	360.73
80 – 87.5	1083.8	1295.7	134.08	1096.9	153.08	198.82
87.5 – 95	1157.5	1459.5	124.18	1267.9	142.97	191.61
95 – 105	1690.5	1502.7	129.47	1582	150.63	–79.23
105 – 115	1794.1	2059.2	122.38	2102.8	138.05	–43.579
115 – 130	2729.7	2925.8	141.1	2813.6	156.76	112.21
130 – 145	2645.5	2753	123.77	2678.2	136.94	74.818
145 – 160	2308.2	2531.8	116.36	2463.5	130.89	68.343
160 – 180	2489.7	2622.9	117.56	2441.9	134.03	181.05
180 – 200	1662.7	1753.9	102.96	1622.4	117.72	131.48
200 – 225	1170.9	1316.6	87.872	1309.5	104.3	7.1786
225 – 250	588.83	527.08	62.727	530.72	77.544	–3.6423
250 – 350	441.99	448.08	62.363	380.77	78.454	67.312

Table 7.11: Electron neutrino flux in neutrino mode: Predicted by the beam Monte Carlo simulation; Extracted from the η_3 fits (after pull corrections) with corresponding statistical error; Extracted from the η_2 fits (after pull corrections) with corresponding statistical error; Difference between the η_3 and η_2 measurements.

Monte Carlo Corrections

The systematic error for each of the Monte Carlo corrections which have been applied to the measurement is conservatively estimated to be 25% of the size of the correction itself.

$\eta_3 - \eta_2$ difference

We perform the shower shape analysis using parameters η_2 and η_3 . The difference in the results of these two analyses after all pull corrections have been applied is added as an additional uncertainty attributed to the overall analysis procedure. Based on the studies shown in Figures 7.5-7.8, an additional uncertainty of 2.25%

E_{cal}, GeV	$\# \nu_e, MC$	$\# \nu_e, \eta_3$	$\delta(\# \nu_e), \eta_3$	$\# \nu_e, \eta_2$	$\delta(\# \nu_e), \eta_2$	$\# \nu_e, \eta_3 - \eta_2$
30 – 40	308.09	173.61	133.27	319.13	144.45	–145.52
40 – 50	355.17	504.4	102.07	538.81	116.92	–34.408
50 – 60	391.63	400.75	83.134	401.38	96.864	–0.62789
60 – 70	387.27	518.25	69.669	497.89	83.068	20.361
70 – 80	414.28	397.19	58.894	421.19	68.942	–24.002
80 – 87.5	315.99	336.7	45.626	325.76	53.856	10.931
87.5 – 95	330.33	303.69	42.858	287.69	48.513	16.006
95 – 105	436.04	430.95	46.381	467.2	50.696	–36.258
105 – 115	437.27	406.19	40.614	389.18	46.136	17.009
115 – 130	597.1	561.69	45.675	514.8	52.291	46.892
130 – 145	541.29	583.88	41.217	586.4	46.815	–2.5207
145 – 160	462.02	431.53	40.609	422.57	40.932	8.9645
160 – 180	470.73	438.52	32.824	407.12	37.473	31.401
180 – 200	278.08	360.93	27.955	377.32	32.084	–16.385
200 – 225	196.74	212.37	22.719	227.99	28.209	–15.62
225 – 250	87.195	116.97	17.981	104.99	20.03	11.984
250 – 350	56.375	36.843	12.627	31.537	18.31	5.3053

Table 7.12: Electron neutrino flux in anti-neutrino mode: Predicted by the beam Monte Carlo simulation; Extracted from the η_3 fits (after pull corrections) with corresponding statistical error; Extracted from the η_2 fits (after pull corrections) with corresponding statistical error; Difference between the η_3 and η_2 measurements.

is assigned to the neutrino mode measurements, and an additional uncertainty of 0.6% is assigned to anti-neutrino mode measurements.

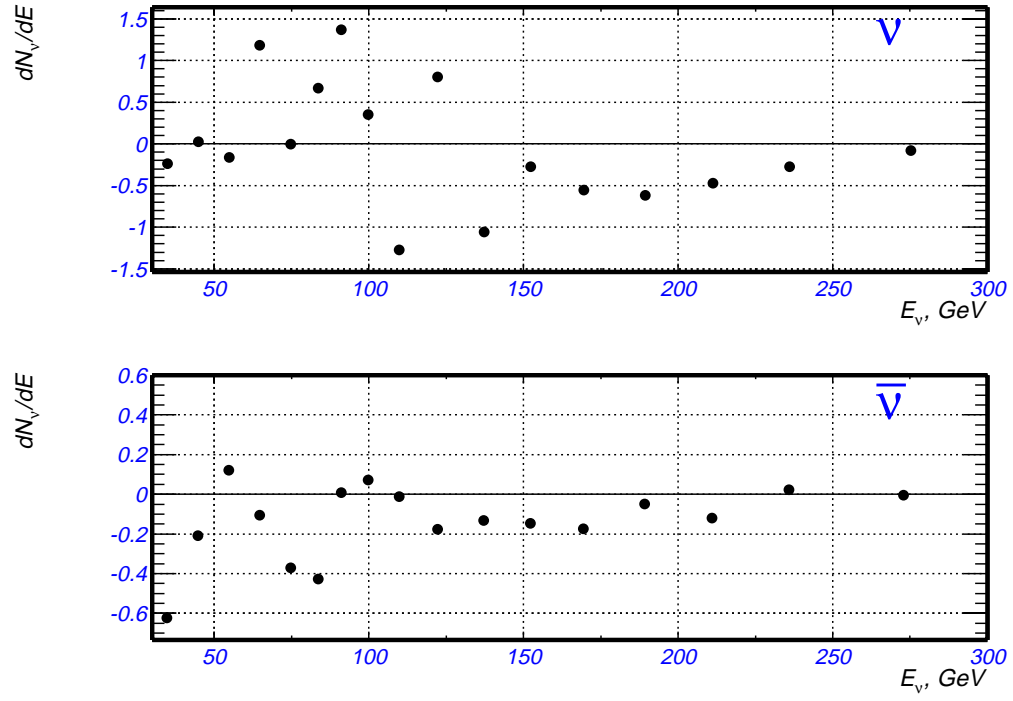


Figure 7.9: Systematic uncertainty from the electron energy scale: change in the measured number of ν_e 's from a one sigma shift in C_e .

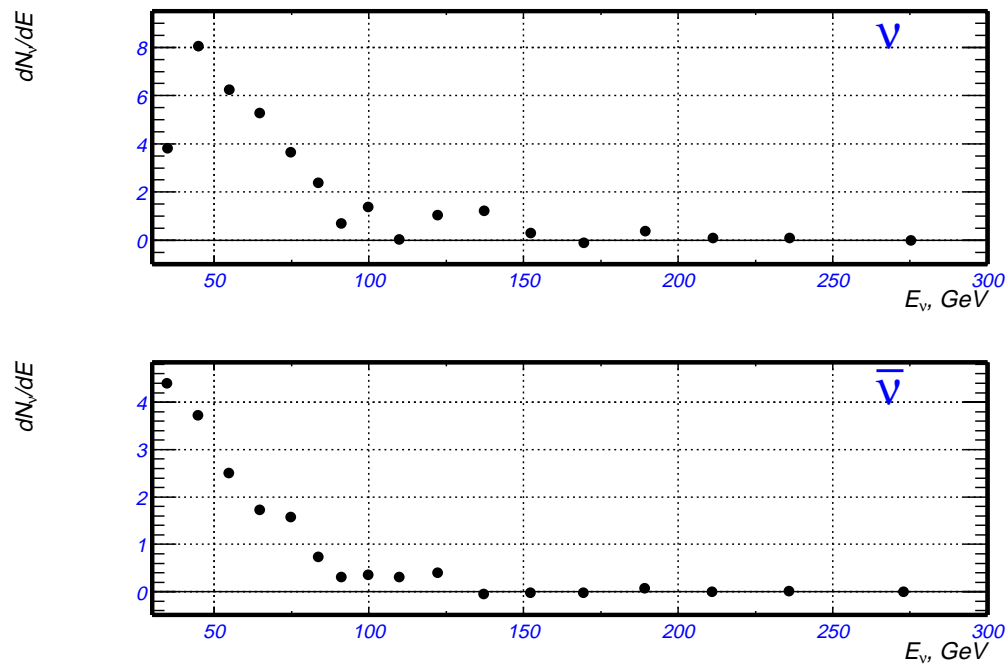


Figure 7.10: Systematic uncertainty from emission of radiative photons.

Chapter 8

Results and Conclusions

8.1 $\nu_\mu \rightarrow \nu_e$ Oscillations

The direct measurements of the electron-neutrino and muon-neutrino events in the NuTeV detector can be used to search for $\nu_\mu \rightarrow \nu_e$ oscillations by comparing the measured number with the prediction from the beam Monte Carlo. In general, two types of searches can be considered. One involves looking for the appearance of an excess of ν_e events relative to the prediction, i.e., a direct test of the hypothesis of $\nu_\alpha \rightarrow \nu_e$ oscillation. The other option is a search for the disappearance of ν_μ events, which is a test of the hypothesis of $\nu_\mu \rightarrow \nu_\beta$ oscillation. Experiments of the first and the second type are usually referred to as the “appearance” and “disappearance” experiments. Since the neutrino beam in the NuTeV experiment consists mostly (approximately 99%) of muon-neutrinos, with only a 1% fraction of electron-neutrinos, the most sensitive neutrino oscillation search would be of an “appearance” type for $\nu_\mu \rightarrow \nu_e$ oscillations.

The results of searches for neutrino oscillations are usually presented in terms of a two-dimensional exclusion region (or allowed region) in the two parameters Δm^2

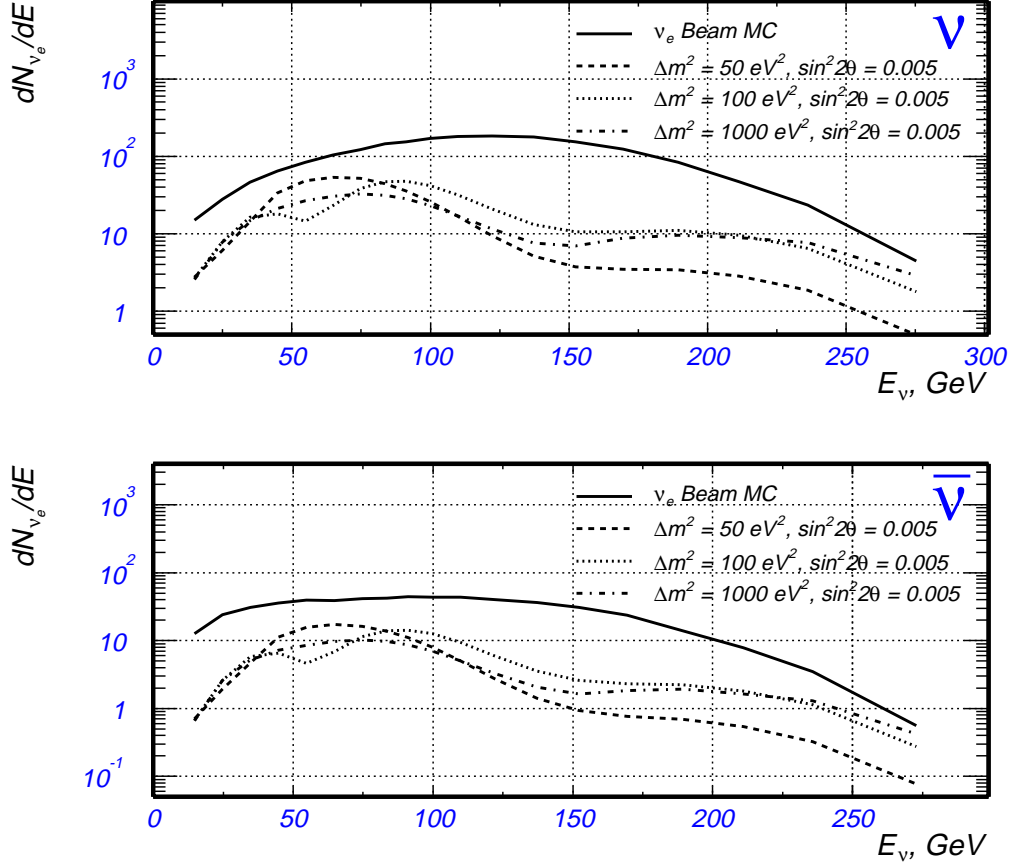


Figure 8.1: Electron neutrino flux in the NuTeV detector: Beam MC prediction for no oscillations is compared to the additional electron neutrino flux that would originate from $\nu_{\mu} \rightarrow \nu_e$ oscillations for $\Delta m^2 = 50, 100, 1000 \text{ eV}^2$ and $\sin^2 2\theta = 0.005$, for neutrino mode - top, anti-neutrino mode - bottom.

and θ . Traditionally Δm^2 is plotted along the vertical axis and $\sin^2 2\theta$ along the horizontal axis. If an oscillation signal is observed, the results are shown in terms of an allowed region of parameters for a given confidence level. For experiments that fail to detect an oscillation signal, an “upper limit”, i.e. the excluded region in the $(\Delta m^2, \sin^2 2\theta)$ plane, is shown for a given level of confidence. The expected

sensitivity of the NuTeV experiment to neutrino oscillations was known before the analysis was performed, and was based on the experience with previous search for $\nu_\mu \rightarrow \nu_e$ oscillations with the CCFR [37] detector. The CCFR analysis failed to find an oscillation signal and published an “upper limit” exclusion region result [19]. The goal of the NuTeV experiment was to improve the CCFR limit by using the larger data sample accumulated by NuTeV, by using improved calibration and analysis techniques, and a better understood beam. In addition, the sign selected beam in NuTeV provided the possibility of a search for oscillations in both neutrino and anti-neutrino running modes independently. Separate searches in neutrino or anti-neutrino events were not possible in the CCFR experiment, because the CCFR beam consisted of a mixture of neutrinos and anti-neutrinos.

The analysis is done within a two generation mixing model for neutrino oscillations as described in Section 1.2.2. The oscillation probability

$$P_{\nu_\mu \rightarrow \nu_e} = \sin^2(2\theta) \sin^2 \left(\frac{1.27 \Delta m^2 (eV^2) L (km)}{E_\nu (GeV)} \right) \quad (8.1)$$

is a function of the two parameters of the model, namely the mixing angle (θ) and the difference between the squares of the masses of the two types of neutrinos (Δm^2). In the above equation, E_ν is the neutrino energy in GeV and L is the path traveled by the neutrino from the point of its creation to the point of interaction in kilometers. The Monte Carlo simulation of the beam is used in combination with the oscillation probability given in Equation (8.1) to predict the additional electron-neutrino flux from $\nu_\mu \rightarrow \nu_e$ oscillations for different values of the model parameters Δm^2 and $\sin^2 2\theta$. The results of such simulations are shown in Figure 8.1 for values of $\Delta m^2 = 50, 100, 1000 \text{ eV}^2$, and $\sin^2 2\theta = 0.005$. These are compared with the overall electron-neutrino flux predicted for no oscillations. The NuTeV experiment is only sensitive to neutrino oscillations in the region $\Delta m^2 > 10 \text{ eV}^2$.

This is because for the combination of neutrino energies and oscillation length at NuTeV, the oscillation probability $P_{\nu_\mu \rightarrow \nu_e}$ (8.1) is very small for $\Delta m^2 < 10 \text{ eV}^2$. For oscillations with $\Delta m^2 > 1000 \text{ eV}^2$, NuTeV is insensitive to the exact value of the Δm^2 , $P_{\nu_\mu \rightarrow \nu_e}$ (8.1) averaged over the path length of neutrinos (L) becomes

$$\langle P_{\nu_\mu \rightarrow \nu_e} \rangle = 0.5 \times \sin^2(2\theta) \quad (8.2)$$

and is independent of Δm^2 . The NuTeV experiment has the greatest sensitivity to an oscillation signal in the region of Δm^2 between $50 - 1000 \text{ eV}^2$. The shape of this signal changes somewhat with Δm^2 , as shown Figure 8.1.

As mentioned previously the NuTeV experiment has an advantage over CCFR because of its “sign-selected” neutrino beam. The analysis with neutrino and anti-neutrino data can be done separately without the need for making the assumption that the oscillation probabilities $P(\nu_\mu \rightarrow \nu_e)$ and $P(\bar{\nu}_\mu \rightarrow \bar{\nu}_e)$ are the same. In the next section, we present separate searches for oscillations in neutrino and anti-neutrino interactions. This is followed by the results of a combined analysis.

8.2 $\nu_\mu \rightarrow \nu_e$ Oscillation Analysis

There are several methods to perform the oscillation analysis to determine the allowed or excluded region in the $(\sin^2 2\theta, \Delta m^2)$. For mostly historical reasons we chose to perform the analysis in the same way as was done in the CCFR analysis. This method is usually referred to as the “raster scan”. For each value of Δm^2 a best fit is made for $\sin^2 2\theta$. Assuming a Gaussian probability distribution, this determines a 1-dimensional interval in $\sin^2 2\theta$, excluded at 90% confidence:

$$\sin^2 2\theta > \sin^2 2\theta_{fit} + 1.28\sigma_{fit} \quad (8.3)$$

The excluded region in the $(\sin^2 2\theta, \Delta m^2)$ plane is then the union of all these separate intervals. For all practical purposes, it is sufficient to perform $\sin^2 2\theta$ fits for a selected subset values of Δm^2 . We chose a set of 38 values of Δm^2 between 1 eV^2 and 20000 eV^2 that are approximately uniformly distributed on a logarithmic scale.

Another important issue is the sensitivity of the oscillation search. This is defined as the excluded region that would be obtained for an experiment with no signal, or, equivalently, when all the best fit values of $\sin^2 2\theta$ equal to zero. For each value of Δm^2 , we determine the sensitivity by the 1-dimensional interval

$$\sin^2 2\theta > 1.28\sigma_{fit}. \quad (8.4)$$

The best values of $\sin^2 2\theta_{fit}$ and $1\sigma_{fit}$ errors are determined using a minimization procedure described in the next section.

8.2.1 Extracting the Parameters

The best value of $\sin^2 2\theta$ for each Δm^2 is based on a comparison between the predicted electron-neutrino flux and the measured flux from the shower shape analysis. We construct a phenomenological χ^2 function that includes the statistical errors and incorporates the systematic uncertainties on both the Monte Carlo prediction and on the measurement. We define the systematic uncertainties in terms of one standard deviation “pulls”, where each such systematic “pull” represents the shift in each of the data/Monte Carlo points that corresponds to a one standard deviation shift in the systematic uncertainty of any parameter. Each of the pulls is allowed to vary by including it in the χ^2 with a weighting factor C_i . The contribution to the χ^2 from any uncertainty is then equal to C_i^2 because, by construction, the standard error on C_i is defined to be 1.. Accordingly, we define the χ^2 function

to be:

$$\chi^2 = \sum_{energy\ bins} \left(\frac{\# \nu_e^{MC}(C_i^{MC}) + \# \nu_e^{Osc}(\Delta m^2, \sin^2 2\theta) - \# \nu_e^{Data}(C_j^{Data})}{\sigma_{Stat}} \right)^2 \quad (8.5)$$

$$+ \sum_{MC\ systematics} (C_i^{MC})^2 + \sum_{Data\ systematics} (C_j^{Data})^2.$$

The quantity $\# \nu_e^{MC}(C_i^{MC})$ is the number of electron-neutrino events predicted by the beam Monte Carlo with the systematic pulls added with weights C_i^{MC} (where index i runs over all systematic uncertainties of the Monte Carlo prediction); the quantity $\# \nu_e^{Osc}(\Delta m^2, \sin^2 2\theta)$ is the number of electron-neutrino events expected from $\nu_\mu \rightarrow \nu_e$ oscillations; the quantity $\# \nu_e^{Data}(C_j^{Data})$ is the measured number of electron-neutrino events extracted from the event sample using the shower shape analysis with the systematic pulls added with weights C_j^{Data} (where index j runs over all systematic uncertainties of the measurement); and σ_{Stat} is the statistical uncertainty of the measurement.

At each Δm^2 we minimize the χ^2 by letting all the C_i^{MC} and C_j^{Data} float along with $\sin^2 2\theta$. This procedure is equivalent to the construction of the full error matrix with all the correlations between the set of data points taken into account. The list of all systematic uncertainties introduced in the fitting procedure is given below. We first list all the systematic uncertainties associated with the simulation of the expected number of events in the detector as predicted by the beam Monte Carlo. This number is sensitive to both the uncertainties in the parameters of the beam Monte Carlo and to detector parameters such as energy calibrations. (Because the polarity of the toroidal beam spectrometer was changed between neutrino and anti-neutrino modes, the muon energy calibration in neutrino and anti-neutrino modes could in principle be different.)

Systematics associated with simulation of number of expected events:

1. Error in the hadron energy scale of the calorimeter
2. Error in the muon energy scale of the toroid spectrometer, neutrino mode
3. Error in the muon energy scale of the toroid spectrometer, anti-neutrino mode
4. Modeling of the production of electron-neutrinos from decays of charged Kaons, i.e. $BR(K_{e3})$ and alignment of beam line elements
5. Error in the electron energy scale of the calorimeter
6. Modeling of the production of electron-neutrinos from decays of charm mesons
7. Modeling of the production of electron-neutrinos from decays of neutral K'_L s

The above systematics are described in greater detail in Section 3.3.

The systematic uncertainties in the measured number of electron-neutrino events extracted from the data sample using the shower shape analysis arise from:

1. Modeling of dilepton events
2. Modeling of the emission of radiative photons (neutrino mode)
3. Modeling of emission of radiative photons (anti-neutrino mode)
4. Modeling of ν_e CC events
5. Modeling of muon energy deposition
6. Modeling of Short CC events
7. Error in the determination of $NN - PLACE$
8. Difference between the η_2 and η_3 analyses, neutrino mode

9. Difference between the η_2 and η_3 analyses, anti-neutrino mode

10. Error in the overall electron energy scale of the calorimeter

The above systematic uncertainties are described in Section 7.3.

One of the C_i coefficients that is allowed to float in the overall fit, namely the systematic uncertainty on the overall electron energy scale in the calorimeter, affects both the prediction of the electron-neutrino rate from the beam Monte Carlo, and also the extracted electron-neutrino rate from the shower shape analysis.

The results of the oscillation analysis for neutrino running mode, anti-neutrino running mode, and for the combined analysis are presented in the next three sections.

8.2.2 Results of the analysis in neutrino mode

Results of the analysis for the neutrino mode are presented in Table 8.1 and in Figure 8.2. We can see that the values of $\sin^2 2\theta$ obtained from the minimization procedure are consistent with zero, except for the region $\Delta m^2 < 10 \text{ eV}^2$, where the signal becomes very small. We determine the experimental sensitivity and the regions, excluded at 90% confidence level according to Equations 8.3-8.4. This is shown in Figure 8.3. It can be seen that the experimental limit is worse than the sensitivity because the best fit values of $\sin^2 2\theta$ are positive.

The values of the systematic coefficients C_i after the minimization procedure are shown in Figures 8.4 and 8.5.

8.2.3 Results of the analysis in anti-neutrino mode

Results of the oscillation analysis for the anti-neutrino mode are presented in Table 8.2 and in Figure 8.6. The values of $\sin^2 2\theta$ obtained from the minimization

$\Delta m^2, eV^2$	$\sin^2(2\theta)$	1σ	<i>Sensitivity</i>	90% <i>CL</i>
1	0.8793	1.172	1.5	2.379
2	0.2204	0.2932	0.3753	0.5958
3	0.0984	0.1307	0.1673	0.2657
4	0.05569	0.07375	0.0944	0.1501
5	0.03592	0.04741	0.06068	0.0966
7	0.01871	0.02446	0.03131	0.05002
9	0.01163	0.01502	0.01923	0.03086
10	0.009545	0.01227	0.01571	0.02525
20	0.002986	0.003478	0.004452	0.007437
30	0.001752	0.001832	0.002345	0.004097
40	0.001296	0.001245	0.001593	0.002889
50	0.001075	0.0009788	0.001253	0.002327
60	0.0009552	0.0008492	0.001087	0.002042
70	0.0008885	0.000801	0.001025	0.001914
80	0.000843	0.0007929	0.001015	0.001858
90	0.0008032	0.0008115	0.001039	0.001842
100	0.0007577	0.0008425	0.001078	0.001836
125	0.0005887	0.0008873	0.001136	0.001724
150	0.0003894	0.0008205	0.00105	0.00144
175	0.00024	0.0007136	0.0009135	0.001153
200	0.0001423	0.0006289	0.000805	0.0009473
225	7.6×10^{-5}	0.0005785	0.0007404	0.0008164
250	3.3×10^{-5}	0.0005592	0.0007158	0.0007489
275	1.5×10^{-5}	0.000567	0.0007257	0.0007407
300	2.223×10^{-5}	0.0005993	0.0007671	0.0007893
350	0.0001113	0.000734	0.0009396	0.001051
400	0.0004264	0.0009576	0.001226	0.001652
450	0.001072	0.001159	0.001483	0.002555
500	0.00125	0.001153	0.001476	0.002726
600	0.0006755	0.0009396	0.001203	0.001878
700	0.0003024	0.0008335	0.001067	0.001369
800	0.0003079	0.0008296	0.001062	0.00137
1000	0.0003921	0.0008982	0.00115	0.001542
1500	0.0004066	0.000889	0.001138	0.001545
2000	0.0004351	0.0008997	0.001152	0.001587
5000	0.0004502	0.0008976	0.001149	0.001599
10000	0.0004502	0.0008976	0.001149	0.001599
20000	0.0004502	0.0008976	0.001149	0.001599

Table 8.1: Oscillation parameter fits in neutrino mode: Δm^2 , central value of $\sin^2 2\theta$, 1σ error, sensitivity, 90% *CL* upper limit.

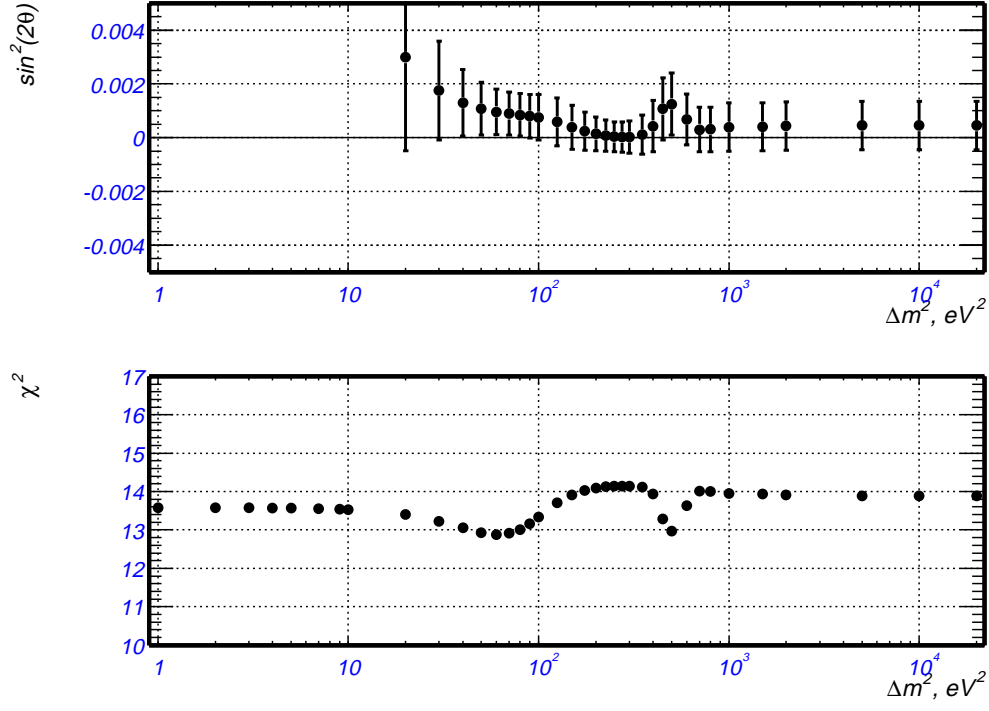


Figure 8.2: Oscillation parameter fits in neutrino mode: Top plot - best fit $\sin^2 2\theta$; Bottom plot - χ^2 at the minimum.

procedure are again consistent with zero. The sensitivity and the excluded region are shown in Figure 8.7. Here the experimental limit is slightly better than the sensitivity because best fit values of $\sin^2 2\theta$ are negative.

The values of the systematic coefficients C_i after the minimization procedure are shown in Figures 8.8 and 8.9.

$\Delta m^2, eV^2$	$\sin^2(2\theta)$	1σ	<i>Sensitivity</i>	90% <i>CL</i>
1	0.8777	1.334	1.708	2.585
2	0.22	0.3333	0.4266	0.6466
3	0.09825	0.1487	0.1903	0.2885
4	0.05563	0.08391	0.1074	0.163
5	0.0359	0.05393	0.06903	0.1049
7	0.01872	0.02781	0.03559	0.05431
9	0.01164	0.01707	0.02184	0.03349
10	0.009584	0.01394	0.01785	0.02743
20	0.002952	0.003921	0.005019	0.007972
30	0.001613	0.002054	0.002629	0.004241
40	0.001004	0.001385	0.001773	0.002776
50	0.000604	0.001078	0.00138	0.001984
60	0.0003072	0.0009267	0.001186	0.001493
70	7.9×10^{-5}	0.0008577	0.001098	0.001177
80	-9.7×10^{-5}	0.0008363	0.00107	0.0009734
90	-0.0002265	0.0008521	0.001091	0.0008642
100	-0.0003072	0.0008856	0.001134	0.0008263
125	-0.0002325	0.0009795	0.001254	0.001021
150	8.5×10^{-5}	0.0009688	0.00124	0.001326
175	0.0001456	0.0008741	0.001119	0.001264
200	-6.5×10^{-6}	0.0007846	0.001004	0.0009977
225	-0.0001776	0.0007314	0.0009362	0.0007585
250	-0.0003379	0.0007151	0.0009154	0.0005774
275	-0.0004992	0.0007307	0.0009353	0.000436
300	-0.0006563	0.0007742	0.000991	0.0003346
350	-0.0009176	0.0009353	0.001197	0.0002796
400	-0.0009125	0.001153	0.001476	0.0005636
450	-0.0002038	0.001286	0.001646	0.001442
500	0.0005675	0.001262	0.001616	0.002183
600	0.0003421	0.001123	0.001438	0.00178
700	-0.0002862	0.001011	0.001294	0.001008
800	-0.0004325	0.001	0.00128	0.0008477
1000	-0.0003267	0.001076	0.001377	0.00105
1500	-0.0003267	0.001076	0.001377	0.00105
2000	-0.0002395	0.001077	0.001379	0.001139
5000	-0.0002661	0.001073	0.001374	0.001108
10000	-0.0002661	0.001073	0.001374	0.001108
20000	-0.0002661	0.001073	0.001374	0.001108

Table 8.2: Oscillation parameter fits in anti-neutrino mode: Δm^2 , central value of $\sin^2 2\theta$, 1σ error, sensitivity, 90% *CL* upper limit.

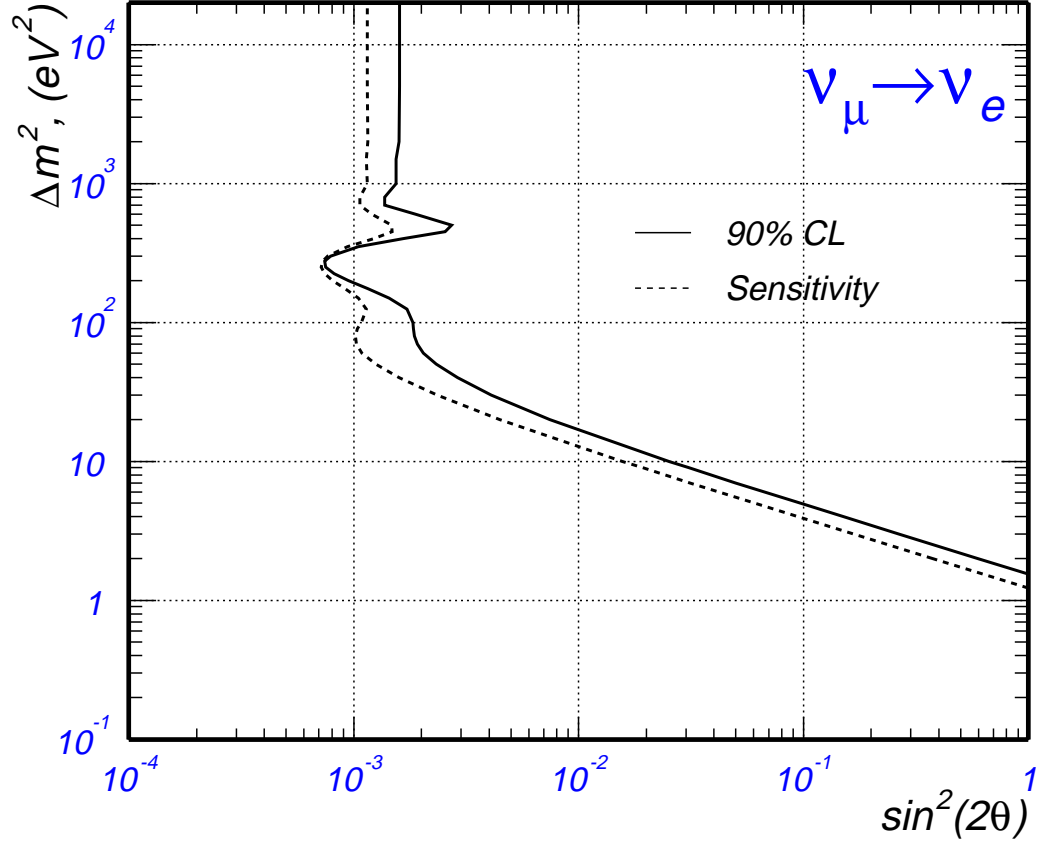


Figure 8.3: Sensitivity and upper limits at 90% confidence level for $\nu_\mu \rightarrow \nu_e$ oscillations. The excluded region of $\sin^2(2\theta)$ and Δm^2 is the area to the right of the solid curve.

8.2.4 Results of the combined analysis of neutrino and anti-neutrino mode

For the combined analysis we assume CP invariant oscillations which implies that the oscillation probabilities $P(\nu_\mu \rightarrow \nu_e)$ and $P(\bar{\nu}_\mu \rightarrow \bar{\nu}_e)$ are equal. The minimiza-

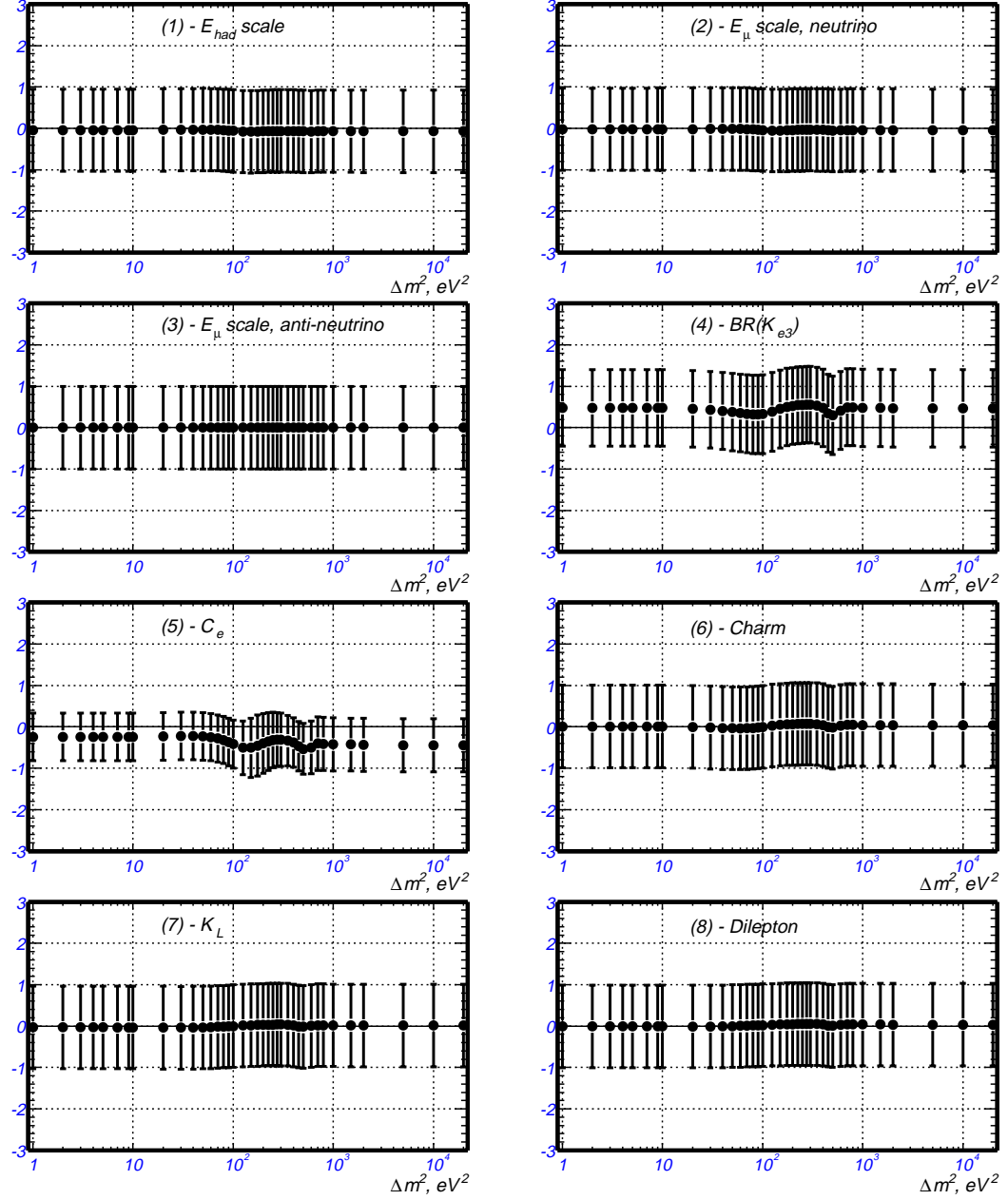


Figure 8.4: Oscillation parameter fits in neutrino mode: Values of the systematic coefficients C_1 through C_8 after χ^2 minimization.

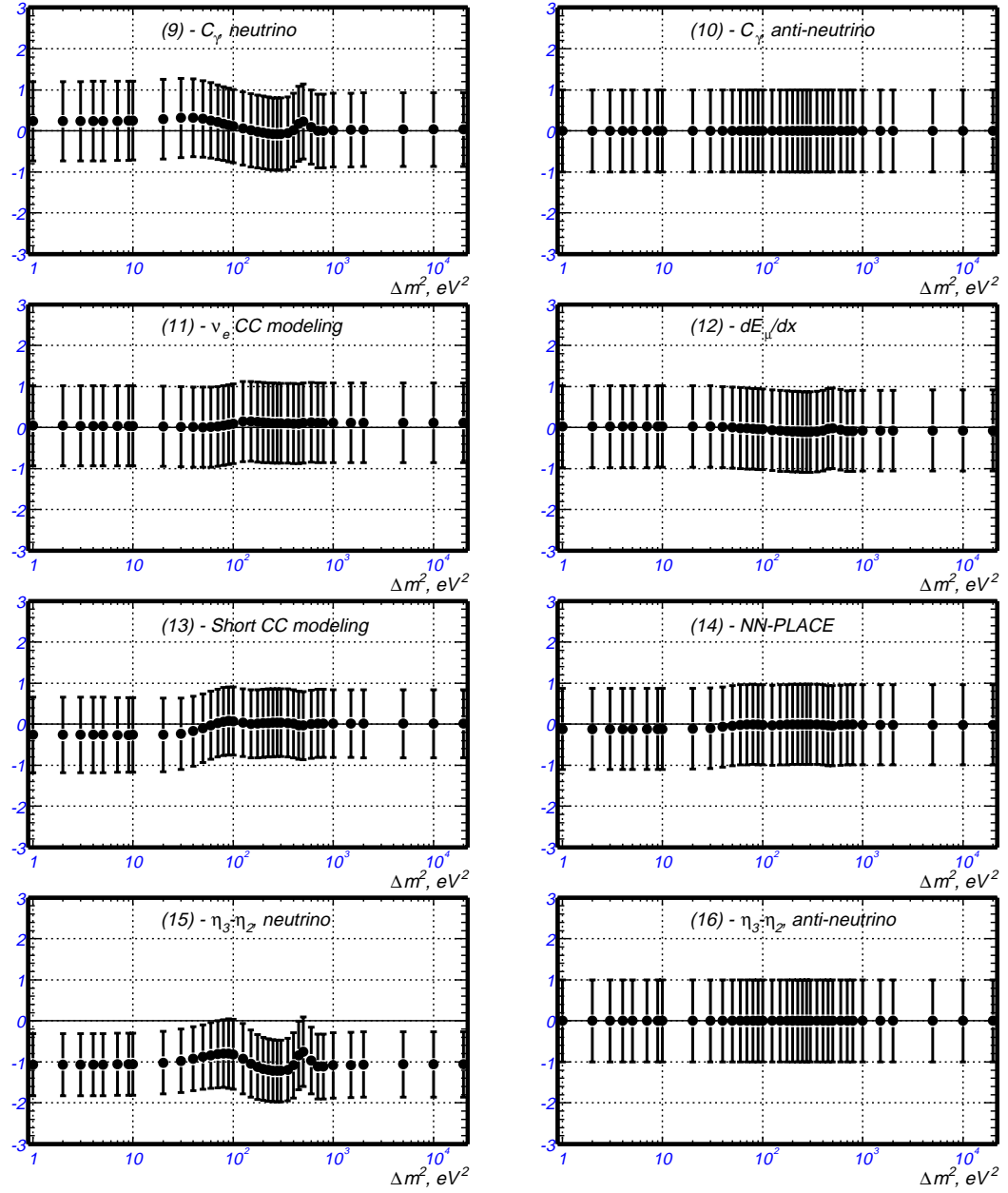


Figure 8.5: Oscillation parameter fits in neutrino mode: Values of the systematic coefficients C_9 through C_{16} after χ^2 minimization.

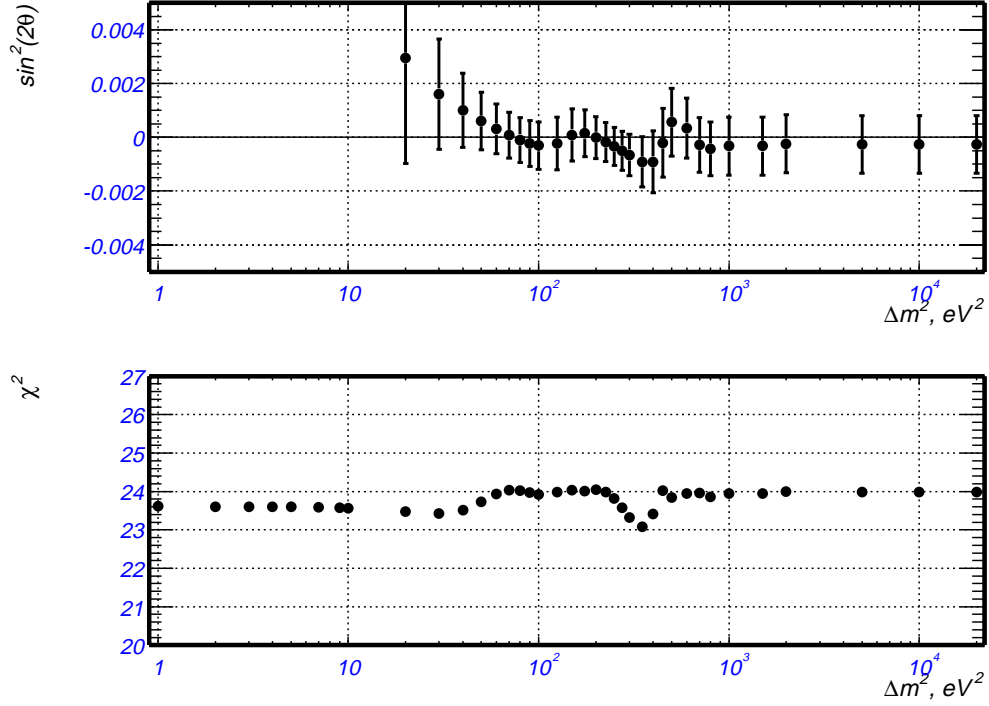


Figure 8.6: Oscillation parameter fits in anti-neutrino mode: Top plot - best fit $\sin^2 2\theta$; Bottom plot - χ^2 at the minimum.

tion function for the combined analysis $\chi_{combined}^2$ becomes

$$\chi_{combined}^2 = \chi_{neutrino}^2(\sin^2 2\theta, C_i) + \chi_{anti-neutrino}^2(\sin^2 2\theta, C_i) \quad (8.6)$$

where both $\chi_{neutrino}^2$ and $\chi_{anti-neutrino}^2$ are calculated according to equation (8.5).

The results of the oscillation parameter fits for the combined analysis are presented in Table 8.3 and in Figure 8.10. The sensitivity and excluded region are shown in Figure 8.11.

The values of the systematic coefficients C_i after the χ^2 minimization procedure are shown in Figures 8.12 and 8.13.

$\Delta m^2, eV^2$	$\sin^2(2\theta)$	1σ	<i>Sensitivity</i>	90% <i>CL</i>
1	0.9789	0.936	1.198	2.177
2	0.2453	0.2336	0.2991	0.5444
3	0.1094	0.1043	0.1334	0.2429
4	0.0619	0.05886	0.07534	0.1372
5	0.03989	0.03783	0.04843	0.08832
7	0.02072	0.01951	0.02497	0.04569
9	0.01283	0.01197	0.01533	0.02816
10	0.01054	0.009785	0.01252	0.02306
20	0.003161	0.00275	0.003521	0.006682
30	0.001721	0.001438	0.00184	0.003562
40	0.001136	0.0009676	0.001239	0.002375
50	0.0008101	0.0007544	0.0009656	0.001776
60	0.0005991	0.0006525	0.0008352	0.001434
70	0.0004471	0.0006094	0.0007801	0.001227
80	0.0003273	0.0006016	0.0007701	0.001097
90	0.0002269	0.0006164	0.0007889	0.001016
100	0.0001432	0.0006442	0.0008246	0.0009677
125	4.66×10^{-5}	0.0007098	0.0009086	0.0009552
150	8.382×10^{-5}	0.0006887	0.0008815	0.0009653
175	4.495×10^{-5}	0.000607	0.000777	0.0008219
200	-6.145×10^{-5}	0.000531	0.0006797	0.0006182
225	-0.0001621	0.000483	0.0006183	0.0004561
250	-0.0002497	0.0004627	0.0005923	0.0003426
275	-0.0003297	0.000466	0.0005965	0.0002667
300	-0.0004014	0.0004949	0.0006335	0.0002321
350	-0.0005012	0.0005951	0.0007617	0.0002605
400	-0.0003818	0.0007669	0.0009817	0.0005999
450	0.0003058	0.0009112	0.001166	0.001472
500	0.000887	0.0009107	0.001166	0.002053
600	0.0004327	0.0007688	0.0009841	0.001417
700	-0.000139	0.0006797	0.0008701	0.0007311
800	-0.0001938	0.0006693	0.0008566	0.0006628
1000	-0.0001184	0.0007281	0.0009319	0.0008136
1500	-9.789×10^{-5}	0.0007191	0.0009204	0.0008225
2000	-4.064×10^{-5}	0.0007309	0.0009355	0.0008949
5000	-4.181×10^{-5}	0.0007288	0.0009329	0.000891
10000	-4.181×10^{-5}	0.0007288	0.0009329	0.000891
20000	-4.203×10^{-5}	0.000728	0.0009318	0.0008898

Table 8.3: Oscillation parameter fits from a combined analysis of data in neutrino and anti-neutrino modes: Δm^2 , central value of $\sin^2 2\theta$, 1σ error, sensitivity, 90% *CL* upper limit.

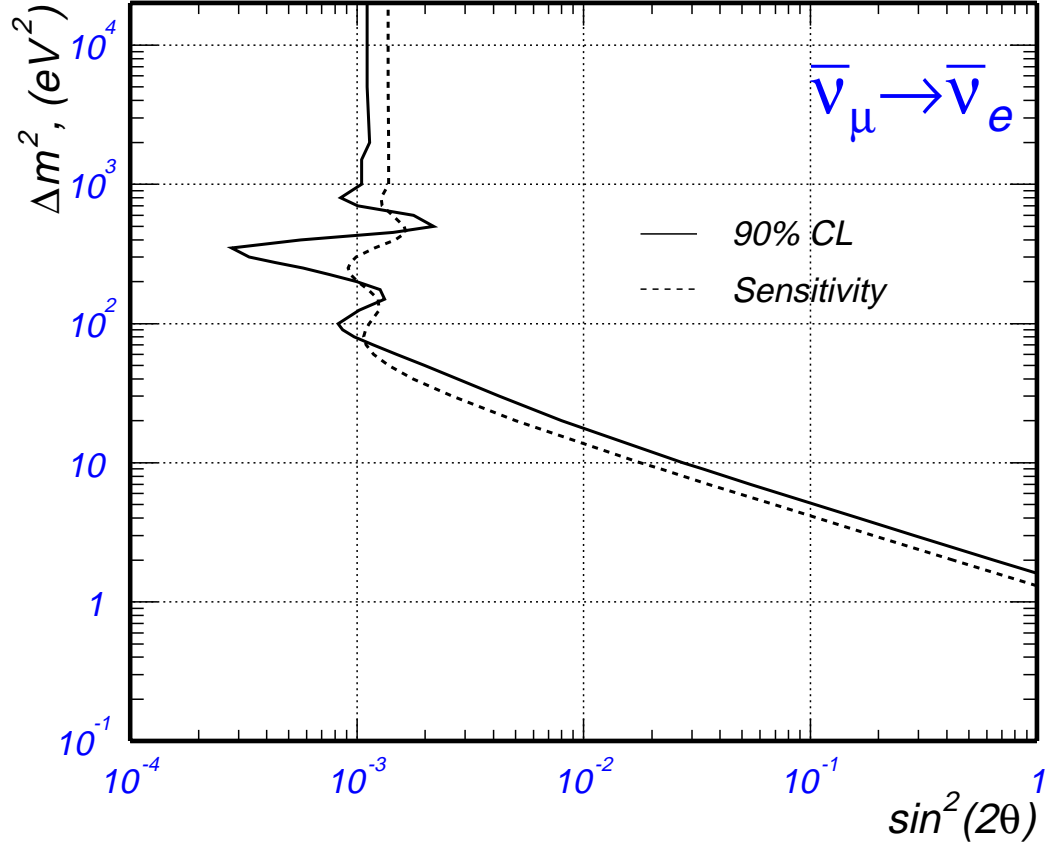


Figure 8.7: Sensitivity and upper limits at 90% confidence level for $\bar{\nu}_\mu \rightarrow \bar{\nu}_e$ oscillations. The excluded region of $\sin^2(2\theta)$ and Δm^2 is the area to the right of the solid curve.

8.2.5 Comparison with other oscillation search experiments

The results of the analysis described in this thesis can be compared with other oscillation experiments that are sensitive to $\nu_\mu \rightarrow \nu_e$ oscillations in the high Δm^2 region ([15]-[19]). These comparisons are shown in Figures 8.14 ($\nu_\mu \rightarrow \nu_e$ search experiments), 8.15 ($\bar{\nu}_\mu \rightarrow \bar{\nu}_e$ search experiments). The limits from the combined analysis are compared to the the results from other experiments in Figure 8.16.

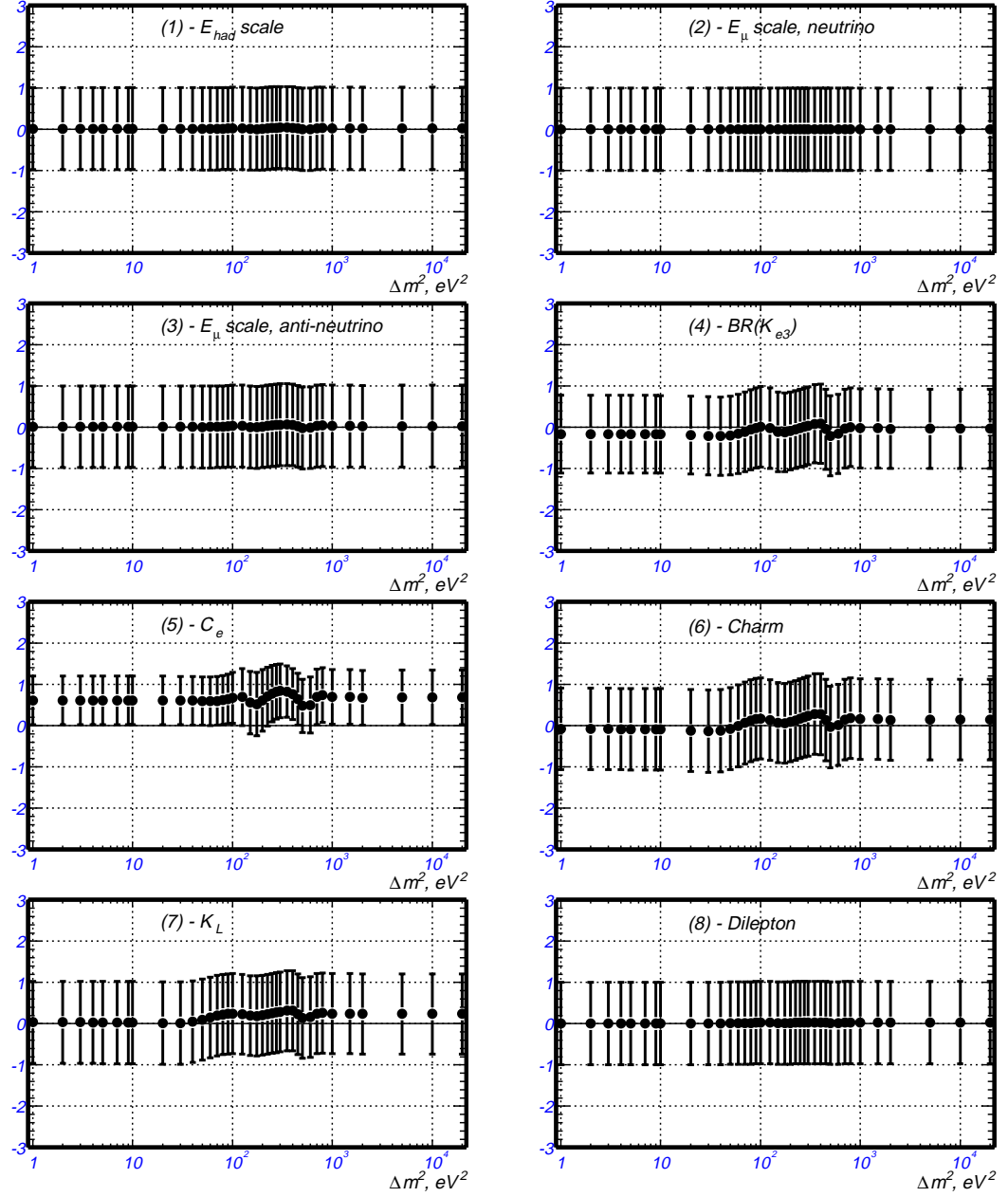


Figure 8.8: Oscillation parameter fits in anti-neutrino mode: Values of the systematic coefficients C_1 through C_8 after χ^2 minimization.

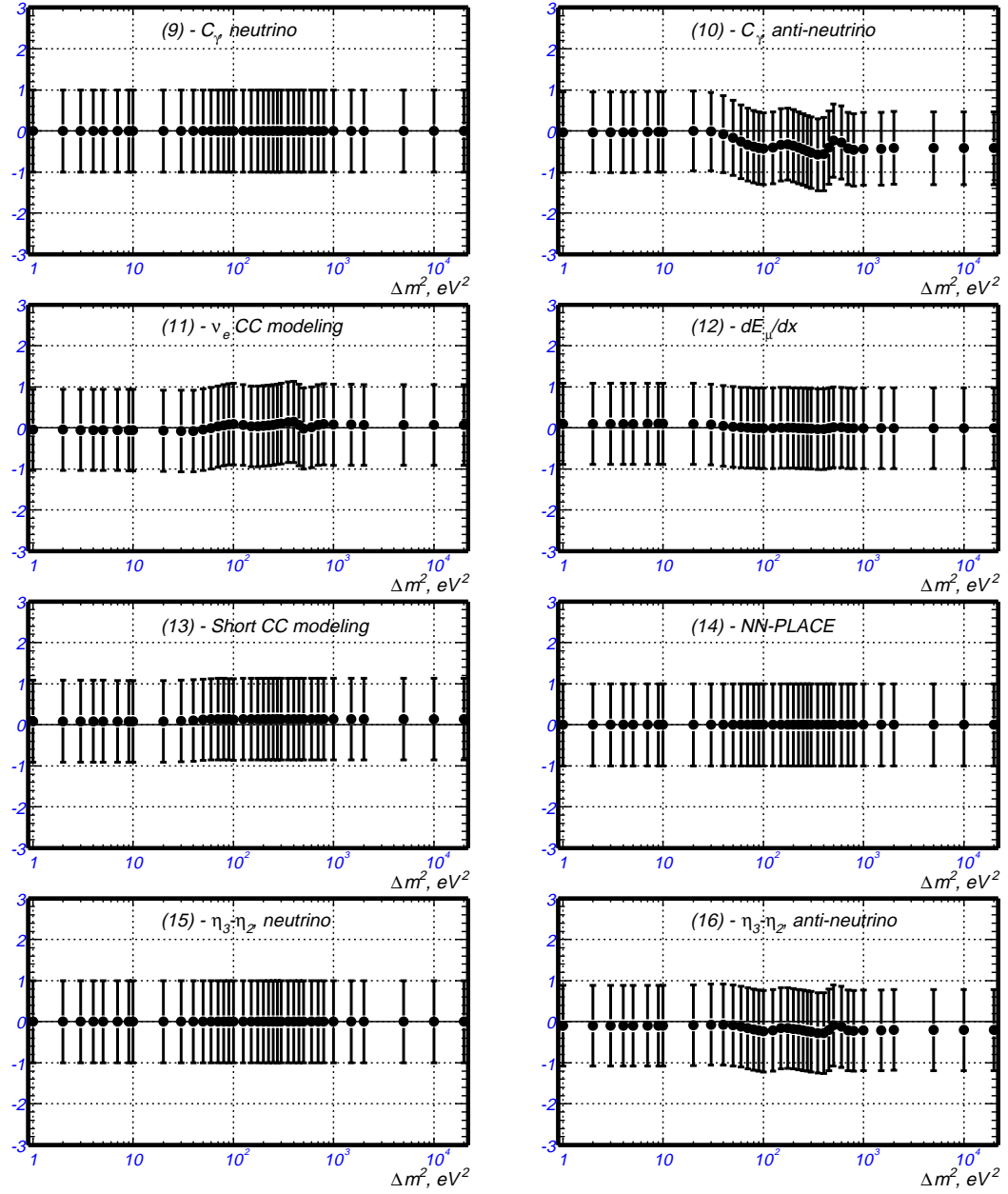


Figure 8.9: Oscillation parameter fits in anti-neutrino mode: Values of the systematic coefficients C_9 through C_{16} after χ^2 minimization.

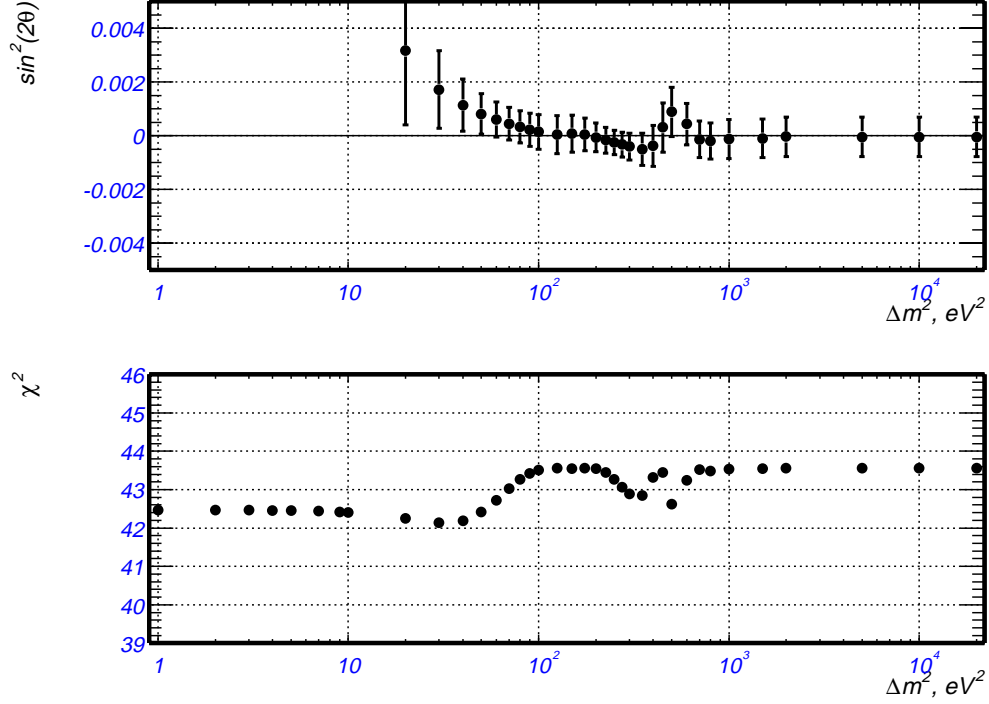


Figure 8.10: Oscillation parameter fits in neutrino and anti-neutrino modes combined: Top plot - best fit $\sin^2 2\theta$; Bottom plot - χ^2 at the minimum.

8.3 Conclusions

We report the result of a search for $\nu_\mu \rightarrow \nu_e$, $\bar{\nu}_\mu \rightarrow \bar{\nu}_e$ oscillations at the NuTeV experiment at Fermilab. The search was done by comparing the direct measurement of the ν_e flux using a sample of neutrino interactions in the NuTeV target-calorimeter with the prediction from the Monte Carlo. In the measurement of ν_e flux we have made use of the difference in the longitudinal shower energy profile of $\nu_e N$ versus $\nu_\mu N$ interactions, as measured in a coarse-grained calorimetric detector. Our results are consistent with no oscillations in $\nu_\mu \rightarrow \nu_e$ and in $\bar{\nu}_\mu \rightarrow \bar{\nu}_e$ for our region of sensitivity, and we present 90% confidence-level exclusion regions in

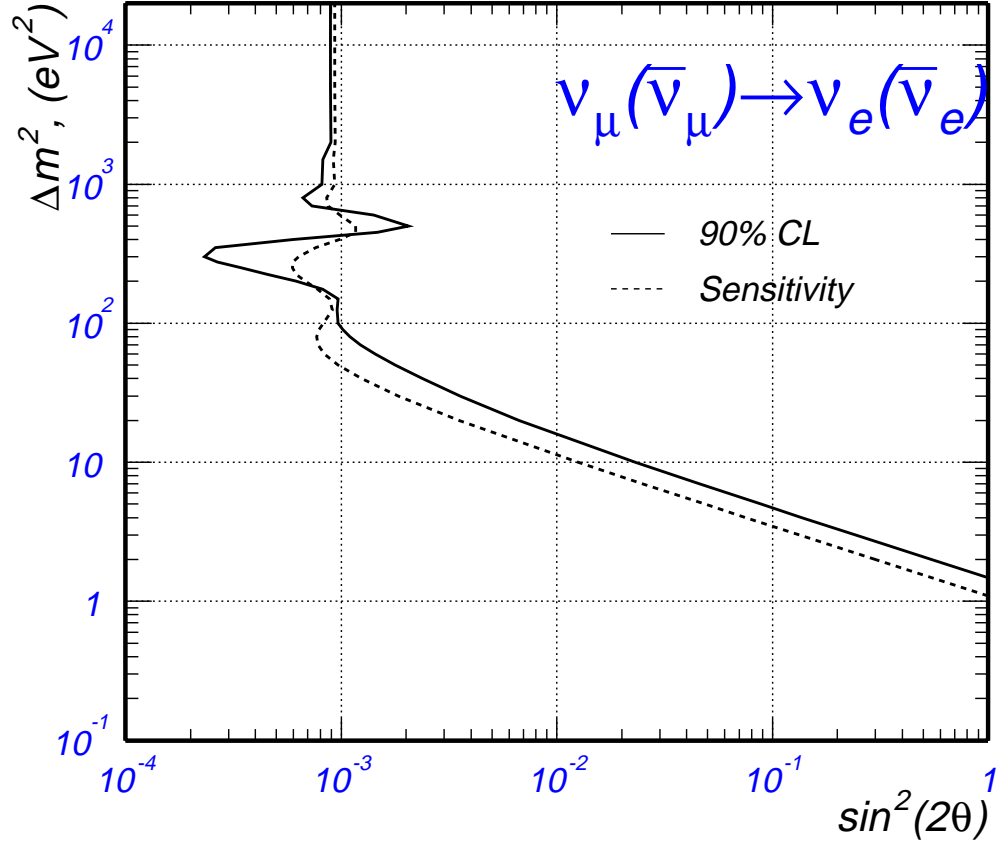


Figure 8.11: Sensitivity and upper limits at 90% confidence level for the combined data for $(\nu_\mu, \bar{\nu}_\mu) \rightarrow (\nu_e, \bar{\nu}_e)$ oscillations. The excluded region of $\sin^2(2\theta)$ and Δm^2 is the area to the right of the solid curve.

the $(\sin^2(2\theta), \Delta m^2)$ parameter space. These results are the most stringent limits on $\nu_\mu \rightarrow \nu_e$ and $\bar{\nu}_\mu \rightarrow \bar{\nu}_e$ oscillations in the high- Δm^2 region ($\Delta m^2 > 50 \text{ eV}^2$). In addition, we perform a combined analysis of both neutrino and anti-neutrino data and search for CP invariant oscillations. The combined analysis improves by a factor of 2 the limits previously reported by the CCFR experiment (using the same detector), for $\nu_\mu(\bar{\nu}_\mu) \rightarrow \nu_e(\bar{\nu}_e)$ oscillations.

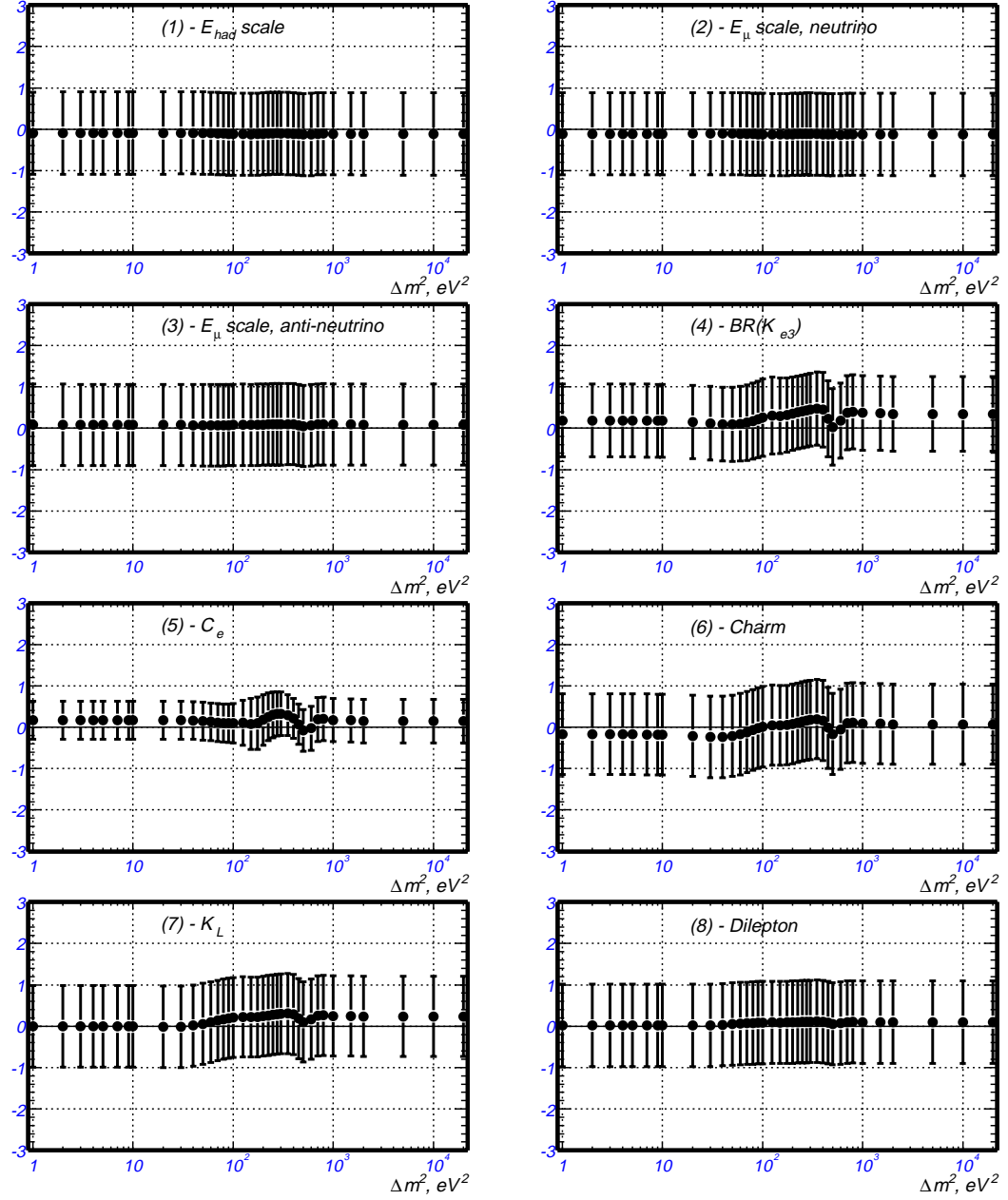


Figure 8.12: Oscillation parameter fits in neutrino and anti-neutrino modes combined: Values of the systematic coefficients C_1 through C_8 after χ^2 minimization.

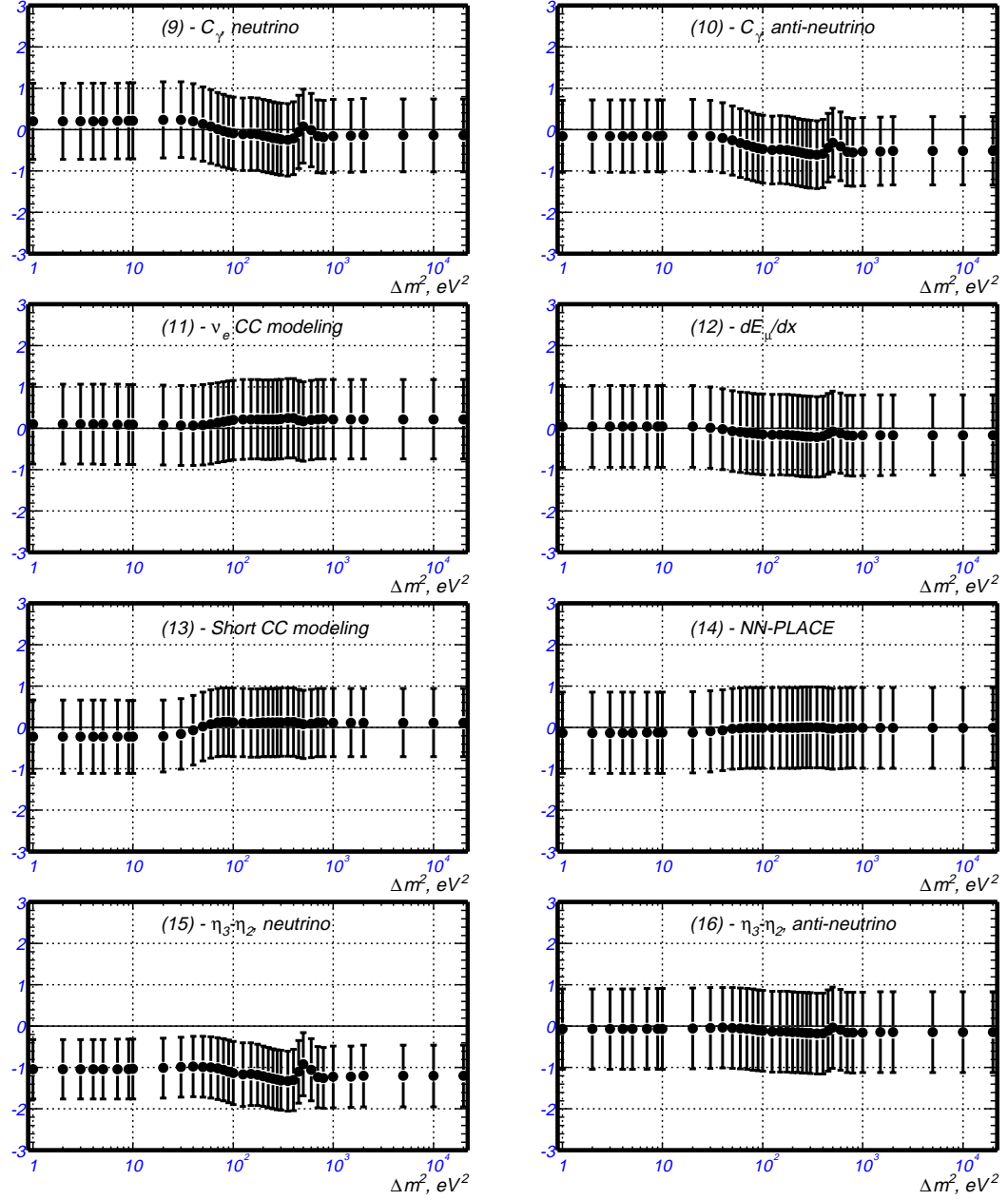


Figure 8.13: Oscillation parameter fits in neutrino and anti-neutrino modes combined: Values of the systematic coefficients C_9 through C_{16} after χ^2 minimization.

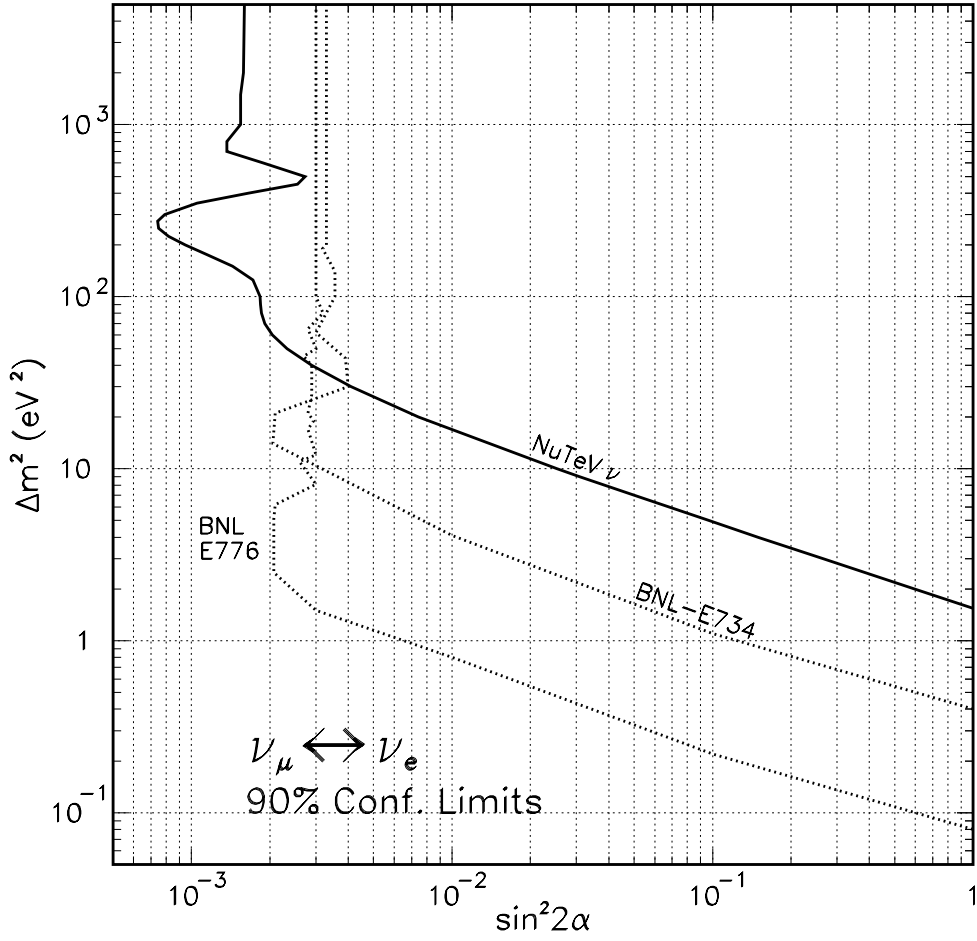


Figure 8.14: Sensitivity and upper limits at 90% confidence level for $\nu_\mu \rightarrow \nu_e$ oscillations compared to data from other experiments. The excluded region of $\sin^2(2\theta)$ and Δm^2 is the area to the right of the solid curve.

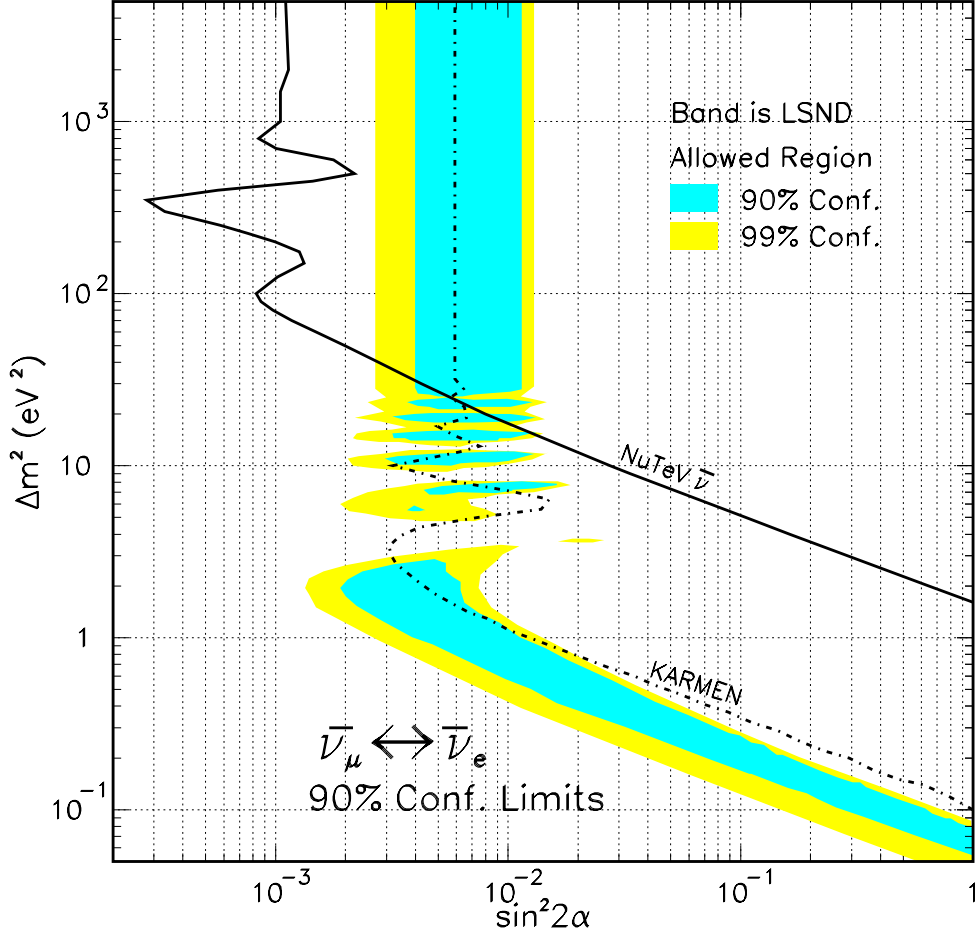


Figure 8.15: Sensitivity and upper limits at 90% confidence level for $\bar{\nu}_\mu \rightarrow \bar{\nu}_e$ oscillations compared to data from other experiments. The excluded region of $\sin^2(2\theta)$ and Δm^2 is the area to the right of the solid curve.

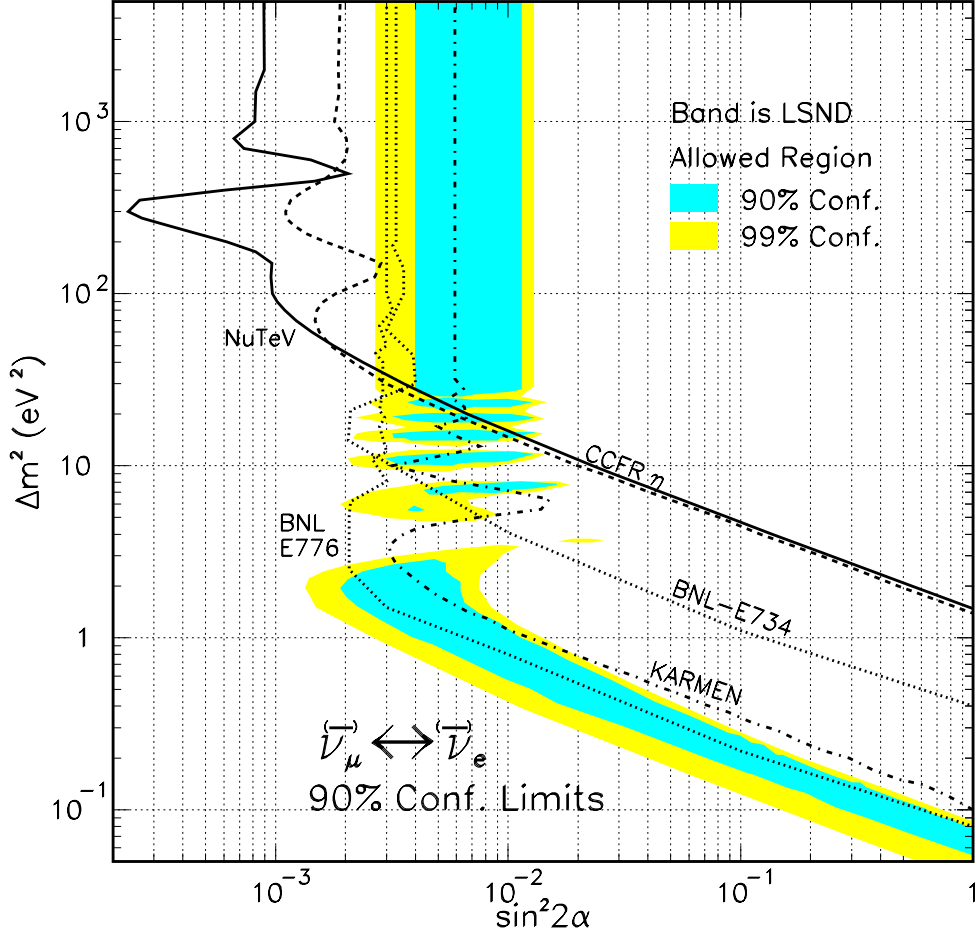


Figure 8.16: Sensitivity and upper limits at 90% confidence level for the combined data for $(\nu_\mu, \bar{\nu}_\mu) \rightarrow (\nu_e, \bar{\nu}_e)$ oscillations compared to data from other experiments. The excluded region of $\sin^2(2\theta)$ and Δm^2 is the area to the right of the solid curve.

Bibliography

- [1] B. Pontecorvo, Zh. Exp. Teor. Fiz. **33**, 549 (1957) [Sov. Phys. JETP **6**, 429 (1958)].
- [2] Z. Maki, M. Nakagawa and S. Sakata, Prog. Theor. Phys. **28**, 870 (1962).
- [3] B. Pontecorvo, Zh. Exsp. Teor. Fiz. **53**, 1717 (1967) [Sov. Phys. JETP **26**, 984 (1968)].
- [4] V. Gribov and B. Pontecorvo, Phys. Lett. B **28**, 493 (1969).
- [5] S.M. Bilenky and B. Pontecorvo, Phys. Lett. B **61**, 248 (1976).
- [6] S.M. Bilenky and B. Pontecorvo, Lett. Nuovo Cim. **17**, 569 (1976).
- [7] R. Davis, Prog. Part. Nucl. Phys. **32**, 13 (1994).
- [8] K.S. Hirata *et al.*, Kamiokande Coll., Phys. Rev. Lett. **77**, 1683 (1996).
- [9] W. Hampel *et al.*, GALLEX Coll., Phys. Lett. B **388**, 384 (1996).
- [10] D.N. Abdurashitov *et al.*, SAGE Coll., Phys. Rev. Lett. **77**, 4708 (1996).
- [11] Y. Fukuda *et al.*, Super-Kamiokande Coll., Phys. Rev. Lett. **81**, 1158 (1998).
- [12] R. Becker-Szendy *et al.*, IMB Coll., Nucl. Phys. B (Proc. Suppl.) **38**, 331 (1995).

- [13] W.W.M. Allison *et al.*, Soudan-2 Coll., Phys. Let. B **391**, 491 (1997).
- [14] M. Ambrosio *et al.*, MACRO Coll., Phys. Lett. B **434**, 451 (1998).
- [15] L. A. Ahrens *et al.* , Phys. Rev. **D36**, 702 (1987).
- [16] L. Borodovsky *et al.* , Phys. Rev. Lett. **68**, 274 (1992).
- [17] B.A. Bodmann *et al.*, Nucl. Phys. **A553**, 831 (1993).
- [18] C. Athanassopoulos *et al.*, LSND Coll., Phys. Rev. Lett. **81**, 1774 (1998).
- [19] A. Romosan *et al.*, Phys. Rev. Lett. **78**, 2912 (1997).
- [20] S.M. Bilenky, C. Giunti, W. Grimus, Prog.Part.Nucl.Phys. **43**, 1 (1999).
- [21] P. Fisher, B. Kayser, K.S. McFarland, Annu. Rev. Nucl. Part. Sci. **49**, 481 (1999).
- [22] J.M.Conrad, M.H.Shaevitz, T.Bolton, Reviews of Modern Physics **70**, No.4 (1998).
- [23] David C. Carey, Karl L. Brown, F.C. Iselin, SLAC-0246, Mar 1982
- [24] H.W. Atherton *et al.*, CERN 80-07 (1980).
- [25] A.J. Malensek, FERMILAB-FN-0341 (1981).
- [26] N.J. Baker *et al.*, Physical Review D, Vol. 41, 9 (1990)
- [27] NuTeV Proposal
- [28] A Precise Determination of Electroweak Parameters in Neutrino Nucleon Scattering. By NuTeV Collaboration (G.P. Zeller et al.). FERMILAB-PUB-01-341-E, Oct 2001. 5pp. Submitted to Phys.Rev.Lett.

- [29] H. Fesefeldt, PITHA 85/02 (Aachen 1985).
- [30] A. Fasso, A. Ferrari, J. Ranft and P. R. Sala, Proc. IV INT. Conf. on Calorimetry in High Energy Physics, La Biodola (Is. d'Elba), Sep. 20–25, 1993 Ed A. Menzione and A. Scribano, World Scientific, p 493.
- [31] C. Zeitnitz and T.A. Gabriel, Nucl. Instr. Meth., **A349**, 106 (1994).
- [32] G. Ingelman, A. Edin and J. Rathsman, Computer Physics Communications 101 (1997) 108-134
- [33] CERN CN/ASD, MINUIT, CERN Program Library Long Writeups D506, CERN 1995
- [34] D. Harris, J. Yu *et al.*, NuTeV Coll., To be published in Nucl. Instrum. Methods A (2000).
- [35] GEANT Detector Description and Simulation Tool, CERN Program Library Long Writeup W5013.
- [36] T. Sjöstrand, Comput. Phys. Commun. **82** , 74 (1994).
- [37] A. Romosan, Doctoral Dissertation, Columbia U, R-1536, CU-402, Nevis-296
- [38] G. Zeller, Doctoral Dissertation, Northwestern U
- [39] U. K. Yang, Doctoral Dissertation, U of Rochester
- [40] A.J. Buras and K.J.F. Gaemers, Nucl. Phys. B132, 1978(249)
- [41] D.Yu. Bardin and V.A. Dokuchaeva, JINR-E2-86-260 (1986)
- [42] R. J. Barlow and S. Wolfram, Phys.Rev.D20:2198,1979

- [43] A. De Rujula, R. Petronzio, A. Savoy-Navarro, Nucl.Phys.B154:394,1979

Appendix A

Shower Length Analysis

The method of the direct measurement of the ν_e flux described in this thesis relies on the difference in the longitudinal energy deposition in the NuTeV calorimeter between hadronic and electromagnetic showers. This method uses the distributions of the variable η_3 (defined by Equation 4.1). An analogous analysis is also performed using the distributions of the η_2 parameter (Equation 7.4) and the η_2 results have been used to estimate the systematic error in this measurement. As an additional consistency check we also perform the analysis using the distributions of the event shower length L_{shower} . We define shower length as the number of counters in the event with energy deposition consistent with that of a hadronic or electromagnetic shower. The start of the shower (counter *PLACE*) is defined in Section 5.2.1; the end of the shower (counter *SHEND*) is defined as the most downstream counter in the event upstream of the three consecutive counters with energy deposition less than 3 *MIP* in each counter. The shower length is defined as:

$$L_{shower} = PLACE - SHEND + 1. \quad (\text{A.1})$$

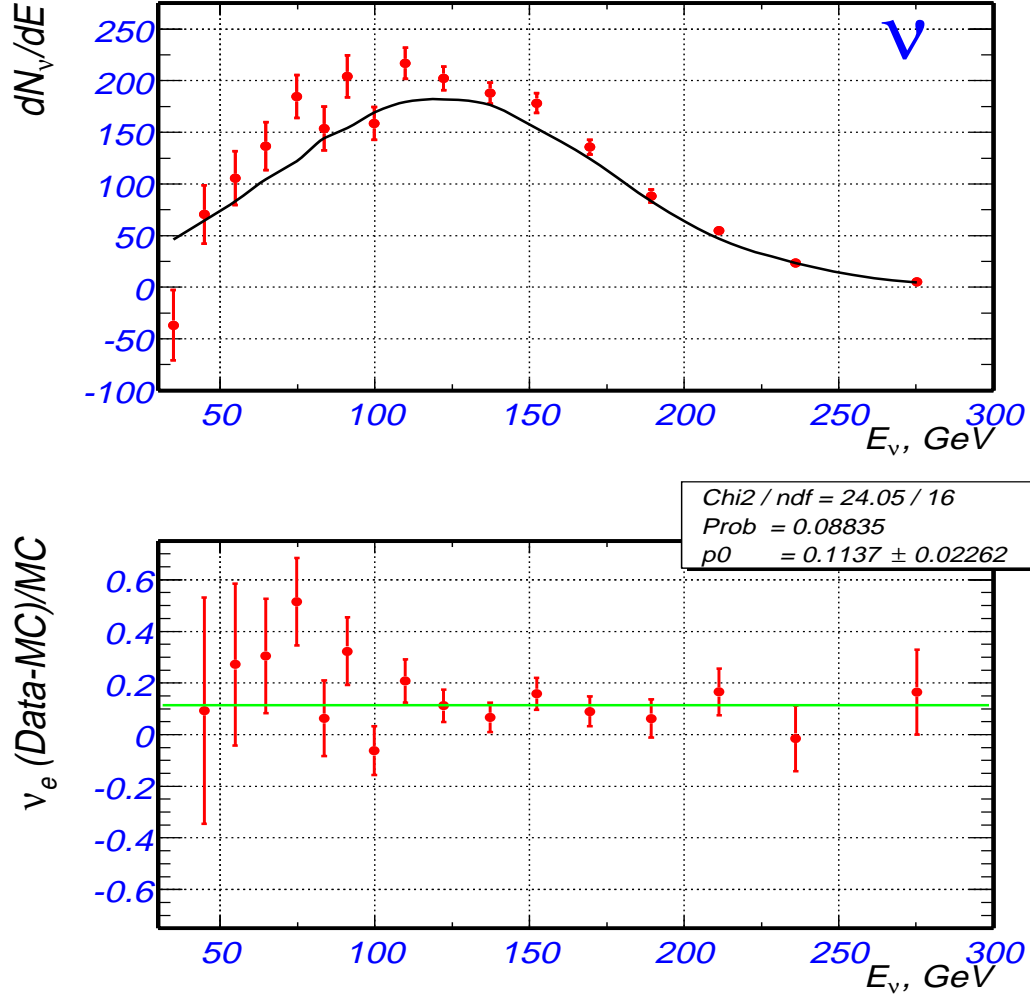


Figure A.1: Results of the analysis using the shower length distributions in neutrino mode. Top plot: ν_e flux. The beam Monte Carlo prediction (no oscillations) are shown as the solid line; the measurements using the shower length distributions are the circles. Bottom plot: The ratio $(\#\nu_e(\text{measured}) - \#\nu_e(\text{MC}))/\#\nu_e(\text{MC})$.

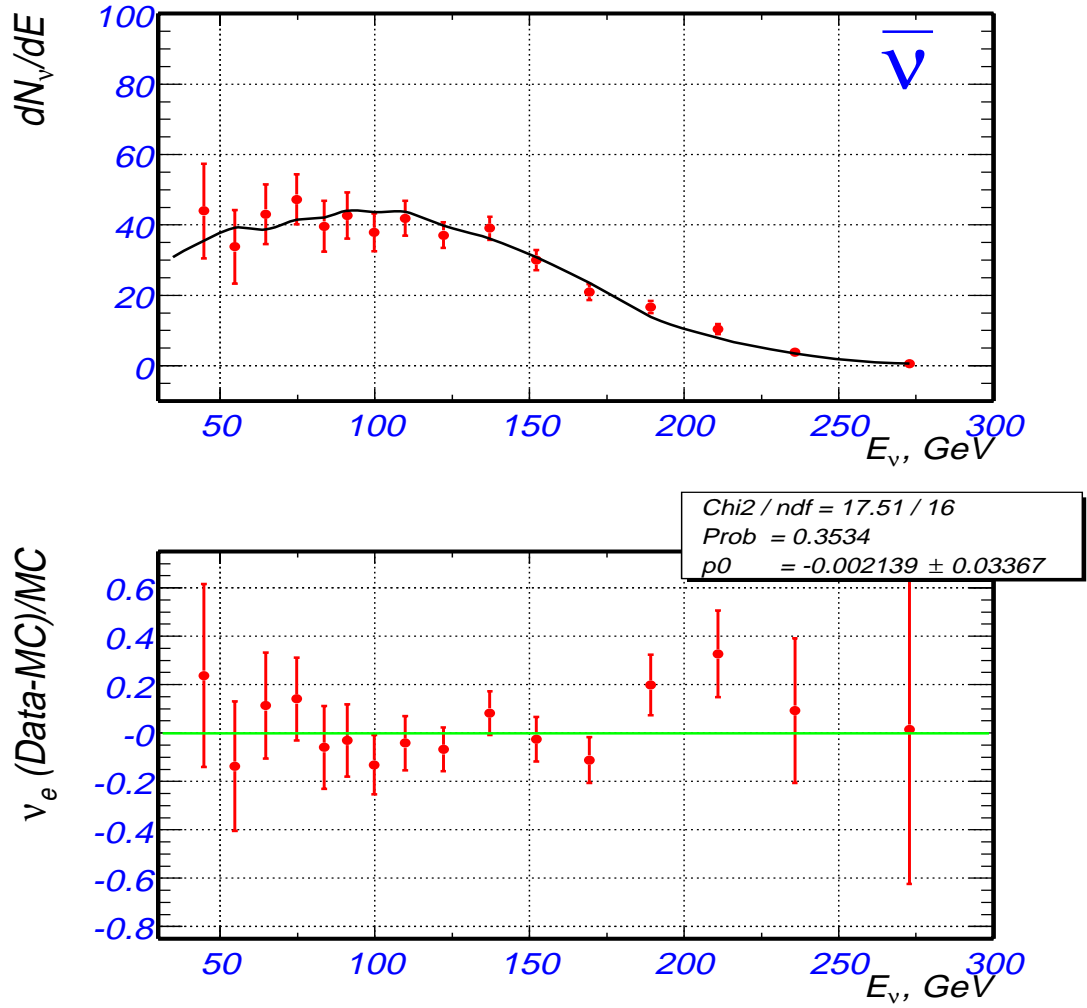


Figure A.2: Result of the analysis of shower length distributions in anti-neutrino mode. Top plot: $\bar{\nu}_e$ flux. The beam Monte Carlo prediction (no oscillations) are shown as the solid line; the measurements using the shower length distributions are the circles. Bottom plot: The ratio $(\#\bar{\nu}_e(\text{measured}) - \#\bar{\nu}_e(\text{MC}))/\#\bar{\nu}_e(\text{MC})$.

The ν_e flux is extracted by fitting the shower length distribution of the sample of short events with extra muon added in software as described in Section 4.2:

$$L_{shower}[Short + \mu] = \alpha L_{shower}[Long] + \beta L_{shower}[\nu_e CC + \mu] \quad (A.2)$$

$$+ C_1 L_{shower}[Short CC + \mu] + C_2 L_{shower}[Cosmic + \mu].$$

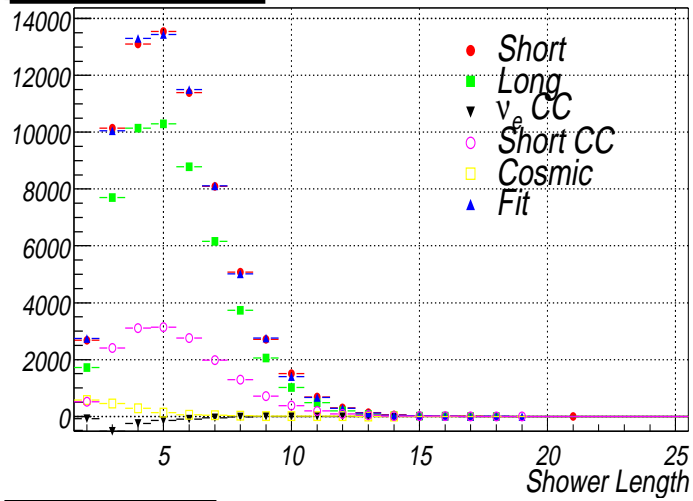
Corrections, based on Monte Carlo studies are applied to the values extracted from the fits of the shower length distributions. This is done in the same way as for the fits to the η_3 distributions as described in Section 7.2. The results of the measurements extracted from the shower length distributions (after all corrections have been applied) are shown in Figure A.1 (neutrino mode) and in Figure A.1 (anti-neutrino mode).

Another analysis in which the end of the shower (counter *SHEND*) is defined as the most downstream counter in the event upstream of last three consecutive counters with energy deposition less than 6 *MIP* (instead of 6 *MIP*) in each counter yields similar results.

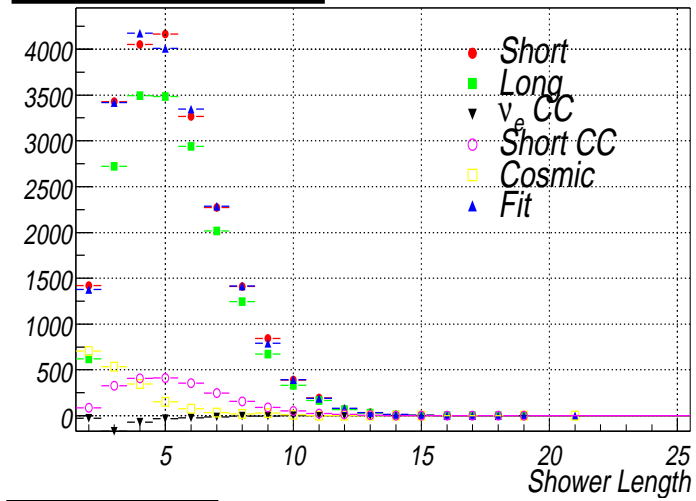
In anti-neutrino mode, there is an excellent agreement between the results of the shower length analysis and the η_3 analysis for. In neutrino-mode, the difference in results from the η_3 and L_{shower} analyses is consistent with the 2.25% systematic error in these measurements as determined from the difference between the results of the η_2 and η_3 analyses.

Graphical representations of the fits of the shower length distributions follow this Section.

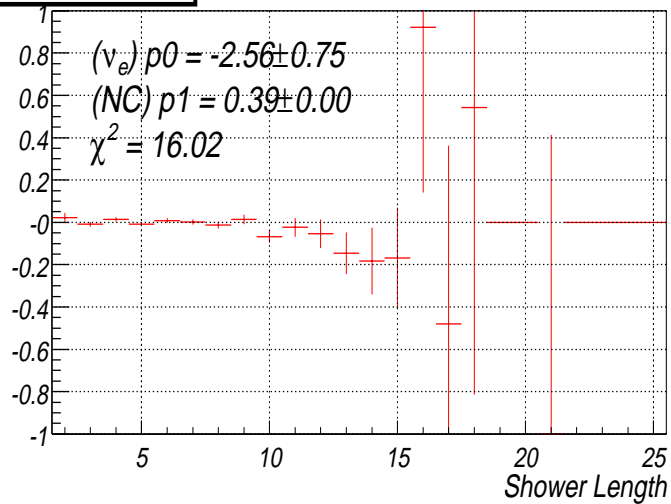
30-40 GeV, neutrino



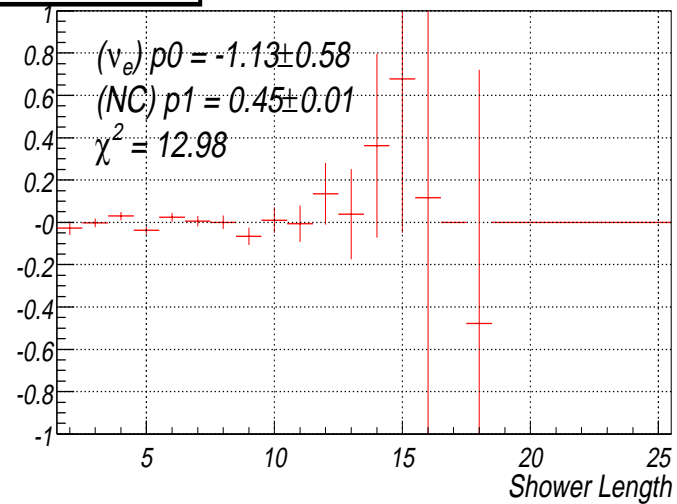
30-40 GeV, anti-neutrino



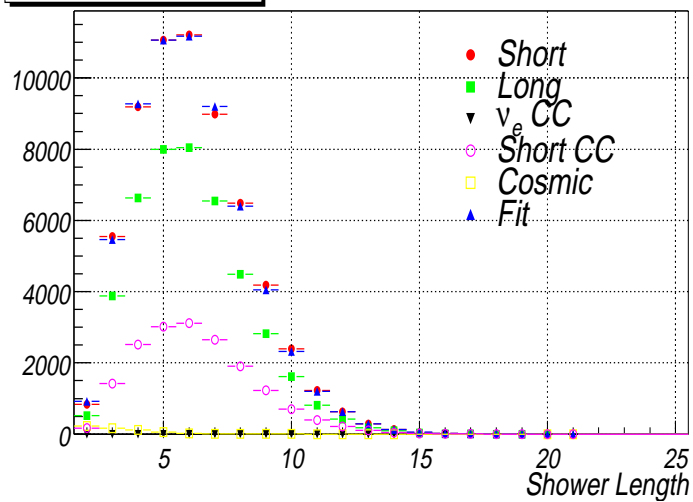
(Fit-Data)/Data



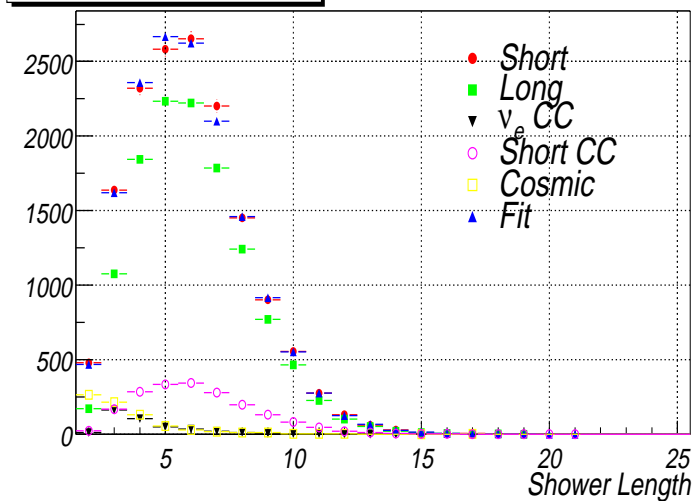
(Fit-Data)/Data



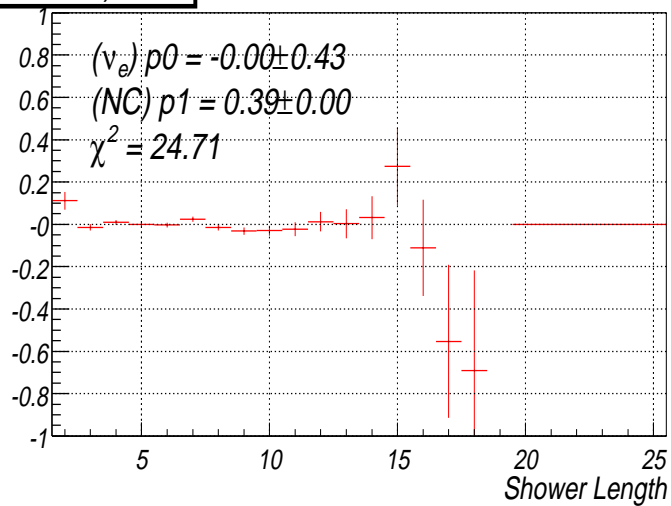
40-50 GeV, neutrino



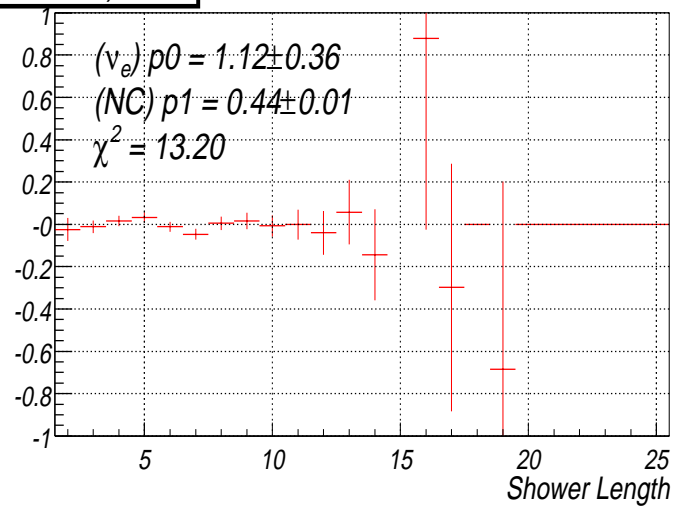
40-50 GeV, anti-neutrino



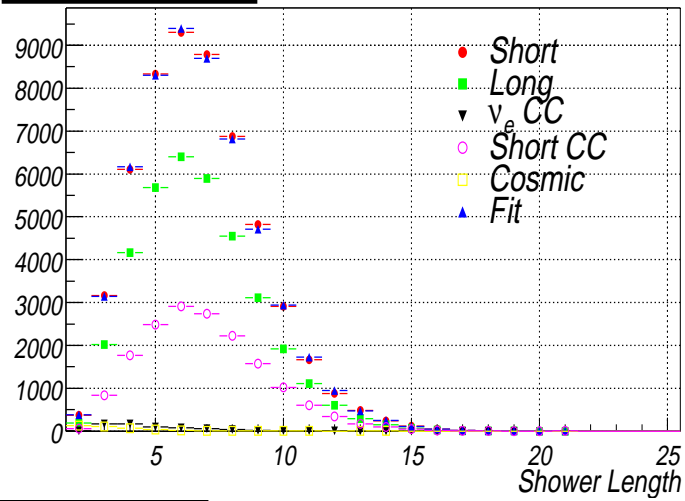
(Fit-Data)/Data



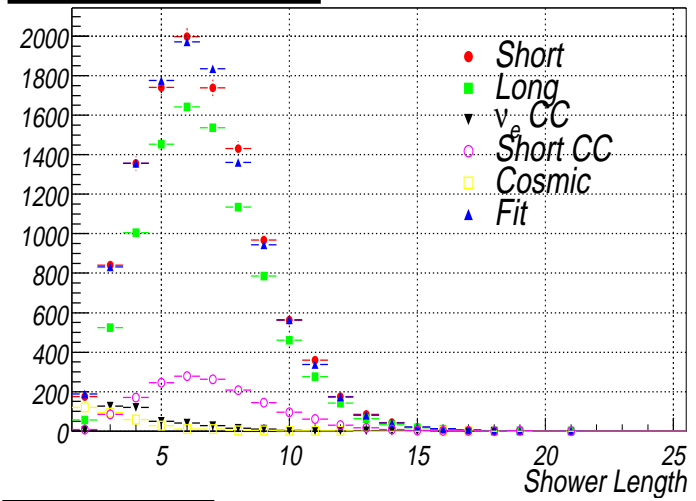
(Fit-Data)/Data



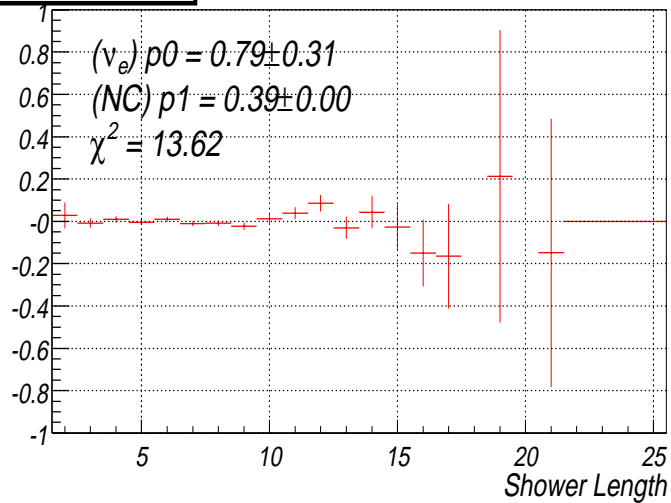
50-60 GeV, neutrino



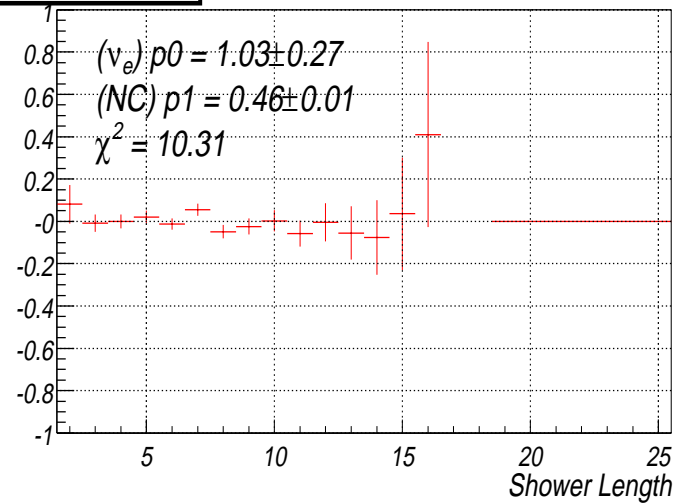
50-60 GeV, anti-neutrino



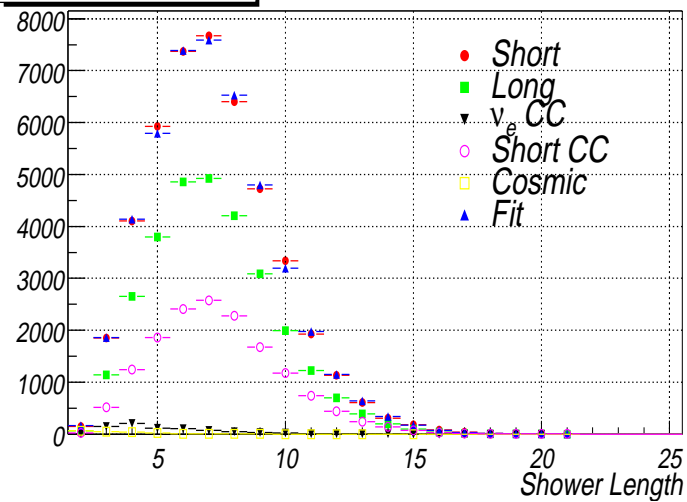
(Fit-Data)/Data



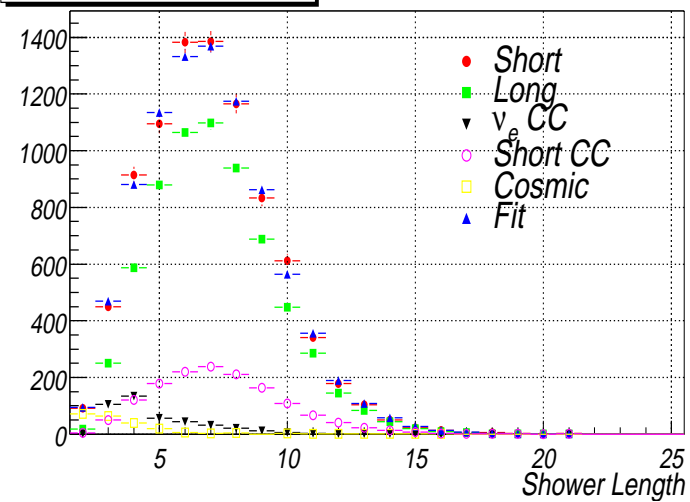
(Fit-Data)/Data



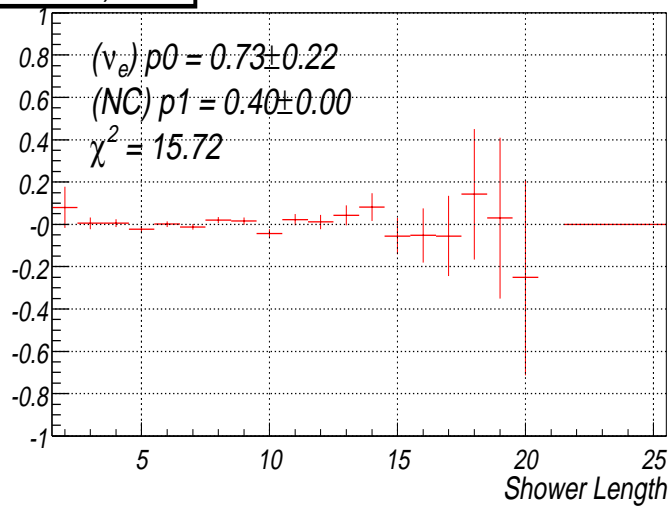
60-70 GeV, neutrino



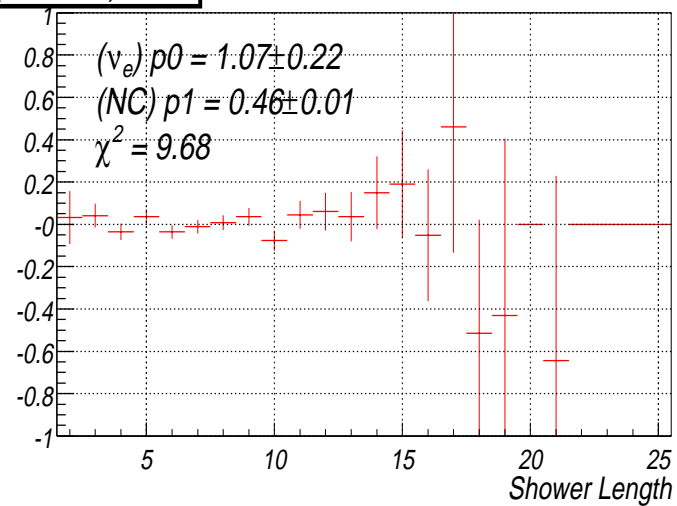
60-70 GeV, anti-neutrino



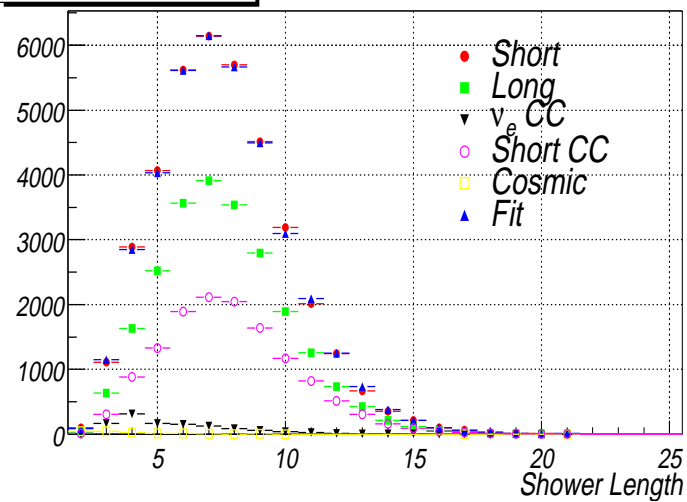
(Fit-Data)/Data



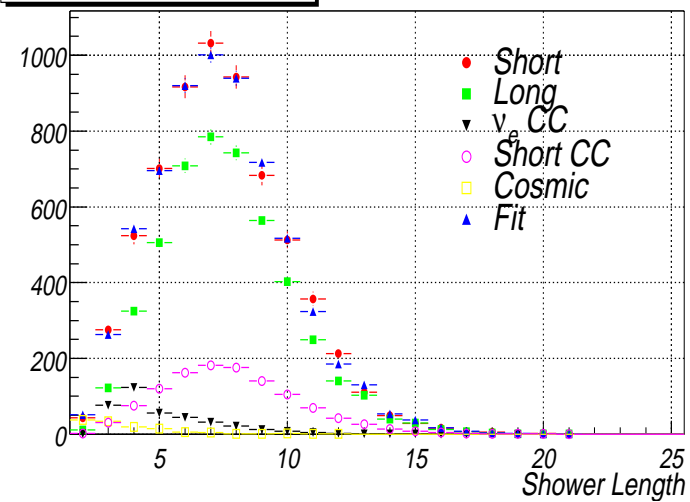
(Fit-Data)/Data



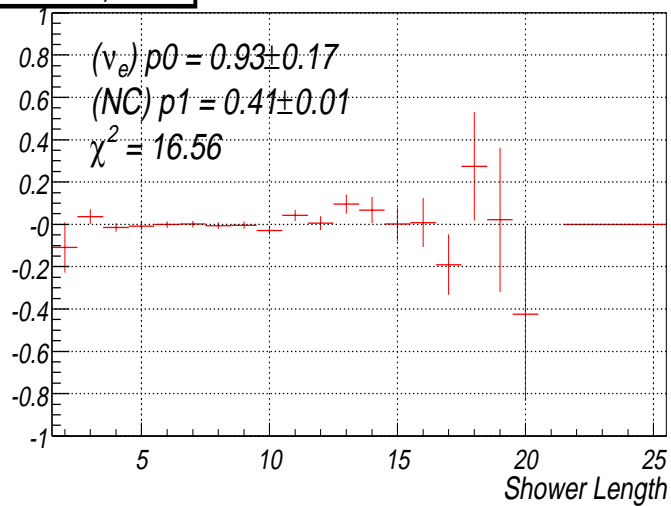
70-80 GeV, neutrino



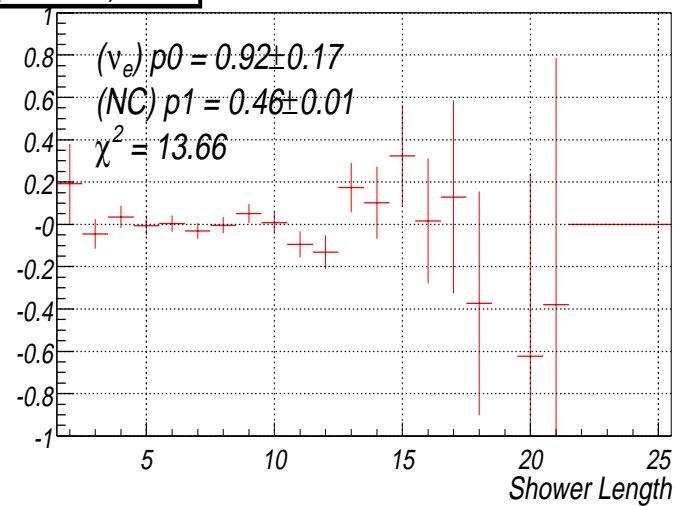
70-80 GeV, anti-neutrino



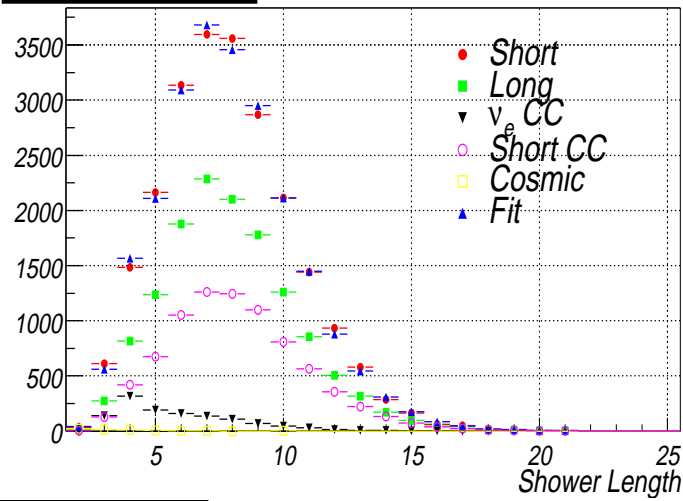
(Fit-Data)/Data



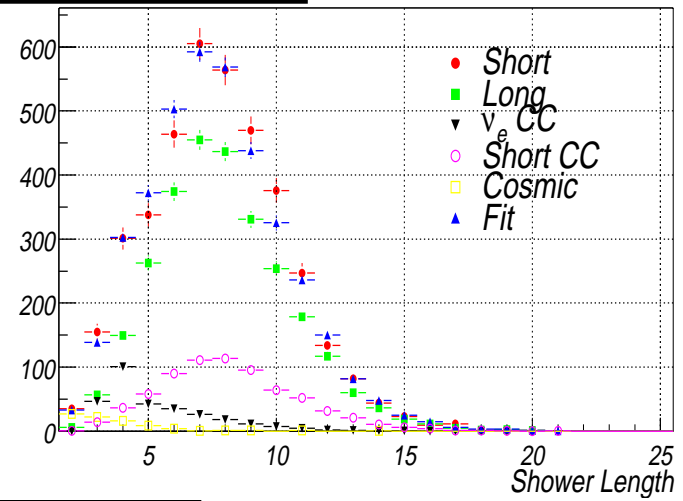
(Fit-Data)/Data



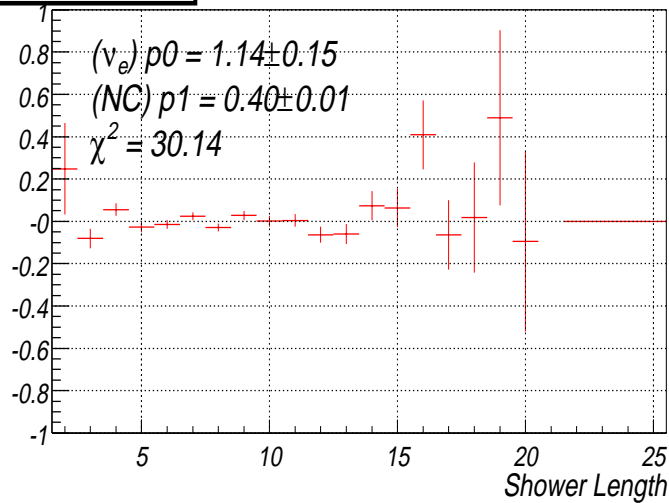
80-87 GeV, neutrino



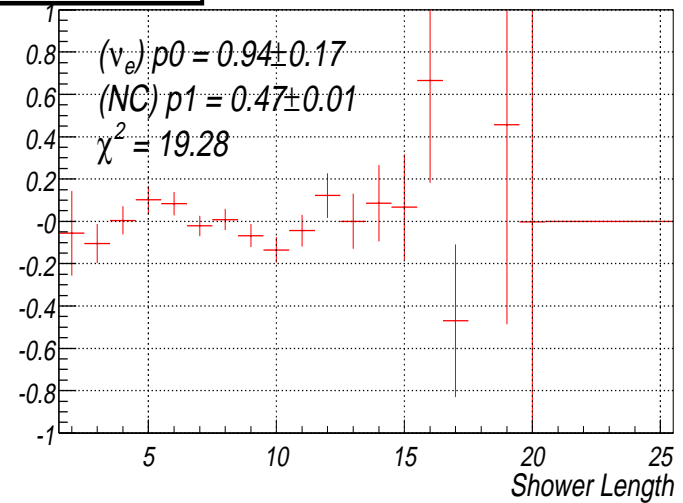
80-87 GeV, anti-neutrino



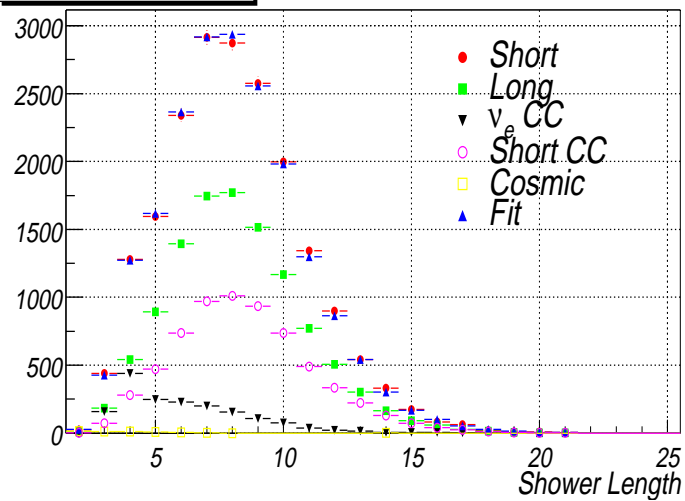
(Fit-Data)/Data



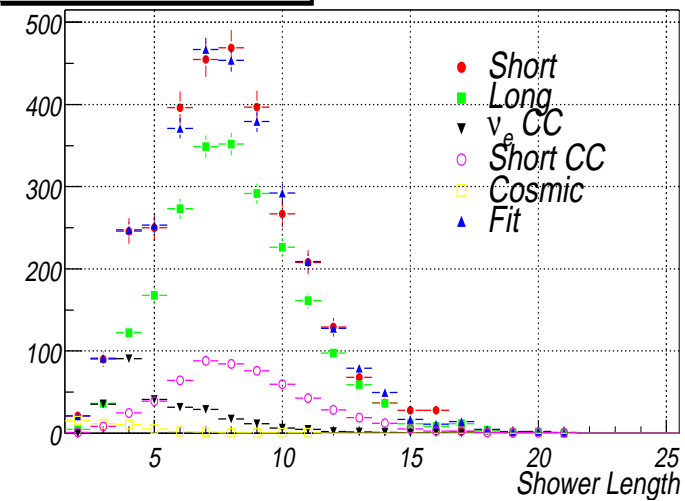
(Fit-Data)/Data



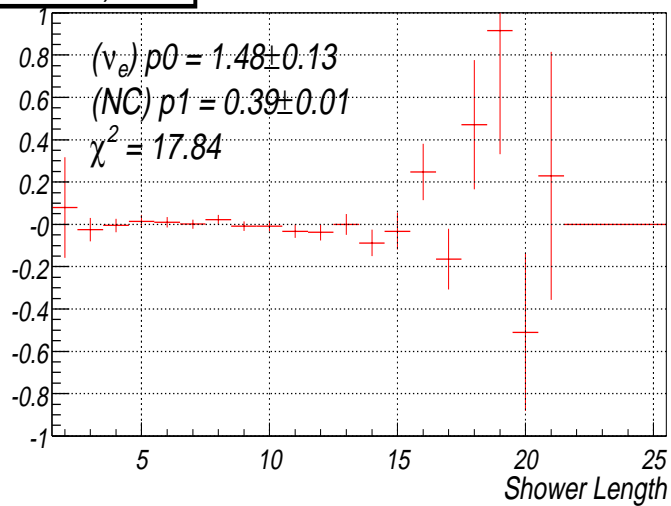
87-95 GeV, neutrino



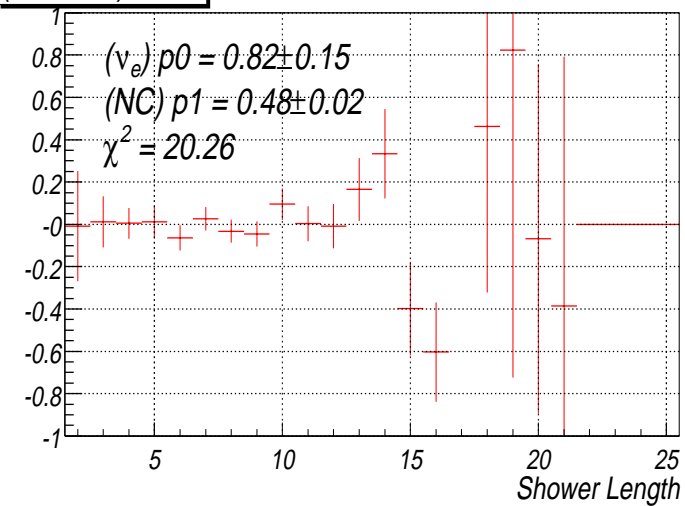
87-95 GeV, anti-neutrino



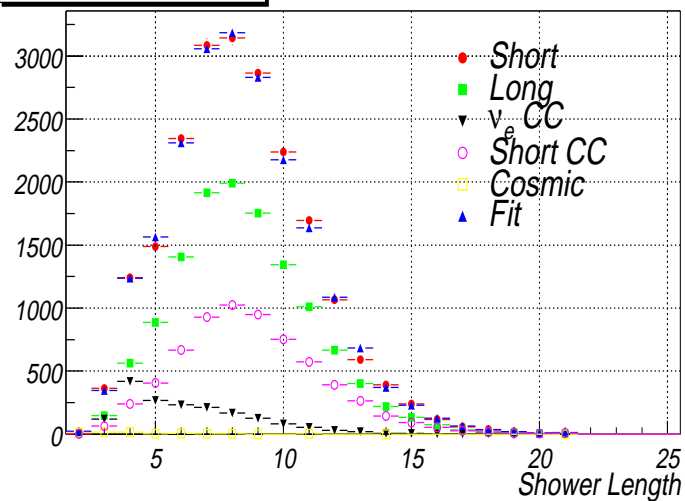
(Fit-Data)/Data



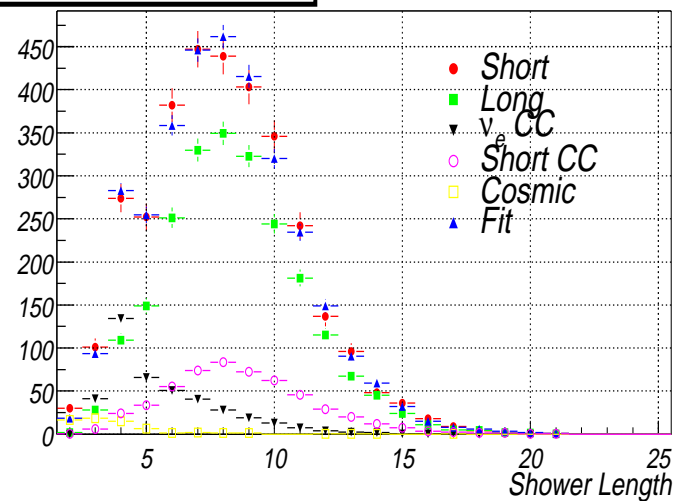
(Fit-Data)/Data



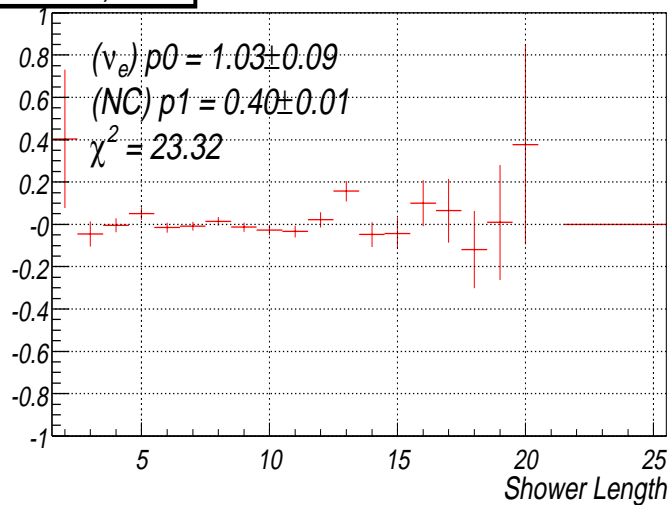
95-105 GeV, neutrino



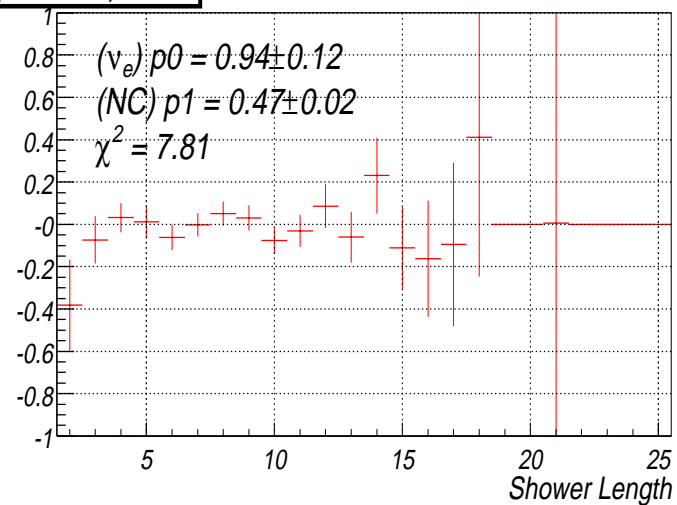
95-105 GeV, anti-neutrino



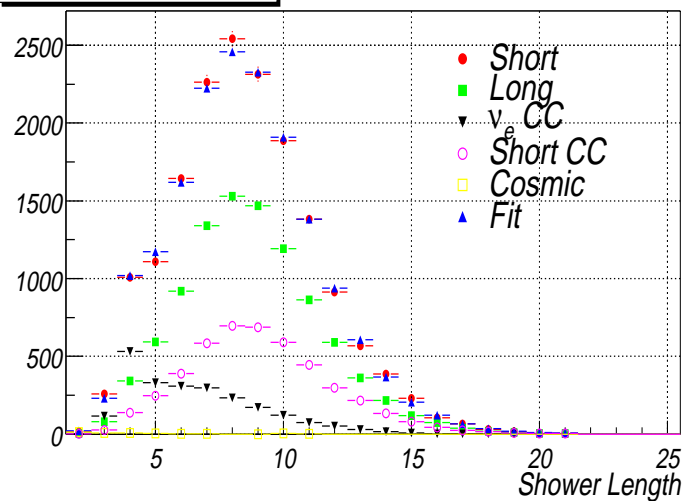
(Fit-Data)/Data



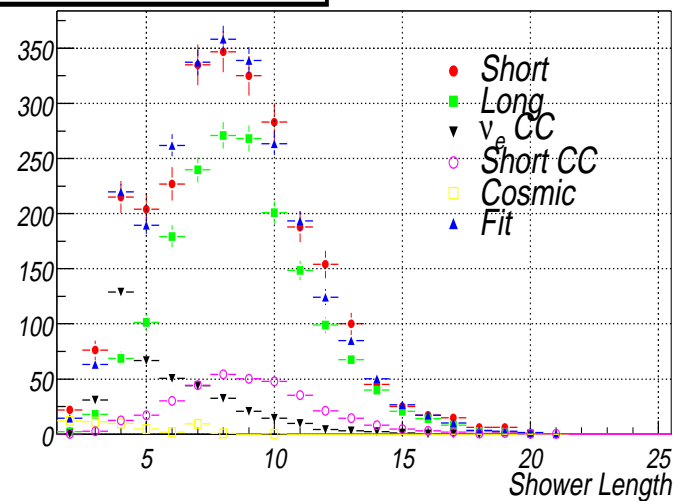
(Fit-Data)/Data



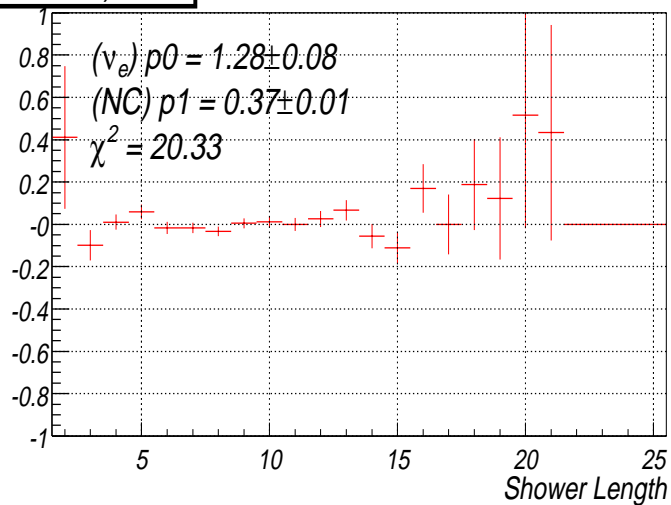
105-115 GeV, neutrino



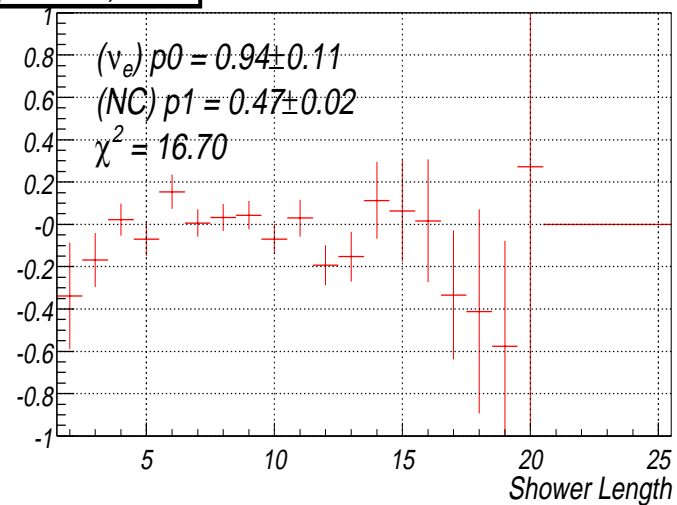
105-115 GeV, anti-neutrino



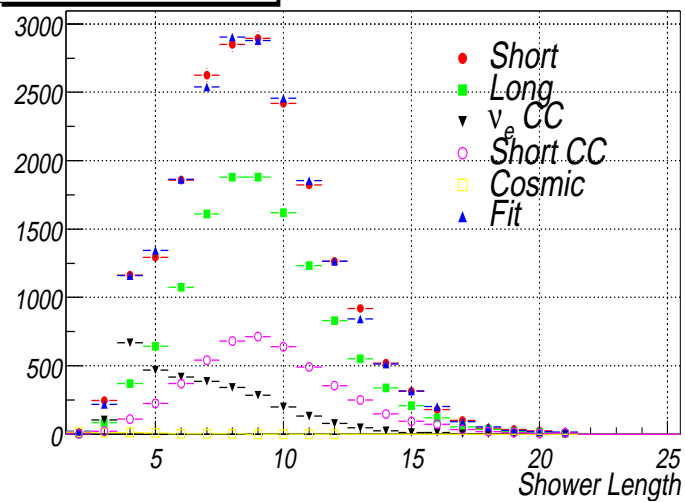
(Fit-Data)/Data



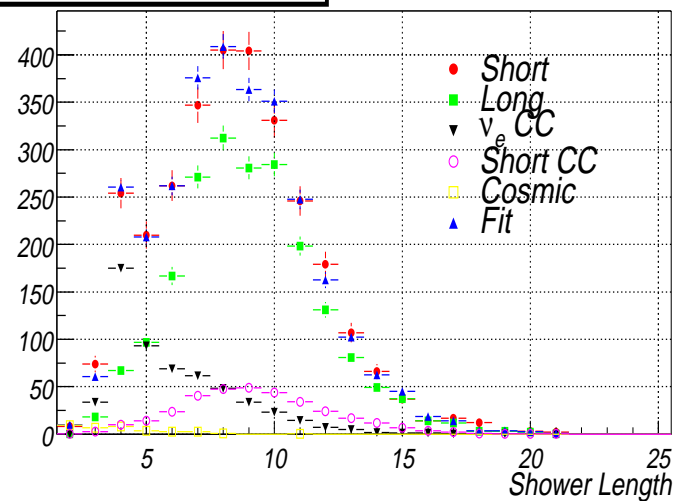
(Fit-Data)/Data



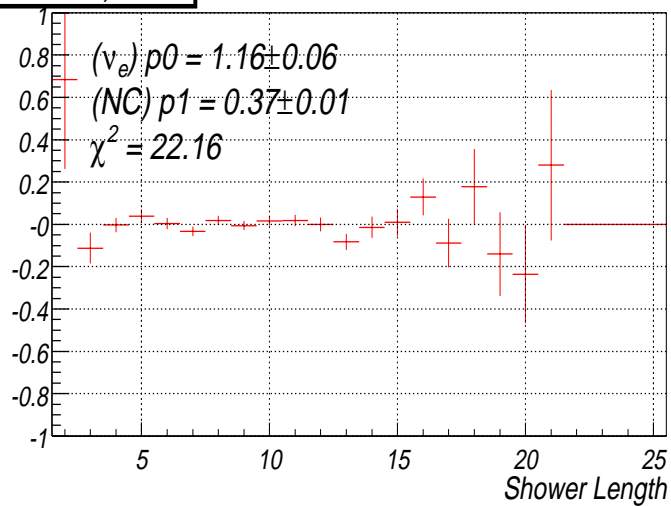
115-130 GeV, neutrino



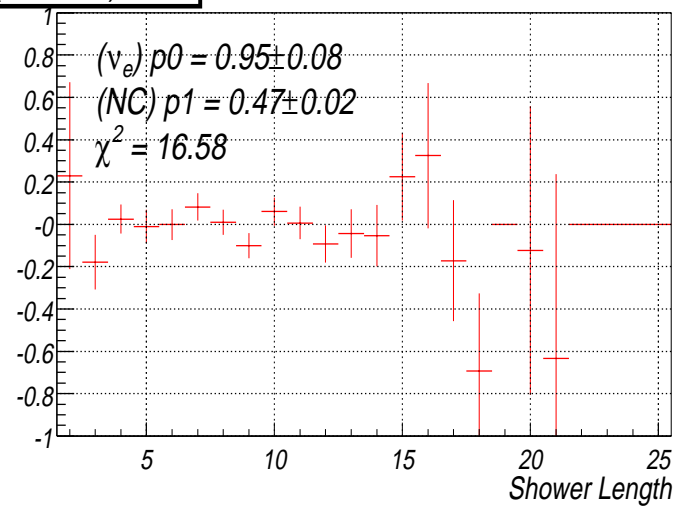
115-130 GeV, anti-neutrino



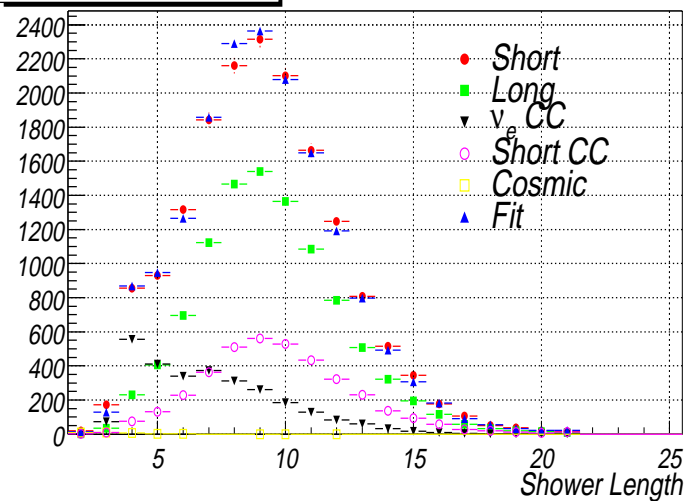
(Fit-Data)/Data



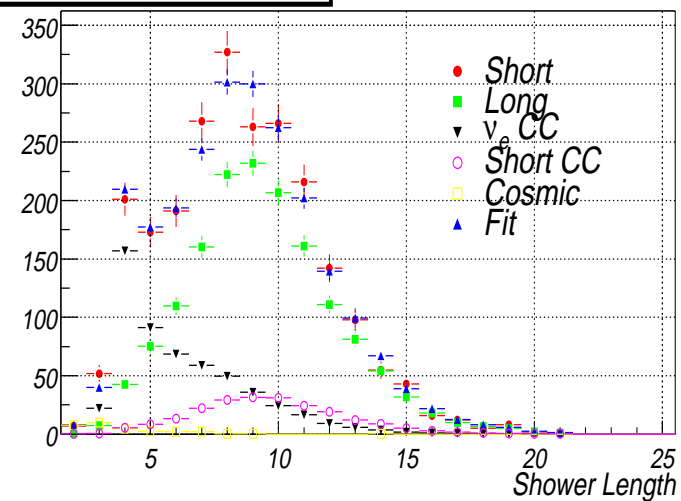
(Fit-Data)/Data



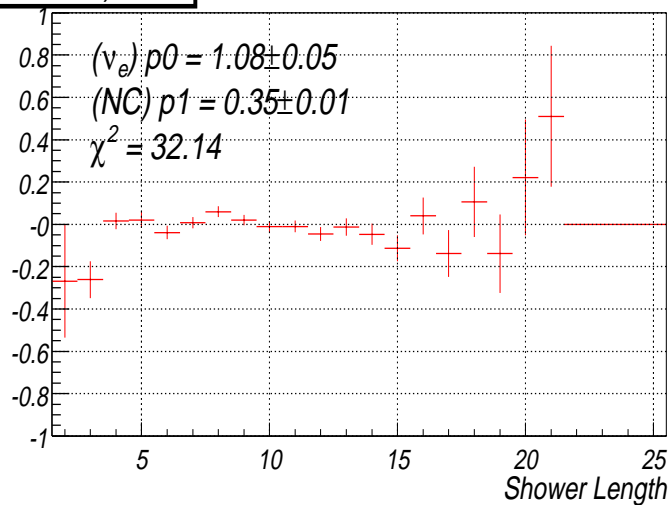
130-145 GeV, neutrino



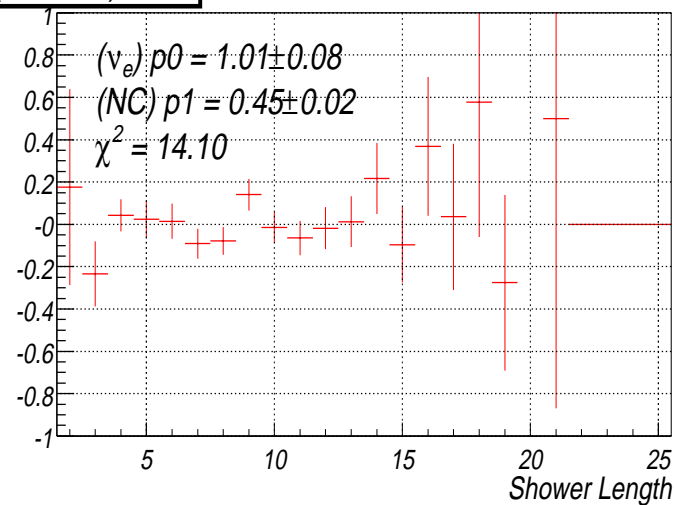
130-145 GeV, anti-neutrino



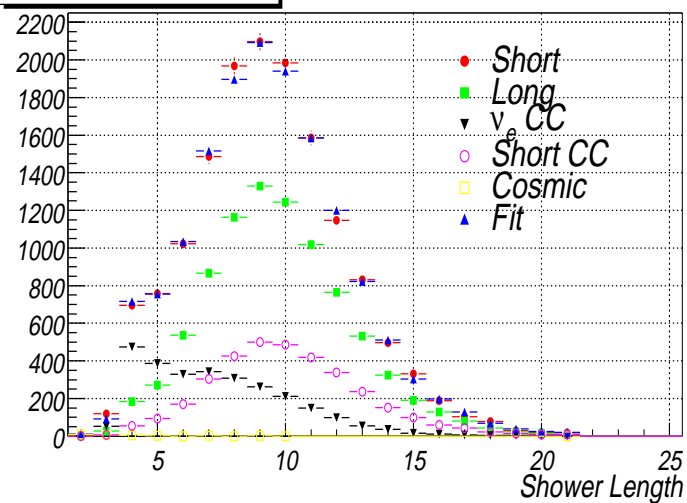
(Fit-Data)/Data



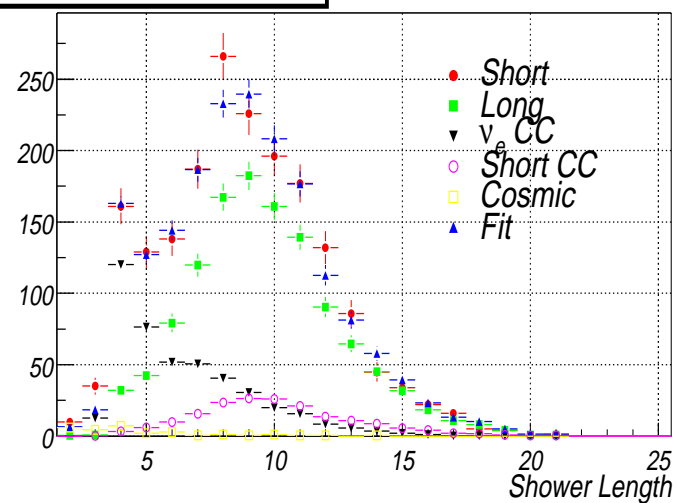
(Fit-Data)/Data



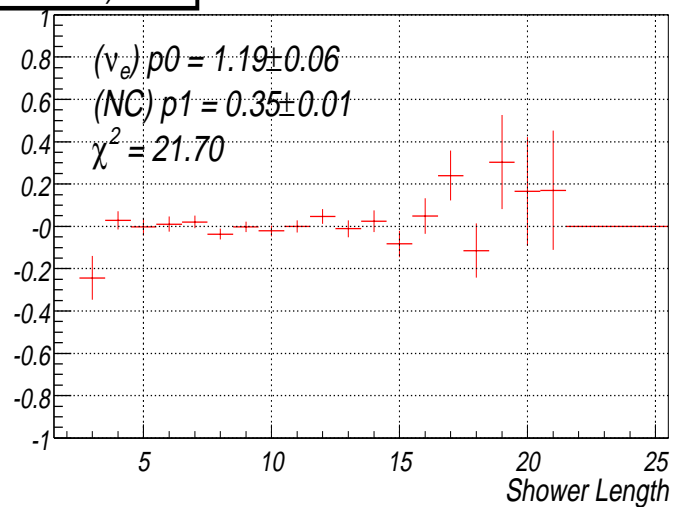
145-160 GeV, neutrino



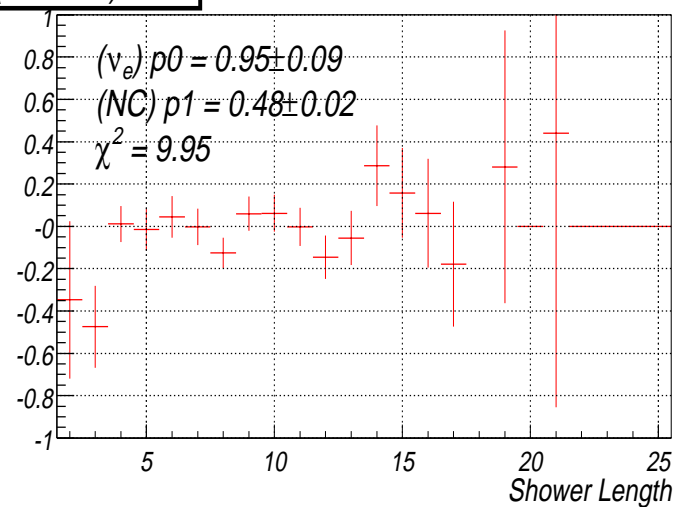
145-160 GeV, anti-neutrino



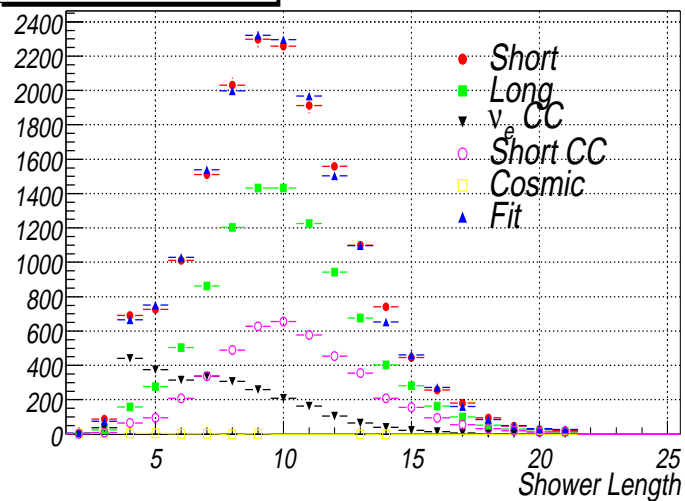
(Fit-Data)/Data



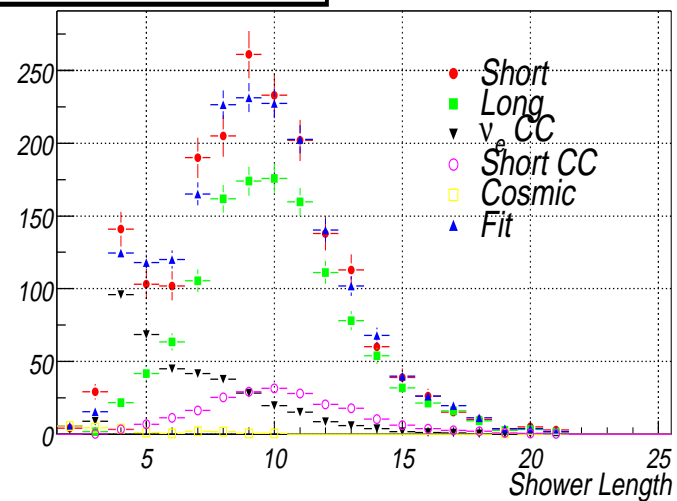
(Fit-Data)/Data



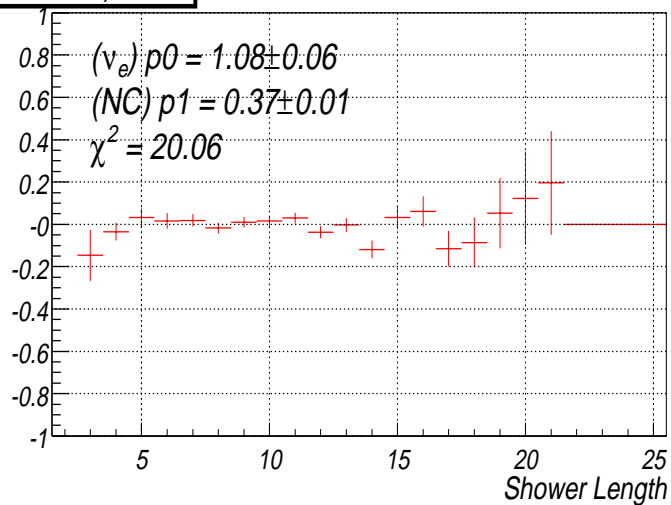
160-180 GeV, neutrino



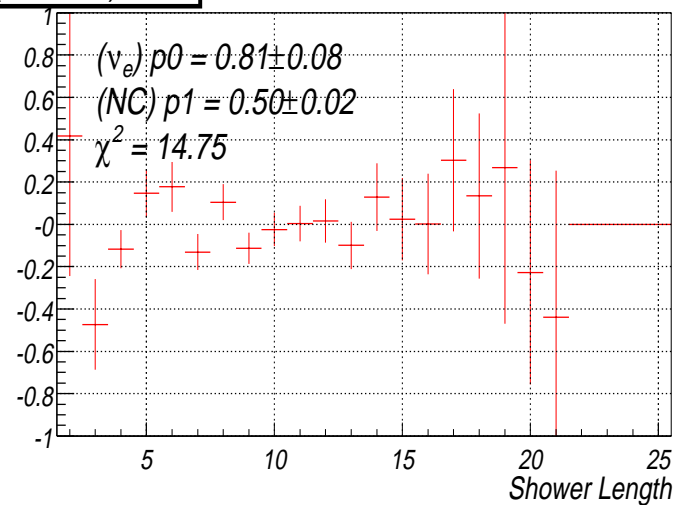
160-180 GeV, anti-neutrino



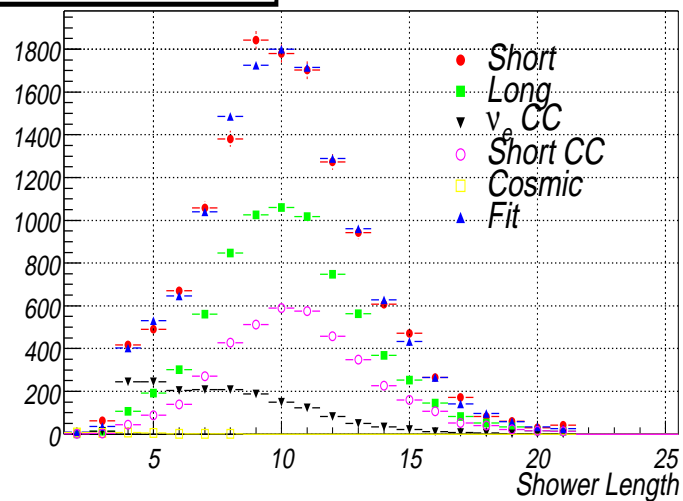
(Fit-Data)/Data



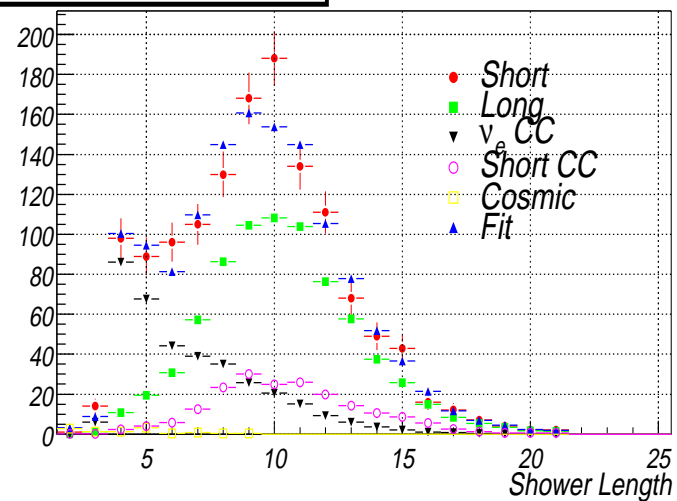
(Fit-Data)/Data



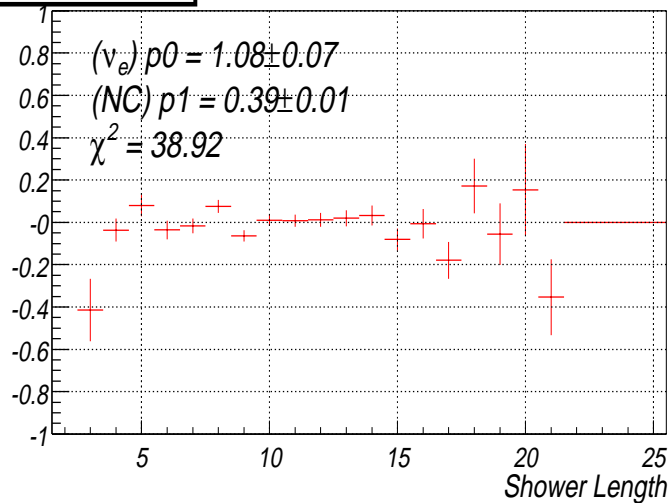
180-200 GeV, neutrino



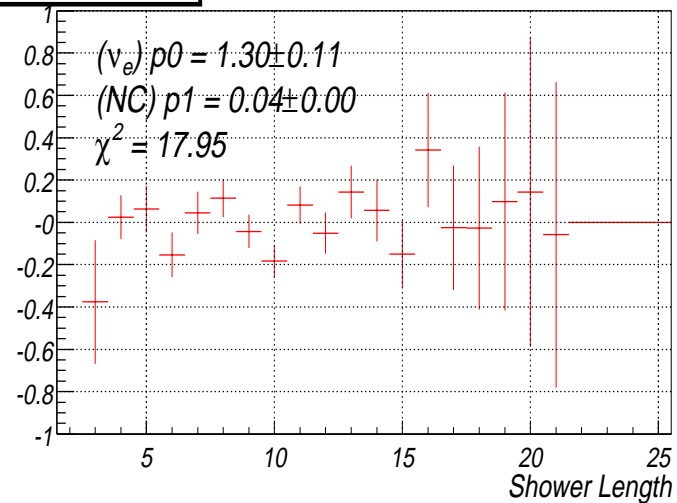
180-200 GeV, anti-neutrino



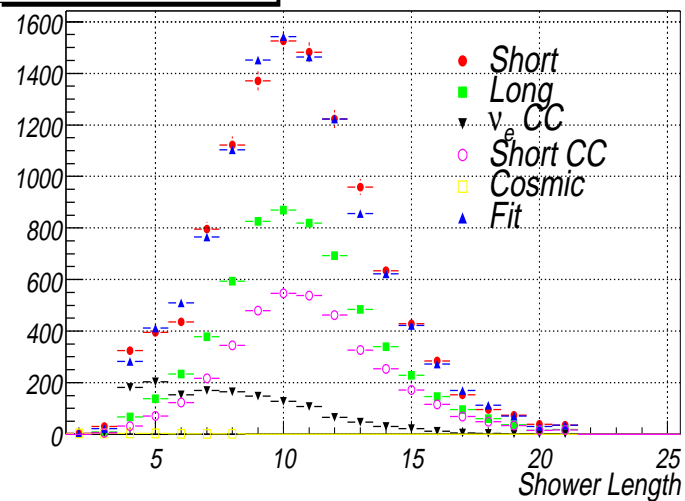
(Fit-Data)/Data



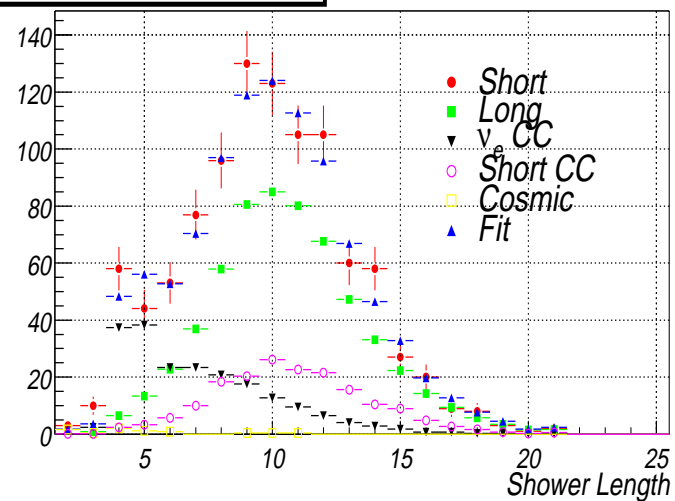
(Fit-Data)/Data



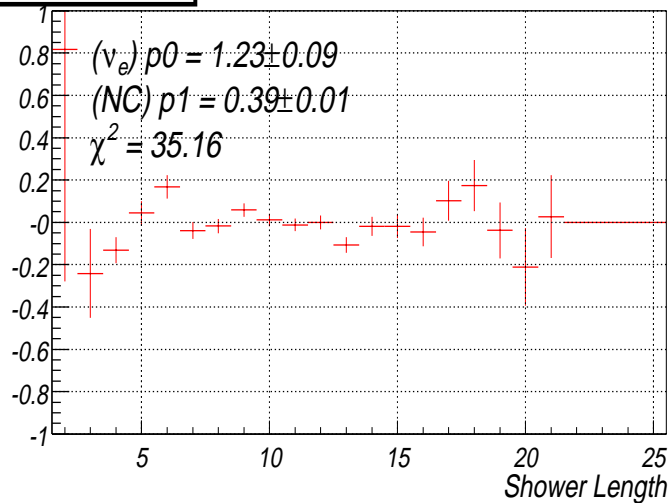
200-225 GeV, neutrino



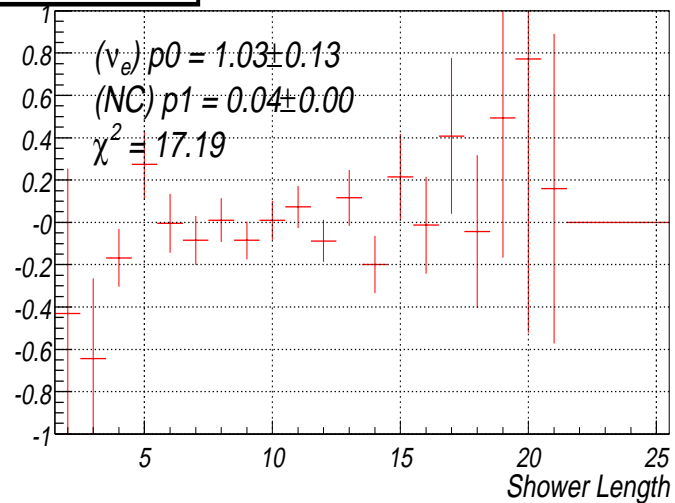
200-225 GeV, anti-neutrino



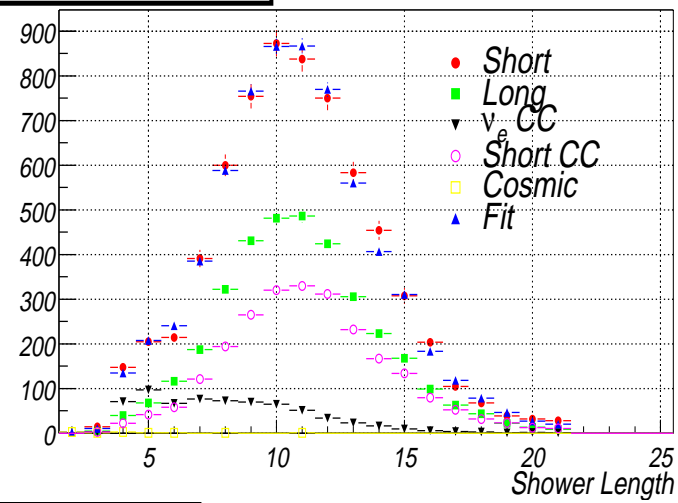
(Fit-Data)/Data



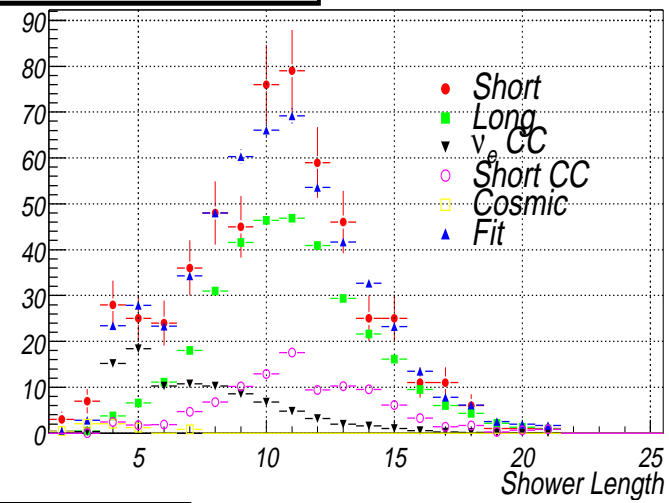
(Fit-Data)/Data



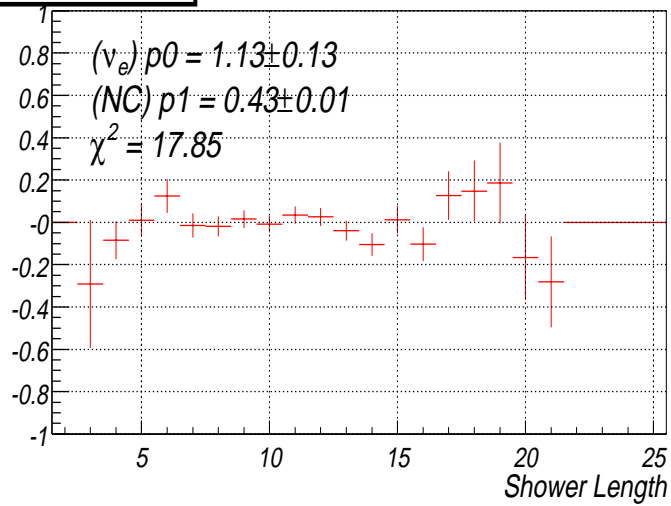
225-250 GeV, neutrino



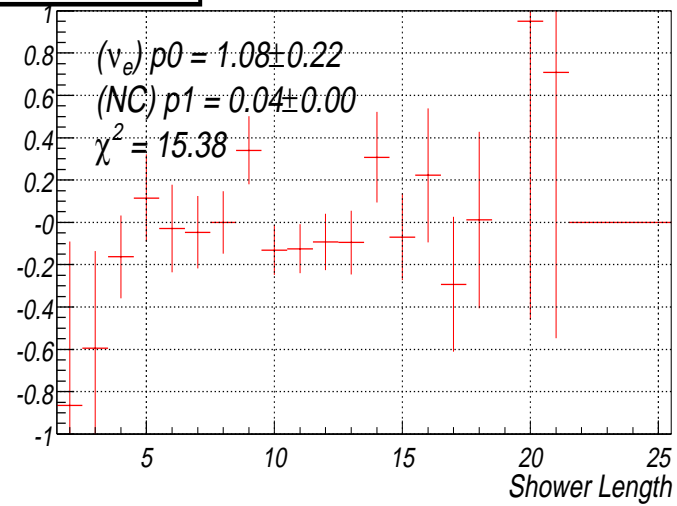
225-250 GeV, anti-neutrino



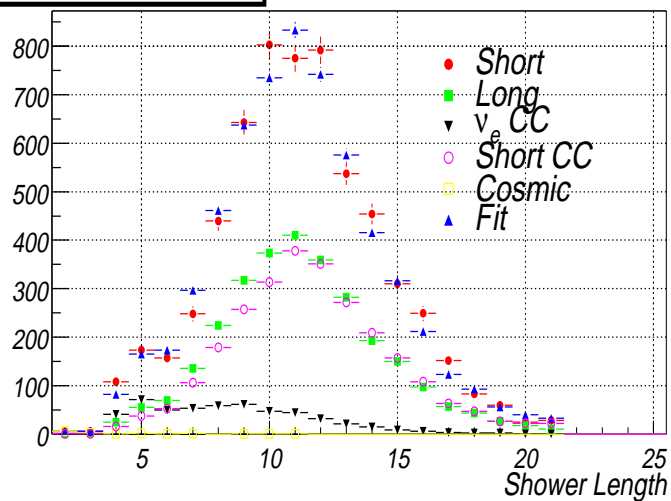
(Fit-Data)/Data



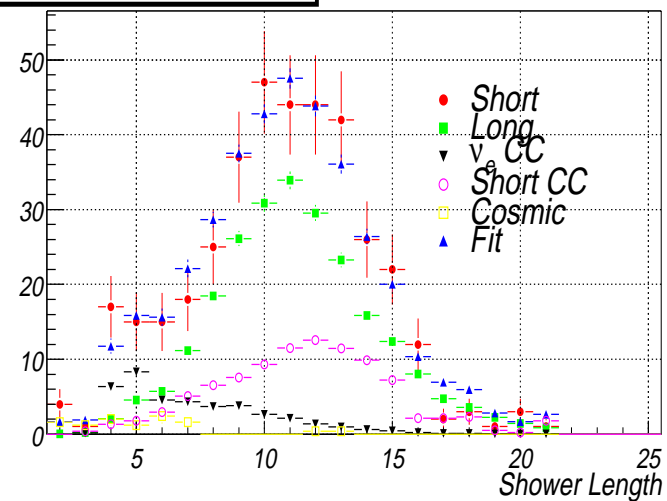
(Fit-Data)/Data



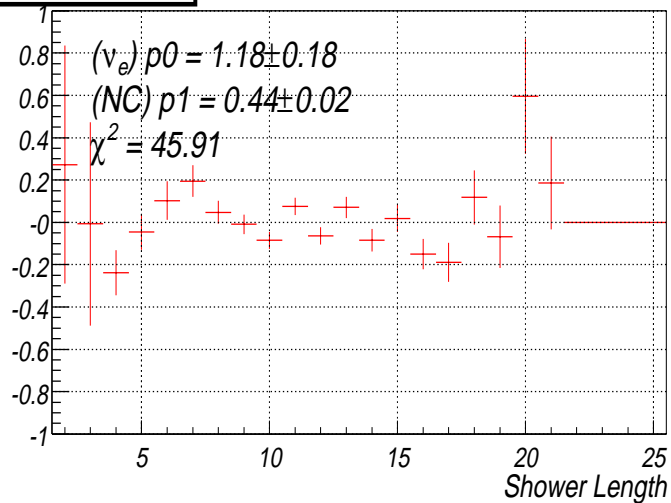
250-350 GeV, neutrino



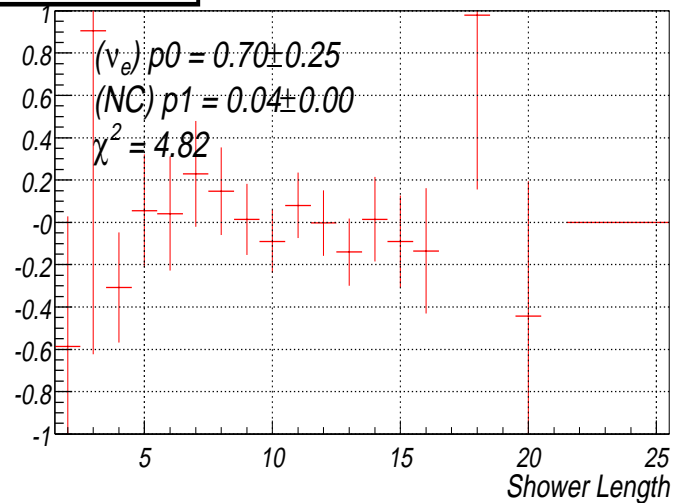
250-350 GeV, anti-neutrino



(Fit-Data)/Data



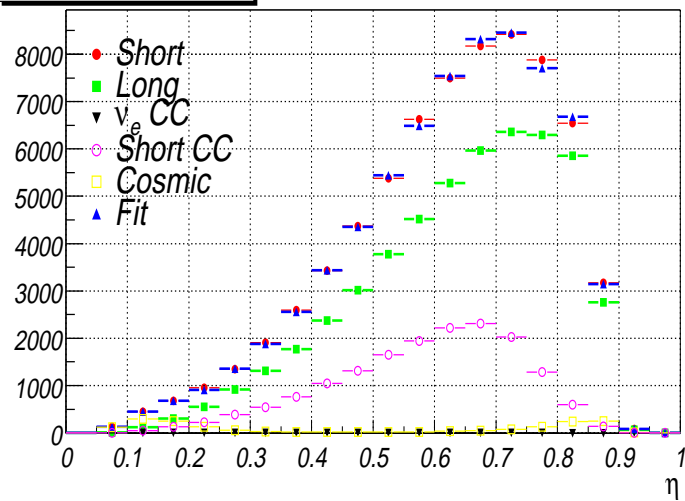
(Fit-Data)/Data



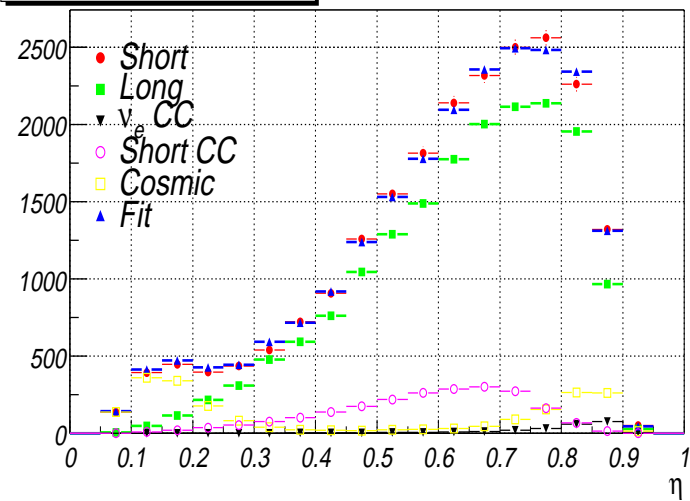
Appendix B

Data Fits η_3

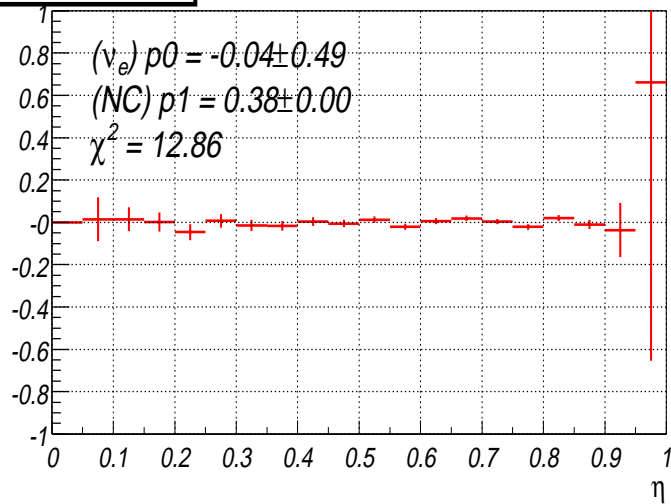
30-40 GeV, neutrino



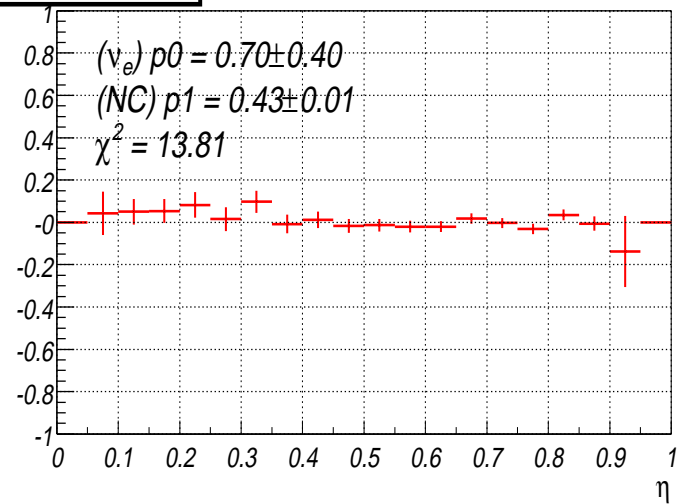
30-40 GeV, anti-neutrino



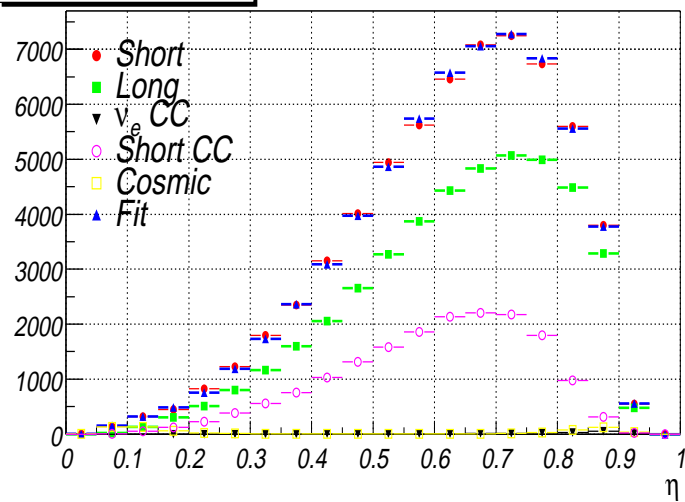
(Fit-Data)/Data



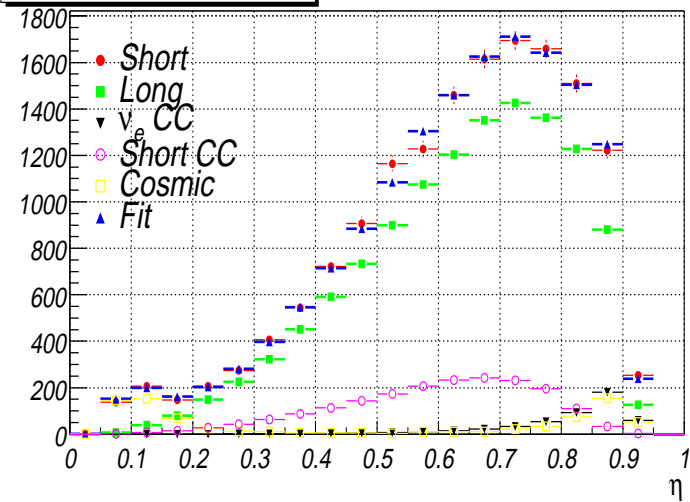
(Fit-Data)/Data



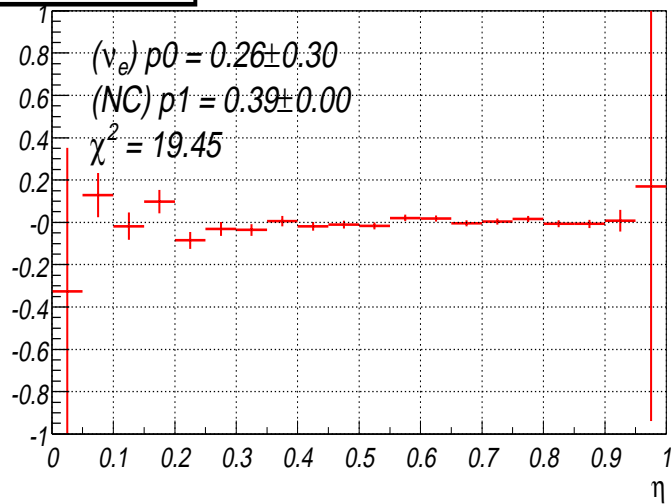
40-50 GeV, neutrino



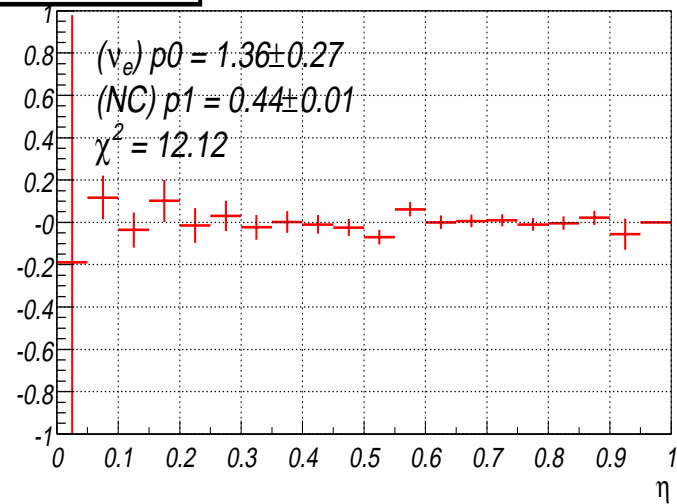
40-50 GeV, anti-neutrino



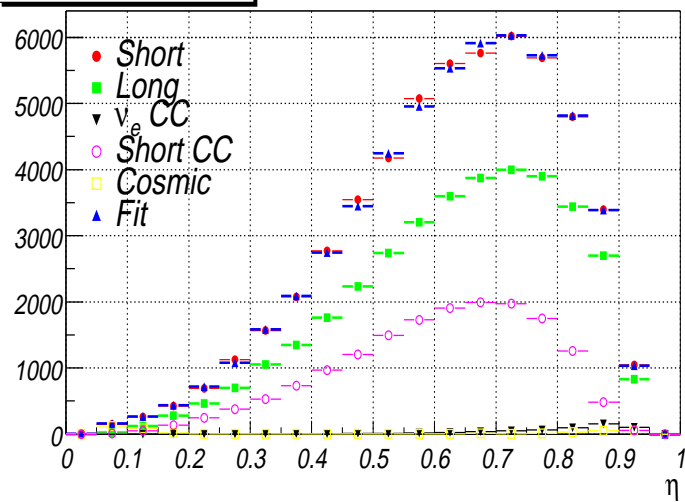
(Fit-Data)/Data



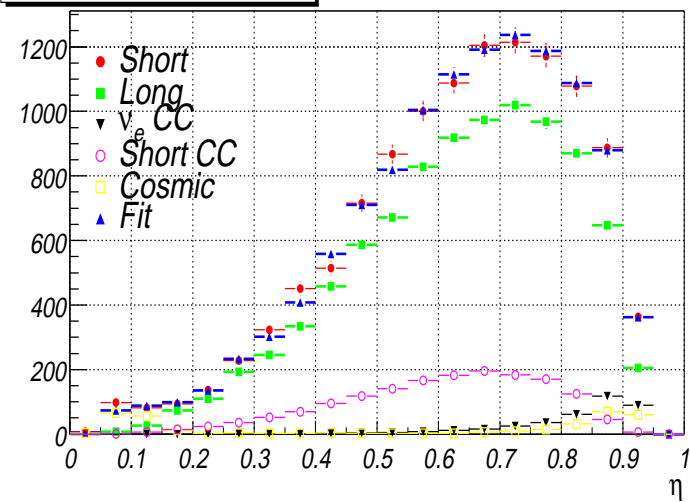
(Fit-Data)/Data



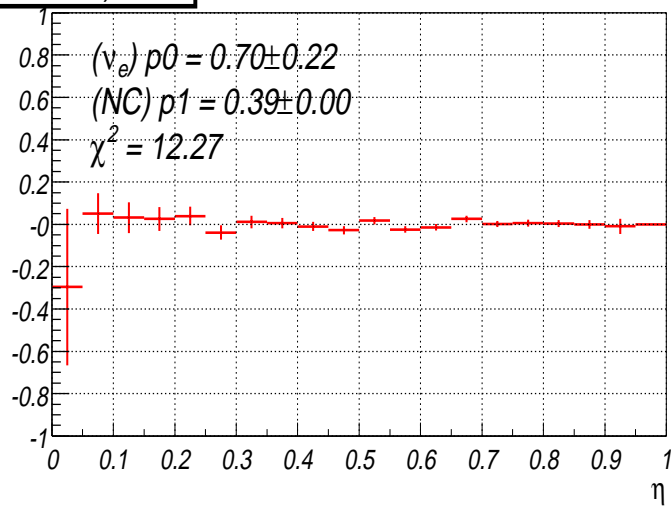
50-60 GeV, neutrino



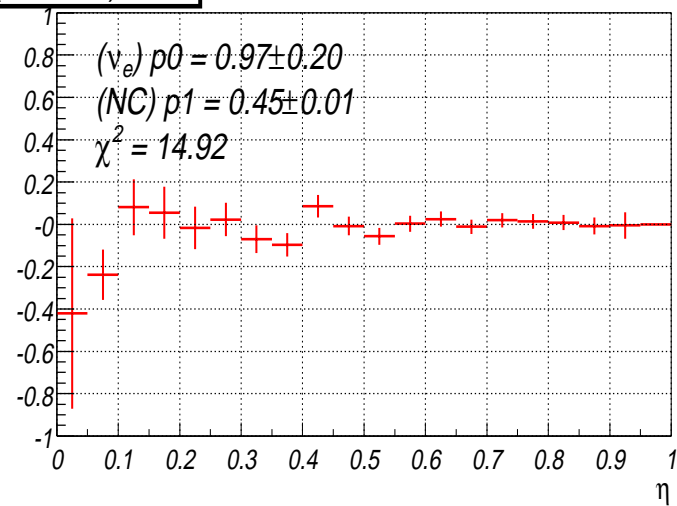
50-60 GeV, anti-neutrino



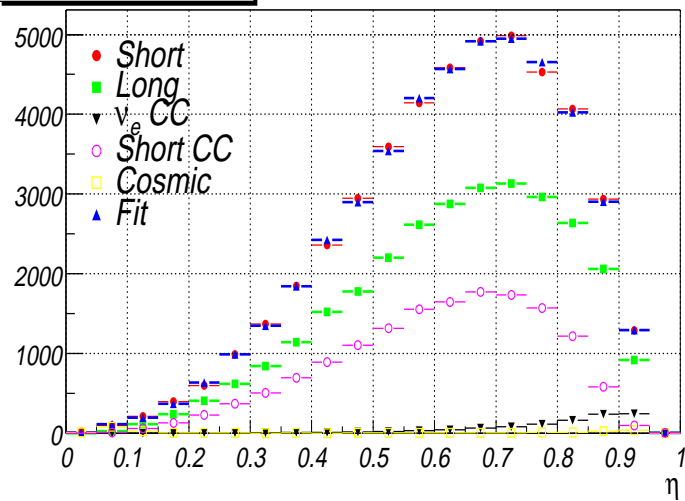
(Fit-Data)/Data



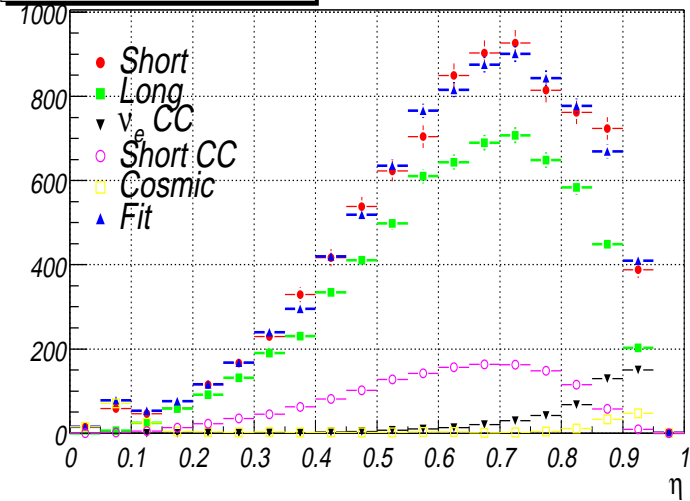
(Fit-Data)/Data



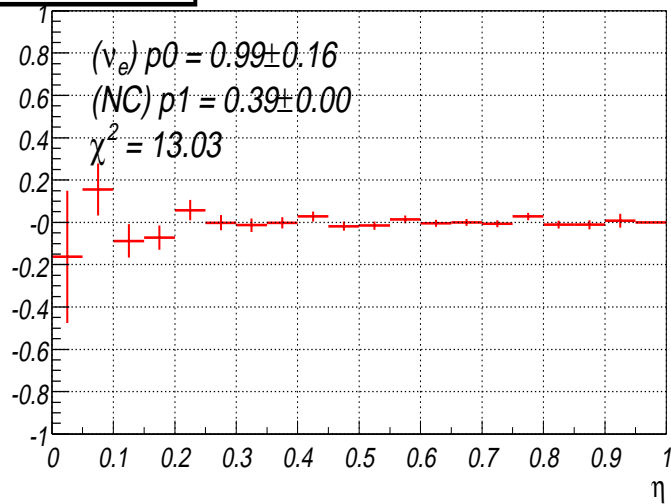
60-70 GeV, neutrino



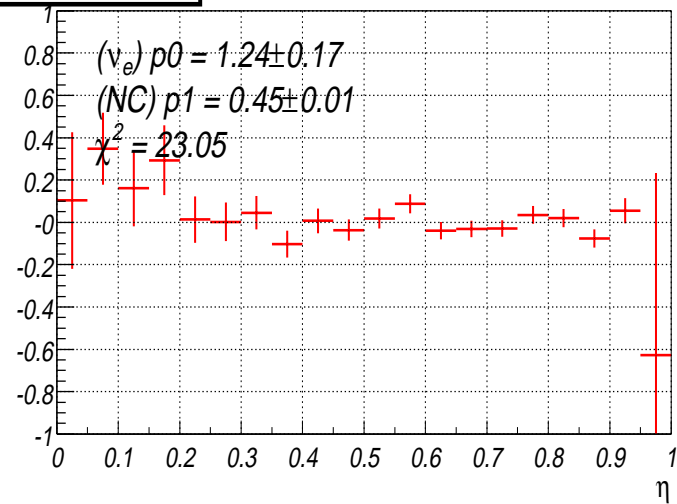
60-70 GeV, anti-neutrino



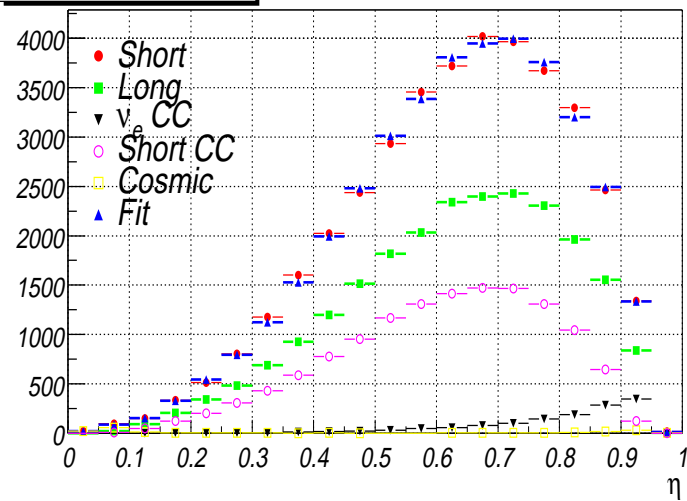
(Fit-Data)/Data



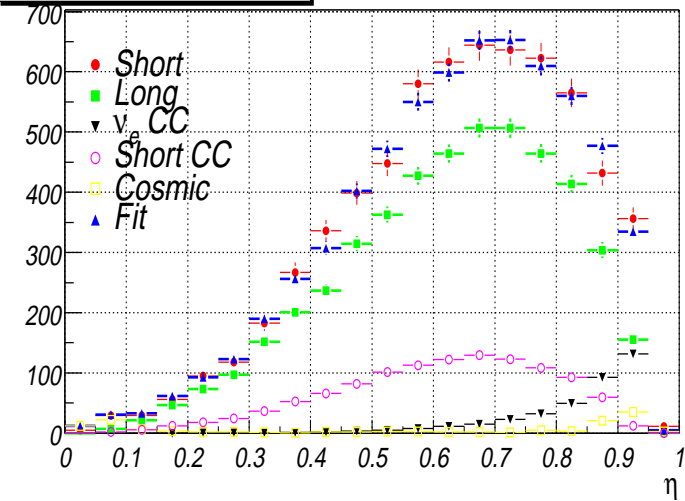
(Fit-Data)/Data



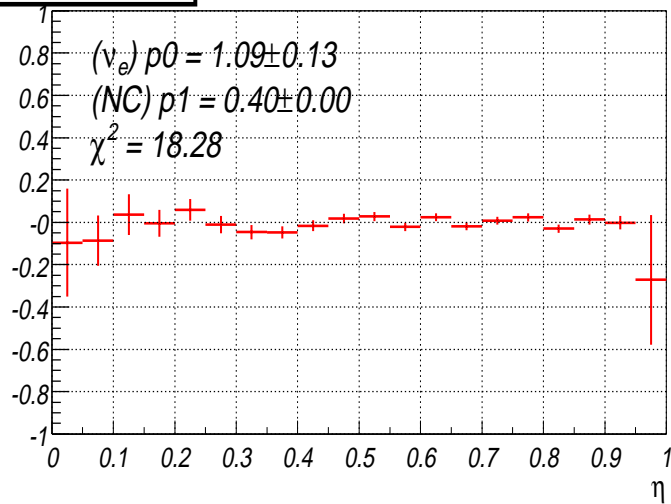
70-80 GeV, neutrino



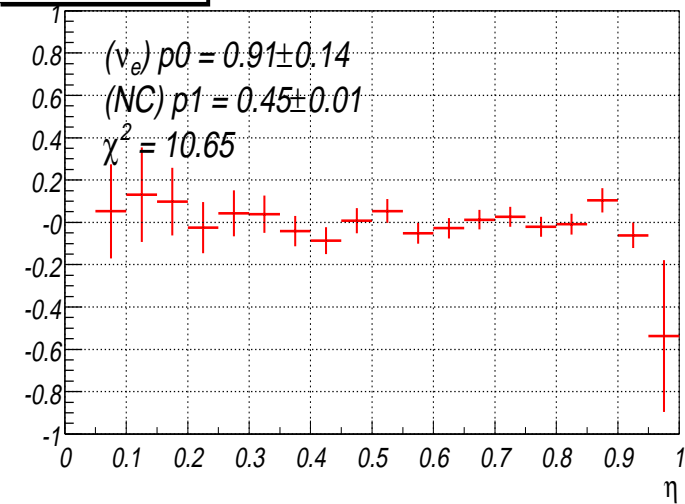
70-80 GeV, anti-neutrino



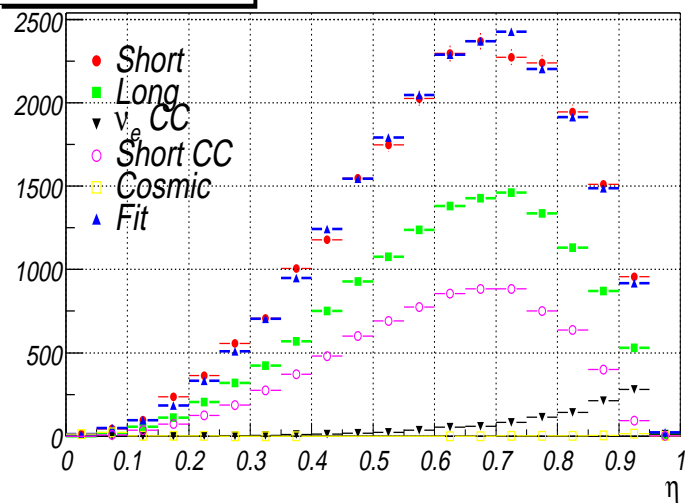
(Fit-Data)/Data



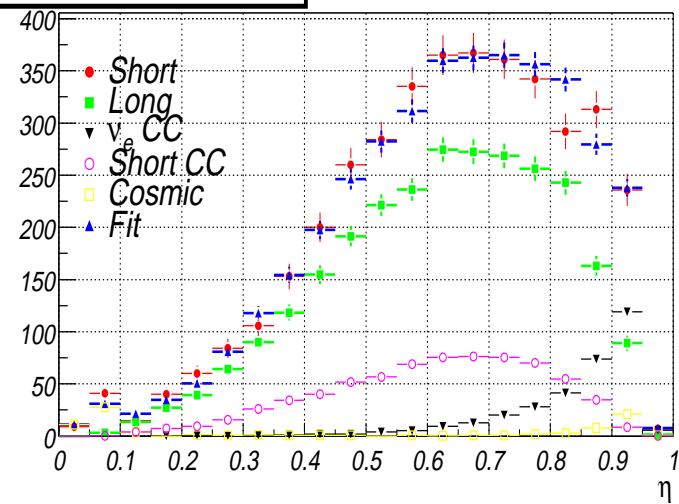
(Fit-Data)/Data



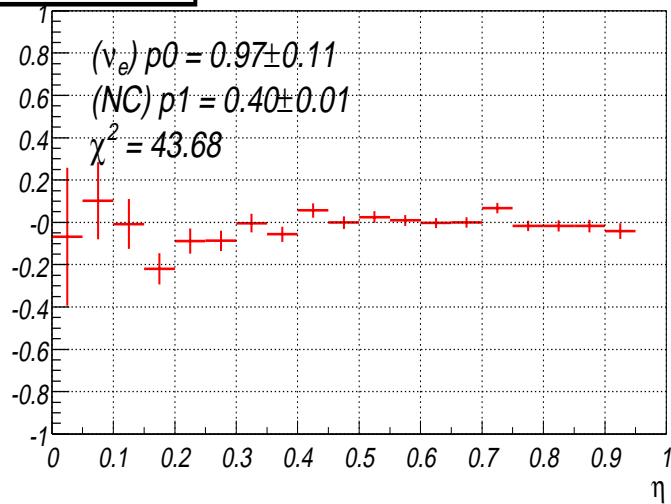
80-87 GeV, neutrino



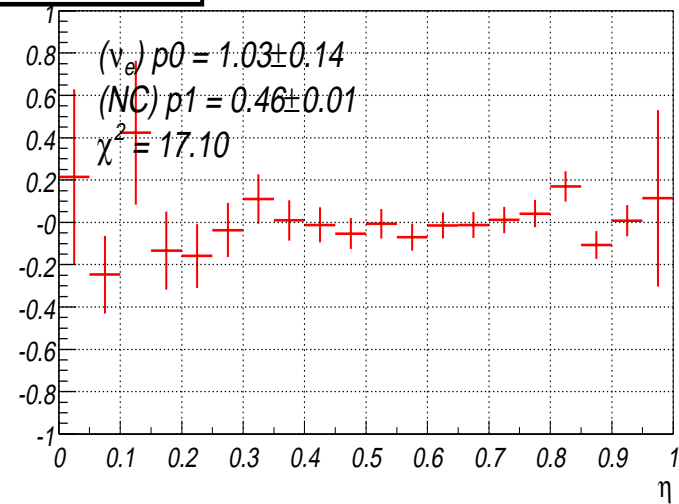
80-87 GeV, anti-neutrino



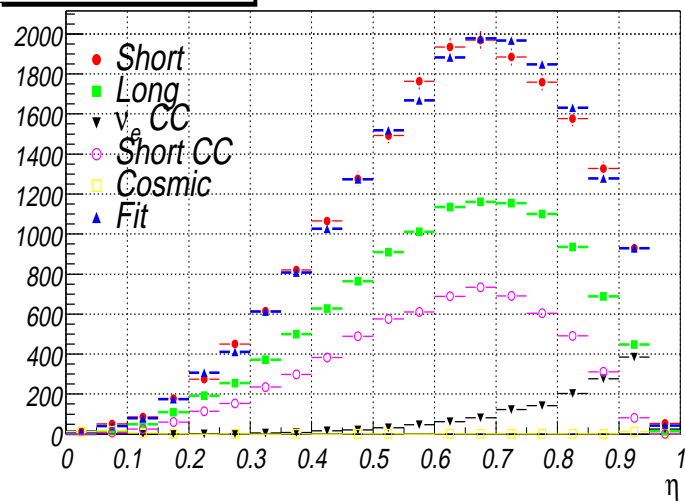
(Fit-Data)/Data



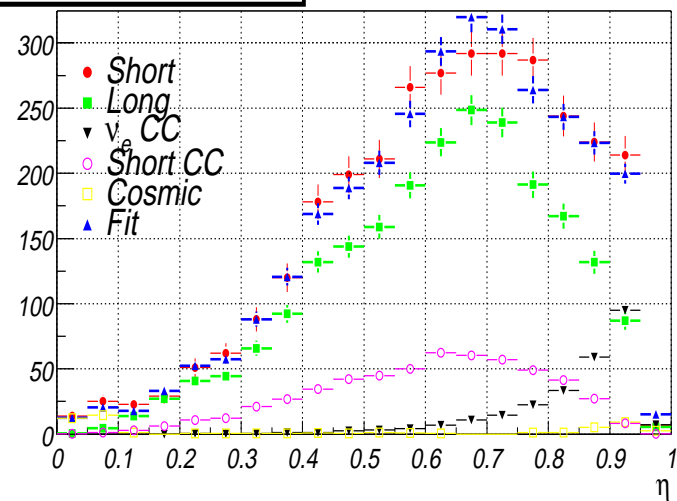
(Fit-Data)/Data



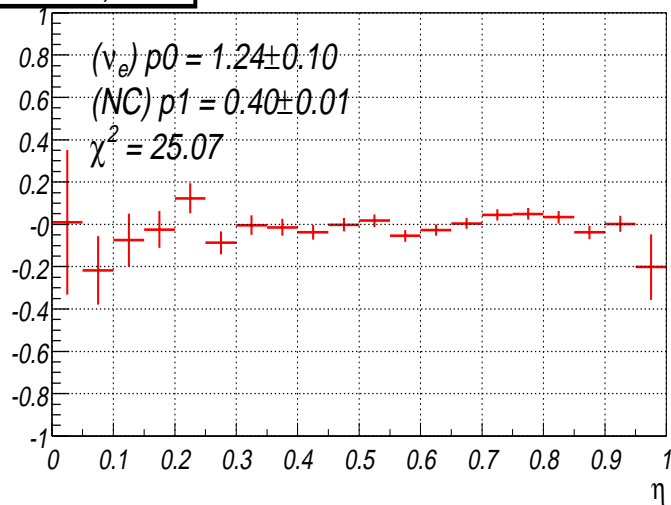
87-95 GeV, neutrino



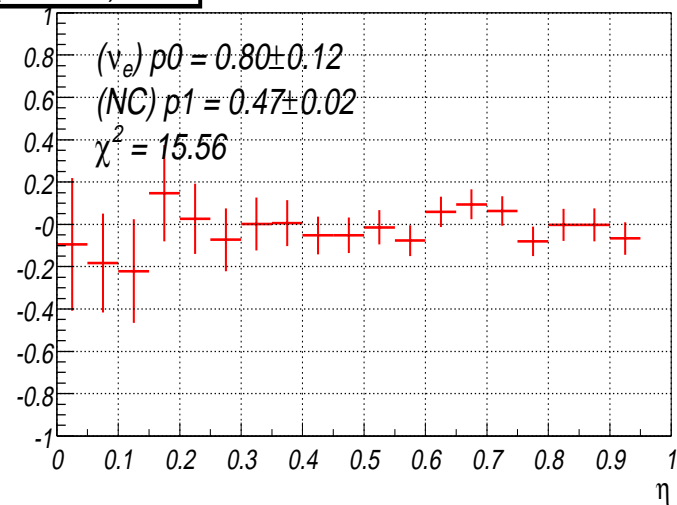
87-95 GeV, anti-neutrino



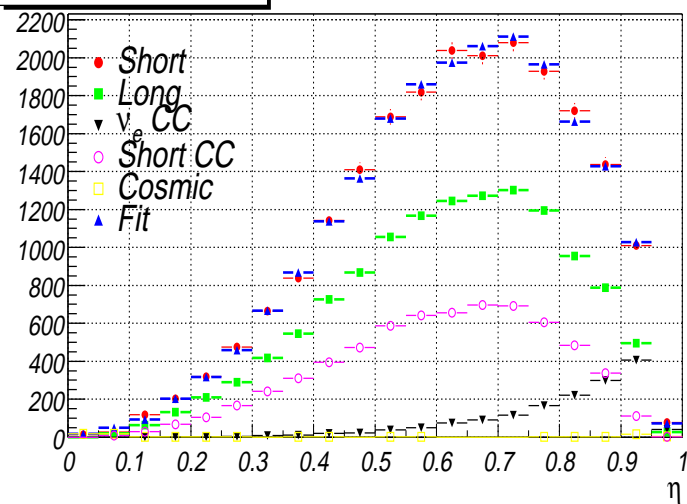
(Fit-Data)/Data



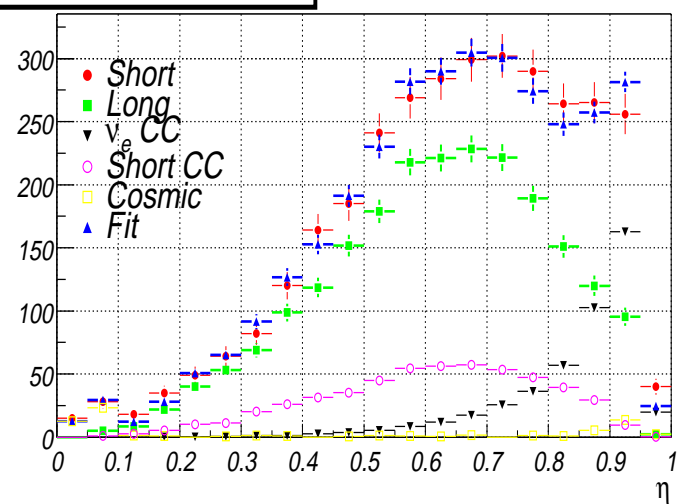
(Fit-Data)/Data



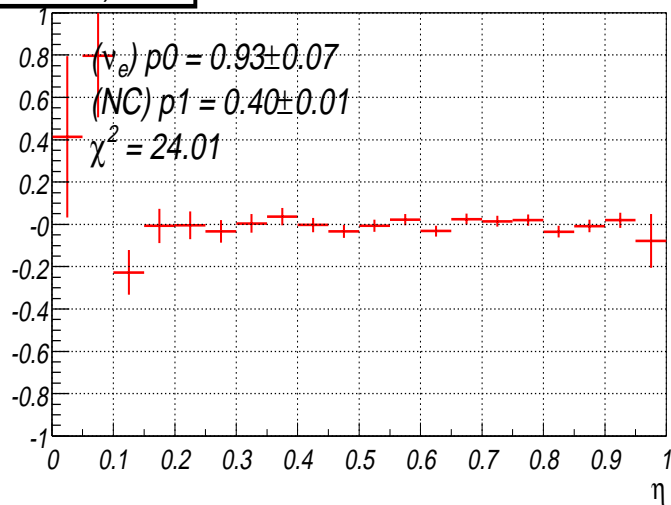
95-105 GeV, neutrino



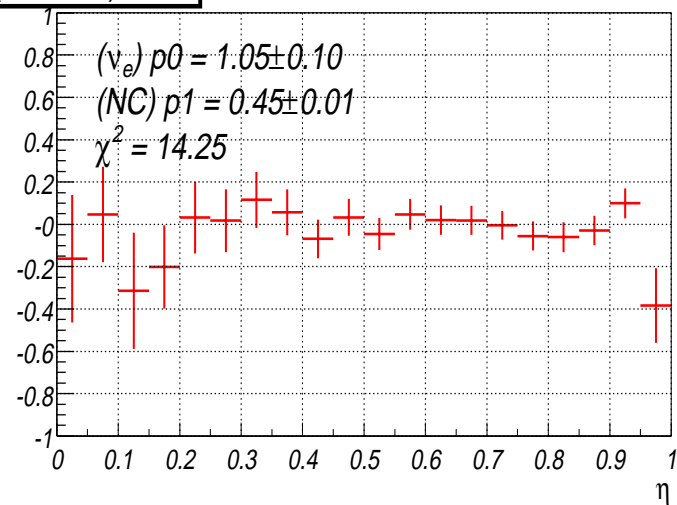
95-105 GeV, anti-neutrino



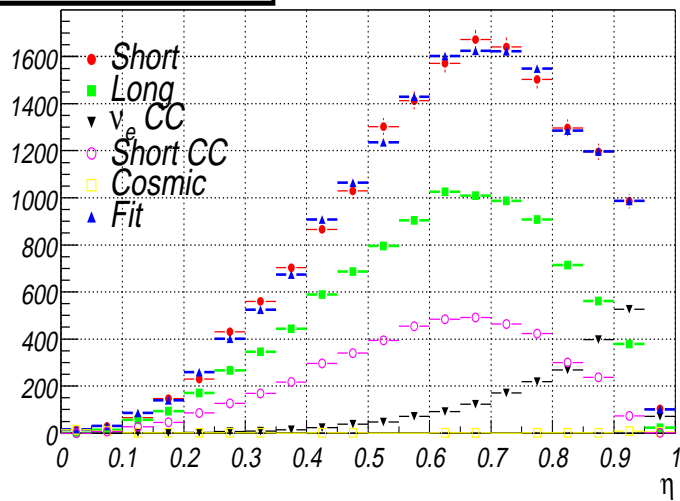
(Fit-Data)/Data



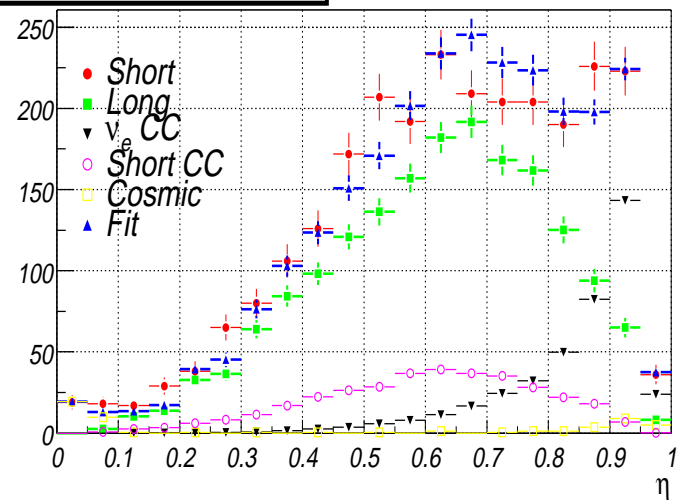
(Fit-Data)/Data



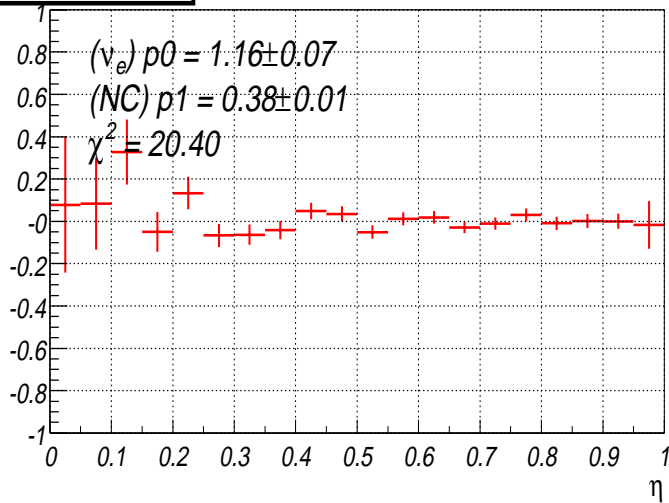
105-115 GeV, neutrino



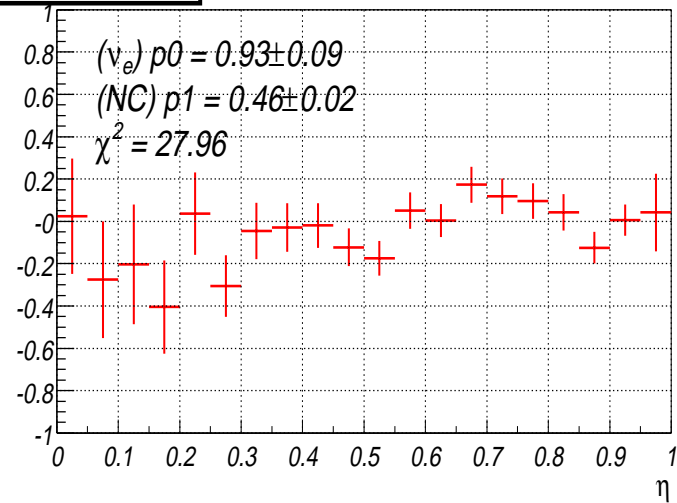
105-115 GeV, anti-neutrino



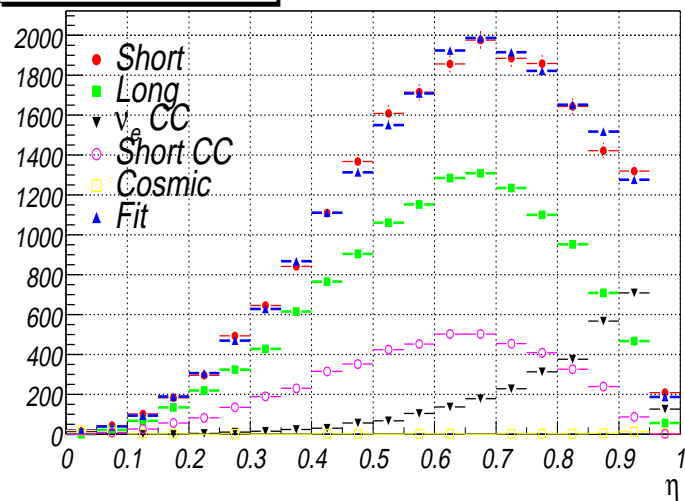
(Fit-Data)/Data



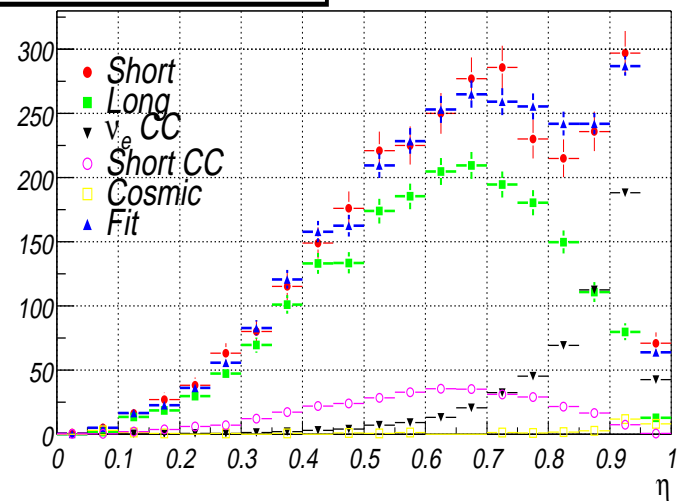
(Fit-Data)/Data



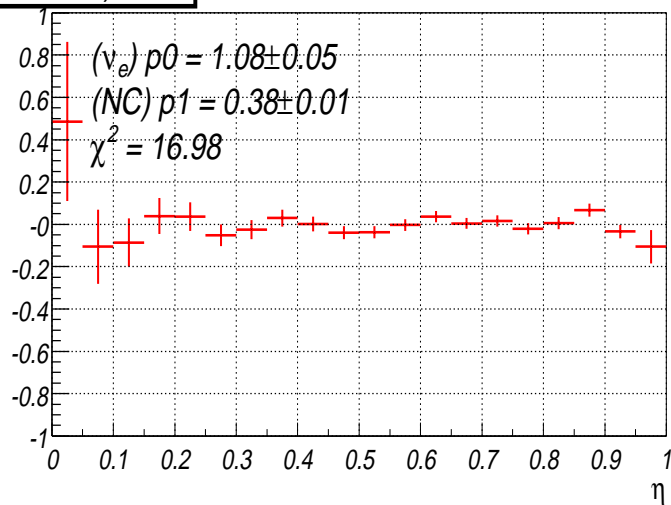
115-130 GeV, neutrino



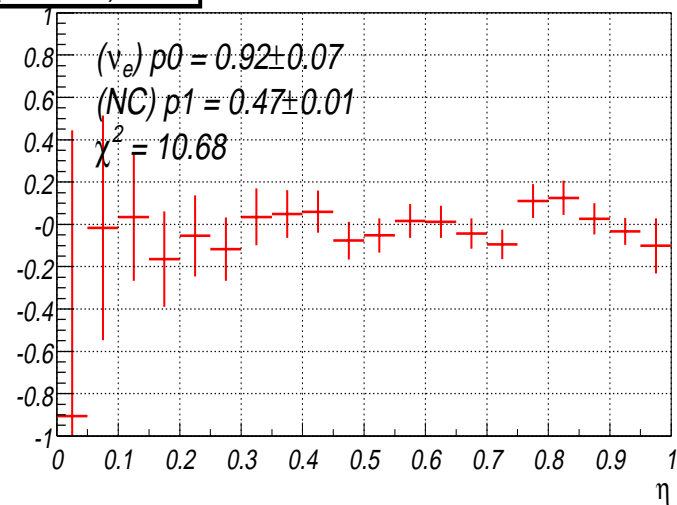
115-130 GeV, anti-neutrino



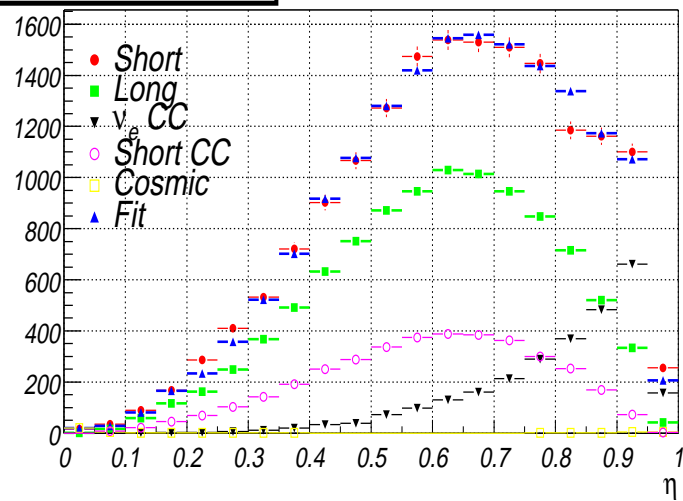
(Fit-Data)/Data



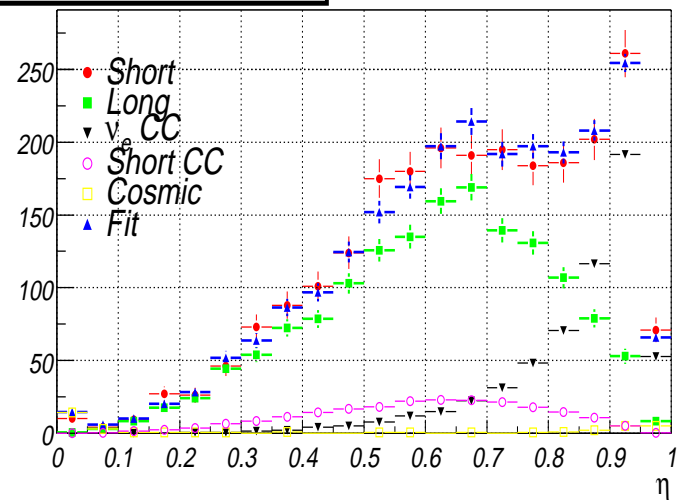
(Fit-Data)/Data



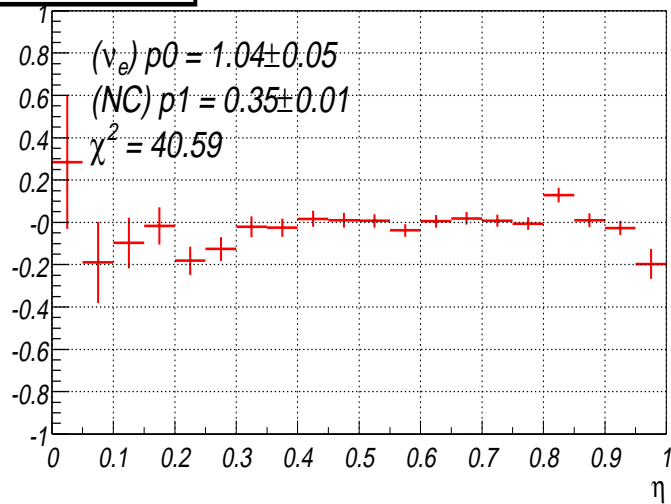
130-145 GeV, neutrino



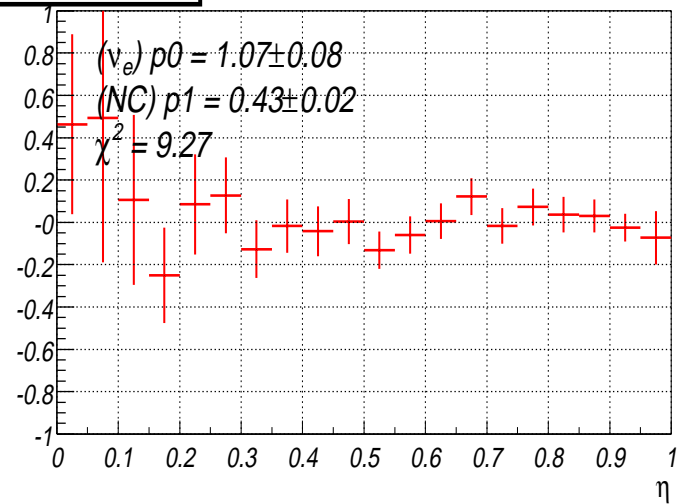
130-145 GeV, anti-neutrino



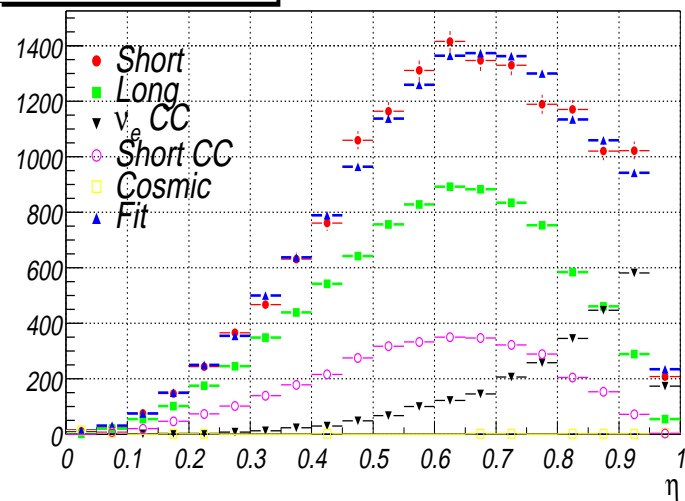
(Fit-Data)/Data



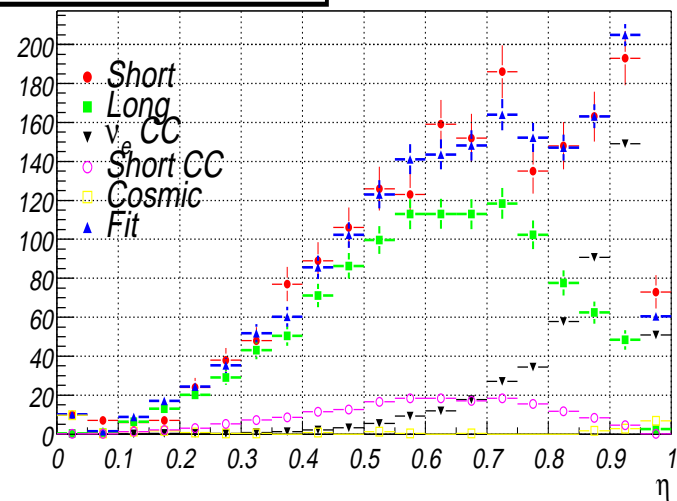
(Fit-Data)/Data



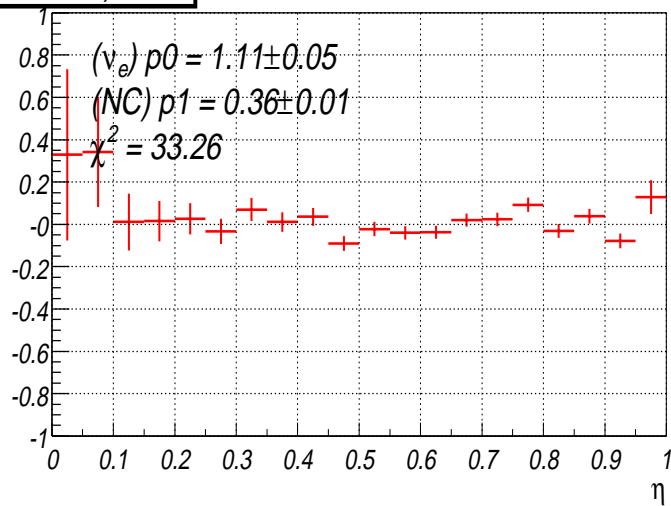
145-160 GeV, neutrino



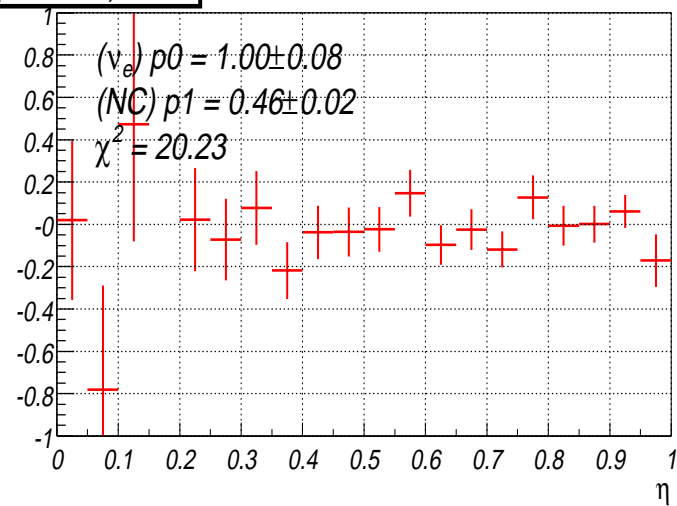
145-160 GeV, anti-neutrino



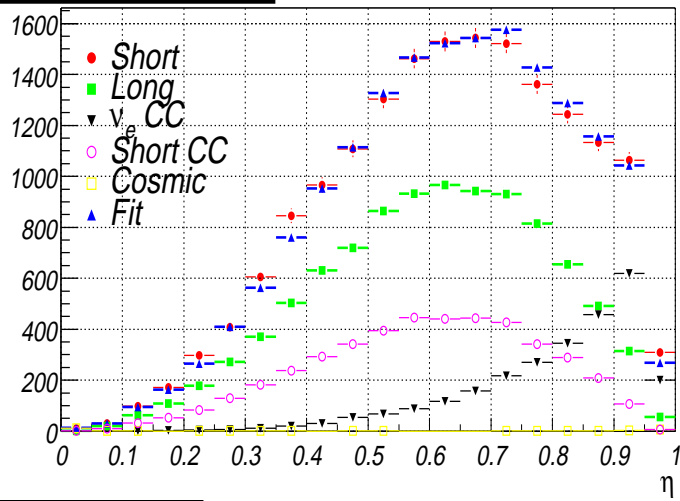
(Fit-Data)/Data



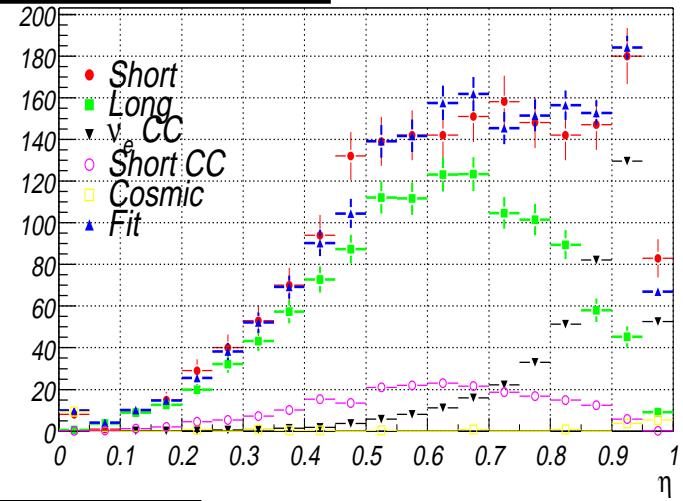
(Fit-Data)/Data



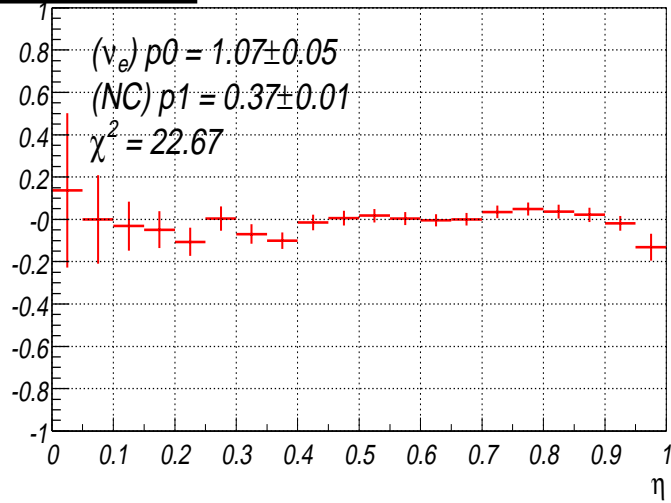
160-180 GeV, neutrino



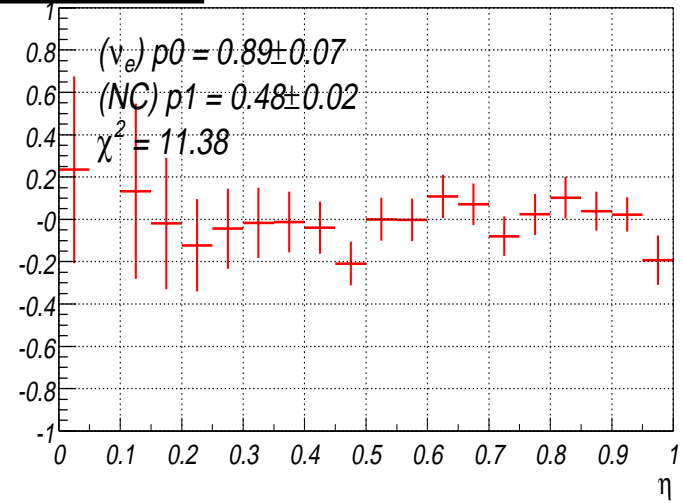
160-180 GeV, anti-neutrino



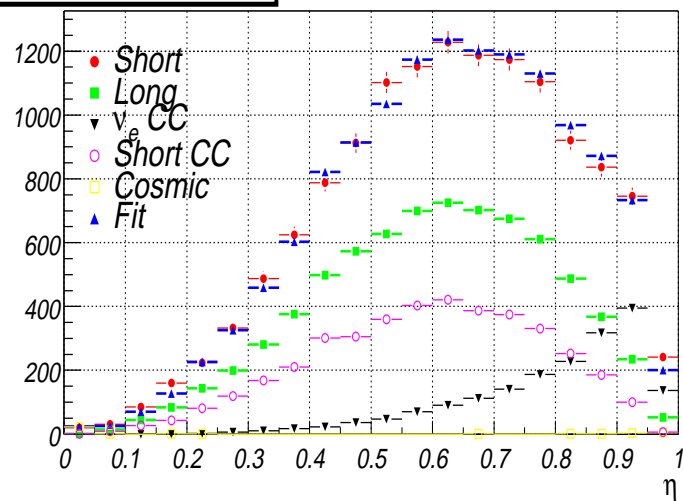
(Fit-Data)/Data



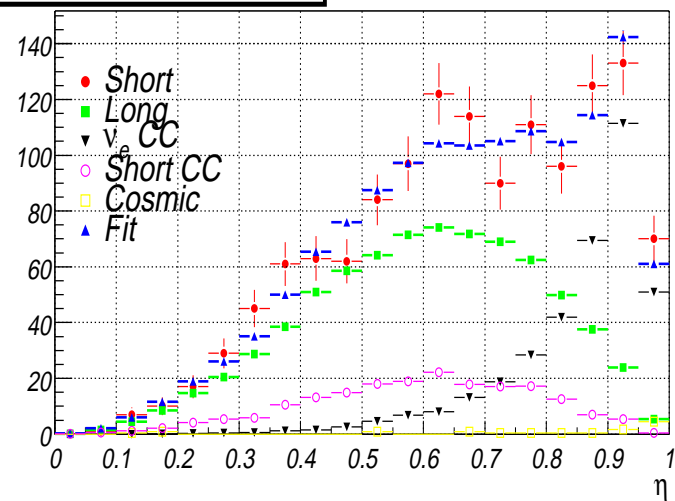
(Fit-Data)/Data



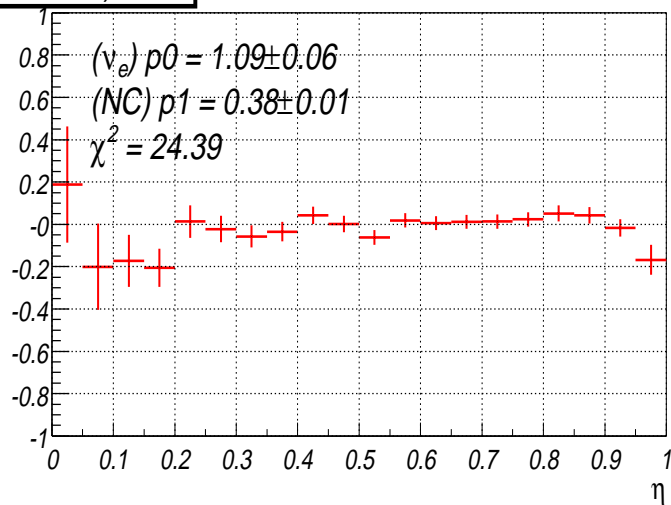
180-200 GeV, neutrino



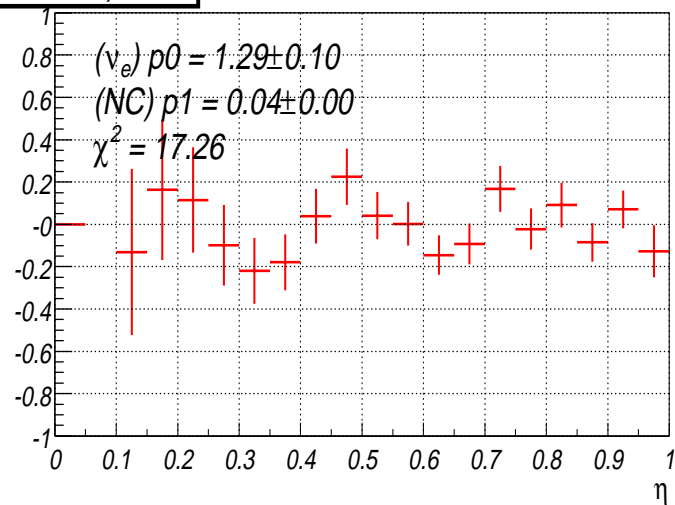
180-200 GeV, anti-neutrino



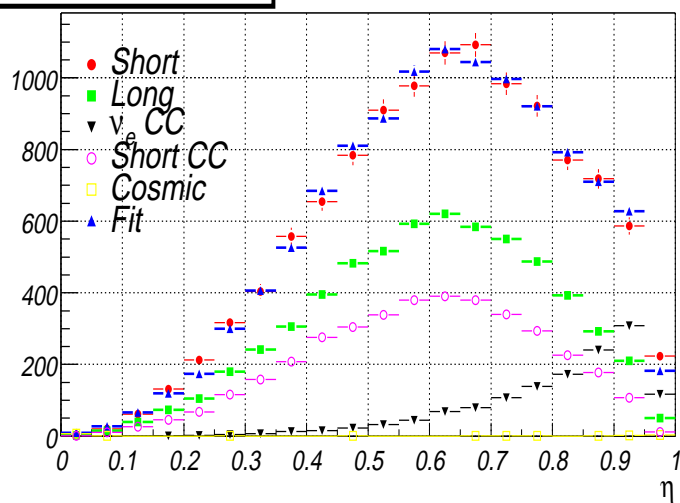
(Fit-Data)/Data



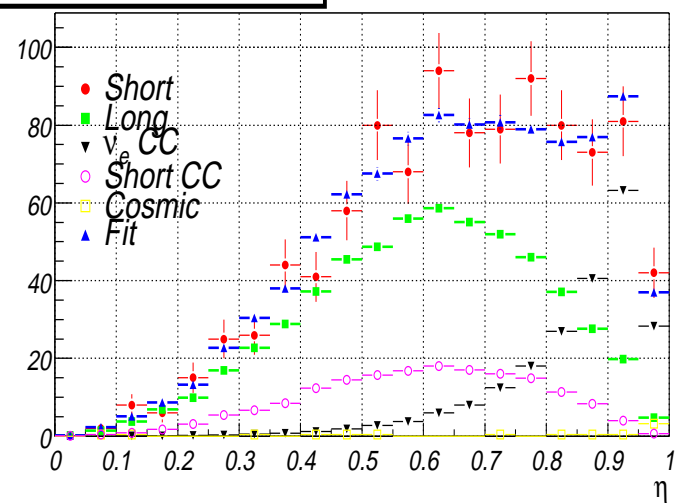
(Fit-Data)/Data



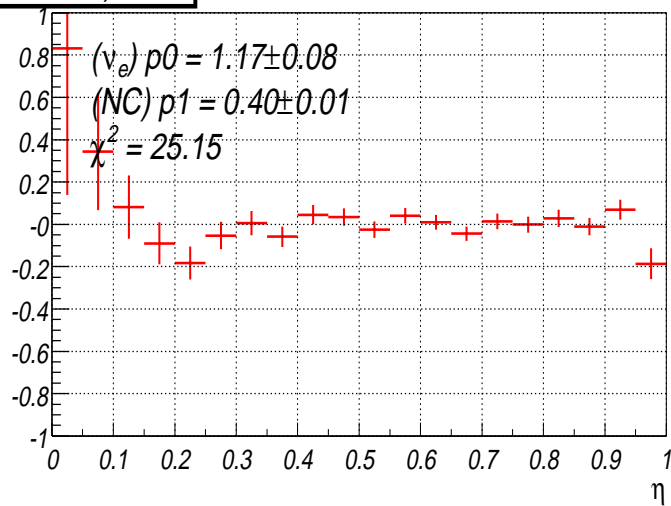
200-225 GeV, neutrino



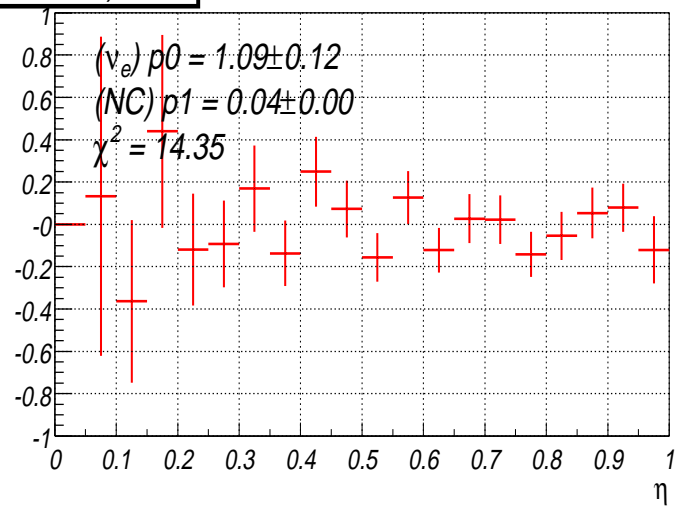
200-225 GeV, anti-neutrino



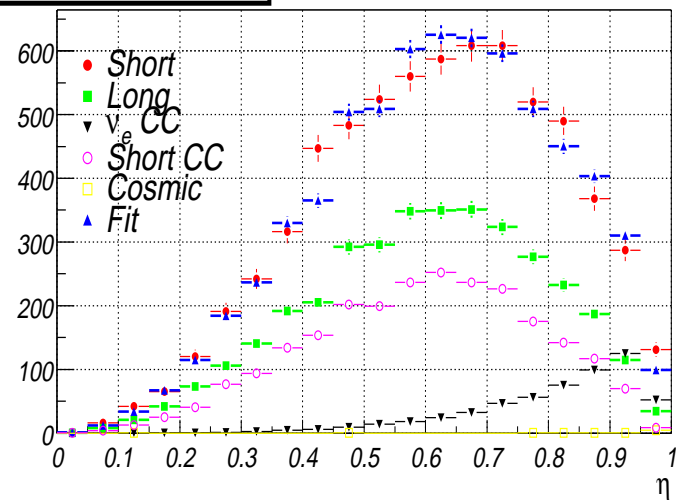
(Fit-Data)/Data



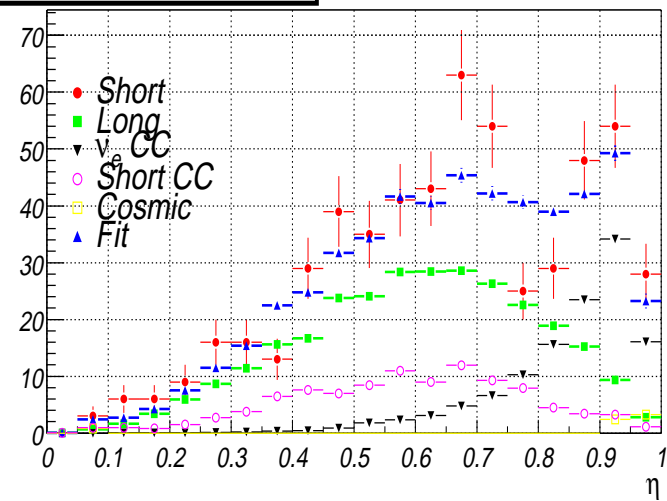
(Fit-Data)/Data



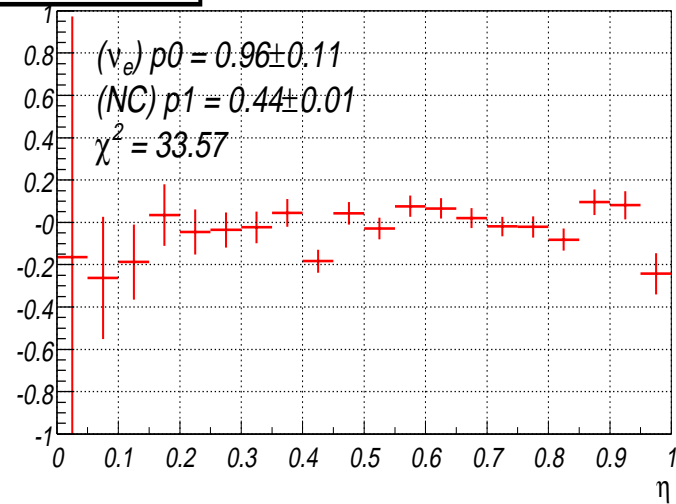
225-250 GeV, neutrino



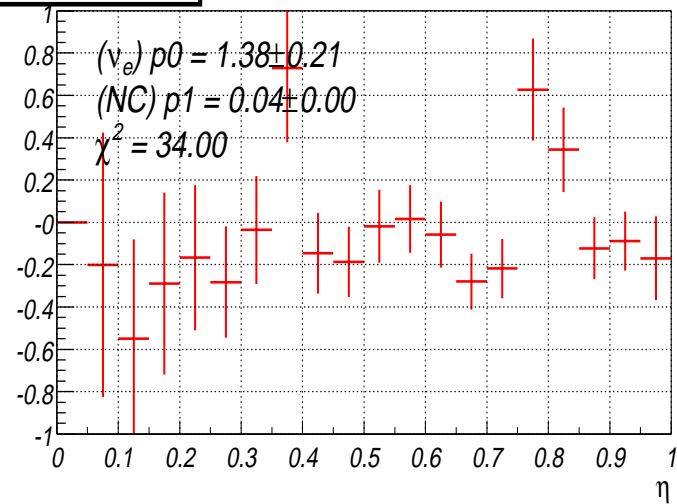
225-250 GeV, anti-neutrino



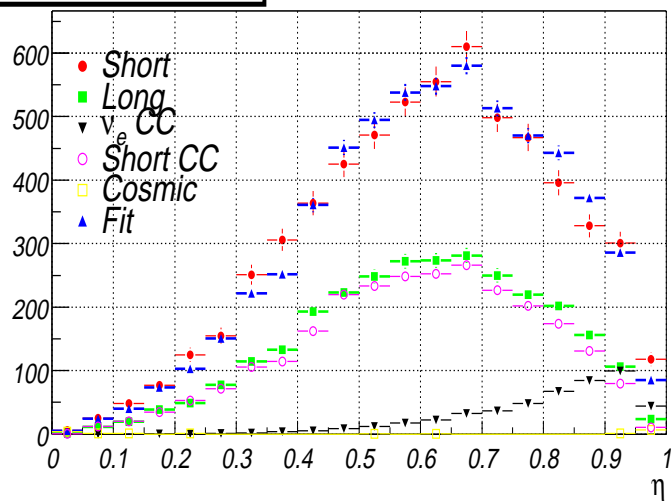
(Fit-Data)/Data



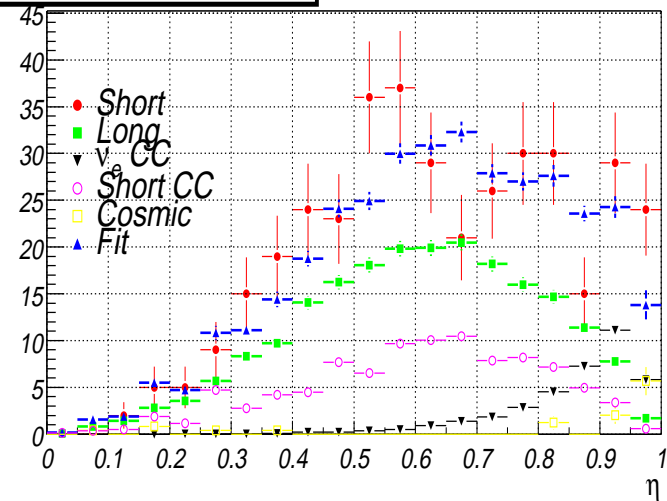
(Fit-Data)/Data



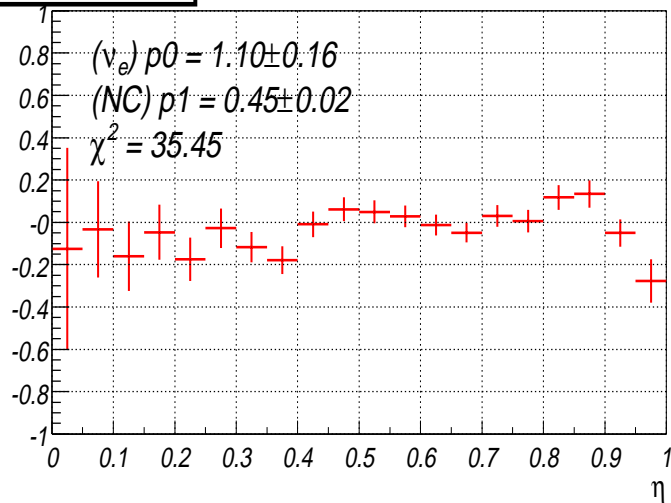
250-350 GeV, neutrino



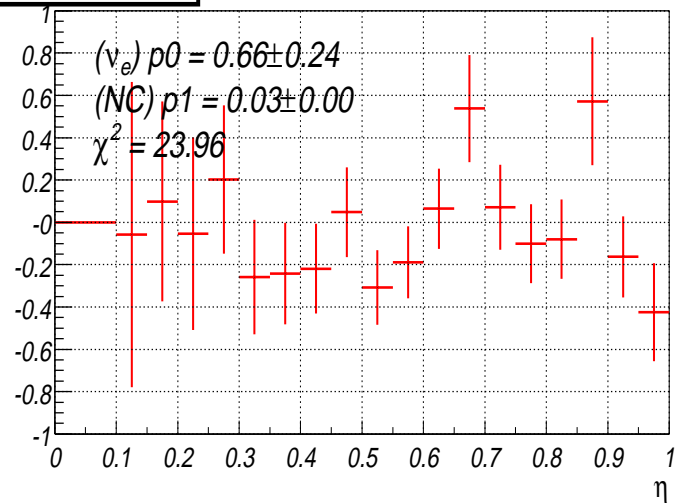
250-350 GeV, anti-neutrino



(Fit-Data)/Data



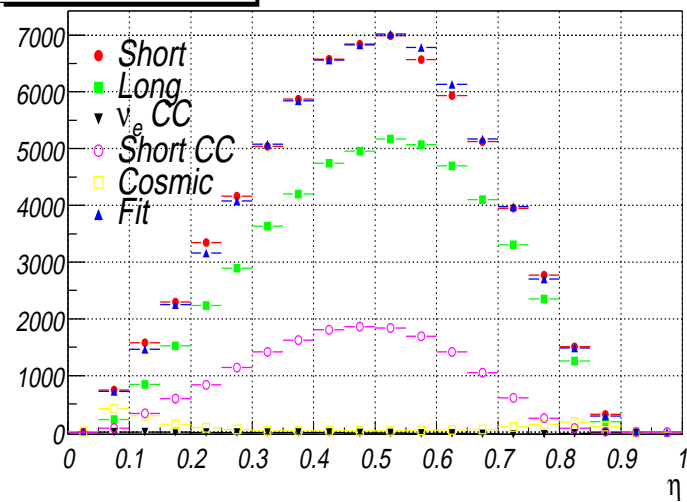
(Fit-Data)/Data



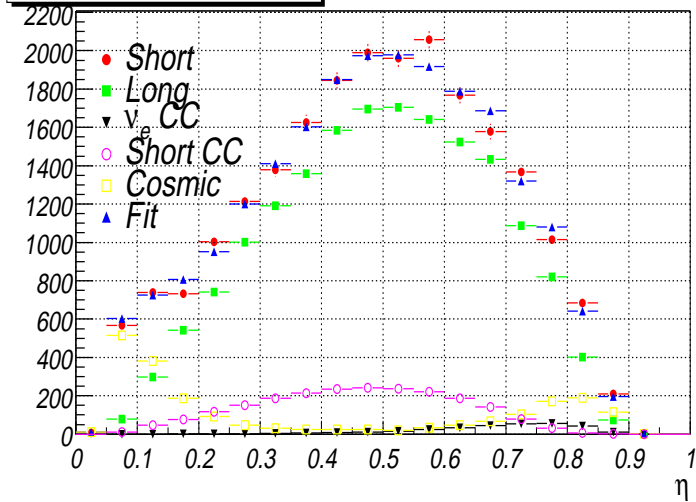
Appendix C

Data Fits η_2

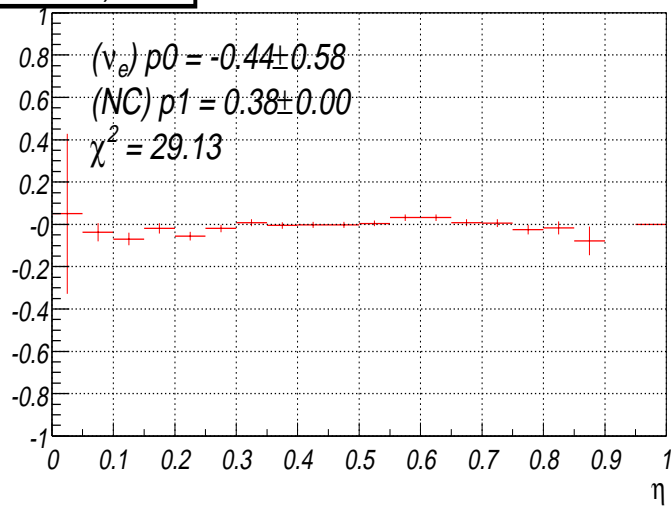
30-40 GeV, neutrino



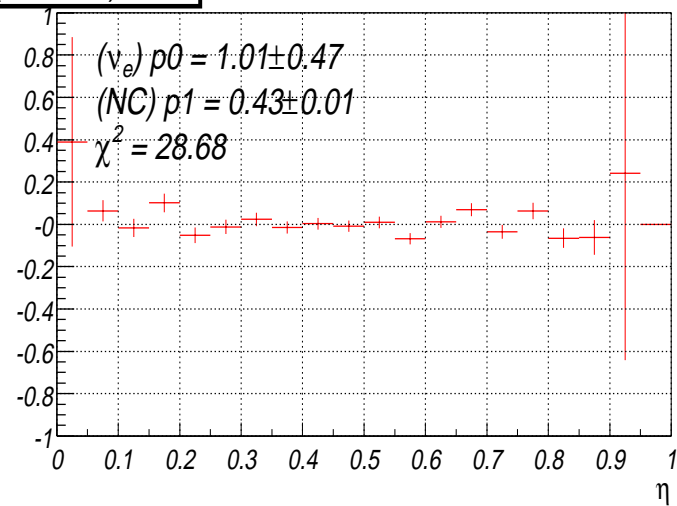
30-40 GeV, anti-neutrino



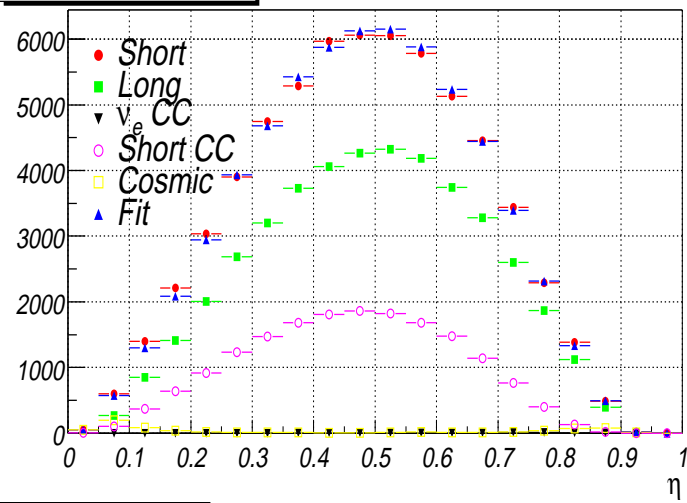
(Fit-Data)/Data



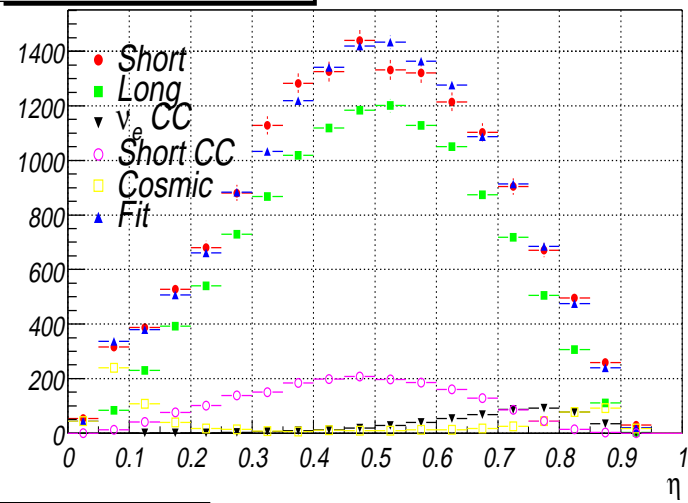
(Fit-Data)/Data



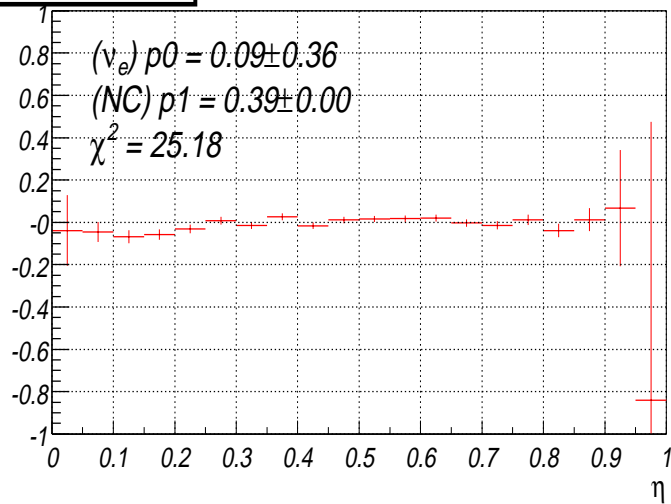
40-50 GeV, neutrino



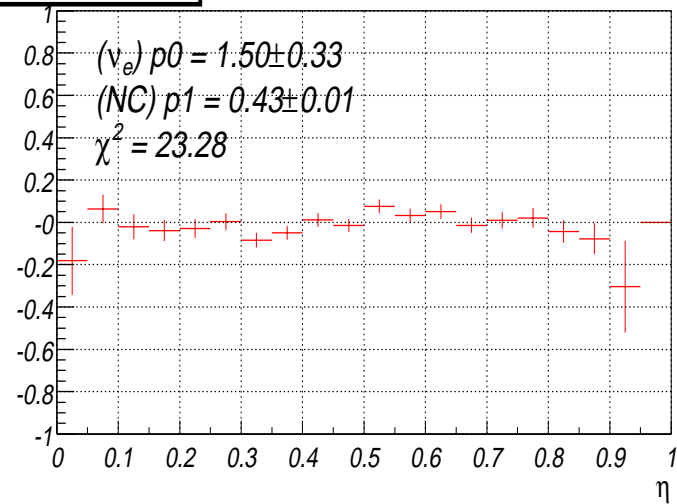
40-50 GeV, anti-neutrino



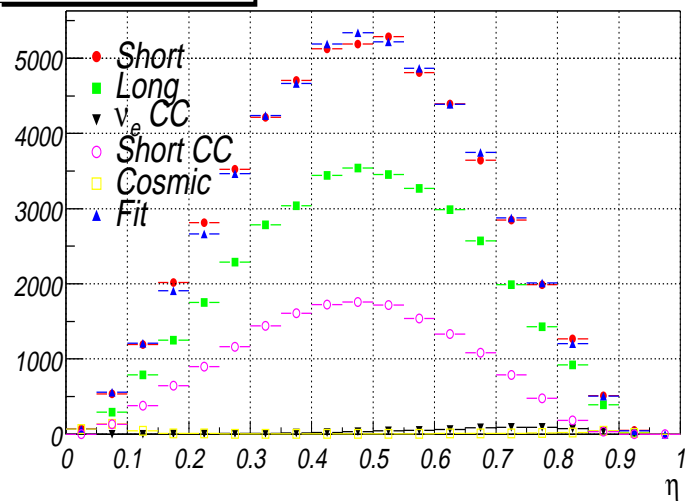
(Fit-Data)/Data



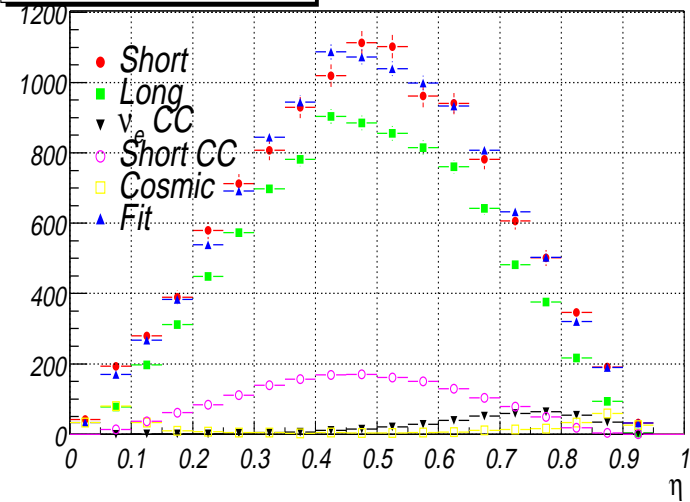
(Fit-Data)/Data



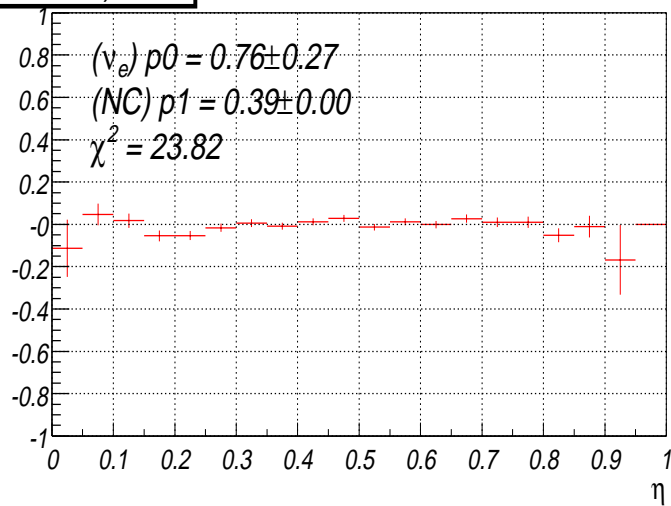
50-60 GeV, neutrino



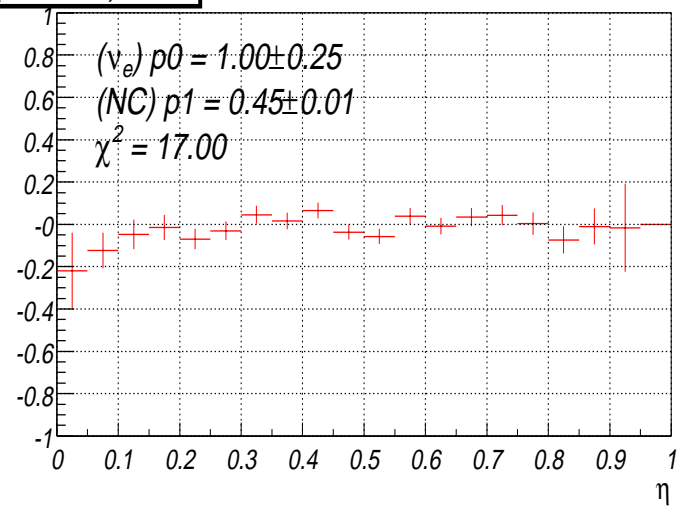
50-60 GeV, anti-neutrino



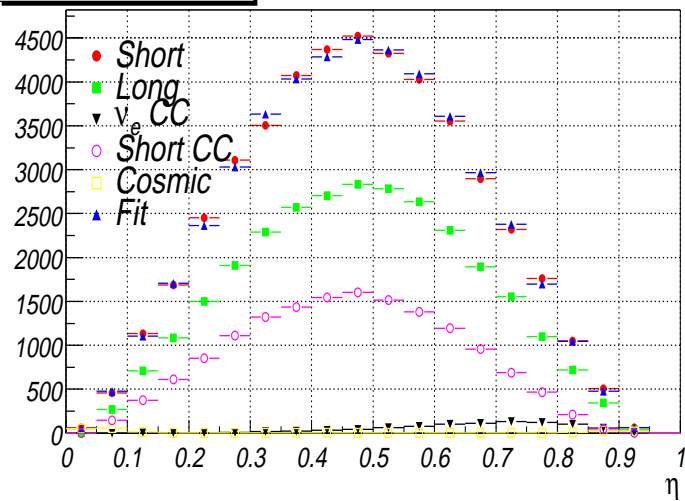
(Fit-Data)/Data



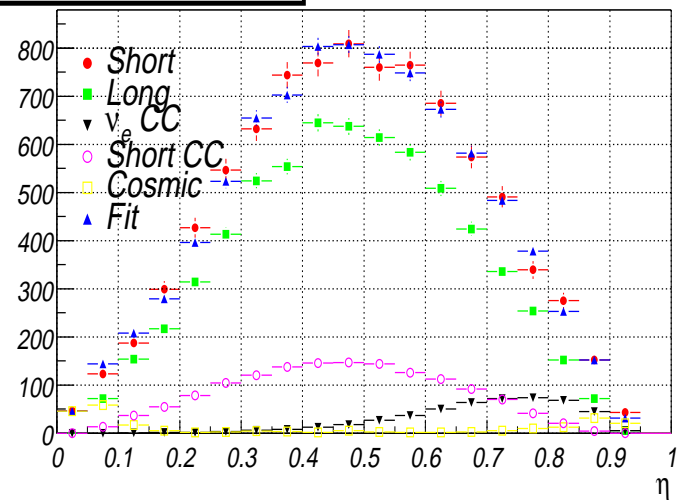
(Fit-Data)/Data



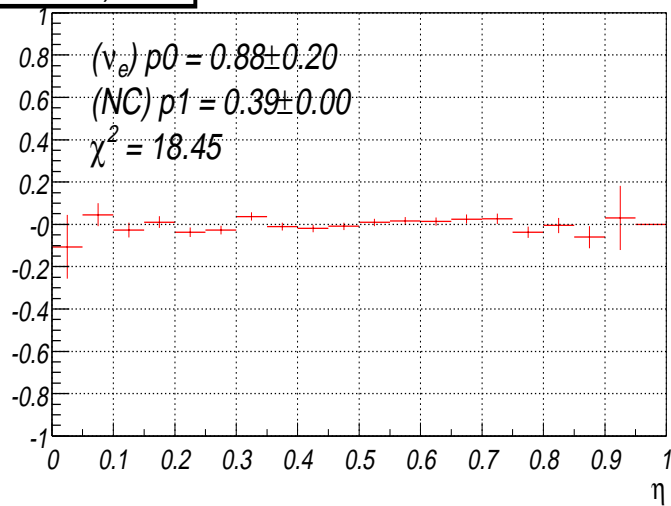
60-70 GeV, neutrino



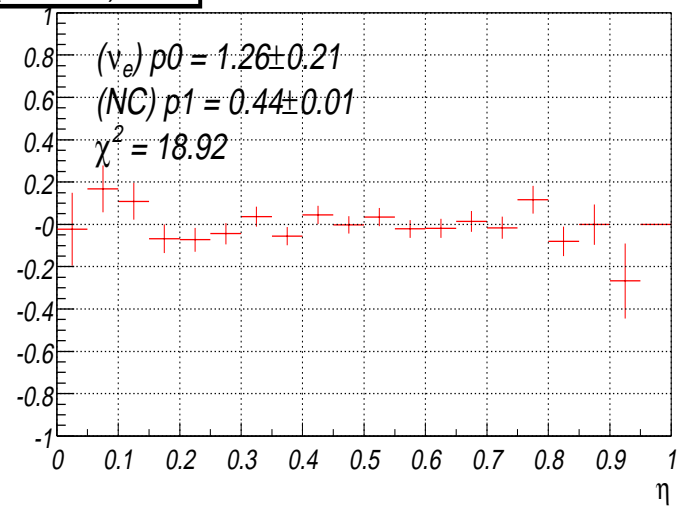
60-70 GeV, anti-neutrino



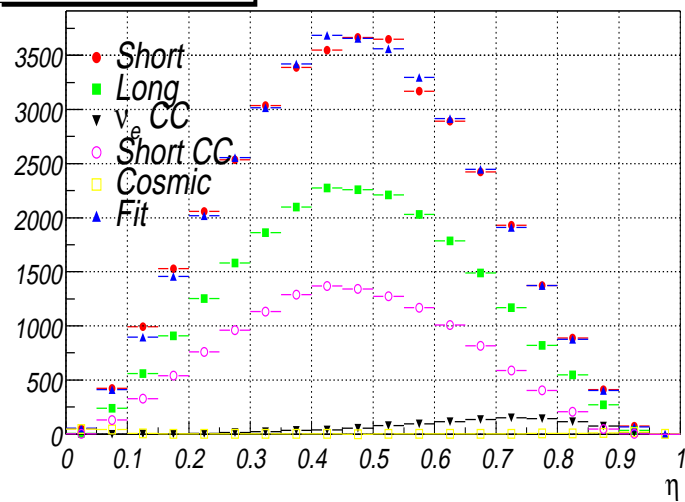
(Fit-Data)/Data



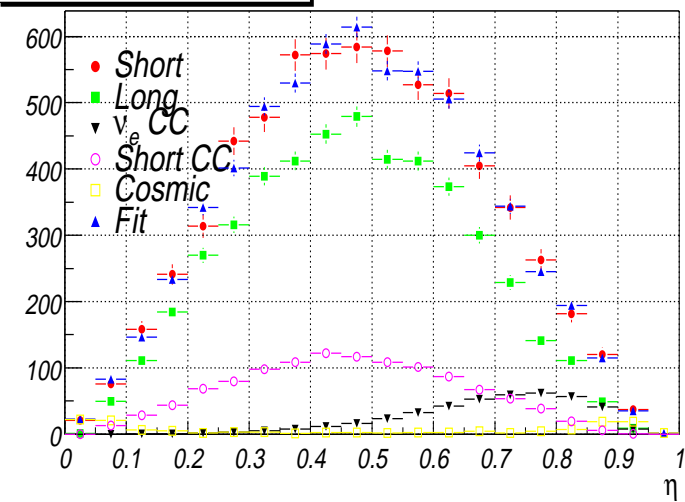
(Fit-Data)/Data



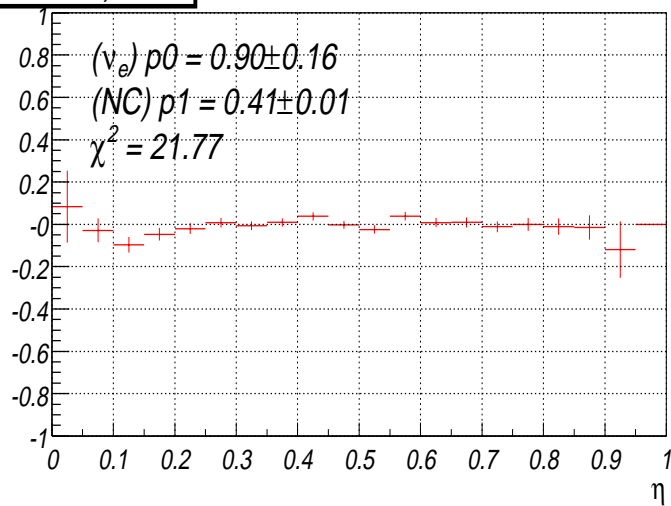
70-80 GeV, neutrino



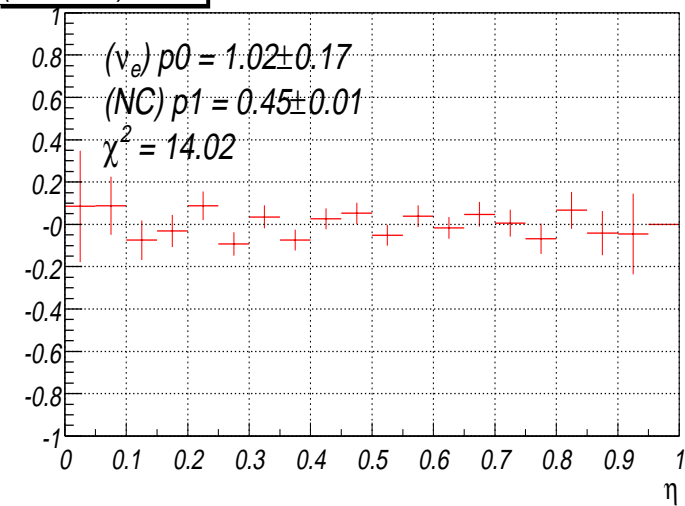
70-80 GeV, anti-neutrino



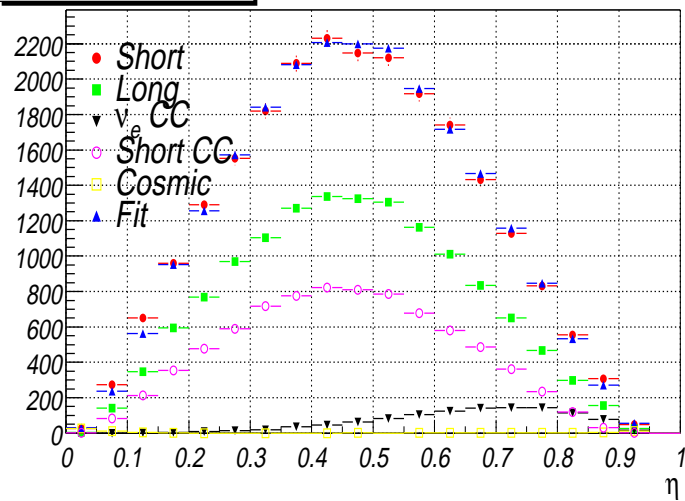
(Fit-Data)/Data



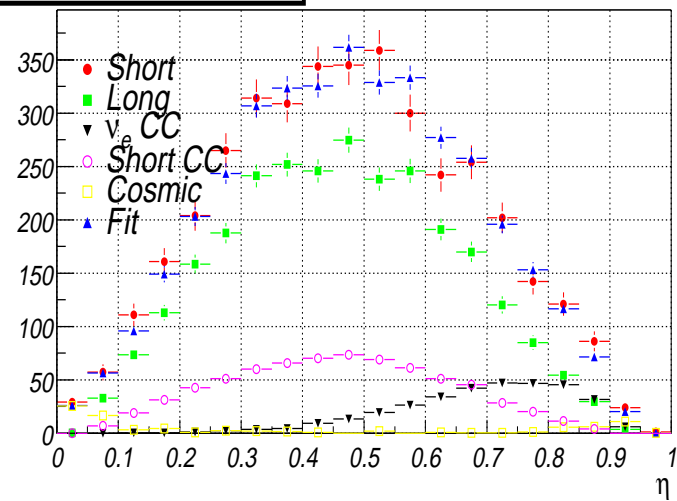
(Fit-Data)/Data



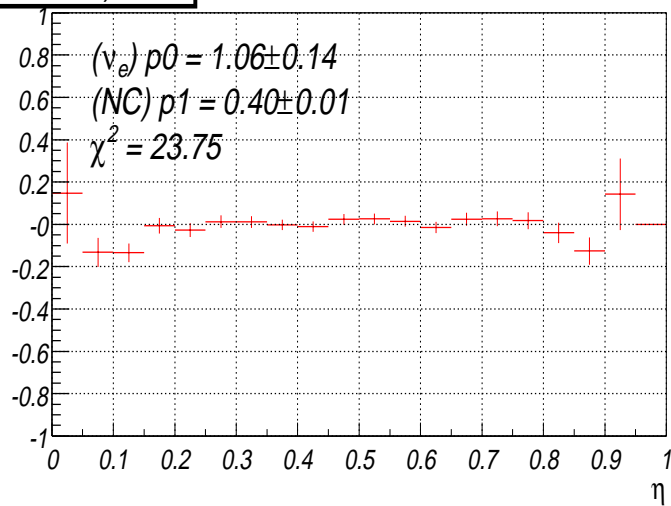
80-87 GeV, neutrino



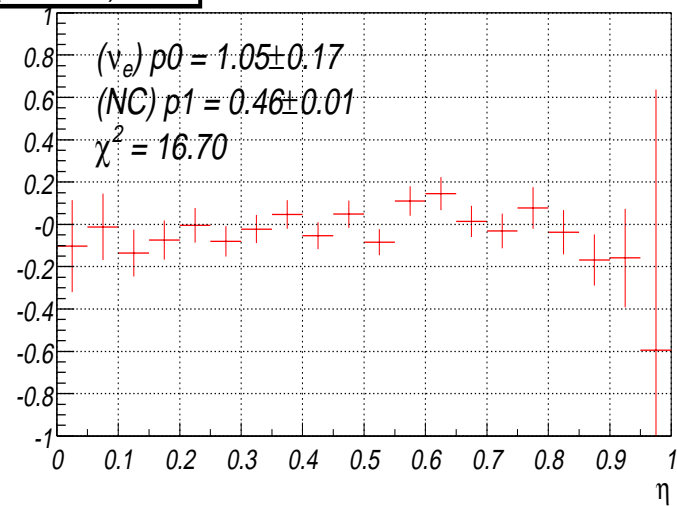
80-87 GeV, anti-neutrino



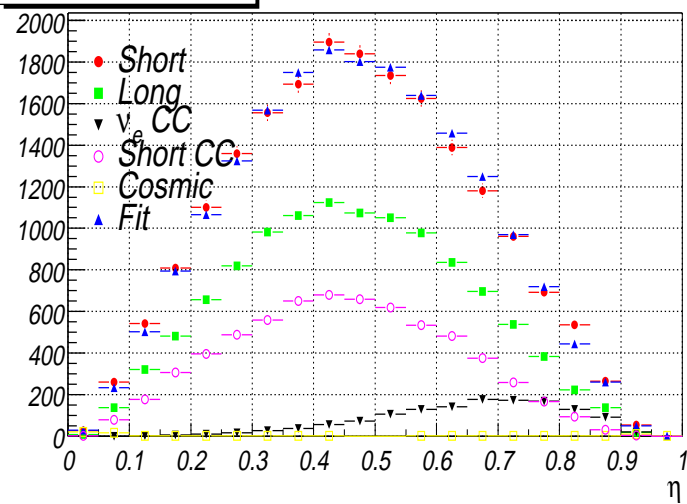
(Fit-Data)/Data



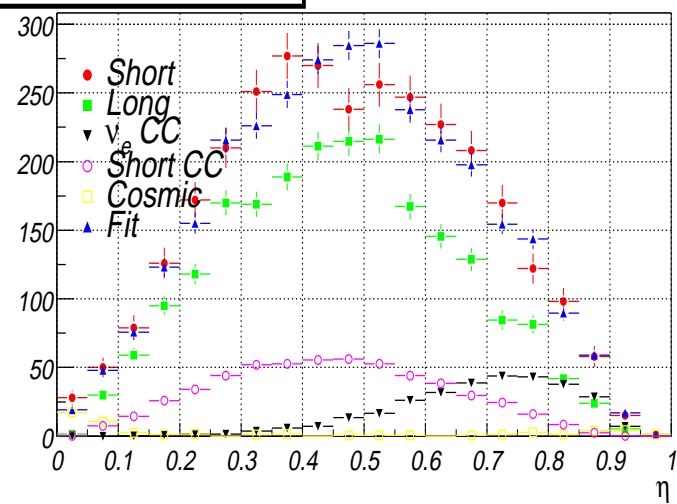
(Fit-Data)/Data



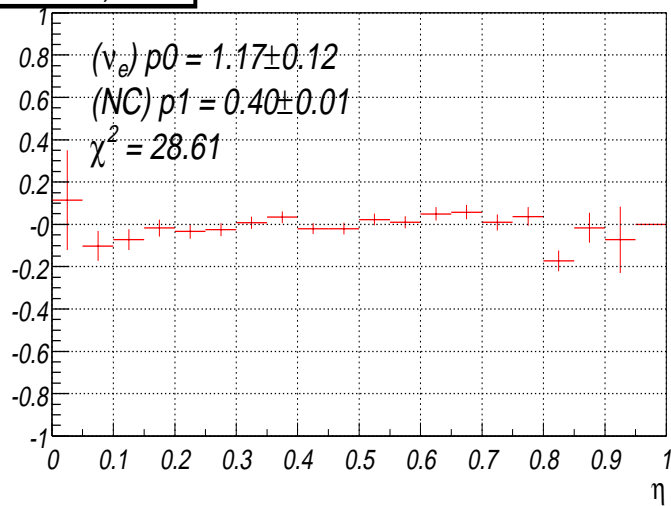
87-95 GeV, neutrino



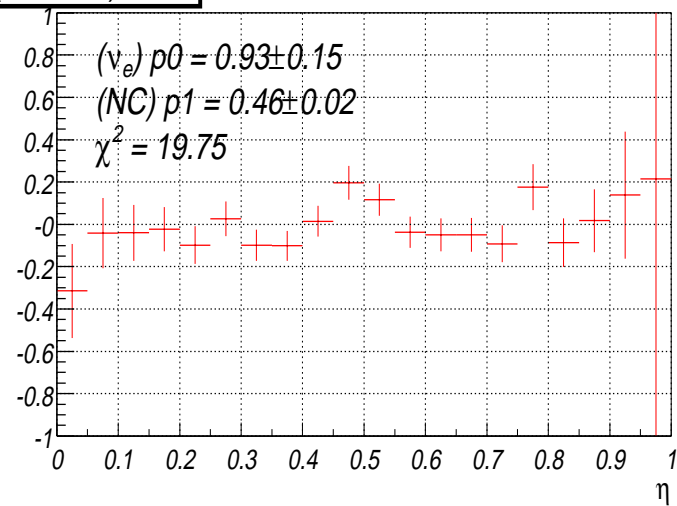
87-95 GeV, anti-neutrino



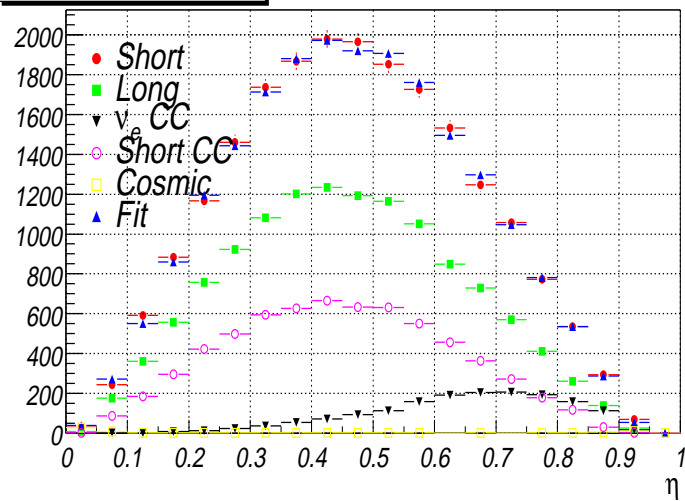
(Fit-Data)/Data



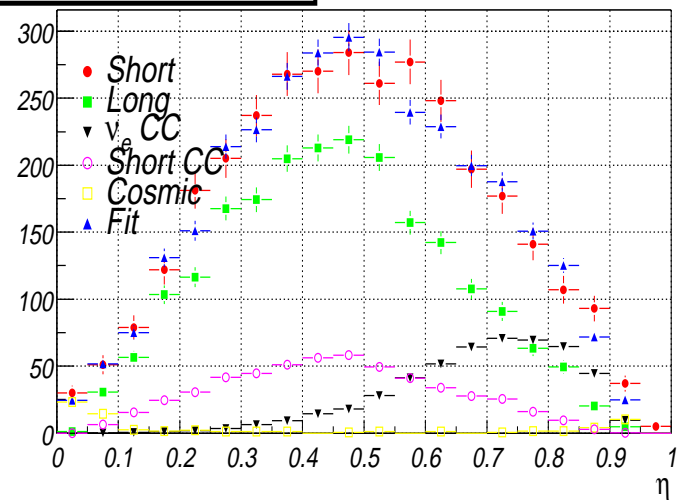
(Fit-Data)/Data



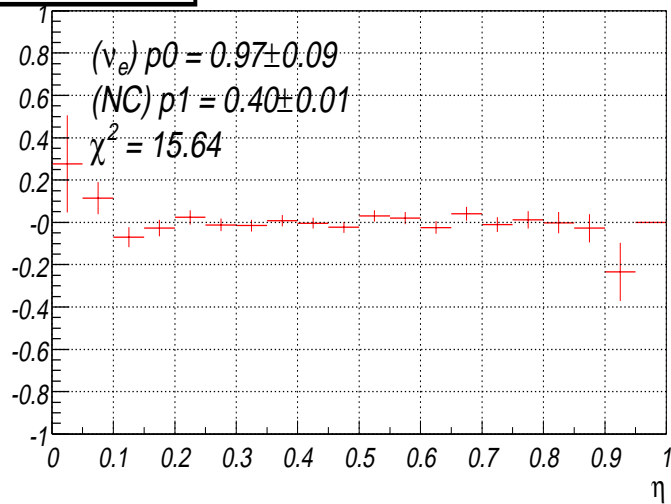
95-105 GeV, neutrino



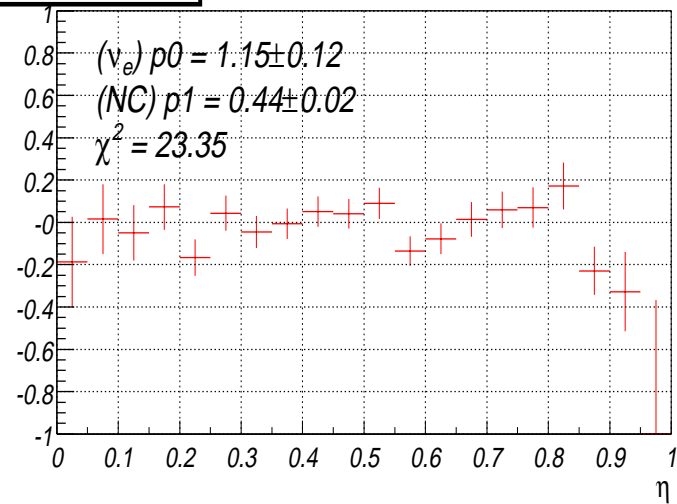
95-105 GeV, anti-neutrino



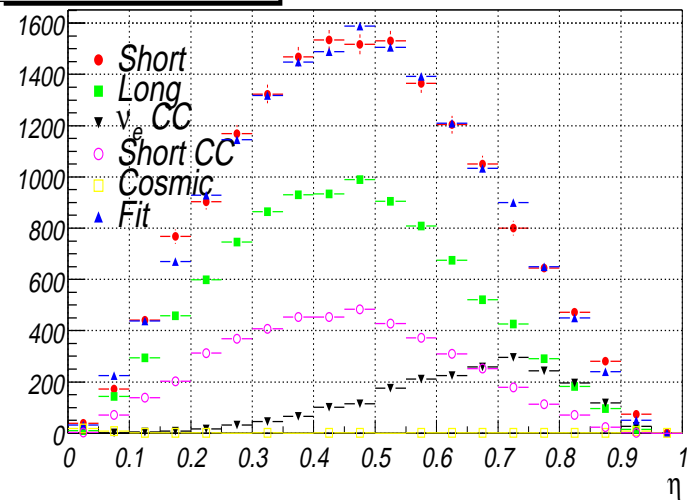
(Fit-Data)/Data



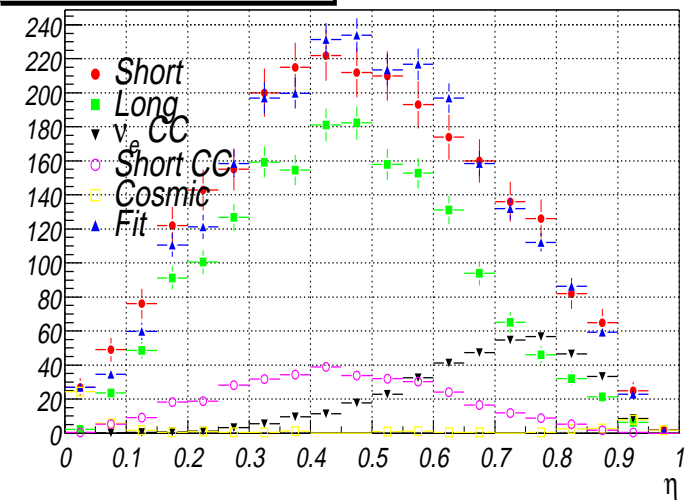
(Fit-Data)/Data



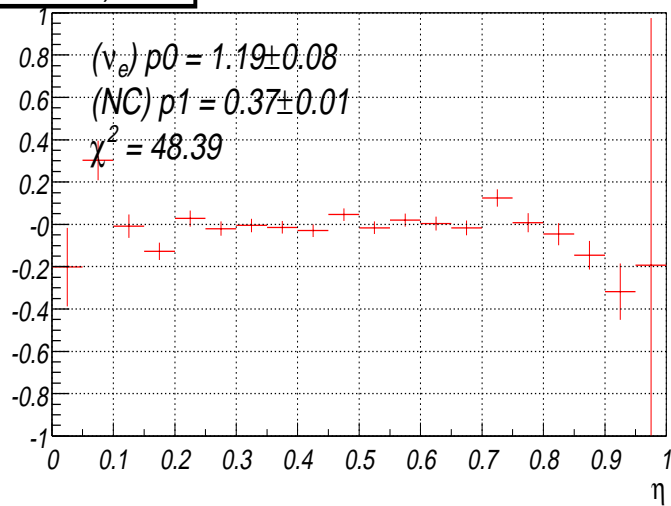
105-115 GeV, neutrino



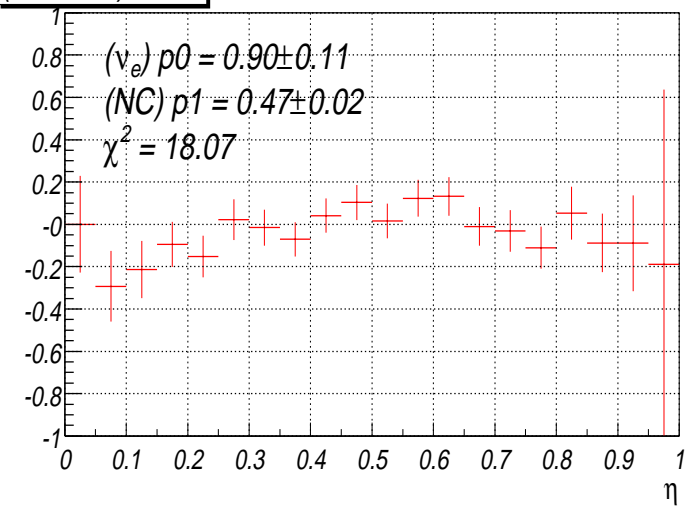
105-115 GeV, anti-neutrino



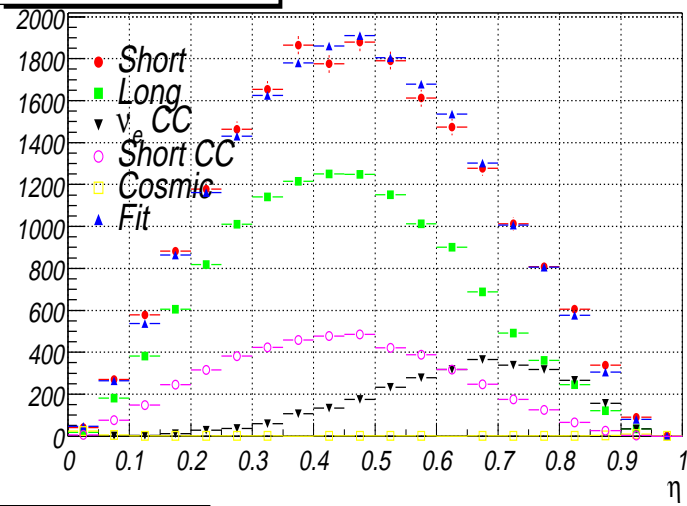
(Fit-Data)/Data



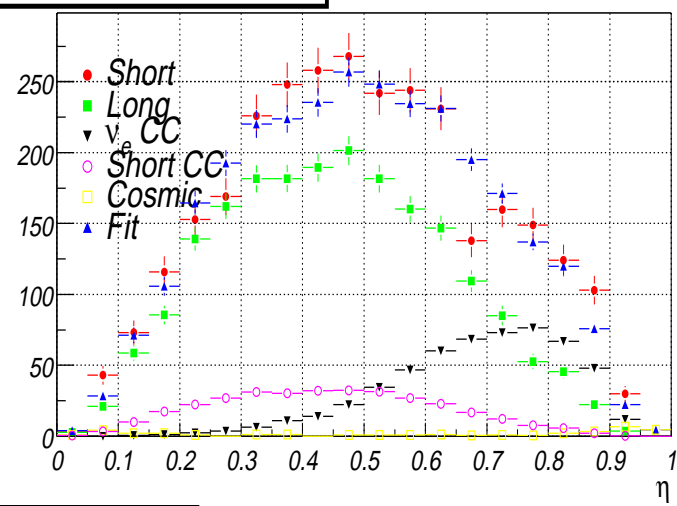
(Fit-Data)/Data



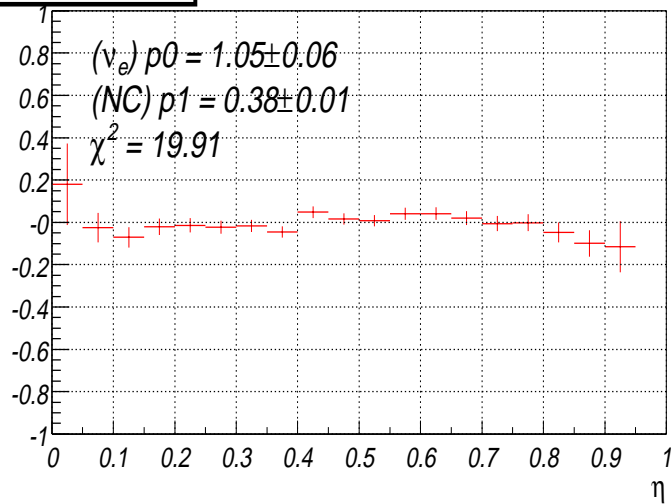
115-130 GeV, neutrino



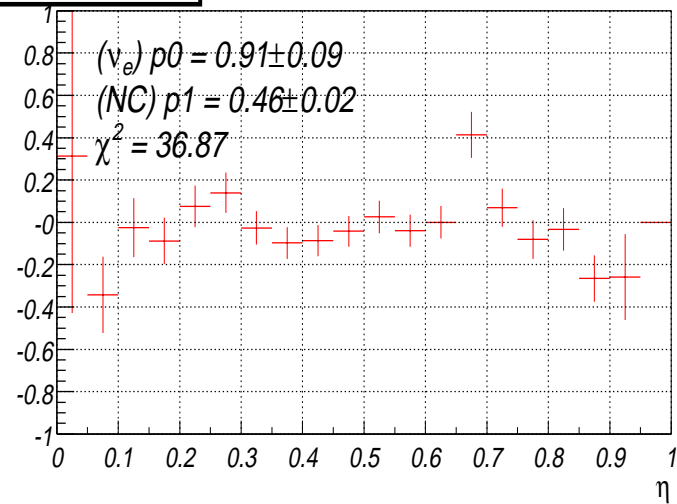
115-130 GeV, anti-neutrino



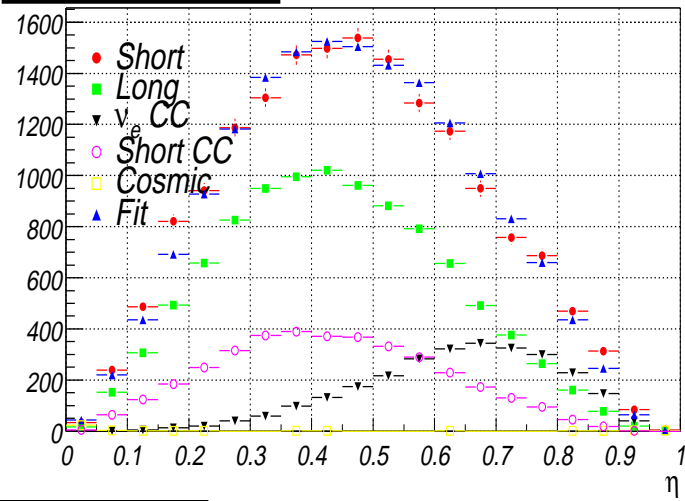
(Fit-Data)/Data



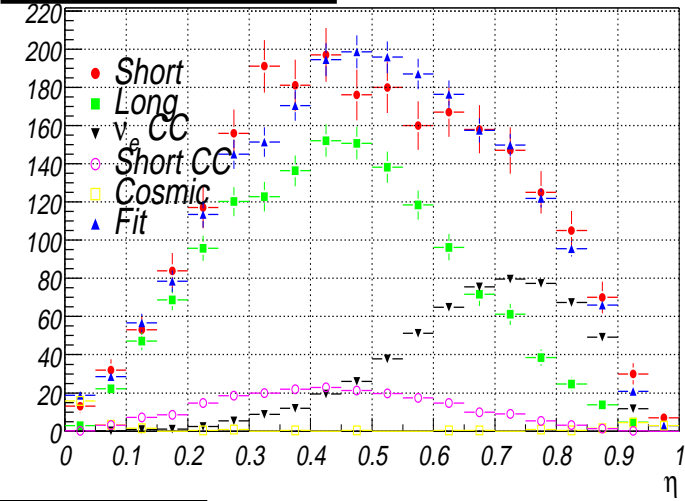
(Fit-Data)/Data



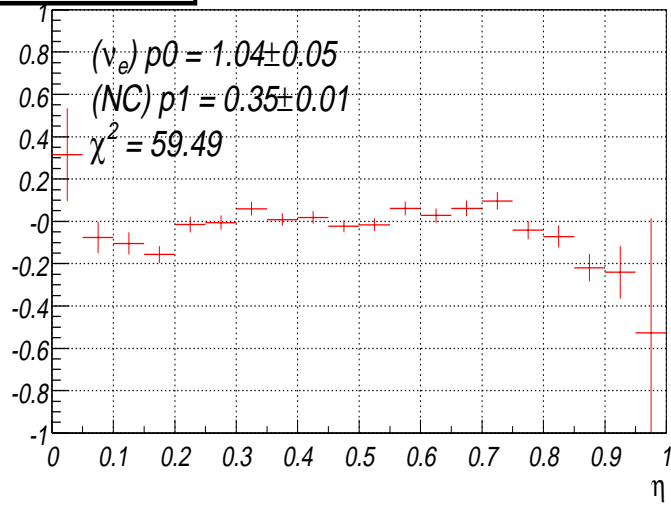
130-145 GeV, neutrino



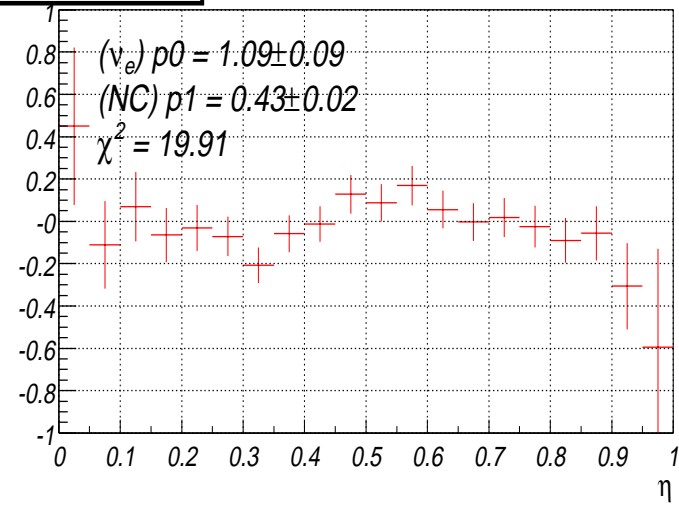
130-145 GeV, anti-neutrino



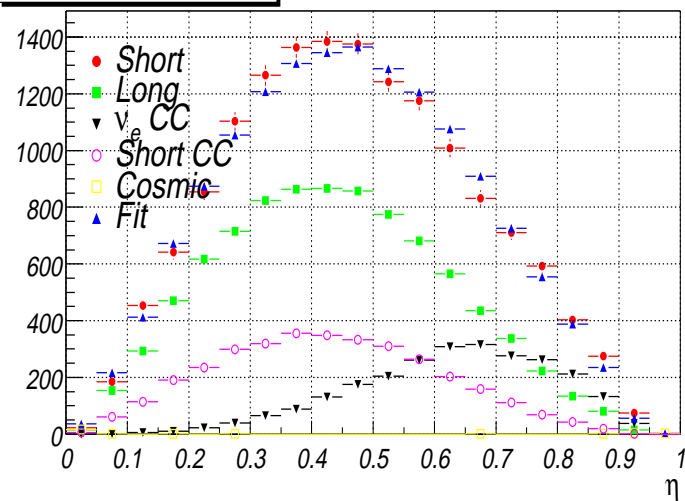
(Fit-Data)/Data



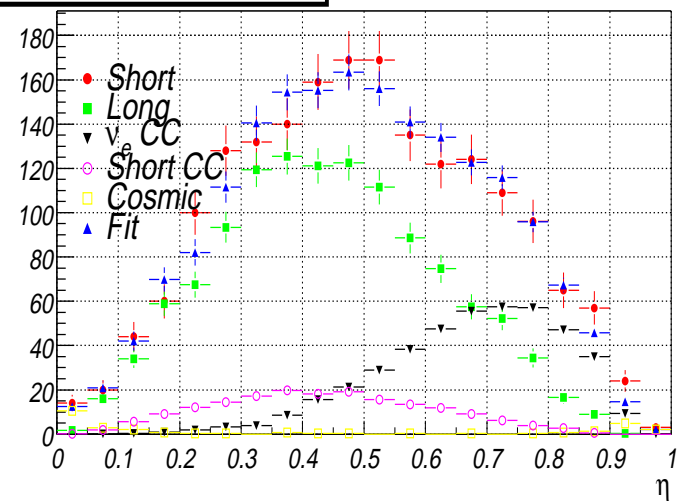
(Fit-Data)/Data



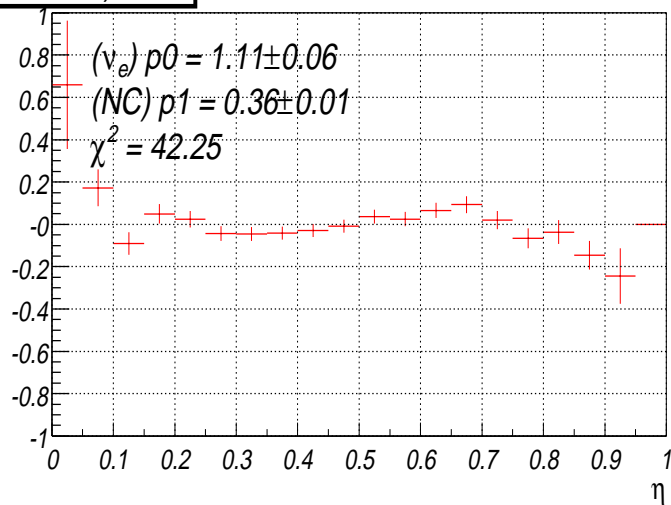
145-160 GeV, neutrino



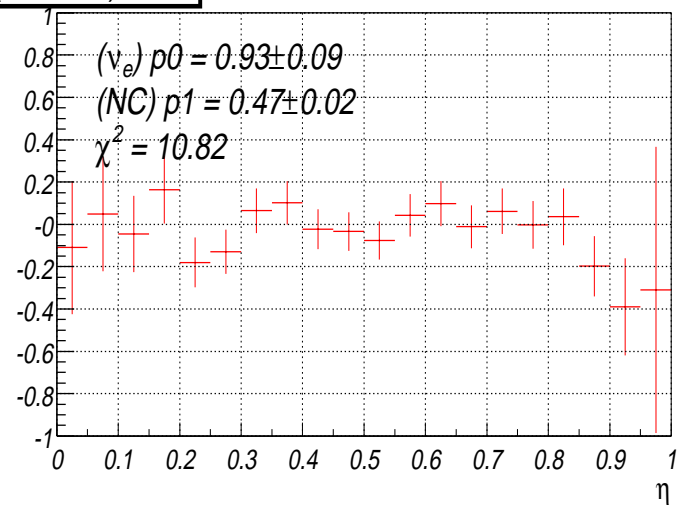
145-160 GeV, anti-neutrino



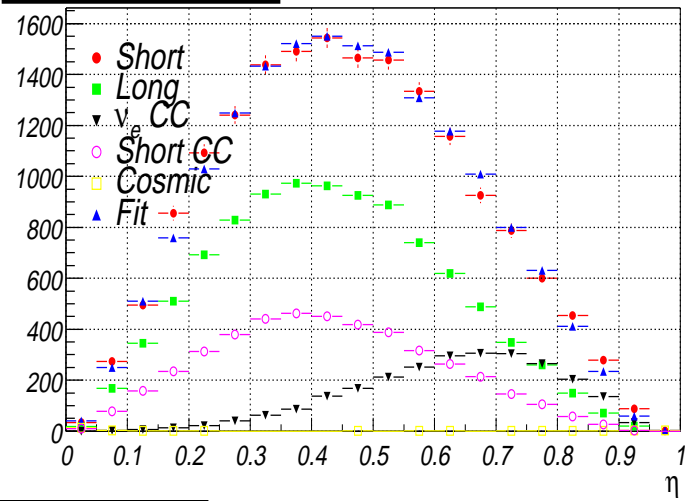
(Fit-Data)/Data



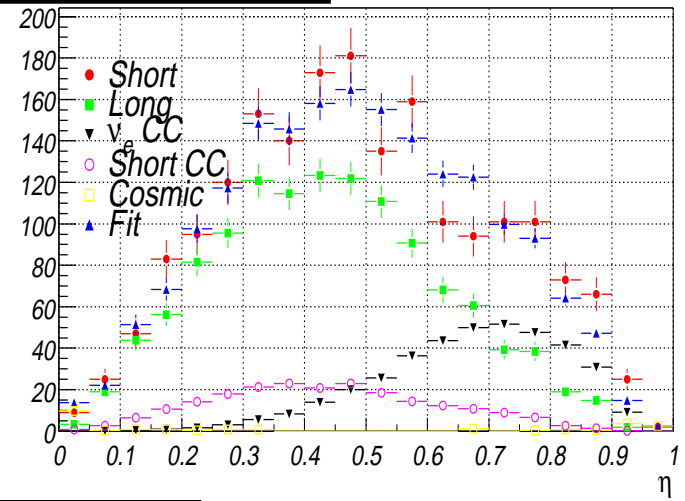
(Fit-Data)/Data



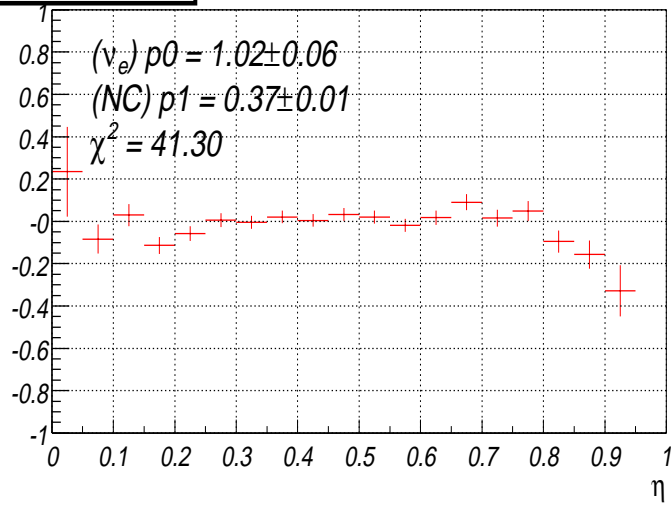
160-180 GeV, neutrino



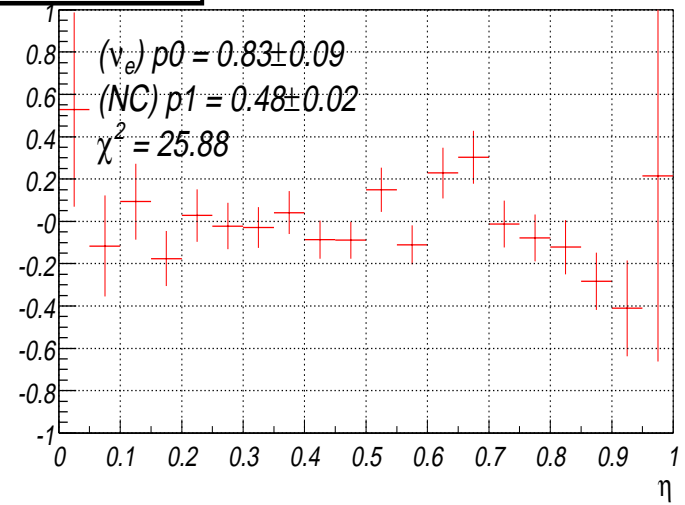
160-180 GeV, anti-neutrino



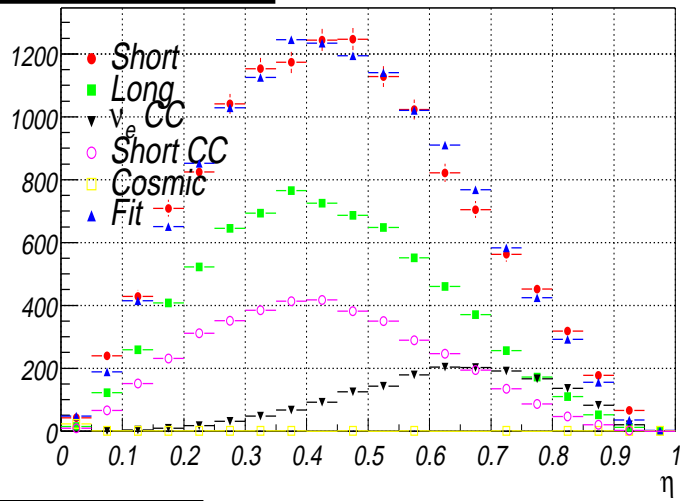
(Fit-Data)/Data



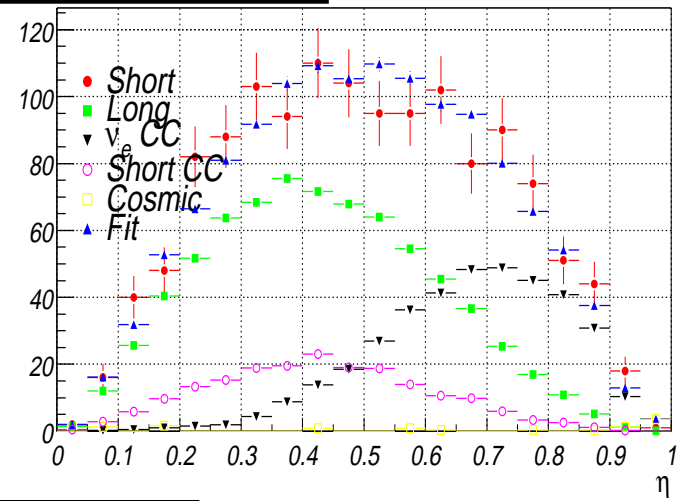
(Fit-Data)/Data



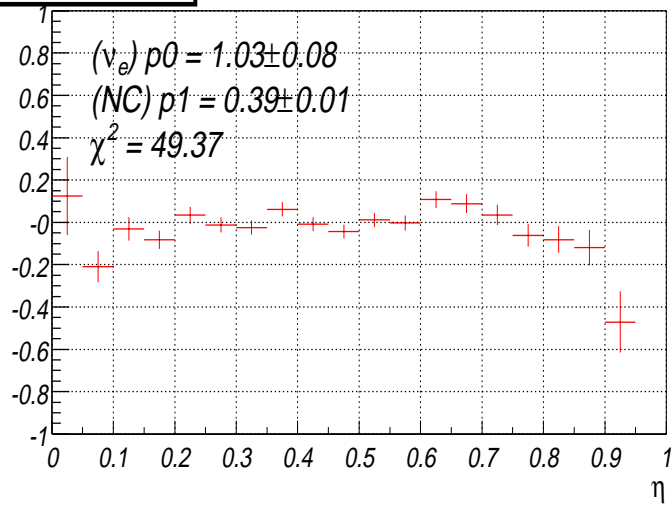
180-200 GeV, neutrino



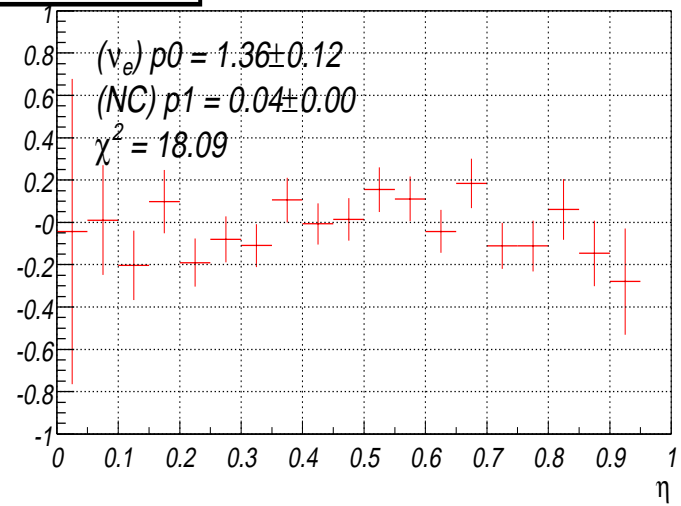
180-200 GeV, anti-neutrino



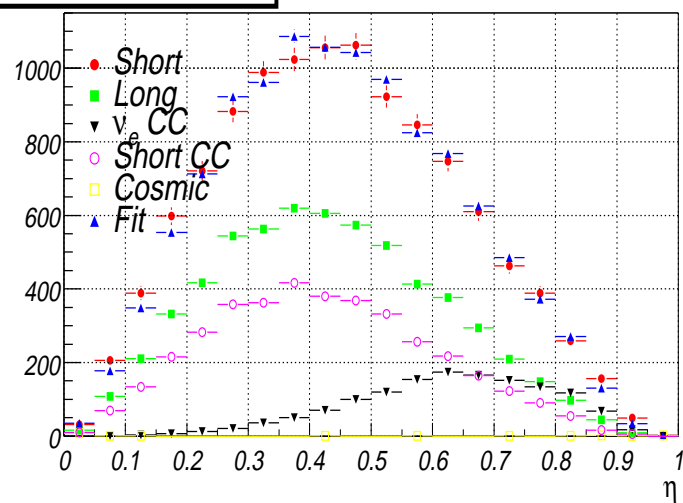
(Fit-Data)/Data



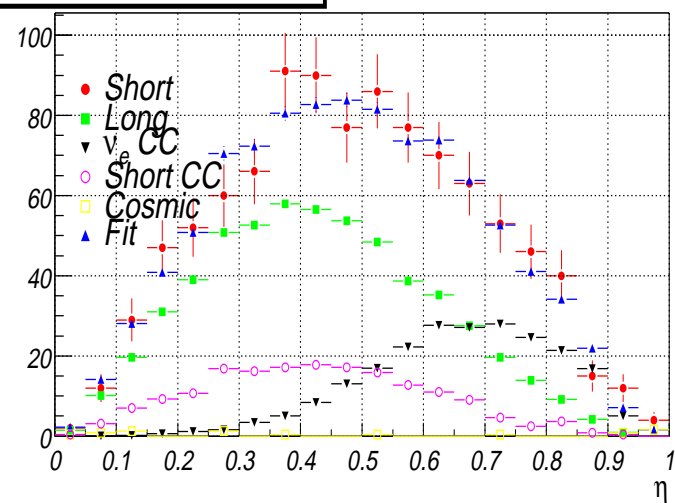
(Fit-Data)/Data



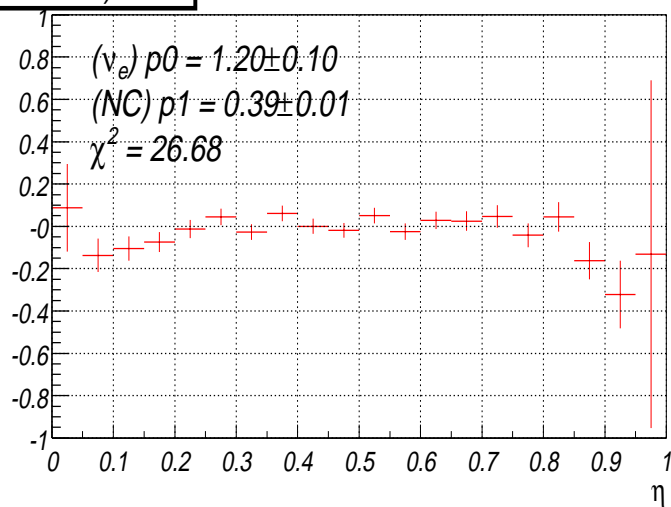
200-225 GeV, neutrino



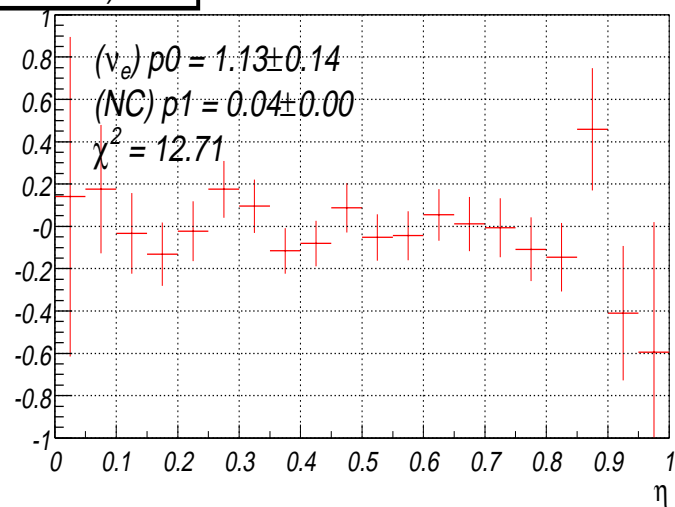
200-225 GeV, anti-neutrino



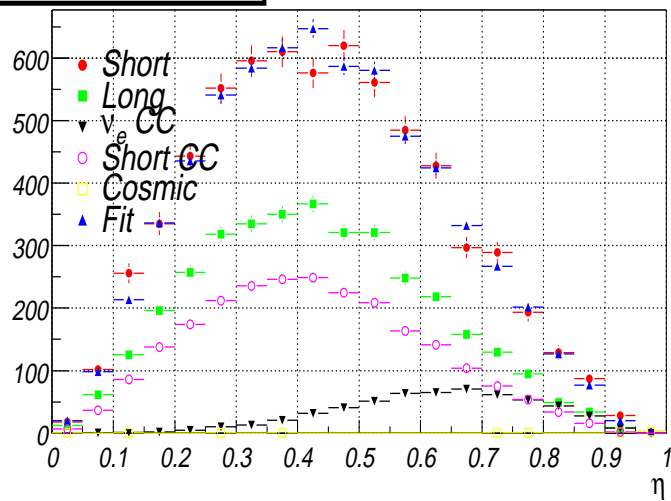
(Fit-Data)/Data



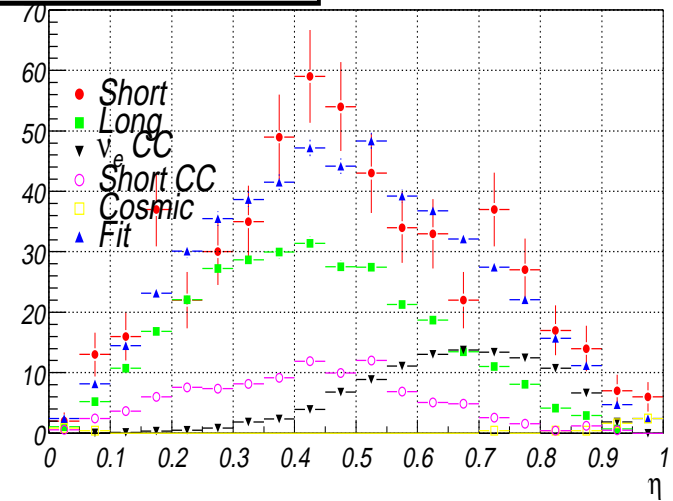
(Fit-Data)/Data



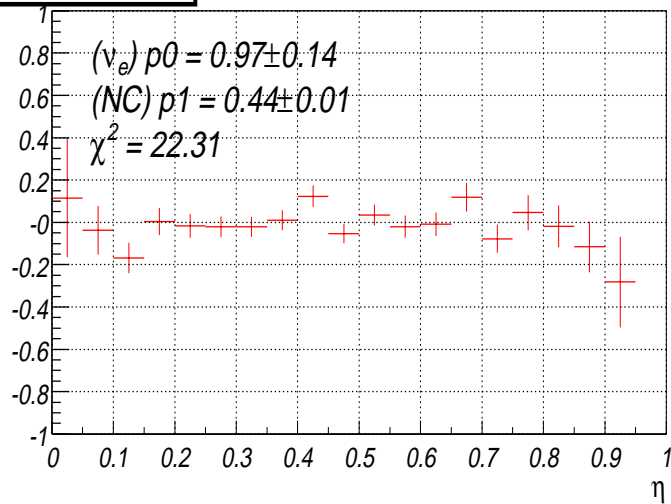
225-250 GeV, neutrino



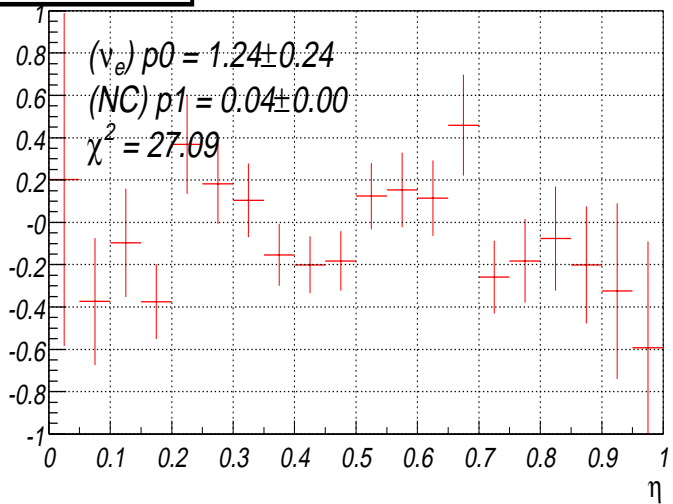
225-250 GeV, anti-neutrino



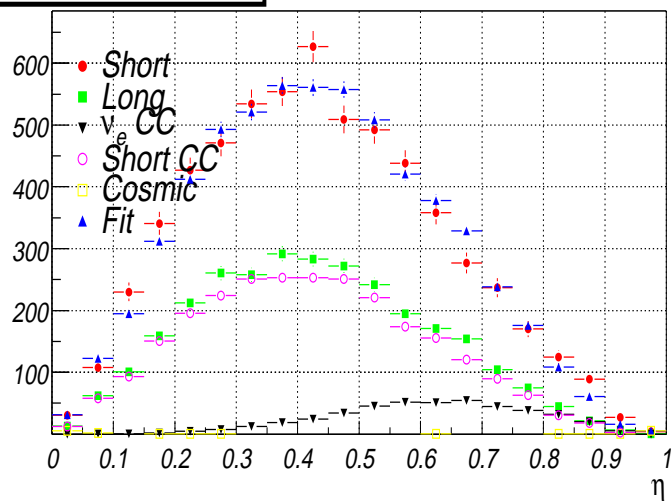
(Fit-Data)/Data



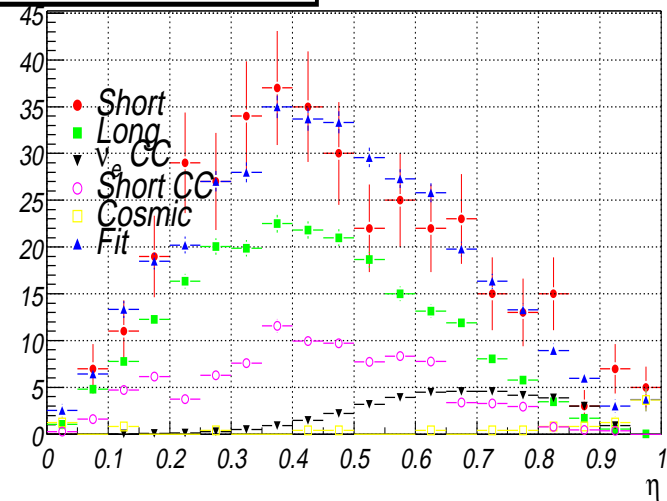
(Fit-Data)/Data



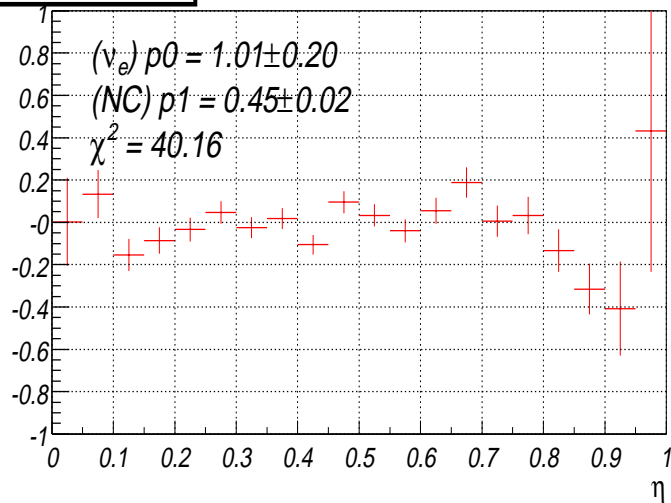
250-350 GeV, neutrino



250-350 GeV, anti-neutrino



(Fit-Data)/Data



(Fit-Data)/Data

